SYNTHESIS AND CHARACTERIZATION OF CORE/SHELL HYDROGEL NANOPARTICLES AND THEIR APPLICATION TO COLLOIDAL CRYSTAL OPTICAL MATERIALS

A Dissertation
Presented to
The Academic Faculty

By

Jonathan G. McGrath

In Partial Fulfillment
of the Requirements for the Degree
Doctor of Philosophy in the
School of Chemistry and Biochemistry
& Petit Institute for Bioengineering and Bioscience

Georgia Institute of Technology

May 2007

SYNTHESIS AND CHARACTERIZATION OF CORE/SHELL HYDROGEL NANOPARTICLES AND THEIR APPLICATION TO COLLOIDAL CRYSTAL OPTICAL MATERIALS

Approved by:

Dr. L. Andrew Lyon, Advisor
School of Chemistry and Biochemistry
& Petit Institute for Bioengineering and Bioscience
Georgia Institute of Technology

Dr. Victor Breedveld
School of Chemical & Biomolecular Engineering
Georgia Institute of Technology

Dr. Art Janata
School of Chemistry and Biochemistry
& Petit Institute for Bioengineering and Bioscience
Georgia Institute of Technology

Dr. Facundo Fernandez
Chemistry and Biochemistry
& Petit Institute for Bioengineering and Bioscience
Georgia Institute of Technology

Dr. Boris Mizaikoff
School of Chemistry and Biochemistry
& Petit Institute for Bioengineering and Bioscience
Georgia Institute of Technology

Date Approved: January 10th, 2007

ACKNOWLEDGEMENTS

All of the following people have helped me be to become a better, more educated person than I was prior to arriving at Georgia Tech. Through this graduate school adventure, I have learned a great deal about science, the world, and myself. Thank you for sharing in this experience with me.

I would like to thank: God, first and foremost, for making this experience possible. Without His guidance, who knows where I would be. My parents and sister, for allowing me to leave home at the age of 16 to attend the Governor's School of Science and Math. This opportunity provided a tremendous foundation for my education. My advisor, L. Andrew Lyon, for his steadfast support and the opportunity to work on many diverse projects, which increased the scope of my research. His positive enthusiasm for research and his creative ideas have made my graduate school experience a very enjoyable one. Past and present Lyon group members: Clint, Jay, Mike, Satish, Christine, Stella, Jongseong, Caroline, Neetu, Bart, Ashlee, Courtney, Hyungie, Zhiyong, Toni, and Daisuke. To our newest member, Grant, who will hopefully benefit from this document. Also, the undergrads who have humored me and allowed me to practice my teaching skills: Kristie, Thomas, Ryan, Kevin, Dustin. My colleagues: Jae Kyu Cho, Robert Bock, Tracie Owens, Victor Breedveld, Christine Kranz. Their assistance and collaboration have been invaluable. My Atlanta friends: AP Black soccer team, pick-up soccer friends, the Sanderson family, Karl, Buck, Kevin.

My graduate experience (and my life) would not be complete without special recognition of my fiancée, Kate. Her love and support throughout our courtship has been indescribable. I look forward to our new life and adventures together. I have been truly blessed and CANNOT wait to try out our new moniker: *Dr.* and *Mrs.* McGrath.

TABLE OF CONTENTS

LIST OF TABLES

LIST OF FIGURES

LIST OF SYMBOLS AND ABBREVIATIONS

% wt	percent by weight
a	particle radius
AAc	Acrylic acid
Ag	silver
AFM	atomic force microscopy
APS	ammonium persulfate
BIS	*N,N'*-methylene(bisacrylamide)
˚C	degrees Celsius
C/S	core/shell
d	particle lattice spacing
d	dimensionality (Chapter 3)
D	diameter
D_T	diffusion coefficient (Chapter 3)
DIC	differential image contrast
fcc	face-centered cubic
IR	infrared spectroscopy
k_b	Boltzmann's constant
LCST	lower critical solution temperature
MALLS	multi-angle laser light scattering
mM	milli-molar
MSD	mean-squared displacement
η	viscosity
NIPAm	N-isopropylacrylamide
PCS	photon correlation spectroscopy
pNIPAm	poly-*N*-isopropylacrylamide
pS-*co*-NIPAm	poly(styrene-*co*-*N*-isopropylacrylamide)
pNIPAm-*co*-AAc	poly(*N*-isopropylacrylamide-*co*-acrylic acid)
R_g	radius of gyration
R_h	hydrodynamic radius

RI	Refractive index
rcf	relative centrifugal force
SDS	sodium dodecyl sulfate
SEM	scanning electron microscopy
T	temperature
TEM	transmission electron microscopy
Tg	glass transition temperature
TMC	total monomer concentration
UV	ultraviolet spectroscopy
VIS	visible spectroscopy
VPT	volume phase transition
VPTT	volume phase transition temperature

SUMMARY

This dissertation describes the use of spherical core/shell type micro- and nanoparticles as building blocks for the fabrication of colloidal crystals. The polymer component used in all of the projects that are described herein is poly-*N*-isopropylacrylamide (pNIPAm). The polymeric identity of particles composed of this soft, hydrogel material, which is also thermoresponsive, contributes to the self-assembly of such particles to form ordered structures. Chapter 2 examines a characterization technique using fluorescence resonance energy transfer (FRET) to investigate the structure of particles that possess a core/shell topology. Chapters 4-6 investigate strategies to impart both hard (dense core) and soft (flexible shell) properties to the particles by using styrene as the main component in a copolymer synthesis with pNIPAm (pS-*co*-NIPAm particles). The resulting crystal assemblies, which could be formed by simple drying procedures, were demonstrated to be robust and their application as processable, photonic inks is also investigated. Chapter 7 examines the ability to cross-link these crystals together by simple heating methods to produce robust films, and the optical properties of these crystal films could be tuned by simple rehydration. Chapters 3 and 5 examine the synthesis and self-assembly strategies of core/shell particles using the properties of pNIPAm shell layers that have been added to different types of core particles (silver or pS-*co*-NIPAm) for the purposes of fabricating colloidal crystals using thermal annealing procedures. Chapter 8 explores the use of silver particles as tracers for the characterization of colloidal crystals composed of thermally annealed colloidal crystals composed of pNIPAm hydrogel particles.

CHAPTER 1

INTRODUCTION TO COLLOIDAL CRYSTALS AND THE ADVANCEMENTS IN FUNCTIONALITY AND ASSEMBLY USING CORE/SHELL PARTICLES AS BUILDING BLOCKS

1.1 Introduction

The ability to fine-tune the properties of micro- and nanoscale polymeric materials increases the diversity of their use in the field of nanotechnology. Specific synthetic techniques are typically necessary to control the introduction of such chemical functionalities to achieve new properties. Particular synthetic designs can also be employed to introduce multiple functionalities that can be localized within the structure of the material to serve distinct purposes. One type of micro- and nanoparticle topology is the core/shell configuration, where different localized functionalities are provided by the specific identity of these distinct regions.

The specific types of core/shell particles that will be discussed in this work are composed of hydrogel-forming polymers. These colloidal materials possess many unique properties based on the their structural design[1-6] and have demonstrated their usefulness in many fields, including biomedicine[7-9] and drug delivery.[3,10,11] The main objective of this work will be to use core/shell particles to produce colloidal assemblies. The main constituent of the hydrogel particles that are investigated herein is poly-*N*-isopropylacrylamide (pNIPAm), which is a temperature-responsive polymer. Such responsive properties are particularly beneficial for many of the applications described above.[2,12]

Uniform spherical particles can also be assembled into 2D and 3D arrangements as a result of specific interparticle interactions. These assemblies can demonstrate optical diffraction due to their long-range order and dielectric periodicity.[13,14] Such assemblies

are classified as colloidal crystals and can be fabricated by a variety of self-assembly techniques. The thermoresponsive properties of pNIPAm particles can also be exploited to fabricate ordered assemblies via self-assembly using thermal annealing procedures.[15-18] The focus of the present work is to gain a fundamental understanding of the application of well-designed core/shell micro- and nano-particles as building blocks for colloidal crystals to enhance their self-assembling capabilities, stability, and their potential as photonic components for optical applications.

1.2 Advanced Assemblies Using Hydrogel Micro- and Nanoparticles

1.2.1 Core/Shell Micro- and Nanoparticles

Spherical polymeric micro- and nanomaterials serve as useful constructs due to their ease of synthesis,[19-21] which can yield particles that possess a myriad of functional groups. These functionalities can be included as comonomers[22] in the polymeric synthesis or can be attached using post-polymerization modification procedures.[23] A multifunctional core/shell construct can be achieved by employing consecutive syntheses[24-26] or utilizing other synthetic designs.[27-29]

The method of aqueous, free-radical precipitation polymerization is particularly useful for the synthesis of colloidally stable core/shell particles using the temperature responsive polymer pNIPAm. The polymerization is typically performed at ~70 °C, which is well above the entropically-favored phase transition of the pNIPAm polymer, which occurs at temperatures above the lower critical solution temperature (LCST) for pNIPAm polymer (~31 ºC). As oligoradicals form in solution during the synthesis, they phase separate at temperatures above the LCST to form collapsed, insoluble polymer globules that can act as nucleation sites for additional polymer growth.[2,30-32] Spherical particles can be created by using a cross-linking comonomer to form a polymer network that retains its shape upon swelling. The resulting particle adopts a swollen conformation

at low temperatures due to hydrophilic interactions, where hydrogen bonding occurs between water and amide groups along individual polymer chains. As the temperature is increased above the polymer LCST, hydrogen bonding with water is disrupted, resulting in an entropically favored expulsion of water from the polymer matrix. At the same time, hydrophobic and hydrogen bonding interactions occur between neighboring polymer chains, inducing the particles to undergo a volume change as a function of temperature.

pNIPAm particles are largely solvent-swollen at temperatures lower than the LCST of the polymer due to hydrophilic interactions of polymer chains. However, when the particle is in its deswollen state, polymer-polymer interactions dominate. These polymer interactions that occur during the volume phase transition of pNIPAm particles is advantageous for the formation of a pNIPAm shell, since deswollen pNIPAm particles can be used as nucleating "seeds" to promote further polymer growth.[22,33,34] The resulting core/shell particles retain there volume phase transition behavior; however, the core has been demonstrated to undergo some degree of compression by the shell.[23,33,34] The characteristics of these soft, hydrogel pNIPAm core/shell materials have been investigated extensively[35-38] and interesting constructs have been prepared, such as hollow particles[39,40] and permselective shells,[3] by taking advantage of this facile synthetic process.

1.2.2 Colloidal Crystals

Spherical nanoparticles have been observed to adopt ordered configurations that resemble atomic crystal structures,[41,42] usually demonstrating face-centered cubic (fcc), body centered cubic (bcc), and hexagonally close-packed (hcp) arrangements, although other diverse structures have also been obtained using binary mixtures of particles.[43-46] These crystal structures demonstrate the same type of Bragg diffraction that is exhibited by atomic structures. However, the diffraction energy associated with colloidal crystals

composed of nanoparticles is commensurate with the particle size, as demonstrated by a modified Bragg's law of diffraction:[18,47]

$$m\lambda = 2nd\sin\theta, \qquad \text{(Eq. 1.1)}$$

where λ is the wavelength of light, n is the effective refractive index of the medium, d is the lattice spacing, θ is the angle of incident light relative to the lattice plane, and m is the diffraction order (where m = 1,2,3…). The effective refractive index for a crystal is given by a weighted sum of the individual components[48,49] given by,

$$n_{eff} = \sum_{a=1}^{\infty} n_a \cdot \phi_a, \qquad \text{(Eq 1.2)}$$

where n_{eff} is the effective refractive index of the sample, based on the refractive index of each component times the volume fraction (ϕ) of each component. Theoretical investigations have demonstrated that three-dimensional structures that possess these types of refractive index periodicities can exhibit unique, well-behaved optical properties.[50,51] The lattice spacing of the crystal can be related to the size of the crystal building blocks by

$$d_{h,k,l} = \frac{1.414D}{(h^2 + k^2 + l^2)^{1/2}}, \qquad \text{(Eq. 1.3)}$$

where D is the diameter of the particles and h, k, and l are the Miller indices for the crystal lattice plane.

The optical properties of photonic materials can be employed in a wide-variety of applications, such as sensors,[47,52,53] optical filters and switches, and even separations strategies.[54,55] Other components that also interact with light, such as fluorescent dyes,[56] organic semiconductor materials,[57,58] and quantum dots[59-62] have been investigated by their inclusion into colloidal crystals. Colloidal crystals can also be fabricated to offer large contrasts in refractive index, which can provide more efficient components for optical devices (e.g. waveguides, filters), by reducing losses in light intensity.[63-65] Conventional waveguides rely on total internal reflection between cladding materials of different dielectric constants. However, this reflection is difficult to attain with some structures when sharp bends or other designs are required for on-chip circuitry. Colloidal crystals offer a distinct advantage to these conventional materials because of their ease of assembly and their potential to form photonic band gap materials.[66]

In order to produce colloidal crystals that can successfully be used for these purposes, it is necessary to maintain control over the assembly of the particles. The main objectives are reproducibility and the minimization of structural defects that affect the optical properties of the material. Self-assembly approaches offer a distinct advantage in that they are efficient, require minimal fabrication efforts, and can be easily modified for widespread manufacturing purposes. However, such approaches are intrinsically tied to obtaining thermodynamic control over assembly, which often requires very slow assembly in order to limit the number and size of kinetically trapped defects. Some of the simplest methods utilize sedimentation or centrifugation procedures. However, sedimentation is time-consuming while rapid centrifugation can cause defects that disrupt the crystalline order. A variety of other self-assembly methods have been explored to increase the speed and the crystalline quality, including capillary action,[67] vertical deposition,[68,69] convective assembly,[70] spin-coating,[71] and electrophoretic assembly.[72,73] Additionally, other innovative designs have been investigated to induce self-assembly,

such as specially designed and patterned cells[74] and solvent evaporation by isothermal heating.[75]

Most of the self-assembly procedures that are listed above employ hard sphere particles as the crystal building blocks.[14,76] An advantage of hard sphere systems is that they are typically fairly stable. However, these systems often require complex deposition configurations or long deposition times in order to form high-quality crystals. Alternatively, spherical pNIPAm hydrogel particles offer an exceptional route for the fabrication of colloidal crystals due to their softness and thermoresponsivity. Since pNIPAm particles undergo a volume phase transition at ~31 °C, the particle size decreases at high temperatures. Thermal annealing of concentrated solutions of pNIPAm particles allows for particle self-assembly as the particles return to their swollen state.[18] This technique presents a convenient and straightforward method for rapid fabrication of crystalline materials, as well as a means of annealing defects in the assembly. Unlike hard-sphere crystal systems that require a narrow range of particle volume fractions in order to form crystals,[77,78] soft, flexible polymer particles allow for diverse interparticle interactions due to the flexible polymer chains the particle periphery.[15,79-82] Additionally, these soft interactions enable simple adjustment, i.e. tunability, of the optical properties of the crystal by varying the polymer volume fractions or the degree of particle swelling.[16,17] Depending on the functionality of these soft polymer particles, this tuning can be accomplished by varying the pH, particle concentration, light intensity, or even the temperature.[17,18,83-85]

Unfortunately, colloidal crystals composed of pNIPAm particles possess intrinsic structural limitations owing to their hydrogel composition, since they are typically composed of >95% water in their swollen state. Many methods have been used to stabilize these soft particles (as well as hard sphere particles) through interparticle cross-linking strategies, [49,81,86-88] however, these soft materials cannot provide the same sample robustness that is intrinsic to hard-sphere crystal systems.

1.2.3 Advancements in Colloidal Crystals Using Core/Shell Building Blocks

In this work, many core/shell systems are investigated for the purposes of fabricating advanced colloidal crystals that can be used for many different optical applications. Because the bulk properties of the colloidal crystal are derived from the characteristics of the individual components, special emphasis was placed on the investigation of synthesis and characterization strategies of the individual building blocks. Chapter 2 provides an investigation of complementary characterization strategies to examine the effects of compression on a pNIPAm core particle due to the introduction of a pNIPAm shell. A synthetic design was employed whereby fluorescence resonance energy transfer (FRET) was observed for a donor and acceptor fluorophore pair located within the core of core/shell particles. This technique was effectively employed in combination with standard light scattering techniques to determine the size contributions from both the core and the shell regions. The development of such distinct analytical tools is necessary to understand the fundamental structural relationship between the core and shell.

Chapters 3-6 discuss synthetic techniques that were used to produce specialized core/shell-type particles using pNIPAm that could be used for colloidal crystal fabrication of unique materials. The study in Chapter 3 discusses an synthetic strategy that takes advantage of fundamental aspects of the precipitation polymerization method to prepare core/shell nanocomposite particles by adding a pNIPAm-type shell to a metallic (silver) core. This shell layer was formed by means of a pseudo-shell precursor that provided a nucleation site for further polymer growth. The Ag particles used in this study exhibit plasmon resonance and can also demonstrate cooperative plasmon modes based on the proximity of nearby particles. The presence of the pNIPAm shells could potentially be used to form 2D and 3D assemblies and to adjust the interparticle spacing between neighboring Ag particles to vary these cooperative plasmon modes.

Chapters 4-6 describe the synthesis and characterization of copolymer poly(styrene-*co*-NIPAm) (pS-*co*-NIPAm) particles that possess both hard *and* soft characteristics that not only promote self-assembly, but also enhance crystalline stability. These attributes suggest that the pS-*co*-NIPAm particles possess a pseudo-core/shell morphology due to phase separation as a result of the relative hydrophobicity and hydrophilicity of the polymer constituents. Fabrication of colloidal crystals using these pS-*co*-NIPAm particles can be performed by simply drying a suspension of the particles to form stable, diffractive crystals. This self-assembly process presents a very easy way to form stable crystals and demonstrates the enhanced processability of these suspensions as "paint-on" photonic inks, as demonstrated by deposition of particles using ink-jet printing techniques. The particle characteristics were investigated extensively in Chapter 4 to ascertain which particle characteristics yielded the best type of "paint-on" samples, and a synthetic strategy that used the method of delayed monomer addition was evaluated in Chapter 6 in efforts to form large pS-*co*-NIPAm particles. Chapter 5 investigates the use of an additional pure-pNIPAm shell to provide thermoresponsive properties, which allows for crystal self-assembly via thermal annealing.

It was discovered that dry pS-*co*-NIPAm crystals could be physically cross-linked using simple baking procedures to form stable, robust crystals that not only retained uniform diffractive properties upon re-wetting with aqueous solvent, but the diffraction wavelength also increased, suggesting that the particle lattice spacing increases due to the rehydration of the hydrogel component of the particle (Chapter 7). This baking procedure was performed using pS-*co*-NIPAm core/pNIPAm shell particles that possessed a pH-responsive functional group in the shell and it was found that the diffractive properties of these cross-linked crystals could be tuned using changes in pH. This investigation demonstrated the versatility of the constructs that can be formed using a combination of different core/shell synthetic techniques.

Chapter 8 discusses a side project where the small (bare) silver particles that were used in Chapter 3 could be employed as tracer agents for particle tracking experiments due to their high scattering efficiencies. In this study, these small Ag particles were used to characterize the interstitial spaces of colloidal crystals composed of large pNIPAm particles. This study served as a proof-of-concept by using unmodified Ag tracer particles to investigate complex systems, effectively avoiding the need for complex particle morphologies for tracking purposes.[89] It also suggests how binary crystals may be formed using two different types of particles. The future directions of this research are discussed in Chapter 9.

References

[1] Xiao, X.-C.; Chu, L.-Y.; Chen, W.-M.; Wang, S.; Xie, R. Preparation of Submicrometer-Sized Monodispersed Thermoresponsive Core-Shell Hydrogel Microspheres. *Langmuir* **2004**, *20*, 5247-5253.

[2] Pelton, R. Temperature-sensitive aqueous microgels. *Adv. Colloid Interface Sci.* **2000**, *85*, 1-33.

[3] Nayak, S.; Lyon, L. A. Ligand-functionalized core/shell microgels with permselective shells. *Angew. Chem. Int. Ed.* **2004**, *43*, 6706-6709.

[4] Suzuki, D.; Kawaguchi, H. Gold Nanoparticle Localization at the Core Surface by Using Thermosensitive Core-Shell Particles as a Template. *Langmuir* **2005**, *21*, 12016-12024.

[5] Suzuki, D.; Kawaguchi, H. Stimuli-sensitive core/shell template particles for immobilizing inorganic nanoparticles in the core. *Colloid Polym. Sci.* **2006**, *284*, 1443-1451.

[6] Berndt, I.; Richtering, W. Doubly Temperature Sensitive Core-Shell Microgels. *Macromolecules* **2003**, *36*, 8780-8785.

[7] Pichot, C.; Elaissari, A.; Duracher, D.; Meunier, F.; Sauzedde, F. Hydrophilic stimuli-responsive particles for biomedical applications. *Macromolecular Symp.* **2001**, *175*, 285-297.

[8] Gan, D.; Lyon, L. A. Amphiphilic, peptide-modified core/shell microgels. *Prog. Colloid Polym. Sci.* **2006**, *133*, 1-8.

[9] Gan, D.; Lyon, L. A. Synthesis and Protein Adsorption Resistance of PEG-Modified Poly(N-isopropylacrylamide) Core/Shell Microgels. *Macromolecules* **2002**, *35*, 9634-9639.

[10] Haag, R. Supramolecular drug-delivery systems based on polymeric core-shell architectures. *Angew. Chem. Int. Ed.* **2004**, *43*, 278-282.

[11] Soppimath, K. S.; Tan, D. C.-W.; Yang, Y.-Y. pH-Triggered thermally responsive polymer core-shell nanoparticles for drug delivery. *Adv. Mat.* **2005**, *17*, 318-323.

[12] Nayak, S.; Lyon, L. A. Soft nanotechnology with soft nanoparticles. *Angew. Chem. Int. Ed.* **2005**, *44*, 7686-7708.

[13] Pieranski, P. Colloidal crystals. *Contemporary Physics* **1983**, *24*, 25-73.

[14] Xia, Y.; Gates, B.; Yin, Y.; Lu, Y. Monodispersed colloidal spheres: Old materials with new applications. *Adv. Mat.* **2000**, *12*, 693-713.

[15] Debord, J. D.; Lyon, L. A. Thermoresponsive Photonic Crystals. *J. Phys. Chem. B* **2000**, *104*, 6327-6331.

[16] Debord, J. D.; Eustis, S.; Debord, S. B.; Lofye, M. T.; Lyon, L. A. Color-tunable colloidal crystals from soft hydrogel nanoparticles. *Adv. Mat.* **2002**, *14*, 658-662.

[17] Debord, S. B.; Lyon, L. A. Influence of Particle Volume Fraction on Packing in Responsive Hydrogel Colloidal Crystals. *J. Phys. Chem. B* **2003**, *107*, 2927-2932.

[18] Lyon, L. A.; Debord, J. D.; Debord, S. B.; Jones, C. D.; McGrath, J. G.; Serpe, M. J. Microgel Colloidal Crystals. *J. Phys. Chem. B* **2004**, *108*, 19099-19108.

[19] Stoeber, W.; Fink, A.; Bohn, E. Controlled growth of monodisperse silica spheres in the micron size range. *J. Coll. Interface Sci.* **1968**, *26*, 62-9.

[20] Forcada, J.; Hidalgo-Alvarez, R. Functionalized polymer colloids: Synthesis and colloidal stability. *Current Organic Chem.* **2005**, *9*, 1067-1084.

[21] Vanderhoff, J. W. Well-characterized monodisperse polystyrene latexes as model colloids. *Pure and Appl. Chem.* **1980**, *52*, 1263-73.

[22] Jones, C. D.; Lyon, L. A. Synthesis and Characterization of Multiresponsive Core-Shell Microgels. *Macromolecules* **2000**, *33*, 8301-8306.

[23] Jones, C. D.; McGrath, J. G.; Lyon, L. A. Characterization of Cyanine Dye-Labeled Poly(N-isopropylacrylamide) Core/Shell Microgels Using Fluorescence Resonance Energy Transfer. *J. Phys. Chem. B* **2004**, *108*, 12652-12657.

[24] Duracher, D.; Sauzedde, F.; Elaissari, A.; Perrin, A.; Pichot, C. Cationic amino-containing N-isopropylacrylamide-styrene copolymer latex particles. Part 1.

Particle size and morphology vs. polymerization process. *Colloid Polym. Sci.* **1998**, *276*, 219-231.

[25] Duracher, D.; Sauzedde, F.; Elaissari, A.; Pichot, C.; Nabzar, L. Cationic amino-containing N-isopropylacrylamide-styrene copolymer particles. Part 2. Surface and colloidal characteristics. *Colloid Polym. Sci.* **1998**, *276*, 920-929.

[26] Zhou, G.; Elaissari, A.; Delair, T.; Pichot, C. Synthesis and characterization of surface-cyano-functionalized poly(N-isopropylacrylamide) latexes. *Colloid Polym. Sci.* **1998**, *276*, 1131-1139.

[27] Caruso, F. Nanoengineering of particle surfaces. *Adv. Mat.* **2001**, *13*, 11-22.

[28] Ma, Q.; Remsen, E. E.; Kowalewski, T.; Schaefer, J.; Wooley, K. L. Environmentally-Responsive, Entirely Hydrophilic, Shell Cross-linked (SCK) Nanoparticles. *Nano Lett.* **2001**, *1*, 651-655.

[29] Joralemon, M. J.; O'Reilly, R. K.; Hawker, C. J.; Wooley, K. L. Shell Click-Crosslinked (SCC) Nanoparticles: A New Methodology for Synthesis and Orthogonal Functionalization. *J. Am. Chem. Soc.* **2005**, *127*, 16892-16899.

[30] Heskins, M.; Guillet, J. E. Solution properties of poly(N-isopropylacrylamide). *J. Macromolecular Sci., Chem.* **1968**, *2*, 1441-55.

[31] Schild, H. G. Poly(N-isopropylacrylamide): experiment, theory and application. *Prog. Polym. Sci.* **1992**, *17*, 163-249.

[32] Wu, X.; Pelton, R. H.; Hamielec, A. E.; Woods, D. R.; McPhee, W. The kinetics of poly(N-isopropylacrylamide) microgel latex formation. *Colloid Polym. Sci.* **1994**, *272*, 467-77.

[33] Jones, C. D.; Lyon, L. A. Dependence of Shell Thickness on Core Compression in Acrylic Acid Modified Poly(N-isopropylacrylamide) Core/Shell Microgels. *Langmuir* **2003**, *19*, 4544-4547.

[34] Jones, C. D.; Lyon, L. A. Shell-Restricted Swelling and Core Compression in Poly(N-isopropylacrylamide) Core-Shell Microgels. *Macromolecules* **2003**, *36*, 1988-1993.

[35] Wang, J.; Gan, D.; Lyon, L. A.; El-Sayed, M. A. Temperature-Jump Investigations of the Kinetics of Hydrogel Nanoparticle Volume Phase Transitions. *J. Am. Chem. Soc.* **2001**, *123*, 11284-11289.

[36] Gan, D.; Lyon, L. A. Interfacial Nonradiative Energy Transfer in Responsive Core-Shell Hydrogel Nanoparticles. *J. Am. Chem. Soc.* **2001**, *123*, 8203-8209.

[37] Gan, D.; Lyon, L. A. Tunable Swelling Kinetics in Core-Shell Hydrogel Nanoparticles. *J. Am. Chem. Soc.* **2001**, *123*, 7511-7517.

[38] Gan, D.; Lyon, L. A. Fluorescence nonradiative energy transfer analysis of crosslinker heterogeneity in core-shell hydrogel nanoparticles. *Anal. Chim. Acta* **2003**, *496*, 53-63.

[39] Nayak, S.; Gan, D.; Serpe, M. J.; Lyon, L. A. Hollow thermoresponsive microgels. *Small* **2005**, *1*, 416-421.

[40] Singh, N.; Lyon, L. A. Au Nanoparticle Templated Synthesis of pNIPAm Nanogels. *Chem. Mater.*, Submitted.

[41] Clark, N. A.; Hurd, A. J.; Ackerson, B. J. Single colloidal crystals. *Nature* **1979**, *281*, 57-60.

[42] Gast, A. P.; Russel, W. B. Simple ordering in complex fluids: colloidal particles suspended in solution provide intriguing models for studying phase transitions. *Phys. Today* **1998**, *51*, 24-30.

[43] Velikov, K. P.; Christova, C. G.; Dullens, R. P. A.; van Blaaderen, A. Layer-by-layer growth of binary colloidal crystals. *Science* **2002**, *296*, 106-109.

[44] Cong, H.; Cao, W. Array Patterns of Binary Colloidal Crystals. *J. Phys. Chem. B* **2005**, *109*, 1695-1698.

[45] Bartlett, P.; Campbell, A. I. Three-Dimensional Binary Superlattices of Oppositely Charged Colloids. *Phys. Rev. Lett.* **2005**, *95*, 128302/1-128302/4.

[46] Kim, M. H.; Im, S. H.; Park, O. O. Fabrication and structural analysis of binary colloidal crystals with two-dimensional superlattices. *Adv. Mat.* **2005**, *17*, 2501-2505.

[47] Holtz, J. H.; Asher, S. A. Polymerized colloidal crystal hydrogel films as intelligent chemical sensing materials. *Nature* **1997**, *389*, 829-832.

[48] Pan, G.; Sood, A. K.; Asher, S. A. Polarization dependence of crystalline colloidal array diffraction. *J. Appl. Phys.* **1998**, *84*, 83-86.

[49] Weissman, J. M.; Sunkara, H. B.; Tse, A. S.; Asher, S. A. Thermally switchable periodicities and diffraction from mesoscopically ordered materials. *Science* **1996**, *274*, 959-960.

[50] Yablonovitch, E. Inhibited spontaneous emission in solid-state physics and electronics. *Phys. Rev. Lett.* **1987**, *58*, 2059-62.

[51] John, S. Strong localization of photons in certain disordered dielectric superlattices. *Phys. Rev. Lett.* **1987**, *58*, 2486-9.

[52] Holtz, J. H.; Holtz, J. S. W.; Munro, C. H.; Asher, S. A. Intelligent Polymerized Crystalline Colloidal Arrays: Novel Chemical Sensor Materials. *Anal. Chem.* **1998**, *70*, 780-791.

[53] Ben-Moshe, M.; Alexeev, V. L.; Asher, S. A. Fast Responsive Crystalline Colloidal Array Photonic Crystal Glucose Sensors. *Anal. Chem.* **2006**, *78*, 5149-5157.

[54] Zheng, S.; Ross, E.; Legg Michael, A.; Wirth Mary, J. High-speed electroseparations inside silica colloidal crystals. *J. Am. Chem. Soc.* **2006**, *128*, 9016-7.

[55] Cichelli, J.; Zharov, I. Chiral Permselectivity in Surface-Modified Nanoporous Opal Films. *J. Am. Chem. Soc.* **2006**, *128*, 8130-8131.

[56] Bechger, L.; Lodahl, P.; Vos, W. L. Directional Fluorescence Spectra of Laser Dye in Opal and Inverse Opal Photonic Crystals. *J. Phys. Chem. B* **2005**, *109*, 9980-9988.

[57] Yoshino, K.; Takeda, H.; Kasano, M.; Satoh, S.; Matsui, T.; Ozaki, R.; Fujii, A.; Ozaki, M.; Kose, A. Novel tunable optical properties of liquid crystals, conjugated molecules and polymers in nanoscale periodic structures as photonic crystals. *Macromolecular Symp.* **2004**, *212*, 179-190.

[58] Dionigi, C.; Stoliar, P.; Porzio, W.; Destri, S.; Cavallini, M.; Bilotti, I.; Brillante, A.; Biscarini, F. Field Effect Transistors with Organic Semiconductor Layers Assembled from Aqueous Colloidal Nanocomposites. *Langmuir*, ACS ASAP.

[59] Wang, W.; Asher, S. A. Photochemical Incorporation of Silver Quantum Dots in Monodisperse Silica Colloids for Photonic Crystal Applications. *J. Am. Chem. Soc.* **2001**, *123*, 12528-12535.

[60] Fleischhaker, F.; Zentel, R. Photonic Crystals from Core-Shell Colloids with Incorporated Highly Fluorescent Quantum Dots. *Chem. Mater.* **2005**, *17*, 1346-1351.

[61] Barth, M.; Schuster, R.; Gruber, A.; Cichos, F. Imaging single quantum dots in three-dimensional photonic crystals. *Phys. Rev. Lett.* **2006**, *96*, 243902.

[62] Paquet, C.; Yoshino, F.; Levina, L.; Gourevich, I.; Sargent, E. H.; Kumacheva, E. High-quality photonic crystals infiltrated with quantum dots. *Adv. Funct. Mater.* **2006**, *16*, 1892-1896.

[63] Joannopoulos, J. D.; Villeneuve, P. R.; Fan, S. Photonic crystals: putting a new twist on light. *Nature* **1997**, *387*, 830.

[64] Thylen, L.; Qiu, M.; Anand, S. Photonic crystals-A step towards integrated circuits for photonics. *ChemPhysChem* **2004**, *5*, 1268-1283.

[65] Istrate, E.; Sargent, E. H. Photonic crystal heterostructures-resonant tunneling, waveguides and filters. *J. Optics A: Pure and Appl. Opt.* **2002**, *4*, S242-S246.

[66] Lee, W.; Pruzinsky, S. A.; Braun, P. V. Multi-photon polymerization of waveguide structures within three-dimensional photonic crystals. *Adv. Mat.* **2002**, *14*, 271-274.

[67] Li, H.-L.; Marlow, F. Solvent Effects in Colloidal Crystal Deposition. *Chem. Mater.* **2006**, *18*, 1803-1810.

[68] Jiang, P.; Bertone, J. F.; Hwang, K. S.; Colvin, V. L. Single-Crystal Colloidal Multilayers of Controlled Thickness. *Chem. Mater.* **1999**, *11*, 2132-2140.

[69] Li, J.; Han, Y. Optical Intensity Gradient by Colloidal Photonic Crystals with a Graded Thickness Distribution. *Langmuir* **2006**, *22*, 1885-1890.

[70] Wostyn, K.; Zhao, Y.; Yee, B.; Clays, K.; Persoons, A.; De Schaetzen, G.; Hellemans, L. Optical properties and orientation of arrays of polystyrene spheres deposited using convective self-assembly. *J. Chem. Phys.* **2003**, *118*, 10752-10757.

[71] Jiang, P.; McFarland, M. J. Large-Scale Fabrication of Wafer-Size Colloidal Crystals, Macroporous Polymers and Nanocomposites by Spin-Coating. *Journal of the American Chemical Society* **2004**, *126*, 13778-13786.

[72] Trau, M.; Saville, D. A.; Aksay, I. A. Field-induced layering of colloidal crystals. *Science* **1996**, *272*, 706-9.

[73] Rogach, A. L.; Kotov, N. A.; Koktysh, D. S.; Ostrander, J. W.; Ragoisha, G. A. Electrophoretic Deposition of Latex-Based 3D Colloidal Photonic Crystals: A Technique for Rapid Production of High-Quality Opals. *Chem. Mater.* **2000**, *12*, 2721-2726.

[74] Park, S. H.; Xia, Y. Assembly of mesoscale particles over large areas and its application in fabricating tunable optical filters. *Langmuir* **1999**, *15*, 266-273.

[75] Wong, S.; Kitaev, V.; Ozin Geoffrey, A. Colloidal crystal films: advances in universality and perfection. *J. Am. Chem. Soc.* **2003**, *125*, 15589-98.

[76] Norris, D. J.; Arlinghaus, E. G.; Meng, L.; Heiny, R.; Scriven, L. E. Opaline photonic crystals: How does self-assembly work? *Adv. Mat.* **2004**, *16*, 1393-1399.

[77] Kose, A.; Hachisu, S. Kirkwood-Alder transition in monodisperse latexes. I. Nonaqueous systems. *J. Coll. Interface Sci.* **1974**, *46*, 460-9.

[78] Pusey, P. N.; Van Megen, W. Phase behavior of concentrated suspensions of nearly hard colloidal spheres. *Nature* **1986**, *320*, 340-2.

[79] Senff, H.; Richtering, W. Temperature sensitive microgel suspensions: Colloidal phase behavior and rheology of soft spheres. *J. Chem. Phys.* **1999**, *111*, 1705-1711.

[80] Hellweg, T.; Dewhurst, C. D.; Bruckner, E.; Kratz, K.; Eimer, W. Colloidal crystals made of poly(N-isopropylacrylamide) microgel particles. *Colloid Polym. Sci.* **2000**, *278*, 972-978.

[81] Hu, Z.; Lu, X.; Gao, J. Hydrogel opals. *Adv. Mat.* **2001**, *13*, 1708-1712.

[82] Alsayed, A. M.; Islam, M. F.; Zhang, J.; Collings, P. J.; Yodh, A. G. Premelting at Defects Within Bulk Colloidal Crystals. *Science* **2005**, *309*, 1207-1210.

[83] Jones, C. D.; Lyon, L. A. Photothermal patterning of microgel/gold nanoparticle composite colloidal crystals. *J. Am. Chem. Soc.* **2003**, *125*, 460-465.

[84] Jones, C. D.; Serpe, M. J.; Schroeder, L.; Lyon, L. A. Microlens Formation in Microgel/Gold Colloid Composite Materials via Photothermal Patterning. *J. Am. Chem. Soc.* **2003**, *125*, 5292-5293.

[85] Reese, C. E.; Mikhonin, A. V.; Kamenjicki, M.; Tikhonov, A.; Asher, S. A. Nanogel Nanosecond Photonic Crystal Optical Switching. *J. Am. Chem. Soc.* **2004**, *126*, 1493-1496.

[86] Asher, S. A.; Holtz, J.; Liu, L.; Wu, Z. Self-Assembly Motif for Creating Submicron Periodic Materials. Polymerized Crystalline Colloidal Arrays. *J. Am. Chem. Soc.* **1994**, *116*, 4997-8.

[87] Iwayama, Y.; Yamanaka, J.; Takiguchi, Y.; Takasaka, M.; Ito, K.; Shinohara, T.; Sawada, T.; Yonese, M. Optically Tunable Gelled Photonic Crystal Covering Almost the Entire Visible Light Wavelength Region. *Langmuir* **2003**, *19*, 977-980.

[88] Kamenetzky, E. A.; Magliocco, L. G.; Panzer, H. P. Structure of solidified colloidal array laser filters studied by cryogenic transmission electron microscopy. *Science* **1994**, *263*, 207-10.

[89] Schartl, W. Crosslinked spherical nanoparticles with core-shell topology. *Adv. Mat.* **2000**, *12*, 1899-1908.

CHAPTER 2

CHARACTERIZATION OF POLY(*N*-ISOPROPYLACRYLAMIDE) CORE/SHELL MICROGELS USING FLUORESCENCE RESONANCE ENERGY TRANSFER (FRET)

2.1 Introduction

Many strategies have been employed to prepare nanomaterials that possess multiple functionalities for the purposes of increasing the scope and diversity of specific applications. One such design that has been widely investigated for the production of multifunctional spherical nanoparticles is the core/shell structure.[1-4] In order to gain an understanding of the attributes of such materials at the nanoscale, it is necessary to employ the appropriate techniques to characterize these constructs. In the case of polymer colloids, light scattering and electron microscopy provide information concerning particle size and distribution,[5] while revealing architectural,[6] and topological details.[7] Both techniques report on the outermost portion of the particle and its immediate surroundings, with a few exceptions.[8,9] The characterization of multilayered nanoparticles becomes complicated due to the need to characterize the inner portion of the particle. Therefore, a comprehensive analysis of the fundamental structural relationships of such materials often requires science to move beyond conventional analytical techniques of a particular field.[10-12] In this investigation, the technique of fluorescence resonance energy transfer (FRET) was used to probe the swelling behavior of the core component of core/shell hydrogel nanoparticles.[13] FRET is a distance-dependent process requiring that two fluorophores, termed the donor and the acceptor, have overlapping emission and excitation spectra, respectively.[14] Energy transfer occurs from excited donor molecules to acceptor molecules when the two are within a certain distance of each other. The intrinsic distance of the particular fluorophore pair at which FRET is 50% efficient is referred to

as the Förster radius (R_o). Energy transfer is the result of long-range dipole induced dipole interactions.[14] In this work, the long-wavelength excitable sulfoindocyanine-based dyes Cy5 and Cy5.5 (Amersham Biosciences) were chosen as the donor and acceptor molecules, respectively, since this fluorescent pair has been shown to have a large R_o value of 68.7 Å in aqueous media.[15]

Our group has focused on the synthesis and characterization of poly(*N*-isopropylacrylamide) (pNIPAm) nanoparticles having a core/shell type morphology, where environmentally responsive polymers comprise both the core and shell components.[6,16-20] Such hydrogel nanoparticles (microgels) are cross-linked, spherical, colloidal particles and are individually composed of a network of randomly oriented polymer chains that have the ability to exist in a swollen or collapsed state depending on local environmental conditions.[21-24] As discussed previously, pNIPAm particles can undergo a temperature-induced, reversible phase transition at ~31 °C as a result of the lower critical solution temperature (LCST) of the polymer.[25,26] We have prepared core/shell microgels for fundamental studies by designing particles with multiple volume phase transitions[6] along with investigating the dynamics and mechanisms of particle phase transition behavior.[18,27] The core/shell structure can be elucidated via photon correlation spectroscopy (PCS) by monitoring size differences between the core and core/shell particles.[6,16] These core/shell particles typically are not highly interpenetrated and possess two distinct components as illustrated by electron microscopy.[6] Previous fluorescence investigations have also suggested that the interface between the core and shell components lacks a large degree of network interpenetration.[18]

Recent investigations involving pNIPAm-*co*-acrylic acid (core)/pNIPAm (shell) microgels illustrate that the swelling ability of the core is indeed modulated by the shell.[16,19] In this case, the pH-responsive nature of the core allowed isothermal investigations of particle size changes by variation of solution conditions. Increasing the solution pH to above the acid pK_a (4.25),[28] resulted in a particle volume increase due to

Coulombic repulsion between charged groups and added osmotic pressure (Donnan effect) from incorporated counterions.[29,30] PCS data demonstrated that the pNIPAm shell restricts the core from swelling to its native volume both above and below the pK_a of acrylic acid at temperatures below 31 ºC. When compared to the volume of the parent core particle at a pH above the pK_a, the core/shell structure actually displays a *smaller* volume due to this compression effect.[16,19] Also under these pH conditions, the parent core particle undergoes only small temperature-induced volume changes above 31 ºC due to the extreme amount of Coulombic repulsion in the network. However, the addition of a pNIPAm shell results in compression of the core and induces a large volume change above the pNIPAm LCST, evidently overcoming the charge repulsion in the core to deswell the particle.

The current investigation involves a pNIPAm core containing a small percentage of amine groups for postpolymerization modification with *N*-hydroxysuccinimidyl (NHS) ester-functionalized cyanine dyes (Cy dyes). The shell is composed of pNIPAm, and both the core and shell components are lightly cross-linked with *N,N'*-methylene(bisacrylamide) (BIS). The amount of energy transfer occurring between the cyanine donor/acceptor pair in the core component is monitored by comparing the emission intensity of the donor and acceptor molecules in the absence and presence of the shell over a range of temperature values. These studies provide two main findings. First, they confirm previous indirect measurements of core compression using the more direct method of FRET, and second, they allow for accurate calculation of the actual shell thickness. PCS studies alone are insufficient for shell thickness calculations, as the apparent particle size increase is a convolution of the shell thickness and the core compression. By independently measuring the core compression using FRET, the thicknesses of various hydrogel shells added under specific synthetic conditions can be directly determined.

2.2 Experimental Section

2.2.1 Particle Synthesis

Materials

The monomer *N*-isopropylacrylamide (NIPAm, Aldrich) was purified via recrystallization from hexanes (J. T. Baker) and dried in vacuo prior to use. The surfactant (sodium dodecyl sulfate, SDS), the cross-linker (*N,N'*-methylene(bisacrylamide), BIS), and the initiator, (ammonium persulfate, APS) were purchased from Sigma-Aldrich and used as received. The comonomer, *N*-(3-aminopropyl)methacrylamide hydrochloride (APMA), was purchased from Polysciences and used as received. Monofunctional *N*-hydroxysuccinimidyl (NHS) esters of Cy5 and Cy5.5 were purchased from Amersham Biosciences and used as received. Distilled water was purified with a Barnstead E-Pure system to a resistance of 18 MΩ then filtered through a 0.2-μm filter to remove particulate matter.

Particle Synthesis

Core/shell microgels were synthesized via two-stage free-radical precipitation polymerization as previously reported.[16] Two sets of core particles were used for this study on to which shells of varying thickness were added by adjusting the total monomer concentration (TMC) of the shell synthesis. In the first case, a thick, lightly crosslinked (2 mol-% BIS) pNIPAm shell (20 mM) was added to a highly crosslinked (5 mol-% BIS) pNIPAm core ("Core #1"). In the second case, thin, lightly crosslinked (2 mol-% BIS) pNIPAm shells (5 mM, 10 mM, 15 mM) were added to lightly crosslinked (2 mol-% BIS) pNIPAm core particles ("Core #2"). For both of the syntheses used to prepare the initial core particles, a 70 mM TMC was used, with a small contribution of APMA (0.2 mol-%) that acts as a functional group for Cy dye coupling to the core.

The amounts of synthesis materials used for the polymerizations of these particles are shown in Table 2.1. The core particles were synthesized by dissolving the NIPAm and BIS monomers, SDS, and APMA (added from a stock solution) in 75 mL of water and heating to 70 ºC under N_2. The free-radical polymerization was initiated with APS (dissolved in ~0.5 mL water) solution and allowed to proceed for 5 hrs at 70 ºC under N_2.

Table 2.1 Synthesis materials for core and shell polymerizations.

Sample	NIPAm, g	BIS, g	SDS, g	APS, g	APMA, mmol
Core #1 (5% BIS)	0.5658	0.0405	0.0239	0.028	0.0106
Core #1/20 mM (2% BIS) Shell	0.0537	0.0015	0.0058	0.009	-------
Core #2 (2% BIS)	0.5816	0.0158	0.0225	0.0264	0.0106
Core #2/5 mM (2% BIS) Shell	0.0142	0.0005	0.0066	0.0094	-------
Core #2/10 mM (2% BIS) Shell	0.0286	0.0008	0.0058	0.0088	-------
Core #2/15 mM (2% BIS) Shell	0.0435	0.0012	0.0064	0.0095	-------

Shell addition was performed by using core particles as nuclei in the subsequent precipitation polymerization of a monomer feed of different types of monomer compositions[6,16] (as shown in Table 2.1). First, a 5.0 mL portion of the core particle solution together with SDS was added to 15.0 mL of water and heated to 70 ºC under N_2. Although core particle solutions contained SDS, added surfactant is necessary for stabilization during heating and subsequent shell polymerization. After thermal

equilibration of the core solution, 5 mL of an aqueous monomer solution containing NIPAm and BIS was heated separately to 70 ºC under N_2, and then added to the core solution under monomer-flooded conditions.[8,31] Free radical polymerization was then initiated with APS (dissolved in ~0.5 mL of water) and polymerization was allowed to proceed at 70 ºC under N_2 for 5 hrs. All particles used for analysis were purified via dialysis (Spectra/Por 7 dialysis membrane, MWCO 10,000, VWR) against daily changes of water for 2 weeks at 5 ºC.

Cyanine Dye Labeling

The dyes used in these studies are not tolerant to free-radical polymerization conditions. Thus, a routine scheme for postpolymerization modification of the microgels was employed. Furthermore, it should be noted that core/shell particles are labeled following shell addition instead of adding shells to prelabeled core particles. Stock solutions of Cy5 and Cy5.5 were prepared by dissolving 1 mg of each NHS-ester functionalized dye separately into 5.0 mL of anhydrous dimethylformamide and stored under N_2. Amide bond formation between the amine moieties in the microgels and the NHS-ester functionalized dyes was performed at room temperature in pH 7.0, 0.01 M NaH_2PO_4 buffer overnight. For all labeling procedures, 0.2 mL of the purified microgel solution was dispersed into 0.8 mL of phosphate buffer. Particles containing only one fluorescent dye were prepared by adding an equimolar amount (NH_2:Cy dye) of the corresponding fluorophore stock to the buffered mixture. Particles containing both Cy5 (donor) and Cy5.5 (acceptor) molecules were prepared in the same manner with only half the molar equivalent of each dye added in this case. The fluorescently-labeled particles were purified by centrifugation (16,100 x *g* rcf for 70 min) at 25 ºC, followed by removal of the supernatant solution and redispersion of the particles in H_2O five times.

2.2.2 Characterization Techniques

Photon Correlation Spectroscopy

Microgel sizes and polydispersities were determined via photon correlation spectroscopy (Protein Solutions Inc.) as previously reported.[5,16] Samples were analyzed in a three-sided quartz cuvette into which was placed 0.5 mL of a 10 μg/mL particle solution. The sample was allowed to thermally equilibrate for 5 min before data collection. Longer equilibration times did not lead to variation in the measured particle size, scattering intensity, or polydispersity. Scattered light was collected at 90º by a single-mode optical fiber coupled to an avalanche photodiode detector. Data were analyzed with Protein Solutions' Dynamics Software Version 5.25.44. Each data point reported here is an average of five separate size determinations. Each size determination consists of 25 total measurements, which individually have a 5 second integration time. Note that the algorithms used for determination of the translational diffusion coefficient allows for non-Gaussian and/or multimodal populations. In all cases, only one particle population is observed with the relative polydispersity of the population being less than ±15%.

Fluorescence Spectroscopy

Fluorescence analysis was performed on a temperature controlled steady-state fluorescence spectrophotometer (Photon Technology International), equipped with a Model 814 PMT photon-counting detector. Measurements were performed in a quartz cuvette and the stirring sample solution was allowed to equilibrate at the proper temperature for 5 min prior to data collection. The cell temperature was controlled with a PE 60 Temperature Controller & Peltier Stage (Linkam Scientific Instruments Ltd., Surrey, UK). The slits were adjusted to achieve a bandwidth of 3.0 nm, and the spectra

were measured with a step size of 1 nm and a 1 second integration time. The excitation wavelengths used for Cy5 and Cy5.5 were 646 and 674 nm, respectively. Fluorescence resonance energy transfer FRET measurements of microgel solutions were made at a particle concentration of ~10 μg/mL at an excitation wavelength of 646 nm. Emission intensity ratios were measured at 671 nm (I_D) to that at 697 nm (I_A) corresponding to the Cy5 donor and Cy5.5 acceptor emission energies, respectively.

2.3 Results and Discussion

It has been demonstrated that during particle growth, *N,N'*-methylene(bisacrylamide) (BIS) cross-linker is statistically incorporated faster than other constituent monomers leading to the creation of a radial distribution of cross-links.[18,22,32,33] Considering this process, the core component possesses a greater polymer network density toward the interior and more loosely cross-linked chains toward the periphery. Chains close to the particle periphery have more degrees of freedom and are able to extend over longer length scales in a good solvent. The gradient model is sufficient for describing the internal microgel structure for cross-linker concentrations below 7 mol-% as experimentally shown by others.[34,35]

Because the synthetic conditions are the same for shell addition, a radial cross-linking density gradient is expected in the shell component as well for loosely cross-linked systems, with the greatest polymer network density being located at the interface of the core and shell.[16] In the second stage of the core/shell synthesis, collapsed core particles serve as preexisting hydrophobic nuclei and capture growing oligomers from solution to form the shell component. Upon particle reswelling below 31 ºC, the rigid interior (more highly cross-linked portion) of the shell prohibits the core from expanding to the maximum volume it occupied before shell addition. Therefore, the same population of loosely cross-linked chains near the core periphery are hindered from reaching their fully extended state in the presence of added material (the shell).[16] If heterogeneity were

not present within both the core and shell in the form of a radial cross-linking density gradient, one would not expect to observe such effects, as the core and shell would have *the same average and local* cross-linker concentration. The average number of chains that are perturbed will differ according to the cross-linker concentration, with lower mol-% cross-linked particles having a higher average number of loosely cross-linked chains near the periphery than highly cross-linked particles (above 7 mol-% BIS) that do not have a well-defined gradient morphology.[35]

Two different types of core/shell systems are presented in this investigation using different cross-linking concentrations. In the first case, the core (5 mol-% BIS) possesses a higher average cross-link density than the shell (2 mol-% BIS). This design is advantageous for these studies, in that *any* observation of core compression can only be attributed to a cross-link gradient, since a more loosely cross-linked shell cannot induce compression in a denser core in the absence of heterogeneous cross-link incorporation. In the second case, the core and shell possess similar cross-linking densities (2 mol-% BIS), whereby the larger swelling capacity of this lightly cross-linked core becomes significantly reduced by the presence of the shell, effectively "shrink-wrapping" the core component. The understanding of the structural relationships using these types of microgel fabrication strategies may prove valuable for the construction of nanoparticles with enhanced functionalities.

Whereas the dendritic morphology due to cross-link density heterogeneity is fundamentally interesting with respect to the particle swelling properties, it presents a real difficulty in accurately determining the amount of polymer added in the second polymerization stage. Knowing the shell thickness with some degree of accuracy is an extremely important aspect of this work. For hard material core/shell particles such as metal and semiconductor core/shell nanoparticles, high-resolution TEM is a standard method for quantifying the amount of added material. This technique is insufficient for

detailed analysis of soft, solvent swollen materials such as hydrogel nanoparticles that dehydrate under vacuum and deform upon immobilization on a surface.

Naively, one could expect routine PCS analysis would offer a measure of shell thickness using the equation,

$$(R_{shell})_T = (R_{h,core/shell})_T - (R_{h,core})_T \qquad \text{(Eq. 2.1)}$$

where $(R_{shell})_T$ is the shell thickness, $(R_{h,core/shell})_T$ is the average hydrodynamic radius of the core/shell particle, and $(R_{h,core})_T$ is the average hydrodynamic radius of the parent core particle. The T subscript indicates radius values at a specific temperature, as the measurement is a temperature-dependent one. Given our previous studies of core compression, it is clear that Eq 2.1 is incorrect. Instead, a more appropriate measure of shell thickness is obtained from:

$$(R_{shell})_T = (R_{h,core/shell})_T - (R_{h,core})_T + (\Delta R_{h,core})_T \qquad \text{(Eq. 2.2)}$$

where $(\Delta R_{h,core})_T$ is the *decrease* in average hydrodynamic radius of the core due to compression. This last term is invisible to the PCS measurement and thus must be determined by an independent method. As described above, the method chosen here is FRET, which will report the mean change in donor-acceptor distance in the core, and thus the change in core volume due to compression.

The core/shell system chosen for this investigation is analogous to pNIPAm homopolymer microgels; the core and shell components are both composed of the same material. A small amount of amine containing comonomer (0.2 mol-%) was incorporated into the core for the sole purpose of modifying the particles with NHS-ester-modified cyanine dyes in a postpolymerization step. The donor/acceptor pair Cy5 and Cy5.5

(Figure 2.1) was chosen due to the ease of incorporation into aqueous-based systems, their large quantum efficiencies, and the large Förster radius (~68.7 Å) for the pair.[15] The low photon energies needed to excite the dyes also reduces the scattering cross-section of the polymer particles in solution during fluorescence analysis. To our knowledge, this is the first use of cyanine-based dyes as probes for synthetic hydrogels.

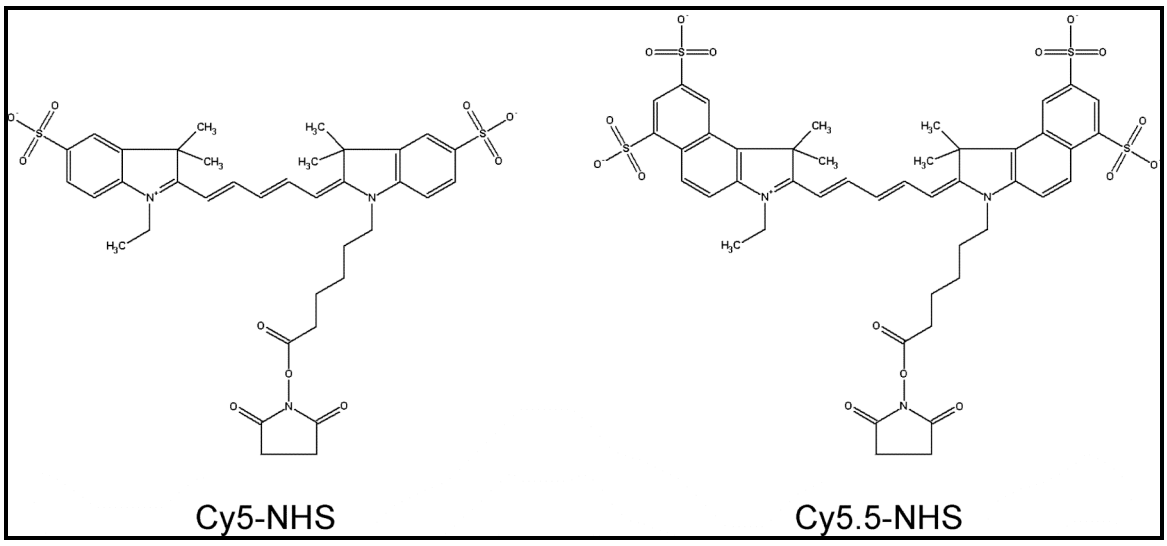

Figure 2.1 Molecular structures of the NHS-functionalized Cyanine dyes.

The monofunctional NHS ester of both Cy5 and Cy5.5 was used to covalently attach the dyes inside of the amine-functionalized core. The amine groups react with the ester to form an amide bond between the dyes and the polymer chains.[36] Figure 2.2 shows the spectral properties after incorporating each individual dye separately into the Core #1 microgels used in this study. The excitation and emission wavelengths of the cyanine dyes are not perturbed in either case and are the same for each dye before and after incorporation into the microgels.[37,38] The Cy5 donor shows a single emission peak centered at 671 nm when excited at 646 nm. When excited at 674 nm, the Cy5.5 acceptor

shows an emission peak centered at 697 nm.[15] Of course, the main requirement for FRET to occur is spectral overlap, which remains, as well.

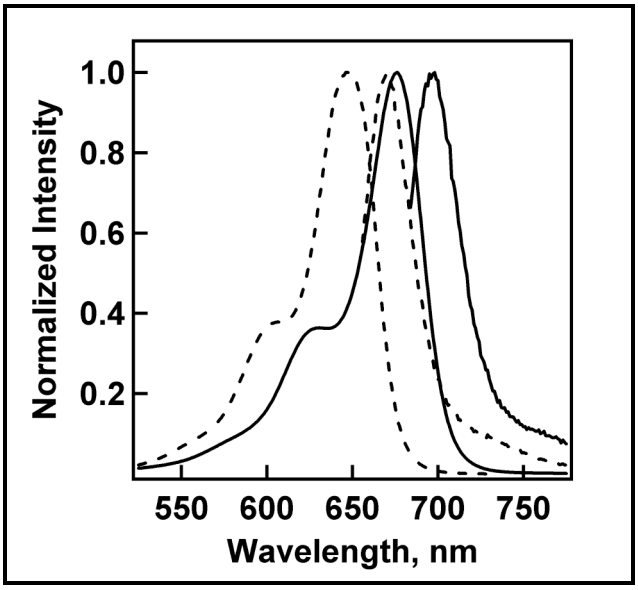

Figure 2.2 Absorbance and emission spectra of Core #1 particles containing only donor (Cy5) or acceptor (Cy5.5) dye molecules. The dashed line represents absorbance and emission from Cy5 labeled microgels showing values of 646 and 671 nm, respectively. The solid line represents the Cy5.5 labeled microgels showing absorbance and emission at 674 and 697 nm respectively. Absorbance spectra were collected with a UV-VIS spectrophotometer. Emission spectra were collected upon excitation of the Cy5 donor and Cy5.5 acceptor at 646 and 674 nm, respectively.

After observing that the spectral properties of each dye did not change when individually incorporated into core particles, equimolar quantities of both donor and acceptor dyes were randomly incorporated together into the core component of core and core/shell microgels. Figure 2.3 illustrates that the presence of both Cy dyes does not change the volume phase transition (VPT) behavior of the microgels when monitored by PCS. The VPT temperature is approximately that of pNIPAm homopolymer microgels (~31 ºC) and is the same for both core and core/shell samples. Furthermore, there is no evidence of the VPT behavior being affected by unreacted amine groups inside the core component. A size difference is obvious between the Core #1 and Core #1/20 mM Shell

microgels at all temperatures, indicating that material was indeed added to the core during the shell polymerization step. An increase in size is also found for the Core #2 microgels with thin shells. However, the differences are not as extreme, especially between shells that were polymerized using very low TMCs. The Core #2/5 mM Shell and the Core #2/10 mM Shell microgels show very similar sizes. Alone, these PCS data may suggest that the shell polymer does not even fully cover the core particles in these cases, which demonstrates the need for enhanced characterization techniques. The Core #2/15mM Shell microgels show the largest increase in particle size of all the thin shell samples, which results from the larger TMC used in the synthesis of these particles.

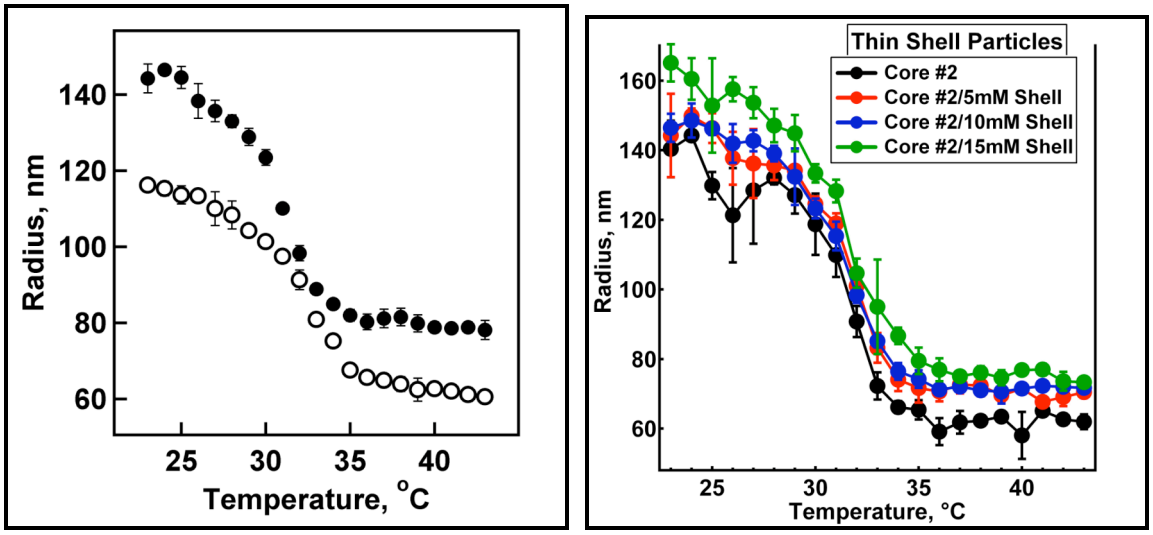

Figure 2.3 Photon correlation spectroscopy analysis of the volume phase transition behavior for Cy5/Cy5.5 labeled particles. Left: Core #1 microgels (open circles) and Core #1/20 mM Shell microgels (solid circles). Right: Core #2 and Core #2/Shell microgels with 5 mM, 10 mM, and 15 mM shells (see legend). In the case of the core/shell particles, the fluorescent dyes are only bound in the core component. These measurements were made in deionized H_2O and show that the covalently bound dyes have no significant effect on the particle phase transition behavior. Error bars represent one standard deviation about the average value of five measurements.

Table 2.2 shows the swollen shell thickness for the core/shell particles using Eq. 2.1 using the average particle sizes at temperatures well below the LCST, as well as the shell thickness for the deswollen radii (T > LCST) and the volume deswelling ratios. Let us first consider the case for the highly cross-linked core particles. From these values one can infer that the Core #1 is indeed compressed by the 20 mM shell. The overall deswelling magnitude of the Core #1/20 mM Shell particle is ~6.3-fold in volume, while the *apparent* deswelling magnitude of the shell is only ~5.8-fold. Furthermore, the deswelling magnitude of the parent Core #1 particle is ~6.9-fold in volume. Together, these values indicate that the Core #1/20 mM Shell particle has an overall higher network density than the parent Core #1.

Table 2.2 Shell thickness measurements and volume deswelling ratios based on particle size data acquired by PCS.

Sample	**Radius (nm)**		**Increase in Shell Thickness (nm)**		**Volume Deswelling Ratio**	
	23 ºC	43 ºC	23 ºC	43 ºC	Overall	Shell
Core #1	116	61	------	------	6.9	------
Core #1/ 20 mM Shell	144	78	28	17	6.3	5.8
Core #2	140	62	------	------	11.5	------
Core #2/ 5mM Shell	144	71	4	9	8.3	2.0
Core #2/ 10 mM Shell	146	72	6	10	8.3	2.7
Core #2/ 15 mM Shell	165	73	25	11	11.5	11.6

Differences are immediately noticed for the Core #2/5 mM Shell and Core #2/10 mM Shell particles compared to the parent Core #2. The *apparent* shell thickness at T<LCST is actually *smaller* than the apparent shell thickness at T>LCST. We can attribute this discrepancy, as well as the unusually low volume deswelling magnitudes for the shell, as consequences of core compression. Interestingly, these PCS data demonstrate some evidence of "shrink-wrapping". The Core #2/15 mM Shell particle shows expected increases in shell thickness at all temperatures below and above the LCST, and shows the same overall core/shell and shell volume deswelling magnitude as the parent Core #2 (~11.5), indicating that the overall cross-linking density is fairly homogeneous. However, we must consult the FRET results to procure a clearer understanding of these hierarchical structures.

Figure 2.4 shows the fluorescence data for the Core #1 microgels below (23 ºC) and above (43 ºC) the polymer LCST. The sample was excited at 646 nm in both cases. When the microgels are in the fully swollen state at 23 ºC, there is a small amount of Cy5.5 emission, as can be seen by comparing this curve to the emission spectrum of the singly labeled Cy5 core microgels (Figure 2.2). The doubly-labeled microgel spectrum taken at 23 ºC is somewhat broader than that of the singly labeled particles due to a small shoulder at ~697 nm, which arises from FRET between the excited-state Cy5 and the ground-state Cy5.5 moieties, as well as direct excitation of Cy5.5. However, a significant amount of energy transfer occurs as the temperature is raised to 43 ºC. The fluorescence spectrum shows a broadening due to a decrease in the donor emission intensity at 671 nm and a simultaneous increase in the acceptor emission intensity at 697 nm due to FRET. In this case, the gel network collapses due to the LCST behavior of pNIPAm, which in turn decreases the average distance between the donor/acceptor pairs in the microgel. Thus, an increase in energy transfer is observed.

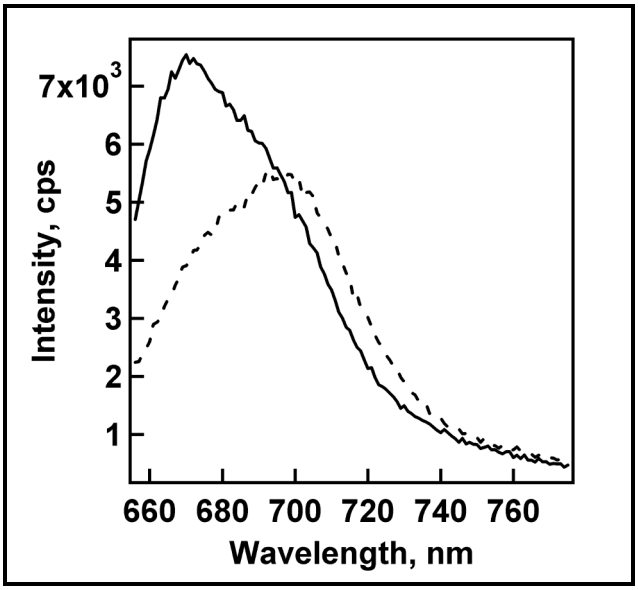

Figure 2.4 Fluorescence emission spectra of the Core #1 microgels containing both Cy5 donor and Cy5.5 acceptor dyes. In the swollen state at 23 ºC (solid line), there is a small amount of Cy5.5 emission, which may be due to direct Cy5.5 excitation, FRET, or a combination of the two effects. Above the phase transition temperature at 43 ºC (dashed line), the average donor-acceptor distance is decreased, resulting in a decrease in the donor:acceptor intensity ratio. The sample was excited at 646 nm in both cases.

The VPT behavior of the core microgels can be monitored with FRET by comparing the ratio of the donor and acceptor emission intensities as a function of temperature. Because of the random nature of the comonomer incorporation, the free rotation of the dyes about the tether, and the relative flexibility of the hydrogel network, we expect that the FRET signal will result from an average of all possible dye orientations. Thus, a simple ratio of the donor to acceptor emission intensities provides a good measure of the relative energy transfer efficiency in this system without the need to incorporate relative donor/acceptor orientation. As shown in Figure 2.5, the ratiometric FRET analysis exactly coincides with the change in particle size as a function of temperature for the Core #1 particles. These data indicate that the two dyes are homogeneously incorporated throughout the microgel. If the dyes were distributed

heterogeneously, one would expect to see phase transition behavior that differed from the PCS analysis.[18] Thus, the amine monomer must also be homogeneously distributed initially within the polymer matrix. Previous investigations indicate homogeneous incorporation can be expected for this particular amine monomer at the low concentrations used in this study.[39]

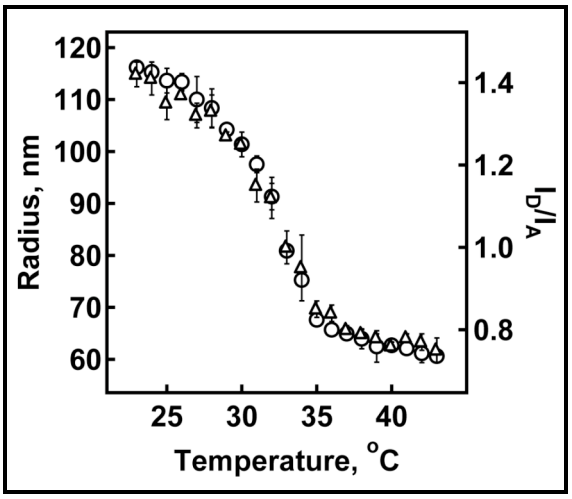

Figure 2.5 Comparison of temperature-programmed PCS analysis (circles) and FRET analysis (triangles) of Core #1 microgels containing both Cy5 donor and Cy5.5 acceptor molecules in deionized H_2O. The donor and acceptor emission intensities were monitored at 671 and 697 nm, respectively. The excitation wavelength was 646 nm. Error bars represent one standard deviation about the average value of five measurements.

The spectra of Core #1/20 mM Shell microgel particles containing the donor/acceptor pair in the core are shown in Figure 2.6. The coupling reaction was performed after shell addition in the same manner as that for the core microgels described above. Restricted core swelling is evident from the fluorescence data in this figure. When excited at 646 nm, Cy5.5 emission is observed even when the particles are held at 23 ºC, which is below the pNIPAm LCST. If we assume that the emission intensity of Cy5.5 due to direct excitation of Cy5.5 does not change following shell addition, we can

attribute the increase in Cy5.5 emission to a greater degree of energy transfer in the core/shell particle relative to that in the core particle. This result suggests that the polymer network comprising the core must be less swollen as compared to its swelling degree prior to shell addition. In other words, the core is apparently prohibited from reswelling to its original state due to the presence of the added shell. In a manner similar to the Core #1 particles illustrated in Figure 2.4, the energy transfer from the Core #1/20 mM Shell particles increases when the temperature is raised above the polymer LCST. The difference in FRET between the swollen and collapsed conformations of the core/shell particles is significantly smaller than the difference observed for the core alone (Figure 3). This observation is expected, since the average donor/acceptor distance in the swollen (T < LCST) core/shell particles is smaller than that in the core particles, yet the donor/acceptor distance at high temperature (T > LCST) should be identical for both particles.

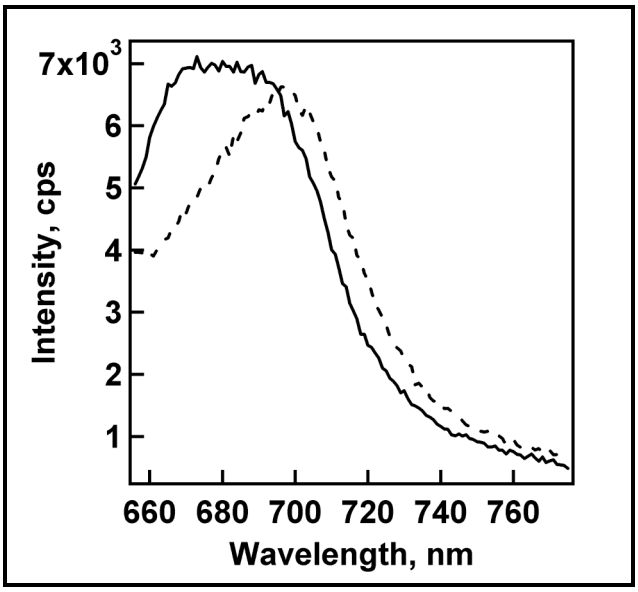

Figure 2.6 Fluorescence emission spectra of Core #1/20 mM Shell microgels containing both Cy5 donor and Cy5.5 acceptor dyes in the core component. When excited at the donor absorbance maximum of 646 nm, energy transfer and direct Cy5.5 excitation occur in the fully swollen state at 23 ºC (solid line) where polymer chains in the core are hindered from swelling to their original state due to the presence of the shell. The efficiency of energy transfer increases when the core/shell particles are collapsed above the phase transition temperature at 43 ºC (dashed line).

FRET analysis of the Core #1 and Core #1/20mM Shell particle VPT behavior is presented in Figure 2.7a; the data corresponding to the core particles is the same as that presented in Figure 2.5. In comparison to the degree of FRET for the Core #2, the Core #1/20mM Shell particles exhibit significant energy transfer at 23 ºC. This behavior shows that the shell restricts the core from reswelling to its original state as shown in Figure 2.6 above. Furthermore, the donor:acceptor emission ratio is identical for the core and core/shell particles above the LCST, suggesting that the deswollen conformation of the core is independent of the added shell. The ratio between the donor and acceptor emission intensity at 23 ºC for the Core #1/20mM Shell particles is approximately the same as that for the Core #2 particles at 31 ºC (as highlighted in Table 2.3). Figure 2.7b shows a full spectral comparison between these two sets of data (Core #1/20mM Shell at 23 ºC and Core #2 at 31 ºC). By observing the shape of the fluorescence emission spectra

in this Figure it is apparent that amount of energy transfer between the donor and acceptor chromophores is approximately the same for each case, suggesting that these points represent the respective conditions where the core has the same network density.

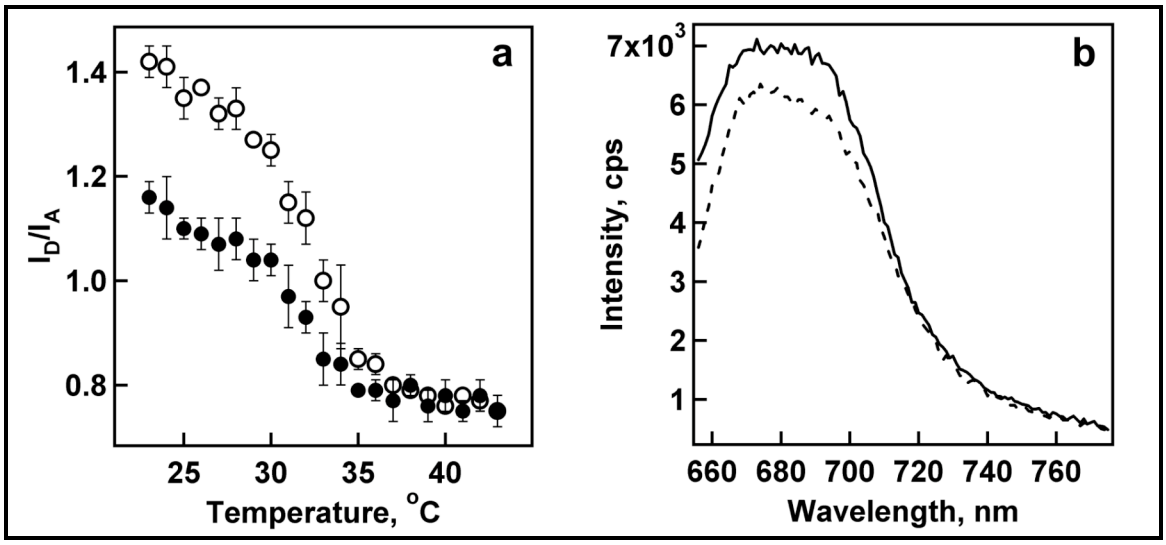

Figure 2.7 (a) Fluorescence resonance energy transfer analysis of Cy5 donor/Cy5.5 acceptor labeled Core #1 (open) and Core #1/20mM Shell (solid) microgels in H_2O. When excited at 646 nm, the core/shell particles exhibit a greater degree of energy transfer than the native core below 33 ºC. (b) Fluorescence analysis of the Core #1 particles at 31 ºC (solid line) and the Core #1/20mM Shell at 23 ºC. The two spectra show that approximately the same amount of energy transfer is occurring for each system at these dissimilar temperatures. Error bars represent one standard deviation about the average value of five measurements.

Table 2.3 Comparison of the Core #1 and Core #1/20 mM Shell particle sizes and FRET efficiency in the swollen, partially swollen, and collapsed states.

Sample	**Radius (nm)** [a]			**Intensity Ratio (671:697 nm)** [b]		
	23 ºC	31 ºC	43 ºC	23 ºC	31 ºC	43 ºC
Core #1	116	97	61	1.42	1.15	0.75
Core #1/20 mM Shell	144	110	78	1.16	0.97	0.75

[a] Radii measured via photon correlation spectroscopy. [b] Wavelength intensity ratios measured via fluorescence, λ_{ex} = 646 nm.

A semiquantitative value of the amount of restricted swelling can be gathered by noting that the core alone undergoes a volume decrease of 40% at 31 ºC when interrogated via PCS. If the FRET data accurately report on the network density in both the native core at 31 ºC and the core/shell at 23 ºC, then it may be assumed that the core swelling is restricted to only 60% of its original volume in the presence of the shell. These values can now be used to determine the geometric shell thickness from Eq. 2.2, as we can now write:

$$(R_{shell})_{23C} = (R_{h,core/shell})_{23C} - (R_{h,core})_{23C} + [(R_{h,core})_{23C} - (R_{h,core})_{31C}]$$

(Eq. 2.3)

where the temperatures at which the radii are measured are now indicated. This equation now indicates that the degree of core compression is equivalent to the difference in parent core radius between 23 °C and 31 °C (which can be found in Table 2.3). Inserting the correct values into Eq. 2.3, one obtains an actual geometric shell thickness of ~47 nm as opposed to the initial PCS estimate of ~28 nm. As stated above, the data in Figure 2.7a indicate that the core density (i.e. the FRET signal) is identical at T > LCST for both the core and core/shell particles, we can assume that the PCS-estimated collapsed shell thickness of ~17 nm very closely approximates the actual geometric thickness of the deswollen shell. Using this value and the new value for the swollen shell thickness of 47 nm, a new shell deswelling ratio of ~8.3-fold is estimated, which is significantly larger than the initial PCS-based estimate of 5.8-fold. This new value is also larger than the deswelling ratio of the parent core of ~6.9-fold, suggesting that the network density of the shell added in the second stage of polymerization is less than that of the core formed in the first polymerization step. This is expected, since the concentration of cross-linker used in the second stage (2%) was less than that used in the core particle (5%). Thus, the

combination of PCS and FRET enables the calculation of what is certainly a more realistic value for shell thickness than what is possible by PCS alone.

We can use this same calculation to determine the actual shell thicknesses at 23 °C based on the size of the parent core (Core #2) for the microgels that possessed thin shells, since Figure 2.8 demonstrates a similar temperature-dependent trend for the PCS particle size data and the FRET efficiency ratios for the Core #2 microgels as was found for the Core #1 microgels. There exists, however, some points that did not match up exactly in Figure 2.8. For example, there were very large standard deviations for some of the PCS data points at low temperatures; therefore this data may not yield accurate results. Also, the particle sizes at 32-33 °C did not line up exactly with the trend in the FRET ratios. Most of the other data points lined up fairly well.

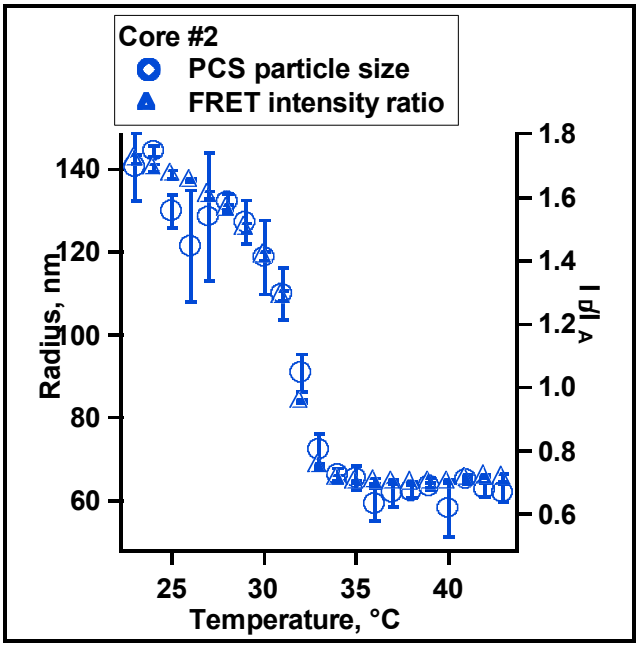

Figure 2.8 Comparison of temperature-programmed PCS analysis (circles) and FRET analysis (triangles) of Core #2 microgels containing both Cy5 donor and Cy5.5 acceptor molecules in deionized H_2O. The donor and acceptor emission intensities were monitored at 671 and 697 nm, respectively. The excitation wavelength was 646 nm. Error bars represent one standard deviation about the average value of five measurements.

Figure 2.9 shows that the FRET ratios for each of the thin shell samples are smaller than for the fully swollen core at 23 °C. By comparing these FRET values to those of the Core #2 samples, we find that, at 23 °C, the Core #2/5mM Shell, Core #2/10mM Shell, and Core #2/15mM Shell particles have compressed cores that correspond to the Core #2 size at 29 °C, 27 °C, and 28 °C, respectively (as shown by the highlighted values in Table 2.4). By using the $R_{h,core}$ for the appropriate temperatures, we find that the Core #2/5mM Shell, Core #2/10mM Shell, and Core #2/15mM Shell particles have swollen shell thicknesses of 17 nm, 18 nm, and 33 nm at 23 °C, which are significantly larger than the values found using PCS in the case of the 5 mM and 10 mM Shells (Table 2.5).

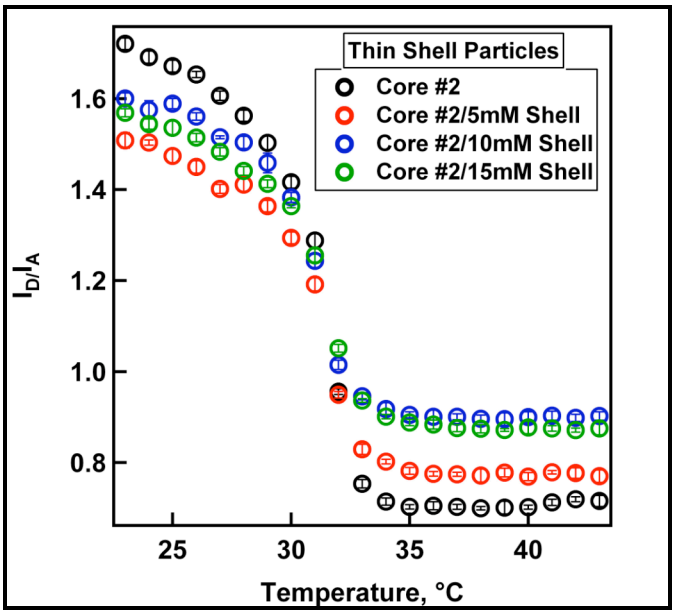

Figure 2.9 Fluorescence resonance energy transfer analysis of Cy5 donor/Cy5.5 acceptor labeled Core #2, Core #2/5mM Shell, Core #2/10 mM Shell, and Core #2/15 mM Shell microgels in H_2O.

Table 2.4 Comparison of the Core #2 and thin shell particle sizes and FRET efficiencies in the swollen, partially swollen, and collapsed states.

Sample	Radius (nm) [a]				
	23 ºC	27 ºC	28 ºC	29 ºC	43 ºC
Core #2	140	**128**	**132**	**127**	62
Core #2/5mM Shell	**144**	-------	-------	-------	71
Core #2/10 mM Shell	**146**	-------	-------	-------	72
Core #2/15 mM Shell	**165**	-------	-------	-------	73

	Intensity Ratio (671:697 nm) [b]				
	23 ºC	27 ºC	28 ºC	29 ºC	43 ºC
Core #2	1.72	**1.61**	**1.56**	**1.50**	0.72
Core #2/5mM Shell	**1.51**	-------	-------	-------	0.77
Core #2/10 mM Shell	**1.60**	-------	-------	-------	0.90
Core #2/15 mM Shell	**1.57**	-------	-------	-------	0.88

[a] Radii measured via photon correlation spectroscopy. [b] Wavelength intensity ratios measured via fluorescence, λ_{ex} = 646 nm.

Table 2.5 New shell thicknesses for the thin-shell particles based FRET results, calculated using Eq. 2.3.

Sample	PCS Radius (nm)		PCS Shell Thickness (nm)	New Shell Thickness (nm)
	23 ºC	43 ºC	23 ºC	23 ºC
Core #2	140	62	------	------
Core #2/ 5mM Shell	144	71	4	**17**
Core #2/ 10 mM Shell	146	72	6	**18**
Core #2/ 15 mM Shell	165	73	25	**33**

Unfortunately, the calculation for the shell thickness for the thin-shell particles at 43 °C is not as simple as it was for the Core #1/20 mM Shells since all of the FRET ratios for the thin-shell particles do not plateau to the same ratio as the Core #2 at T>LCST. A visual comparison of the FRET ratios tells us that all of the core/shell particle sizes at 43 °C possess parent core sizes are commensurate with the Core #2 size between 32-33 °C, yielding a parent core radius between 72-91 nm. In order to determine the correct parent core size, a more thorough FRET analysis would need to be performed between 32-33 °C. However, the level of the plateau of the FRET ratios yields some qualitative information as to the structure of these core/shell particles with thin shells. These FRET results demonstrate that the core does not deswell to the same extent with the shells at T>LCST as it does without a shell. These results seem to suggest that there may indeed be some degree of interpenetration between the interfacial boundaries due to the lightly cross-linked core and shell regions. This effect may, in fact, also be the result of a cross-linking density gradient, as described above. If the periphery of the core is only lightly cross-linked compared to its interior, then it may be infiltrated by shell polymer that contains a slightly higher cross-linking density (even though the same mol-% of BIS is used). In this case, there may be some limitations in energy transfer if the freedom of motion of the fluorophores is constrained. The fact that larger amounts of shell monomer lead to decreasing amounts of FRET at high temperatures supports this explanation. Interestingly, whereas less FRET is observed at high temperatures for these core/shell particles, higher FRET efficiencies are still observed at low temperatures, demonstrating that core compression still occurs, which would not be detectable using standard PCS experiments. The highest degree of FRET occurred with the 5 mM shell, suggesting that "shrink-wrapping" of the parent core may indeed be possible. Other cross-linking strategies should be implemented to further characterize this objective, such as using a very lightly cross-linked core (e.g. 0.5 mol-%) and a relatively highly cross-linked, thin shell (e.g. 5 mol-%, 5-10 mM TMC).

This cross-linking description may also explain why this same effect was not observed for the Core #1 and Core #1/20 mM Shell particles, since the core contained a higher cross-linking density (5 mol-%) than the shell (2 mol-%). It is expected that there would not be much interpenetration between the core and shell in this case, as demonstrated by the fairly equivalent FRET ratios for these particles at high temperatures. Regardless of the cause of these variations of the structure of the deswollen parent core, this FRET technique provides information about the core/shell structure that would be otherwise unattainable using PCS alone.

2.4 Conclusions

The structure-function relationship between the core and shell components in pNIPAm core/shell microgels has been studied via fluorescence resonance energy transfer measurements. FRET was used to observe the decreased swelling ability of the core in the presence of the added shell. Below the phase transition temperature of pNIPAm (31 ºC), core particles are able to swell and achieve a volume that is limited by the polymer chain elasticity. The degree of FRET is minimal under these conditions. Core/shell particles display a significant increase of FRET due to a decreased swelling ability of the core in the presence of the added shell under the same solution conditions. Together, these studies allow for a semiquantitative determination of the actual geometric thickness of the added shell by accounting for the degree of core compression resulting from shell addition.

References

[1] Nayak, S.; Lyon, L. A. Ligand-functionalized core/shell microgels with permselective shells. *Angew. Chem. Int. Ed.* **2004**, *43*, 6706-6709.

[2] Nayak, S.; Lee, H.; Chmielewski, J.; Lyon, L. A. Folate-mediated cell targeting and cytotoxicity using thermoresponsive microgels. *J. Am. Chem. Soc.* **2004**, *126*, 10258-10259.

[3] Gan, D.; Lyon, L. A. Amphiphilic, peptide-modified core/shell microgels. *Prog. Colloid Polym. Sci.* **2006**, *133*, 1-8.

[4] Berndt, I.; Richtering, W. Doubly Temperature Sensitive Core-Shell Microgels. *Macromolecules* **2003**, *36*, 8780-8785.

[5] Pecora, R. *Dynamic Light Scattering*; Plenum Press: New York, 1985.

[6] Jones, C. D.; Lyon, L. A. Synthesis and Characterization of Multiresponsive Core-Shell Microgels. *Macromolecules* **2000**, *33*, 8301-8306.

[7] Tiarks, F.; Landfester, K.; Antonietti, M. Silica Nanoparticles as Surfactants and Fillers for Latexes Made by Miniemulsion Polymerization. *Langmuir* **2001**, *17*, 5775-5780.

[8] Haridas, M. M.; Bellare, J. R. Differences in particle sizes measured by cryo-SEM and quasi-elastic light scattering in latex particles. *Colloids and Surfaces, A: Physicochemical and Engineering Aspects* **1998**, *133*, 165-171.

[9] Thiagarajan, V. S.; Huang, Z.; Scriven, L. E.; Schottel, J. L.; Flickinger, M. C. Microstructure of a biocatalytic latex coating containing viable Escherichia coli cells. *Journal of Colloid and Interface Science* **1999**, *215*, 244-257.

[10] Berndt, I.; Pedersen, J. S.; Richtering, W. Structure of Multiresponsive \"Intelligent\" Core-Shell Microgels. *J. Am. Chem. Soc.* **2005**, *127*, 9372-9373.

[11] Berndt, I.; Popescu, C.; Wortmann, F.-J.; Richtering, W. Mechanics versus thermodynamics: swelling in multiple-temperature-sensitive core-shell microgels. *Angew. Chem. Int. Ed.* **2006**, *45*, 1081-1085.

[12] Berndt, I.; Pedersen, J. S.; Lindner, P.; Richtering, W. Influence of Shell Thickness and Cross-Link Density on the Structure of Temperature-Sensitive Poly-N-Isopropylacrylamide-Poly-N-Isopropylmethacrylamide Core-Shell Microgels Investigated by Small-Angle Neutron Scattering. *Langmuir* **2006**, *22*, 459-468.

[13] Jones, C. D.; McGrath, J. G.; Lyon, L. A. Characterization of Cyanine Dye-Labeled Poly(N-isopropylacrylamide) Core/Shell Microgels Using Fluorescence Resonance Energy Transfer. *J. Phys. Chem. B* **2004**, *108*, 12652-12657.

[14] Lakowicz, J. R. *Principles of Fluorescence Spectroscopy, 2nd ed.*; Kluwer Academic: New York, 1999.

[15] Schobel, U.; Egelhaaf, H. J.; Brecht, A.; Oelkrug, D.; Gauglitz, G. New-donor-acceptor pair for fluorescent immunoassays by energy transfer. *Bioconjugate Chemistry* **1999**, *10*, 1107-1114.

[16] Jones, C. D.; Lyon, L. A. Shell-Restricted Swelling and Core Compression in Poly(N-Isopropylacrylamide) Core-Shell Microgels. *Macromolecules* **2003**, *36*, 1988-1993.

[17] Gan, D.; Lyon, L. A. Synthesis and Protein Adsorption Resistance of PEG-Modified Poly-N-isopropylacrylamide Core/Shell Microgels. *Macromolecules* **2002**, *35*, 9634-9639.

[18] Gan, D.; Lyon, L. A. Interfacial Nonradiative Energy Transfer in Responsive Core-Shell Hydrogel Nanoparticles. *J. Am. Chem. Soc.* **2001**, *123*, 8203-8209.

[19] Jones, C. D.; Lyon, L. A. Dependence of Core Compression on Shell Thickness in Acrylic Acid Modified Poly(N-Isopropylacrylamide) Core/Shell Microgels. *Langmuir* **2003**, *19*, 4544-4547.

[20] Nayak, S.; Gan, D.; Serpe, M. J.; Lyon, L. A. Hollow thermoresponsive microgels. *Small* **2005**, *1*, 416-421.

[21] Pelton, R. Temperature-sensitive aqueous microgels. *Adv. Colloid. Interface Sci.* **2000**, *85*, 1-33.

[22] Saunders, B. R.; Crowther, H. M.; Morris, G. E.; Mears, S. J.; Cosgrove, T.; Vincent, B. Factors affecting the swelling of poly(N-isopropylacrylamide) microgel particles: fundamental and commercial implications. *Colloid Surf. A-Physicochem. Eng. Asp.* **1999**, *149*, 57-64.

[23] Pelton, R. H.; Chibante, P. Preparation of aqueous latices with N-isopropylacrylamide. *Colloids and Surfaces* **1986**, *20*, 247-56.

[24] Kawaguchi, H.; Kisara, K.; Takahashi, T.; Achiha, K.; Yasui, M.; Fujimoto, K. Versatility of thermosensitive particles. *Macromol. Symp.* **2000**, *151*, 591-598.

[25] Tanaka, T. Collapse of Gels and the Critical Endpoint. *Physical Review Letters* **1978**, *40*, 820-823.

[26] Heskins, M.; Guillet, J. E. Solution properties of poly(N-isopropylacrylamide). *J. Macromol. Sci. Chem.* **1968**, *A2*, 1441-1455.

[27] Gan, D.; Lyon, L. A. Tunable Swelling Kinetics in Core-Shell Hydrogel Nanoparticles. *J. Am. Chem. Soc.* **2001**, *123*, 7511-7517.

[28] Lide, D. R., Ed. *The CRC Handbook of Chemistry and Physics*; 74th ed.; CRC Press: Boca Raton, 1994; Vol. 124.

[29] Flory, P. J. *Principles of Polymer Chemistry*; Cornell University Press: London, 1953.

[30] Fernandez-Nieves, A.; Fernandez-Barbero, A.; Vincent, B.; de las Nieves, F. J. Charge controlled swelling of microgel particles. *Macromolecules* **2000**, *33*, 2114-2118.

[31] Jones, C. D.; Lyon, L. A. Dependence of Shell Thickness on Core Compression in Acrylic Acid Modified Poly(N-isopropylacrylamide) Core/Shell Microgels. *Langmuir* **2003**, *19*, 4544-4547.

[32] Wu, X.; Pelton, R. H.; Hamielec, A. E.; Woods, D. R.; McPhee, W. The kinetics of poly(N-isopropylacrylamide) microgel latex formation. *Colloid Polym. Sci.* **1994**, *272*, 467-477.

[33] Wu, C.; Zhou, S. Volume Phase Transition of Swollen Gels: Discontinuous or Continuous? *Macromolecules* **1997**, *30*, 574-576.

[34] Varga, I.; Gilanyi, T.; Meszaros, R.; Filipcsei, G.; Zrinyi, M. Effect of Cross-Link Density on the Internal Structure of Poly(N-isopropylacrylamide) Microgels. *J. Phys. Chem. B* **2001**, *105*, 9071-9076.

[35] Guillermo, A.; Addad, J. P. C.; Bazile, J. P.; Duracher, D.; Elaissari, A.; Pichot, C. NMR investigations into heterogeneous structures of thermosensitive microgel particles. *J. Polym. Sci. Pt. B-Polym. Phys.* **2000**, *38*, 889-898.

[36] Grabarek, Z.; Gergely, J. Zero-Length Crosslinking Procedure with the Use of Active Esters. *Anal. Biochem.* **1990**, *185*, 131-135.

[37] Mujumdar, R. B.; Ernst, L. A.; Mujumdar, S. R.; Lewis, C. J.; Waggoner, A. S. Cyanine Dye Labeling Reagents - Sulfoindocyanine Succinimidyl Esters. *Bioconjugate Chemistry* **1993**, *4*, 105-111.

[38] Mujumdar, S. R.; Mujumdar, R. B.; Grant, C. M.; Waggoner, A. S. Cyanine-labeling reagents: Sulfobenzindocyanine succinimidyl esters. *Bioconjugate Chemistry* **1996**, *7*, 356-362.

[39] Meunier, F.; Elaissari, A.; Pichot, C. Preparation and Characterization of Cationic Poly(N- Isopropylacrylamide) Copolymer Latexes. *Polym. Adv. Technol.* **1995**, *6*, 489-496.

CHAPTER 3

SYNTHESIS AND CHARACTERIZATION OF POLY-*N*-ISOPROPYLACRYLAMIDE SHELLS ON SILVER CORE NANOPARTICLES

3.1 Introduction

Silver (Ag) particles on the nanoscale have been found to interact with light to produce excitation of surface plasmon polariton resonances due to the large density of conducting electrons and the frequency dependence of the real and imaginary parts of the dielectric function of the material.[1-3] These plasmon resonances, which are due to both non-radiative absorption and a near-field interaction that evolves into far-field scattering, are dependent on the particle size, shape, and the dielectric medium.[4-6] The surface plasmons of nearly spherical Ag particles also possess a multipolar character which becomes more prominent as the size of the particles becomes comparable to the wavelength of light.[2,7,8] Efficient coherent coupling of these plasmon modes has been demonstrated when nearby particles are in close proximity, even without long-range order.[7] Such coherent interactions between neighboring Ag particles suggest that a dipolar character dominates when Ag particles are lined up together and that quadrupolar, hexapolar, or even octupolar characters emerge when Ag particles are surrounded by additional particles.[5,8,9] These effects may lead to interesting optical properties that can be controlled by modification of the particle order and interparticle spacing in assembled arrays.[5,9-11]

Unfortunately, metal nanoparticles have a tendency to aggregate when high particle densities are employed in attempts to achieve such highly-ordered assemblies.[12] Many approaches have been investigated to gain better control of Ag particle assemblies to yield stability of the desired configurations. By affixing metal particles to modified

substrates, the particle order can be stabilized and the interparticle distances can be varied in some cases.[5,13-15] However, this approach is limited to the investigation to 2D assemblies of particles.

Some groups have elected to introduce metallic components on the surface or within conventional spherical particles, which can provide a basic, stable construct that is more suitable for producing 3D, ordered assemblies.[16-26] However, the positions of the metal components were not necessarily well defined within the bulk particle. Discrete arrangements of the metal particles would be advantageous for optical and plasmonic applications. Methods for direct modification of metal nanoparticles has been shown to be more promising for the fabrication of such materials.[6,12,27,28] Polymer coatings have been of particular interest because they can introduce both stability and functionality to the metal nanoparticle, which can be useful for the construction of ordered assemblies. The particular synthetic procedures that are used to prepare such core/shell nanocomposite materials are of foremost importance. For example, the Chumanov group succeeded in adding thin, polymer shells to Ag particles by adsorbing specific stabilizing agents or initiators directly to the surface of the Ag particles.[12,27] In the studies presented in this chapter, a core/shell synthesis approach was utilized to add a shell composed of the thermosensitive polymer, poly-*N*-isopropylacrylamide (pNIPAm) using Ag particles as seed cores. As discussed previously, pNIPAm particles undergo a volume phase transition at ~31 °C. The presence of this polymer coating should not only stabilize the Ag particles, but also introduce a functionality that can provide a means for particle self-assembly to form 3D colloidal crystals using simple thermal annealing procedures.[29-32] The tunability of the soft, pNIPAm shell can also facilitate changes in the interparticle distances, which can be used to investigate the cooperative plasmon modes of neighboring Ag particles.

The pNIPAm shell synthesis was performed using a “seed and feed” synthetic approach similar to the method described in Chapter 2. In order to promote pNIPAm

polymer growth at the surface of the Ag particles, a novel approach was implemented whereby short chains of linear pNIPAm were adsorbed to the particles at room temperature by means of an amino end group.[33] As the temperature is raised to the levels that are typically used for free-radical, precipitation polymerization of pNIPAm (~70 °C, which is well-above the phase transition temperature for pNIPAm), the linear pNIPAm chains collapse and effectively coat the Ag particles, providing a hydrophobic precursor nucleation site for shell polymer growth. Acrylic acid (AAc) was used as a functional comonomer, which provided charged groups that were used for electrostatic stabilization of the particles for characterization by atomic force microscopy (AFM) in liquid and also rendered the particles responsive to changes in pH. The resulting Ag core/pNIPAm-*co*-AAc shell particles were also characterized using transmission electron microscopy (TEM), and the existence of the polymer shell was unambiguously confirmed by particle tracking techniques using video microscopy.

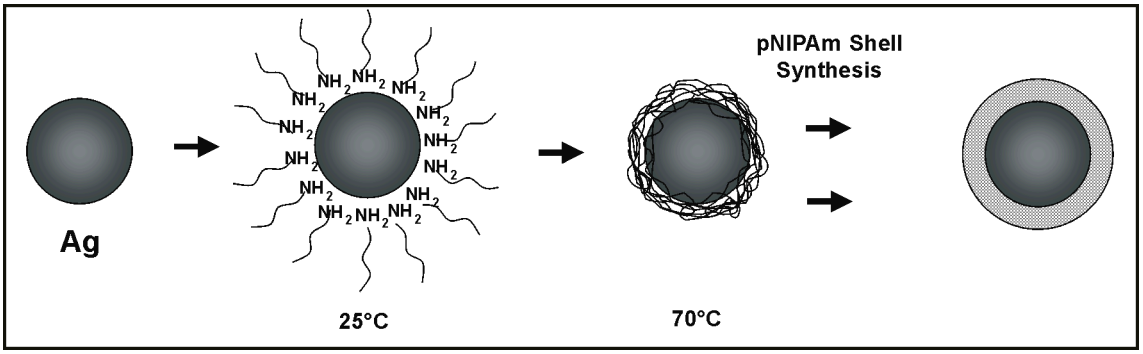

Figure 3.1 Synthetic approach for adding a pNIPAm shell to Ag seed particles using linear chains of amino-terminated pNIPAm to form a precursor shell.

3.2 Experimental Section

3.2.1 Particle Synthesis

Materials

Some of the materials used in this study can be found in the Experimental Section of Chapter 2. Additionally, Ag nanoparticles (diameter ~70 nm) were provided by the Chumanov group who synthesized the particles by hydrogen reduction procedures and purified the dispersions as described elsewhere.[34] Acrylic acid (AAc, Aldrich) was distilled under reduced pressure. Linear amino terminated poly(N-isopropylacrylamide) (NH_2-pNIPAm, M_n = 10,400) was purchased from Polymer Source, Inc., and used as received. The cationic silane, 3-aminopropyltrimethoxysilane (APTMS), was purchased from United Chemical Technologies, Inc., and used as received. Buffered aqueous solvents, (formate, pH 3.0, or MES, pH 5.5; 10 mM ionic strength)

pNIPAm Shell Synthesis

Two types of Ag core/pNIPAm-*co*-AAc shell nanoparticles were prepared by employing two different total monomer concentrations (40 mM or 75 mM) to yield shell thicknesses of different sizes. First, linear NH_2-pNIPAm was absorbed to the Ag nanoparticles by combining 2.5 mL of a stock solution of Ag particles (~10^{11}-10^{12} particles/mL; OD = 25) with 3.0 mL of a 1.0 mM NH_2-pNIPAm stock solution and mixing overnight. Free linear NH_2-pNIPAm chains were removed from this solution by centrifugation. Because the density of the Ag particles is rather high, a very low centrifugation speed (150 x g rcf) was employed for several hours at 25 °C, to avoid aggregation of Ag particles. Using this low speed allowed for easy redispersion of the Ag pellet. 4.0 mL of the supernatant was removed, leaving 1.5 mL of solution remaining.

This solution was transferred to a 40 dram vial. Table 3.1 shows the components used for each of the shell syntheses. The NIPAm and BIS monomers (dissolved in 3.0

mL water) and the SDS (dissolved in 1.0 mL water) were added to the vial, bringing the total volume to 5.5 mL. This vial was capped with a rubber stopper and a needle for N_2 was inserted through the stopper and into the solution for purging. Another needle was added to the stopper to allow for venting of the gas. This solution was placed in a water bath and heated to ~70 °C for 30 min while stirring. AAc was added just prior to initiation. The APS was dissolved in ~0.1 mL of water and added to the vial for initiation. The reaction proceeded for ~ 4 hrs.

Table 3.1 Components for pNIPAm-*co*-AAc shell syntheses using Ag core nanoparticles.

Shell Synthesis	NIPAm, g	BIS, g	AAc, µL	SDS, g	APS, g
40 mM	0.0238	0.0007	1.5	0.0023	0.0013
75 mM	0.0414	0.0013	2.8	0.0024	0.0016

The Ag core/pNIPAm-*co*-AAc shell particles were cleaned three times by centrifugation at 25 °C for 45 min. Since the hydrogel shell increases the buoyancy of the particles, higher speeds were used to form a pellet of the core/shell particles. Centrifugation speeds of 830 x *g* rcf and 1040 x *g* rcf were used for the 40 mM and 75 mM core/shell particles, respectively.

Substrate Preparation

Functionalized substrates were prepared so that the core/shell particles could be stabilized using electrostatic interactions for AFM studies in liquid, using water (as depicted in Figure 3.2). The glass substrates possessed a positive surface charge due to primary amine groups (*vide infra*), which are protonated at neutral pH conditions. The shells of the particles contain AAc groups which can be made negatively charged by

deprotonating the AAc by adjusting the pH to above the pKa of AAc (pK_a ~4.25).[35] The Ag core particles could also be affixed in this fashion due to interactions with the lone pair of electrons of the amine groups on the functionalized surface.[14] The functionalized substrates were prepared by silanization of the glass cover slips (VWR, 22 x 30 mm). First, the cover slips were cleaned using a plasma cleaner/sterilizer (PDC-32 G, Harrick). The cover slips were then transferred to a 1% APTMS solution (prepared with 200 proof ethanol) for 2 hrs. After silane functionalization, the cover slips were washed with 95% ethanol and stored in ethanol. Sample preparation was performed by placing a few drops of a dilute dispersion of the particles (in water) on to the functionalized substrates and allowing the solution to dry open to the atmosphere at ambient temperature.

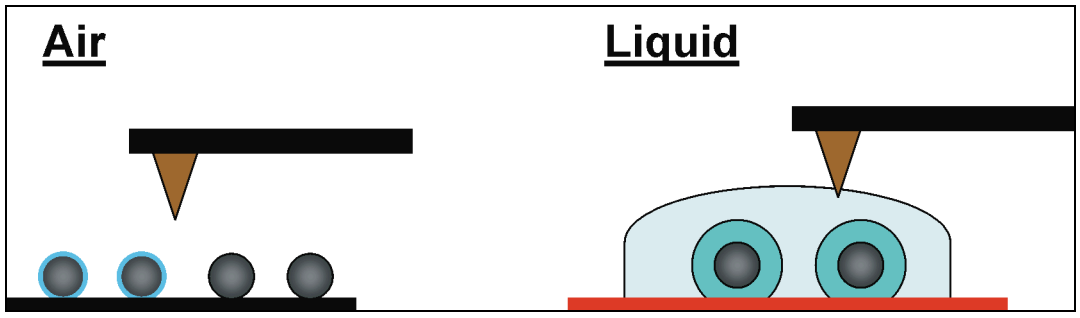

Figure 3.2 Illustration of particle stabilization using a functionalized glass substrate (red block) for AFM measurements in liquid.

3.2.2 Characterization Techniques

UV-VIS Spectroscopy

Absorbance spectra were collected using Shimadzu UV-1601 spectrophotometer to characterize the plasmon resonance of the Ag particles.

Transmission Electron Microscopy

The dry sizes and morphologies of the Ag and Ag core/shell particles were examined using transmission electron microscopy (TEM). Samples were prepared by placing multiple drops of dilute solutions of particles on TEM copper grids (coated with either Formvar or Carbon-B Type; 200 mesh, Ted Pella, Inc.) leaving at least one drop to dry overnight under ambient conditions. A JEOL 100CX II operating at 100 kV was used for TEM characterizations.

Atomic Force Microscopy

Dr. Christine Kranz, a member of the Mizaikoff Group at Georgia Tech, performed all atomic force microscopy (AFM) experiments. A PicoPlus SPM system (Molecular Imaging) was used for all of the AFM studies. All images were acquired using MACmode with a MAC nose cone (magnetic coil integrated in the nose cone) using MACII silicon cantilevers with a magnetic coating. The cantilevers possessed a nominal spring constant of 1.62 N/m or 2.8 N/m (as determined using a thermal noise method). Image processing was performed using PicoScan 5.3.3 software (Molecular Imaging) using a maximum scan range of 100 x 100 μm. Measurements were performed in air and in liquid using functionalized glass substrates (*vide supra*) to stabilize the particles. The force applied by the cantilever against the particles was adjusted by controlling the oscillating amplitude of the cantilever, using dynamic force measurements.[36]

Particle Tracking Experiments

Particle tracking experiments based on passive microrheology methods were employed by monitoring diffuse thermal motion that originates from the intrinsic Brownian motion of the Ag C/S particles to determine the particle size. Video microscopy was utilized to analyze this thermally-driven particle behavior.[37,38] Using a Newtonian liquid as the sample medium, the size of the particles can be calculated using

the Stokes-Einstein equation, which is related to the mean-squared displacement (MSD) of the particles:[38-40]

$$\langle \Delta r^2(\tau) \rangle \equiv \langle |r(t+\tau) - r(t)|^2 \rangle = 2dD_T\tau = \frac{dk_BT}{3\pi\eta a}\tau \quad , \qquad \text{(Eq 3.1)}$$

where the left-hand side of this equation is the MSD of the particles as a function of the lag time, τ, starting at time, t, which represents the average particle trajectories. For the right-hand side of the equation, D_T is the translational diffusion coefficient, d is the dimensionality of the particle trajectories, η is the viscosity of the medium, k_B is the Boltzmann constant, T is the temperature of system, and a is the particle radius. The dimensionality is usually 2 for conventional microscopy applications.

Jae Kyu Cho, a member of Breedveld Group at Georgia Tech, performed all of the particle tracking experiments for this study. All data were collected at T = 297 K. The core/shell particles were dispersed in buffers of pH 3 or 5.5 to determine the radius of these particles in each environment (η = 0.9142 x 10^{-3} Pa·sec for water at 297 K). A Leica DMIRB microscope equipped with a reflectance light source was used for the particle tracking experiments using a 100x oil-immersion objective. Since large Ag particles can scatter light very efficiently,[1-3,41,42] Ag particles of this size (~70 nm) could be easily observed using reflectance microscopy. Movies of the core/shell particles were collected using a Cohu CCD camera (Poway, CA; 640 x 480 pixels) that has a fixed frame rate of 30 frames/second. Because the non-coated Ag particles diffuse rapidly, they were suspended in a glycerin/water (13.81 g/1.71 g) mixture (η = 144 x 10^{-3} Pa·sec at 297 K) and the images of these particles were collected using a Hamamatsu C9100 CCD camera (1000 x 1000 pixels) using a frame rate of 60 frames/second.

The positions of the particles were analyzed in each frame of the movie using Interactive Data Language (IDL) analysis software (Research Systems, Inc., v.6.2). By tuning the tracking parameters of the software, artificial bias due to aggregation can be screened, allowing for the efficient characterization of single particles. At least 15 particles were observed for the statistical analysis of each movie. The particle positions for each image were combined to determine the particle trajectories, which were then used to determine the MSD of the particles over time. For diffusive motion, the d-dimensional MSD is given by:

$$\frac{MSD}{\tau} = 2D_T = \frac{dk_BT}{3\pi\eta a}, \qquad \text{(Eq 3.2)}$$

such that the slope of MSD vs. time curve corresponds to two times the diffusion coefficient of the particles in their respective media. By inserting this slope into Eq. 3.2, the particle radius can be obtained.

3.3 Results and Discussion

Images of the Ag and Ag core/shell particles that were collected using TEM are shown in Figure 3.3. Unfortunately, it is difficult to draw any significant conclusions as to the presence of a shell in the images of the core/shell samples since the TEM images were collected under high vacuum conditions where the volume of the dried pNIPAm hydrogel polymer becomes significantly reduced. However, qualitative features can be ascertained from these images. Compared to the polyhedral surface structure demonstrated by the bare Ag particles,[7] the core/shell particles appear slightly more rounded, such that the shape approaches that of a spherical structure. Similar globular features have been observed for Ag particles where a polymer shell has been added.[12,27] This feature may be caused by the uniform distribution of pNIPAm polymer around the

Ag core as a result of the precipitation polymerization.[33,43] This effect is emphasized by the lighter areas of the core/shell particles, which may correspond to polymer regions of lower electron density.

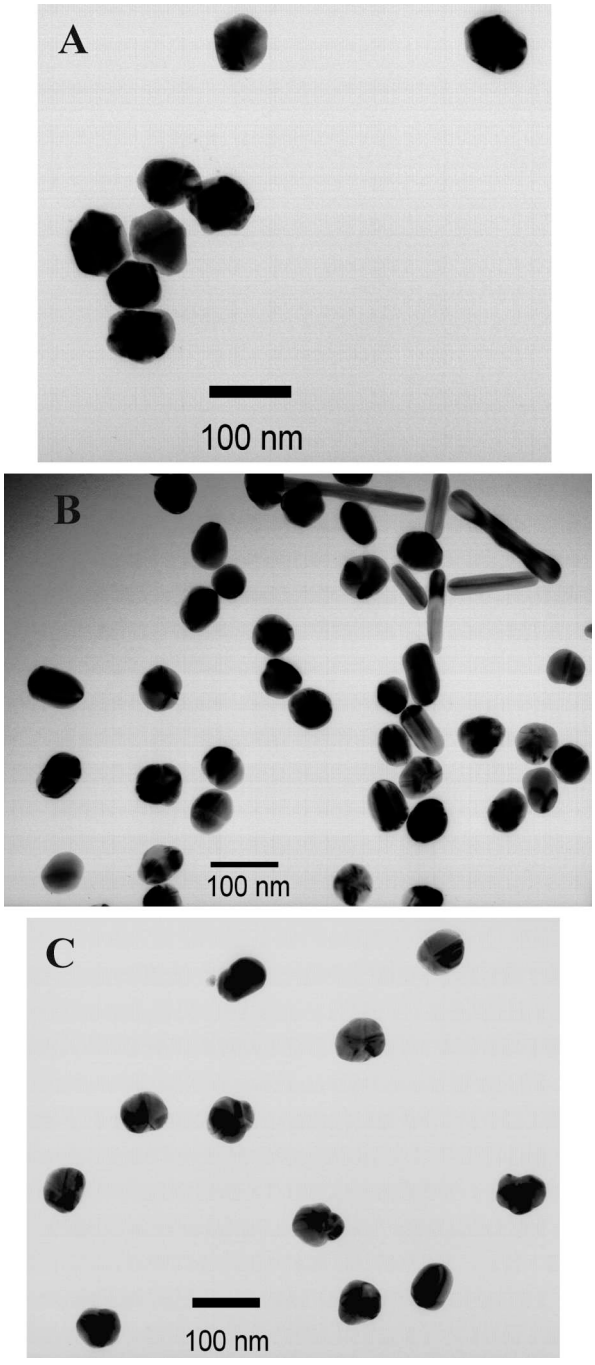

Figure 3.3 TEM images of bar Ag particles and Ag core/pNIPAm-*co*-AAc shell particles: A) Ag cores, B) Ag C/S 40, and C) Ag C/S 75.

Ag rods and pyramids are sometimes obtained during the synthesis of Ag particles, representing ~10-15% of the total number of particles, and they can typically be removed by filtration procedures.[7,34] Some rods were, in fact, present in these samples, as demonstrated in Figure 3.3, Panel B. Fortunately, the presence of these rod-shaped Ag particles did not impact the polymerization of the pNIPA-*co*-AAc shell, even though these Ag particles had been filtered prior to use. However, it should be noted that the presence of this contamination could produce defects in the formation of well-defined ordered assemblies.

Since TEM cannot efficiently detect the presence of the pNIPAm-*co*-AAc shell, AFM experiments were performed both in air and in liquid to investigate changes in the particle size due to swelling of the hydrogel shell polymer. Preliminary data are shown in Table 3.2. Although there were only modest increases in the height of the core/shell particles in air, experiments performed in liquid demonstrated a larger variation in this height, showing increases of 14 nm and 30 nm for the Ag C/S 40 and Ag C/S 75 particles, respectively.

Table 3.2 Preliminary results of particle size using AFM.

Sample	Height in Air, nm	Height in Liquid, nm
Ag Core	73	-------
Ag C/S 40	78	92
Ag C/S 75	82	112

To further investigate the presence of the polymer shell, in liquid AFM experiments were performed by applying different forces to the particles by adjusting the oscillating amplitude of the cantilever (higher amplitude values, shown in parentheses

next to the sample name in Table 3.3, correspond to lower applied forces).[36] Particles were diluted using water and affixed to APTMS-functionalized glass cover slips. Initial experiments in air showed that the height for the Ag C/S 75 sample, ~76 nm, was fairly similar to the height found for bare Ag particles, ~72 nm. When lower forces were applied to the fixed Ag particles, no significant height change was found in liquid. However, when this same experimental method was used to analyze the Ag C/S 75 particles, larger variations in particle height were found, which stabilized at ~100 nm as lower forces were applied. Images for both sets of particles are shown in Figure 3.4.

Table 3.3 Particle sizes of Ag Core and Ag C/S 75 particles using AFM in air and in liquid. The force applied to the particles was varied by adjusting the oscillating amplitude of the cantilever (shown in parentheses with the sample name; as this value increases, the force decreases). The numbers of particles that were measured are shown in parentheses with the standard deviation.

Sample	Height, nm	Std Dev, nm
Ag Core (Air)	72	7 (n = 10)
Ag Core (6.4)	74	10 (n = 10)
Ag Core (7.0)	73	6 (n = 10)
Ag Core (7.3)	75	9 (n = 10)
Ag C/S 75 (Air)	76	5 (n = 10)
Ag C/S 75 (5.2)	82	8 (n = 9)
Ag C/S 75 (7.2)	101	6 (n = 7)
Ag C/S 75 (7.6)	100	13 (n = 9)

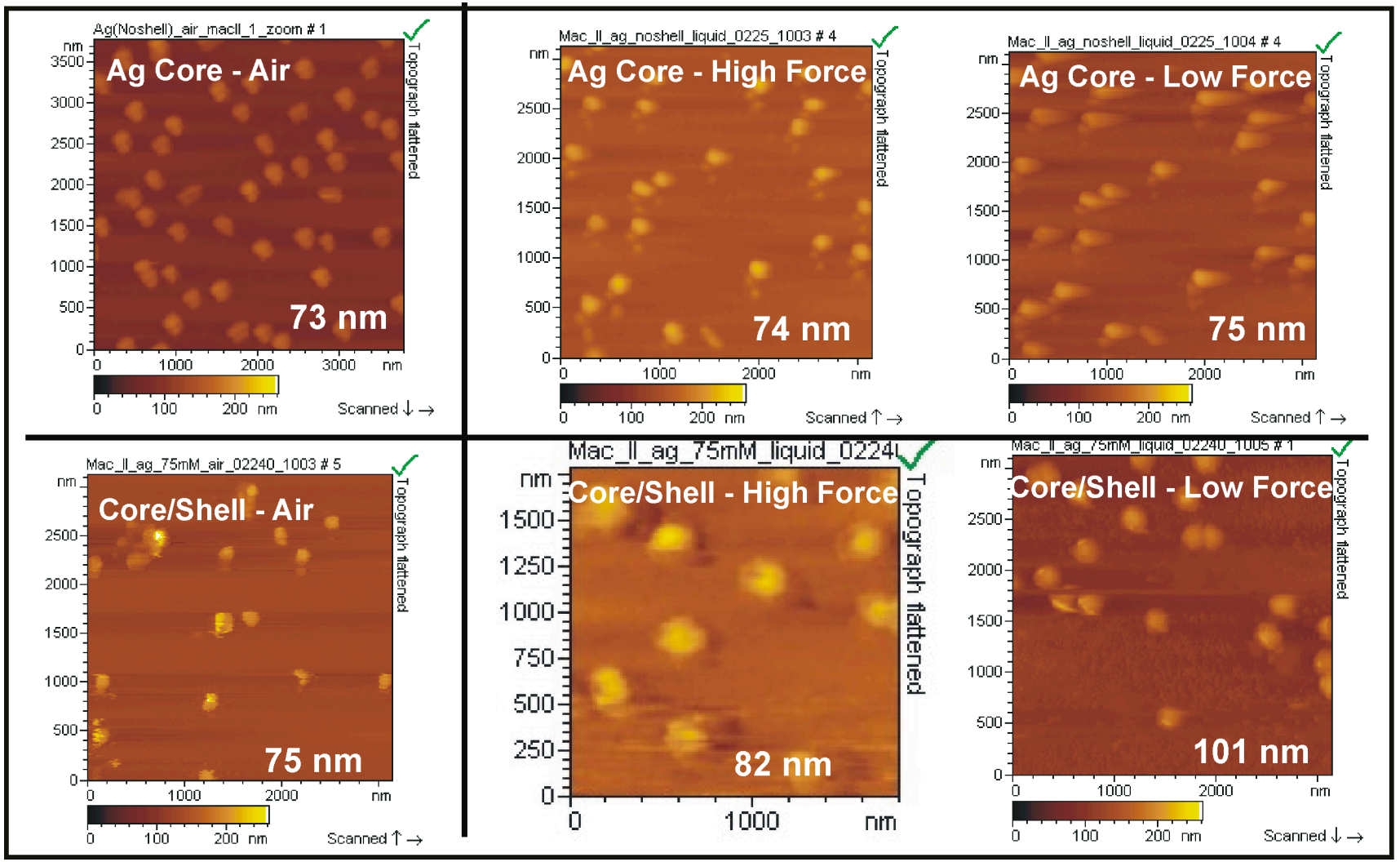

Figure 3.4 AFM images (topography scans) of Ag core (top row) and Ag C/S 75 particles (bottom row). Left: In air. Center: In liquid, high force. Right: In liquid, low force.

The additional increase of 25 nm in height demonstrated for the Ag C/S 75 particles assists in confirming the presence of a shell polymer, but it is unclear whether this measurement corresponds to the total increase in particle size or only to the thickness of the shell polymer. This uncertainty in the particle size exists because the particle may be situated such that the Ag core touches the substrate and the bottom shell layer is compressed, in which case the 25 nm increase indicates the thickness of the shell polymer. However, this interpretation may overestimate the true shell thickness if the shell polymer that is situated against the substrate experiences some degree of swelling. Therefore, these images may not provide the best quantitative measurements for the determination of the size of these core/shell particles. Unfortunately, these preceding microsocopy measurements may also not be statistically accurate with respect to the particle size since it has been shown that capillary forces will segregate Ag particles different sizes and shapes during drying procedures.[34] It has shown that special modification techniques are necessary for adequate immobilization of Ag particles to accurately determine their size and shape.[14] However, these observations provide some indication of the presence of a shell component.

Particle tracking experiments, which are based on passive microrheology methods, were performed to successfully characterize the size of the Ag core/shell particles by monitoring the diffusive thermal motion of the particles. The core/shell particles were characterized by dispersing the particles in different buffered aqueous media (pH 3 and 5.5). Since the acrylic acid groups in the polymer shell impart pH responsivity to the particle, these groups will be mostly protonated at pH's below the pK_a for acrylic acid and will be mostly deprotonated at pH's above this pK_a. This latter effect should cause swelling of the hydrogel shell due to Coulombic repulsion of the acrylic acid groups.[44-46] The particle sizes found for the bare Ag and Ag core/pNIPAm-*co*-AAc shell particles are shown in Table 3.4.

Table 3.4 Particle size data obtained using particle tracking experiments.

Sample	pH	Diameter, nm	Std Dev, nm
Ag Core	-------	71.0	3.2
Ag C/S 40	3.0	131.5	3.0
Ag C/S 40	5.5	152.6	1.1
Ag C/S 75	3.0	157.5	0.7
Ag C/S 75	5.5	165.5	0.7

The particle size for the non-modified Ag corresponds very well with the size that was determined by the Chumanov group, as well as with the TEM measurements. These data not only demonstrate an increase in the particle size with the addition of the pNIPAm-*co*-AAc shell, but they also show increases in size when more monomer is used in the shell synthesis. The Ag C/S 40 particles show ~60 nm increase in particle size and the Ag C/S 75 particles demonstrate an increase of ~87 nm (at pH 3.0). These measurements correspond to shell thickness of ~30 nm and ~44 nm, respectively. As the pH is increased to pH 5.5, there is a noticeable swelling of the particle, confirming the presence of pH responsivity of the core/shell particles.

The surface plasmon properties of the core/shell particles were also investigated using absorbance spectroscopy (Figure 3.5). There was a slight blue shift (~3 nm) in the absorption maxima for both of the core/shell particles compared to the plasmon absorption for the bare Ag particles. The Chumanov group observed a similar effect with Ag particles that possessed thin poly(styrene-*co*-4-styrene-sulfonic acid sodium salt) shells (~5-10 nm, by TEM) and attributed this result to electric insulation from neighboring particles, although, in their case, the plasmon wavelength shift was rather large (~12 nm).[12] Interestingly, this effect was barely noticeable for the Ag C/S 40 and Ag C/S 75 particles, even though these particles were comprised of shells of relatively

large thickness. The lack of this interference may be due to the less dense, hydrogel character of the pNIPAm-*co*-AAc shell, and this behavior may be especially advantageous when these particles are employed in optical applications. A simple aggregation test was also performed to examine the particle stability provided by the polymer shell. Typically, the addition of high concentrations of NaCl causes instantaneous aggregation of the Ag particles as well as particle etching due to Cl^-, causing a decrease in the plasmon absorption.[9,27] Whereas the Ag particles demonstrated a distinct decrease in plasmon absorption with the addition of NaCl, the core/shell particles effectively retained their optical properties (Figure 3.5).

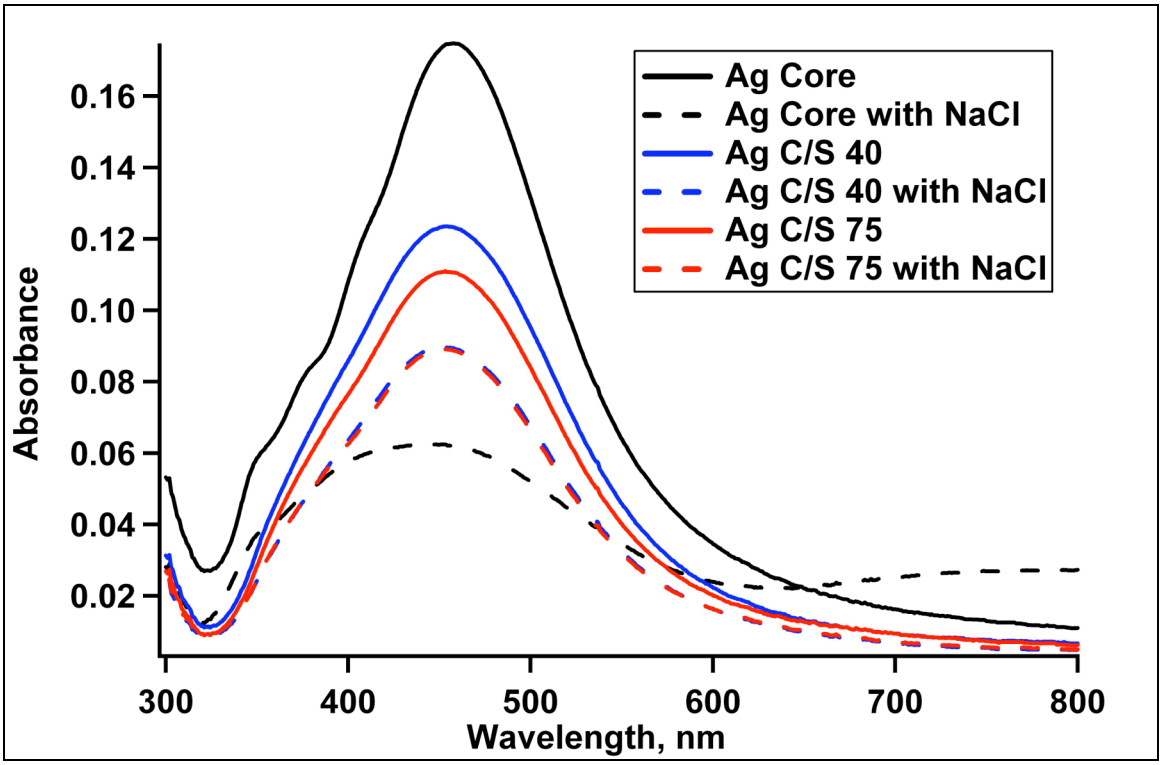

Figure 3.5 Absorption spectra of bare silver particles and Ag C/S 40 and Ag C/S 75 core/shell particles, with and without the addition of NaCl to induce particle aggregation.

3.4 Conclusions

A polymer shell composed of pNIPAm-*co*-AAc was successfully added to Ag core particles to form a core/shell nanocomposite particle. This synthesis was accomplished using a seeded precipitation polymerization method whereby linear chains of pNIPAm were adsorbed to the Ag particles. This precursor particle acts as a nucleation site for the shell growth at the high temperature levels used for the synthesis. The presence of this shell was confirmed by performing particle tracking experiments using video microscopy, whereby the highly efficient scattering of the Ag cores were easily observed using reflectance microscopy. The resulting core/shell particles were found to be pH responsive due to the AAc constituent in the shell and the surface plasmon properties of these particles were preserved. The presence of this tunable shell can be used to for advances in the fabrication of ordered assemblies of Ag particles to investigate their optical properties of their cooperative plasmon resonances.

References

[1] Bohren, C. F.; Huffman, D. R. *Absorption and Scattering of Light by Small Particles*; John Wiley and Sons, Inc.: New York, 1998.

[2] Evanoff, D. D., Jr.; Chumanov, G. Size-Controlled Synthesis of Nanoparticles. 2. Measurement of Extinction, Scattering, and Absorption Cross Sections. *J. Phys. Chem. B* **2004**, *108*, 13957-13962.

[3] Messinger, B. J.; Von Raben, K. U.; Chang, R. K.; Barber, P. W. Local fields at the surface of noble-metal microspheres. *Phys. Rev. B: Cond. Matt. Mater. Phys.* **1981**, *24*, 649-57.

[4] Mulvaney, P. Surface Plasmon Spectroscopy of Nanosized Metal Particles. *Langmuir* **1996**, *12*, 788-800.

[5] Malynych, S.; Chumanov, G. Light-Induced Coherent Interactions between Silver Nanoparticles in Two-Dimensional Arrays. *J. Am. Chem. Soc.* **2003**, *125*, 2896-2898.

[6] Evanoff, D. D., Jr.; White, R. L.; Chumanov, G. Measuring the Distance Dependence of the Local Electromagnetic Field from Silver Nanoparticles. *J. Phys. Chem. B* **2004**, *108*, 1522-1524.

[7] Chumanov, G.; Sokolov, K.; Cotton, T. M. Unusual Extinction Spectra of Nanometer-Sized Silver Particles Arranged in Two-Dimensional Arrays. *J. Phys. Chem.* **1996**, *100*, 5166-8.

[8] Kumbhar, A. S.; Kinnan, M. K.; Chumanov, G. Multipole Plasmon Resonances of Submicron Silver Particles. *J. Am. Chem. Soc.* **2005**, *127*, 12444-12445.

[9] Evanoff, D. D., Jr.; Chumanov, G. Synthesis and optical properties of silver nanoparticles and arrays. *ChemPhysChem* **2005**, *6*, 1221-1231.

[10] Daniels, J. K.; Chumanov, G. Spectroelectrochemical studies of plasmon coupled silver nanoparticles. *J. Electroanalytical Chem.* **2005**, *575*, 203-209.

[11] Malynych, S.; Chumanov, G. Coupled planar silver nanoparticle arrays as refractive index sensors. *J. Optics A: Pure and Appl. Opt.* **2006**, *8*, S144-S147.

[12] Bao, H.; Chumanov, G.; Czerw, R.; Carroll, D. L.; Foulger, S. H. Synthesis of core-shell silver colloidal particles by surface immobilization of an azo-initiator. *Colloid Polym. Sci.* **2005**, *283*, 653-661.

[13] Lu, Y.; Liu, G. L.; Lee, L. P. High-Density Silver Nanoparticle Film with Temperature-Controllable Interparticle Spacing for a Tunable Surface Enhanced Raman Scattering Substrate. *Nano Lett.* **2005**, *5*, 5-9.

[14] Malynych, S.; Luzinov, I.; Chumanov, G. Poly(Vinyl Pyridine) as a Universal Surface Modifier for Immobilization of Nanoparticles. *J. Phys. Chem. B* **2002**, *106*, 1280-1285.

[15] Malynych, S.; Robuck, H.; Chumanov, G. Fabrication of Two-Dimensional Assemblies of Ag Nanoparticles and Nanocavities in Poly(dimethylsiloxane) Resin. *Nano Lett.* **2001**, *1*, 647-649.

[16] Chen, C.-W.; Chen, M.-Q.; Serizawa, T.; Akashi, M. In-situ formation of silver nanoparticles on poly(N-isopropylacrylamide)-coated polystyrene microspheres. *Adv. Mat.* **1998**, *10*, 1122-1126.

[17] Cassagneau, T.; Caruso, F. Contiguous silver nanoparticle coatings on dielectric spheres. *Adv. Mat.* **2002**, *14*, 732-736.

[18] Kim, J.-W.; Lee, J.-E.; Kim, S.-J.; Lee, J.-S.; Ryu, J.-H.; Kim, J.; Han, S.-H.; Chang, I.-S.; Suh, K.-D. Synthesis of silver/polymer colloidal composites from surface-functional porous polymer microspheres. *Polymer* **2004**, *45*, 4741-4747.

[19] Liang, Z.; Susha, A. S.; Caruso, F. Metallodielectric opals of layer-by-layer processed coated colloids. *Adv. Mat.* **2002**, *14*, 1160-1164.

[20] Chen, Z.; Zhan, P.; Wang, Z.; Zhang, J.; Zhang, W.; Ming, N.; Chan, C. T.; Sheng, P. Two- and three-dimensional ordered structures of hollow silver spheres prepared by colloidal crystal templating. *Adv. Mat.* **2004**, *16*, 417-422.

[21] Lu, L.; Eychmueller, A.; Kobayashi, A.; Hirano, Y.; Yoshida, K.; Kikkawa, Y.; Tawa, K.; Ozaki, Y. Designed fabrication of ordered porous Au/Ag nanostructured films for surface-enhanced Raman scattering substrates. *Langmuir* **2006**, *22*, 2605-2609.

[22] Wang, W.; Asher, S. A. Photochemical Incorporation of Silver Quantum Dots in Monodisperse Silica Colloids for Photonic Crystal Applications. *J. Am. Chem. Soc.* **2001**, *123*, 12528-12535.

[23] Chen, C.-W.; Serizawa, T.; Akashi, M. Synthesis and Characterization of Poly(N-isopropylacrylamide)-Coated Polystyrene Microspheres with Silver Nanoparticles on Their Surfaces. *Langmuir* **1999**, *15*, 7998-8006.

[24] Lu, Y.; Mei, Y.; Ballauff, M.; Drechsler, M. Thermosensitive Core-Shell Particles as Carrier Systems for Metallic Nanoparticles. *J. Phys. Chem. B* **2006**, *110*, 3930-3937.

[25] Lu, Y.; Mei, Y.; Drechsler, M.; Ballauff, M. Thermosensitive core-shell particles as carriers for Ag nanoparticles: modulating the catalytic activity by a phase transition in networks. *Angew. Chem. Int. Ed.* **2006**, *45*, 813-816.

[26] Sun, Q.; Deng, Y. Encapsulation of Polystyrene Latex with Temperature-Responsive Poly(N-isopropylacrylamide) via a Self-Assembling Approach and the Adsorption Behaviors Therein. *Langmuir* **2005**, *21*, 5812-5816.

[27] Quaroni, L.; Chumanov, G. Preparation of Polymer-Coated Functionalized Silver Nanoparticles. *J. Am. Chem. Soc.* **1999**, *121*, 10642-10643.

[28] Sun, X.; Li, Y. Ag@C Core/Shell Structured Nanoparticles: Controlled Synthesis, Characterization, and Assembly. *Langmuir* **2005**, *21*, 6019-6024.

[29] Senff, H.; Richtering, W. Temperature sensitive microgel suspensions: Colloidal phase behavior and rheology of soft spheres. *J. Chem. Phys.* **1999**, *111*, 1705-1711.

[30] Debord, J. D.; Lyon, L. A. Thermoresponsive Photonic Crystals. *J. Phys. Chem. B* **2000**, *104*, 6327-6331.

[31] Hu, Z.; Lu, X.; Gao, J. Hydrogel opals. *Adv. Mat.* **2001**, *13*, 1708-1712.

[32] Hellweg, T.; Dewhurst, C. D.; Bruckner, E.; Kratz, K.; Eimer, W. Colloidal crystals made of poly(N-isopropylacrylamide) microgel particles. *Colloid Polym. Sci.* **2000**, *278*, 972-978.

[33] Singh, N.; Lyon, L. A. Au Nanoparticle Templated Synthesis of pNIPAm Nanogels. *Chem. Mater.*, Submitted.

[34] Evanoff, D. D., Jr.; Chumanov, G. Size-controlled synthesis of nanoparticles. 1. Silver-only aqueous suspensions via hydrogen reduction. *J. Phys. Chem. B* **2004**, *108*, 13948-13956.

[35] Lide, D. R. *Handbook of Chemistry and Physics, 74th ed.*; CRC Press: Boca Raton, FL, 1994.

[36] Wiedemair, J.; Serpe, M. J.; Kim, J.; Masson, J.-F.; Lyon, L. A.; Mizaikoff, B.; Kranz, C. In-Situ AFM Studies of the Phase-Transition Behavior of Single Thermoresponsive Hydrogel Particles. *Langmuir*, ACS ASAP.

[37] Crocker, J. C.; Grier, D. G. Methods of digital video microscopy for colloidal studies. *J. Coll. Interface Sci.* **1996**, *179*, 298-310.

[38] Mukhopadhyay, A.; Granick, S. Micro- and nanorheology. *Current Opinion Coll. Inter. Sci.* **2001**, *6*, 423-429.

[39] Breedveld, V.; Pine, D. J. Microrheology as a tool for high-throughput screening. *J. Materials Sci.* **2003**, *38*, 4461-4470.

[40] Slopek, R. P.; McKinley, H. K.; Henderson, C. L.; Breedveld, V. In situ monitoring of mechanical properties during photopolymerization with particle tracking microrheology. *Polymer* **2006**, *47*, 2263-2268.

[41] Bohren, C. F. How can a particle absorb more than the light incident on it? *Am. J. Phys.* **1983**, *51*, 323-7.

[42] Sönnichsen, C.; Franzl, T.; Wilk, T.; von Plessen, G.; Feldmann, J. Plasmon Resonances in Large Nobel-Metal Clusters. *New J. Phys.* **2002**, *4*, 93.1-93.8.

[43] Pelton, R. Temperature-sensitive aqueous microgels. *Adv. Colloid Interface Sci.* **2000**, *85*, 1-33.

[44] Jones, C. D.; Lyon, L. A. Synthesis and Characterization of Multiresponsive Core-Shell Microgels. *Macromolecules* **2000**, *33*, 8301-8306.

[45] Jones, C. D.; Lyon, L. A. Dependence of Shell Thickness on Core Compression in Acrylic Acid Modified Poly(N-isopropylacrylamide) Core/Shell Microgels. *Langmuir* **2003**, *19*, 4544-4547.

[46] Jones, C. D.; Lyon, L. A. Shell-Restricted Swelling and Core Compression in Poly(N-isopropylacrylamide) Core-Shell Microgels. *Macromolecules* **2003**, *36*, 1988-1993.

CHAPTER 4

SELF-ASSEMBLY OF COLLOIDAL CRYSTALS USING POLY(STYRENE-*CO*-*N*-ISOPROPYLACRYLAMIDE) MICROPARTICLES

4.1 Introduction

The ability to create ordered structures with refractive index periodicity has been under investigation since initial theoretical investigations were performed for the purposes of designing materials that exhibit unique, well-behaved optical properties,[1,2] as discussed previously. The implementation of spherical micro- and nanoparticles has been of great interest for the fabrication of such optical materials since they can be easily synthesized using various simple techniques[3-5] to yield particles possessing different functionalities and sufficient size monodispersity and length-scale appropriate for the manipulation of the wavelengths of light useful for optical applications.

The manufacturing of such high-quality, optical materials requires the ability to assemble such microparticles *quickly*, *reproducibly*, and *effectively*, with few unwanted defects, while allowing for the introduction of intended defects for the purposes of making functional optical materials.[6] As mentioned earlier, most colloidal crystal systems that have been studied employ hard-sphere particles that can form ordered lattices, which exhibit Bragg diffraction (Section 1.2.1). A variety of techniques have been explored as potential methods to achieve this assembly. However, as described in Chapter 1, most self-assembly methods that utilize hard-sphere colloids are unable to provide all of the above-described characteristics that are advantageous for manufacturing purposes.

Polymeric hydrogels that possess inherent flexibility are particularly useful for the self-assembly and stability of colloidal crystals and can be exploited to make tunable optical materials and sensors[7] by providing for changes in the lattice spacing between

particle centers.[8,9] As noted in Chapter 1, the Bragg diffraction of colloidal crystals composed of multi-responsive pNIPAm particles can be varied by temperature, pH, and particle concentration.[10-15] The ability to introduce functional groups (using the facile synthesis technique for pNIPAm particles), as well as their inherent permeability in the aqueous phase (due to the cross-linked, hydrogel network) make these particles attractive for the creation of functional colloidal crystalline materials for optical devices.[16,17]

Although thermal annealing of pNIPAm particles allows for quick and simple self-assembly of colloidal crystals, these particles are inherently unstable due to the fact that the particles themselves are composed of such a soft, hydrogel material. Efforts to stabilize colloidal crystals that possess hydrogel properties have employed various inter-particle cross-linking strategies[15] as well as introducing a polymer to effectively "glue" the system together.[8,18-20] However, these soft materials cannot provide the same sample robustness that is fundamental to hard-sphere crystal systems.

These structural challenges prompted our endeavor to make a particle that possesses properties of both hard and soft sphere particles such that a crystalline system can be produced quickly and simply, while being robust enough to maintain the stability of crystalline order under non-ideal conditions. Since self-assembly and stability can be achieved by taking advantage of the properties yielded by the particle's composition, an ideal particle might provide both structural integrity (hard, dense core) and tunable, responsive, hydrogel properties (soft shell). The gold standard particle should allow for ease of self-assembly, while providing for stability long-range order upon drying. To accomplish this objective, a core/shell construct was investigated in which the core was composed of a polystyrene-*co*-*N*-isopropylacrylamide (pS-*co*-NIPAm) copolymer and the shell was synthesized using a crosslinked pNIPAm homopolymer, so that the thermoresponsive shell could be used for self-assembly and the core would yield stability in its dried state. The synthesis, characteristics, and self-assembly of these core/pNIPAm shell particles will be the topic of Chapter 5. During this investigation, it was determined

that the initial pS-*co*-NIPAm core particles could fortuitously self-assemble via a simple drying process to provide stable crystals. Consequently, this finding encouraged the present investigation of pS-*co*-NIPAm core particles as processable, photonic inks.

4.2 Experimental Section

4.2.1 Synthesis Strategies

Materials

Most of the materials used in this chapter can be found in the Experimental Section of Chapter 2. Additionally, the styrene monomer and Tween 80, which was used as a surfactant in some cases, were purchased from Sigma-Aldrich.

Core Particle Synthesis

Copolymer poly(styrene-*co*-*N*-isopropylacrylamide) (pS-*co*-NIPAm) microparticles were prepared using an emulsion polymerization sythesis. The Hellweg group[21] and others[22-26] have reported copolymer particle syntheses using styrene and NIPAm where the relative amounts of each monomer directly affect the final particle properties. For example, higher NIPAm concentrations introduce thermoresponsivity. For the synthesis of a dense core particle, it was decided that the synthesis monomer concentration should contain at least ~75 mol-% styrene to provide pS-*co*-NIPAm particles with adequate density to yield particle stability when dry. Table 4.1 shows the amounts of monomer (styrene:NIPAm:BIS), initiator (APS), and water used for various pS-*co*-NIPAm particle reactions.

Table 4.1 Polymerization conditions for pS-*co*-NIPAm particle syntheses.

Sample Name	Total Monomer Concentration; mM mol-% (Sty:NIPAm:BIS)	Water mL	Styrene mL	NIPAm g	BIS, g	APS, g	Reaction Time
150-1	150 mM (75:24:1)	100	1.29	0.04064	0.0245	0.0064	4.5 hrs
300-1	300 mM (75:24:1)	200	4.68	1.6366	0.0928	0.0107	4.3 hrs
280-2	280 mM (73:26:1)	100	2.34	0.8115	0.0477	0.0062, 0.0099	23 hrs
500-2	500 mM (75:24:1)	100	4.3	1.3443	0.0767	0.0070, 0.0101	23 hrs
600-1	600 mM (75:24:1)	200	10	3.2535	0.1855	0.0120, 0.0122	24 hrs
600-2	600 mM (75:24:1)	200	10	3.2548	0.1885	0.0132, 0.0117, 0.0142	24 hrs

The following procedure was used for the synthesis of all of the pS-*co*-NIPAm particles, unless noted otherwise. The NIPAm and BIS monomers were dissolved in water and placed in a three-necked, round-bottom flask equipped with a condenser, thermometer, and inlet for gas purging. While stirring, this solution was heated to ~70 ˚C while purging with N_2 for at least 30 min. Styrene monomer was added ~5 min prior to initiation. The reaction was initiated by introducing APS (dissolved in ~1 mL of water) to the hot monomer mixture. The reaction solution normally changed from clear to turbid within 15-30 minutes, indicating successful particle nucleation and growth. The syntheses were allowed to react under heated conditions while purging and stirring for the lengths of time listed in Table 4.1. It was decided that longer reaction times might ensure the formation of larger particles when large concentrations of monomer were used.[22,23,25,27] All particle suspensions were filtered using Whatman filter paper (No. 2) to remove any coagulum and cleaned by centrifugation at least three times for approximately 15-45 min at 15,400 x *g* rcf at 25 ˚C (times and speeds varied depending

on particle size) to remove any unreacted monomer or oligomeric species, using water for resuspension of the pellet.

Initial core syntheses (150-1) used a surfactant (Tween 80) to stabilize the growing particles (0.015 mM Tween 80 based on the total reaction volume). However, in most cases, these core syntheses were performed under surfactant-free conditions, in order to achieve large particles. A small amount of initial APS was consistently used for all reactions (~0.25 mM APS, based on the total reaction volume) to procure relatively large particle sizes so that all particles could be compared based on the total monomer concentration of the reaction. In some cases, additional APS was added to ensure reaction went to completion (although this addition was probably not necessary).

In the case of sample 600-2, a method of delayed monomer addition was used in an attempt to make larger particles. All of the monomer was mixed together in 200 mL water; however, the reaction was initiated using only 100 mL of this monomer stock at the outset. The remaining 100 mL was added to the reaction every 30 min in 25 mL increments. A more comprehensive investigation of syntheses that employ this delayed monomer addition can be found in Chapter 6.

Crystal Sample Preparation.

Dried crystals were prepared by spreading a drop of a concentrated pS-*co*-NIPAm aqueous suspension on a glass cover slip (VWR, 22 x 30 mm) over an area of approximately 2 cm in diameter. These colloidal suspensions possessed polymer concentrations typically between 10–50 mg/mL. This sessile drop was allowed to dry open to the atmosphere at ambient temperature, which usually took about 60-90 minutes. This sample preparation was used to prepare dried samples for SEM and reflectance spectroscopy characterizations.

4.2.2 Characterization Techniques

Photon Correlation Spectroscopy

The particle hydrodynamic radius (R_h) was determined using photon correlation spectroscopy using the same instrumental set up as described in the Experimental Section of Chapter 2. Samples were prepared using dilute solutions of pS-*co*-NIPAm microparticles and were allowed to equilibrate at the appropriate temperature for 10 min before data collection. The data was analyzed with Dynamics Software Version 5.20.05 (Protein Solutions, Inc.) using the Cumulants method for monomodal (Gaussian) size distribution analysis. Typically, at least three measurements were obtained at each temperature for statistical analysis of the R_h. Each measurement consisted of at least 5 data points, each collected using an acquisition (integration) time of 60 sec.

Static Light Scattering

Multi-angle laser light scattering (MALLS, Wyatt Technology, Inc.) was employed to determine the radius of gyration (R_g) of the hydrated particles. Asymmetric field flow fractionation (AFFF, Eclipse, Wyatt Technology, Inc.) was utilized to achieve particle separation based on hydrodynamic volume using a solvent cross-flow.[28,29] The AFFF method that was employed first concentrated the sample at one end of the AFFF channel using the focusing mode, followed by sample elution using a cross-flow rate of 0.25 mL/min that decreased consistently over a period of 36 min, followed by an additional elution time of 20 min with no cross-flow. Particle elution continued to the MALLS detector, which was equipped with a Peltier device to maintain a flow-cell temperature of 25 °C. Scattered light from a GaAs laser operating at 684 nm was collected at 16 fixed angle detectors and ASTRA 5.1.5.0 software was used to determine R_g values using the Debye fit method. Samples were diluted as necessary to achieve appropriate light scattering signals following the AFFF separation. Uncertainty in

calculated R_g values was determined from the standard deviations of each slice of data in the Debye plot, using the ASTRA software.

Transmission Electron Microscopy

The particle size and interparticle interactions of dried pS-*co*-NIPAm core particles were examined using transmission electron microscopy (TEM). Samples were prepared by placing multiple drops of dilute solutions of particles on TEM copper grids (coated with either Formvar or Carbon-B Type; 200 mesh, Ted Pella, Inc.) leaving at least one drop to dry overnight under ambient conditions. A JEOL 100CX II operating at 100 kV was used for TEM characterizations. Particle size distributions were calculated by analyzing each image using ImageJ software.[30]

Scanning Electron Microscopy

A Hitachi S800 field emission gun scanning electron microscope operating at 10 kV was used to characterize the structural properties of dried samples of pS-*co*-NIPAm particles. Scanning electron microscopy (SEM) samples were prepared by drying a concentrated suspension of particles on a glass cover slip, onto which a 5 nm gold film was added using a Denton Vacuum Evaporator (DV-502A) equipped with an Inficon deposition monitor. Samples were placed on a cylindrical specimen mount for imaging the top of the dried sample. To obtain images of sample cross-sections, a drop of the particle suspension was dried on a scored glass cover slip. After the sample dried completely, the cover slip was broken along a scored line, followed by deposition of a gold film, as described above. A 45° specimen mount was used for obtaining images of the crystal cross-section by tilting the sample relative to the incident electron beam.

Optical Spectroscopy

The Bragg diffraction peaks of the dried crystals were characterized using reflectance spectroscopy, since the scattering background was often too high to allow for

transmission studies. These spectra were collected using a fiber optic spectrophotometer (Ocean Optics, Inc., USB2000 with integrated OFLV-3 detector) and OOIBase32 software. A bifurcated source and detector reflectance probe (R400-7-VIS/NIR) consisting of a bundle of 7 optical fibers was employed by positioning the probe above the sample at near-normal incidence. A dark spectrum was obtained by covering the reflectance probe using the probe cap and a 100% reflectance reference was obtained using a diffuse reflectance standard. For some of the samples, in situ reflectance spectra were collected during the drying process for further characterization of the self-assembly process. The diameter of the reflectance probe was 400 μm, which allowed for the interrogation of a wide sampling area during these in situ drying experiments. These data were collected over a span of 5-10 minutes between the onset of the initial peak to the stabilization of the final peak, which indicated that the region being interrogated was completely dried.

4.3 Results

4.3.1 Characterization of PS-co-NIPAm Microparticles

Copolymer microparticles composed of polystyrene-*co*-*N*-isopropylacrylamide (pS-*co*-NIPAm) were synthesized using different total molar concentrations of monomer to yield particles of various sizes. In most cases, the mole ratio of monomers for styrene:NIPAm:BIS was 75:24:1, so that these particles would exhibit qualities of both hard *and* soft colloids, which would be advantageous for crystal assembly and stability.

Given that the particle size contributes to the lattice spacing of colloidal crystals, the knowledge of this particle size is essential to gain a comprehensive understanding of the properties of the subsequent optical materials. For most hard-sphere systems, identical particle sizes can be assumed for particles in the wet state as well as in the dry state (either as isolated particles or as part of a crystalline structure). Even though all of

the pS-*co*-NIPAm particles that were prepared in this chapter contain a majority of hydrophobic styrene components, the presence of the hydrophilic pNIPAm component may have produced swelling of the particle in the wet state and consequently imparted some degree of softness. This latter feature could also result in distortion of the spherical shape of these particles under dry conditions. Therefore, the pS-*co*-NIPAm particles were characterized by PCS to determine the particle size when fully hydrated and by TEM to determine the dry particle size. The hydrodynamic radius at 40 ˚C was also determined to ascertain if the pNIPAm constituent had introduced any thermoresponsivity to the particles. These values are included in Table 4.2 along with the percent volume decrease that was observed between the swollen and thermally-induced, deswollen particles (both in the wet state), as well as the percent volume decrease between swollen and dried particles.

Table 4.2 Hydrated and dried particle size for pS-*co*-NIPAm particles acquired using PCS and TEM.

Sample	Diameter, nm (PCS at 25 ˚C)	Diameter, nm (PCS at 40 ˚C)	Volume Decrease (PCS at 25 ˚C vs. PCS at 40 ˚C)	Diameter, nm (TEM)	Volume Decrease (PCS @ 25 ˚C vs. TEM)
150-1	182 (± 1)	178 (± 2)	7%	126 (± 3)	66%
300-1	246 (± 2)	243 (± 1)	4%	219 (± 8)	29%
280-2	278 (± 4)	270 (± 3)	9%	203 (± 5)	61%
500-2	318 (± 2)	312 (± 2)	5%	268 (± 7)	40%
600-1	458 (± 5)	352 (± 1)	55%	318 (± 16)	67%
600-2	547 (± 9)	400 (± 3)	61%	300 (± 18)	83%

For the samples synthesized with the lowest amounts of total monomer (150-1, 300-1, 280-2, and 500-2), only slight thermoresponsivity was observed with temperature changes between 25 ˚C and 40 ˚C, corresponding to small decreases in hydrated volume, ranging from 3-9%. However, there is a distinct decrease in volume between the hydrated state at 25 ˚C and the dried state for these same particles, ranging from ~30% to over 65%.

For the 600-1 and 600-2 pS-*co*-NIPAm particles, a significant change in hydrated particle size was observed between high and low temperatures, corresponding to a volume decrease of 55% and 61% between this two states for the 600-1 and 600-2 particles, respectively. A detailed examination of the temperature dependent changes in particle size are shown in Figure 4.1 for these thermosensitive particles. Compared to the initial swollen, hydrated size, the dried particle size shows a volume decrease of 67% for the 600-1 particles and 83% for the 600-2 particles.

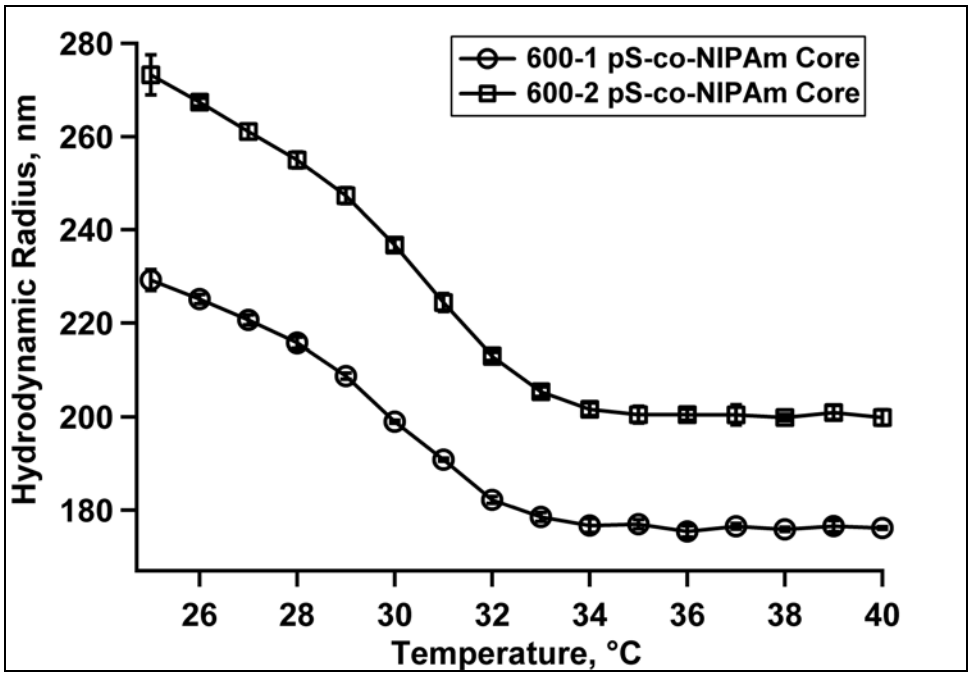

Figure 4.1 Temperature dependent changes in hydrated size for the 600-1 and 600-2 pS-*co*-NIPAm particles.

To characterize the radial mass distribution (or polymer chain segment density), the radius of gyration (R_g) was determined for some of these particles using MALLS and compared to the observed R_h values (Table 4.3). For a sphere of uniform density, the ratio of R_g/R_h is typically ~0.775.[31] The R_g/R_h ratio for fully swollen pNIPAm homopolymer particles corresponds to this uniform sphere structure, which has also been demonstrated by other groups.[32,33] Examination of the 500-2 particles demonstrated a similar ratio. However, the 280-2 particles possess a lower R_g/R_h value and the R_g/R_h for the thermoresponsive 600-1 particles is even smaller.

Table 4.3 Radius of gyration compared to hydrodynamic radius for pS-*co*-NIPAm particles.

Sample	PCS: R_h @ 25 °C	MALLS: R_g @ 25 °C	R_g/R_h
2% BIS, pNIPAm	111 (± 1)	81.3 (0.2%)	0.74
280-2	139 (± 2)	87.8 (0.3%)	0.63
500-2	159 (± 1)	124.4 (0.2%)	0.78
600-1	229 (± 2)	127.3 (0.2%)	0.56

The dried morphologies of the pS-*co*-NIPAm particles that were acquired by TEM are shown in Figure 4.2. These samples were prepared using dilute suspensions of the particles. The inset images were used for the particle size analysis. Distinct, spherical particles are easily observed for all of the samples. However, the 150-1, 300-1, 280-2, and 500-2 pS-*co*-NIPAm particles show distinctive physical properties compared to the 600-1 and 600-2 particles. The former particles (Panels A-D) exhibit unique interactions between neighboring particles, such that they appear to stick to one another with

interparticle contacts that display ambiguous edges. Such particles that are adjacent to each other also appear to deform slightly relative to the position of these contacts. Although the 600-1 particles demonstrate similar interparticle adhesion, the 600-1 and 600-2 particles (Panels E and F) both exhibit a type of extended connection between nearby particles that are not directly adjacent to each other, typified by a long, thin threadlike feature. The individual particle interactions at this dimension offer clues to the self-assembly process which may influence the final macro-structure and properties for dried samples composed of different types of pS-*co*-NIPAm particles.

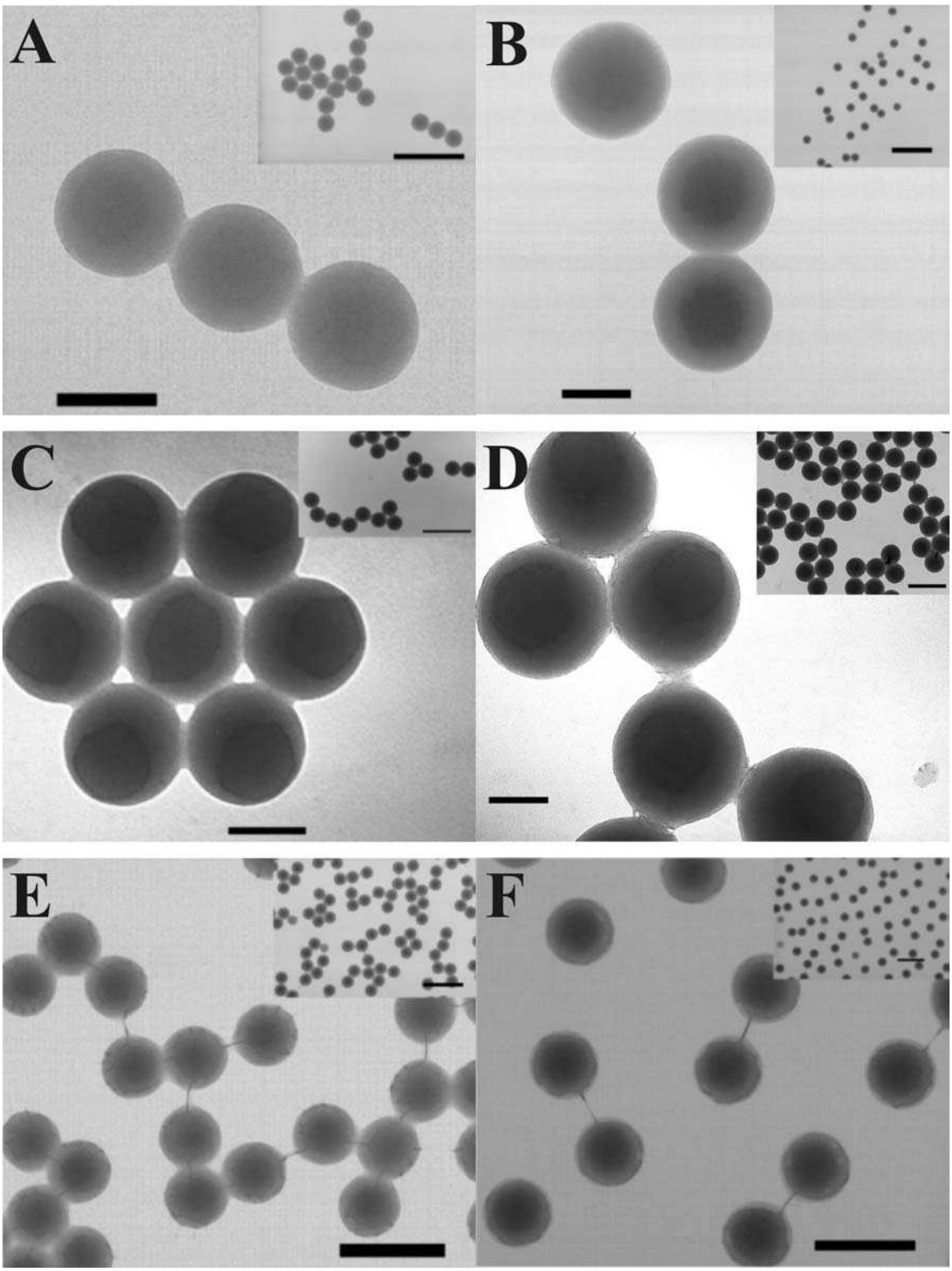

Figure 4.2 Images of the (A) 150-1, (B) 300-1, (C) 280-2, (D) 500-2, (E) 600-1, and (F) 600-2 pS-*co*-NIPAm particles acquired by TEM. The inset images were used to determine the dried particle size distribution. Scale bars for the large images are 100 nm for A-D and 500 nm for E and F. For the insets, scale bars are 500 nm for A, C, D and 1 μm for B, E, F.

One sample in particular was prepared for TEM analysis to examine how multiple particle interactions affect the final dried configuration. This sample was prepared by drying a suspension of 500-2 pS-*co*-NIPAm particles that was slightly more concentrated than those previously used for TEM sample preparation. An image of this dried sample displays a single layer of particles that possess 2D ordering, as observed in Figure 4.3. Particles that are not completely surrounded by neighboring particles appear to have smooth edge morphologies along spaces in the layer. However, a majority of the particles are in contact with neighboring particles and appear to deform considerably along these interparticle contacts, such that the edges are not distinct. These close-packed particles lose their spherical shape, and the overall configuration displays long-range, hexagonal ordering, resembling a honeycomb pattern.

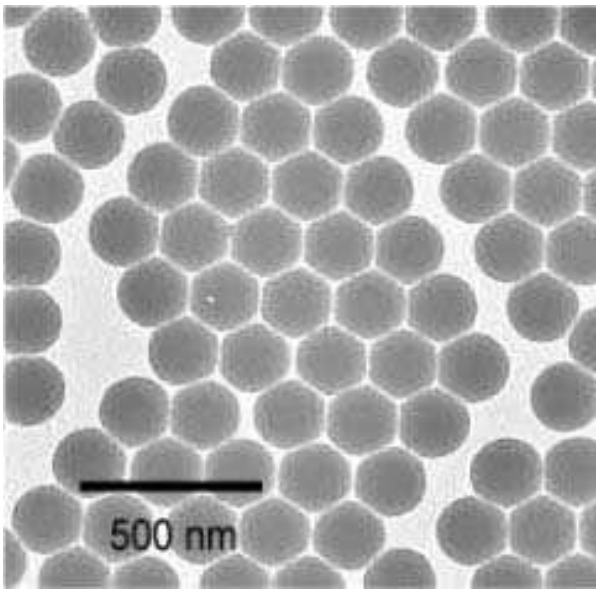

Figure 4.3 Close-packed, 2D ordered array of 500-2 pS-*co*-NIPAm particles.

4.3.2 Dried pS-co-NIPAm Crystal Characterization

Colloidal crystals were fabricated by spreading suspensions of the different pS-*co*-NIPAm particles on to glass cover slips and allowing each sample to dry under ambient conditions. Images of each bulk crystal were acquired using a digital camera, as shown in Figure 4.4. Brilliant diffraction colors are observed for the 280-2 (blue), 300-1 (green) and 500-2 (red) samples. The 150-1 sample appears slightly purple, but is not as vivid as the previous samples, which may be due non-visible diffraction because of the small particle size of this sample. These increases in the wavelength of the diffraction colors (as observed by eye) are consistent with the increases in dried particle size, qualitatively following Bragg's Law. The uniformity of these colors throughout the area of each sample suggests high quality crystalline order. The 600-1 and 600-2 samples, however, appear white and very opaque. This lack of color may be attributable to the large particle sizes of these samples or could be a product of low quality or even no crystalline order.

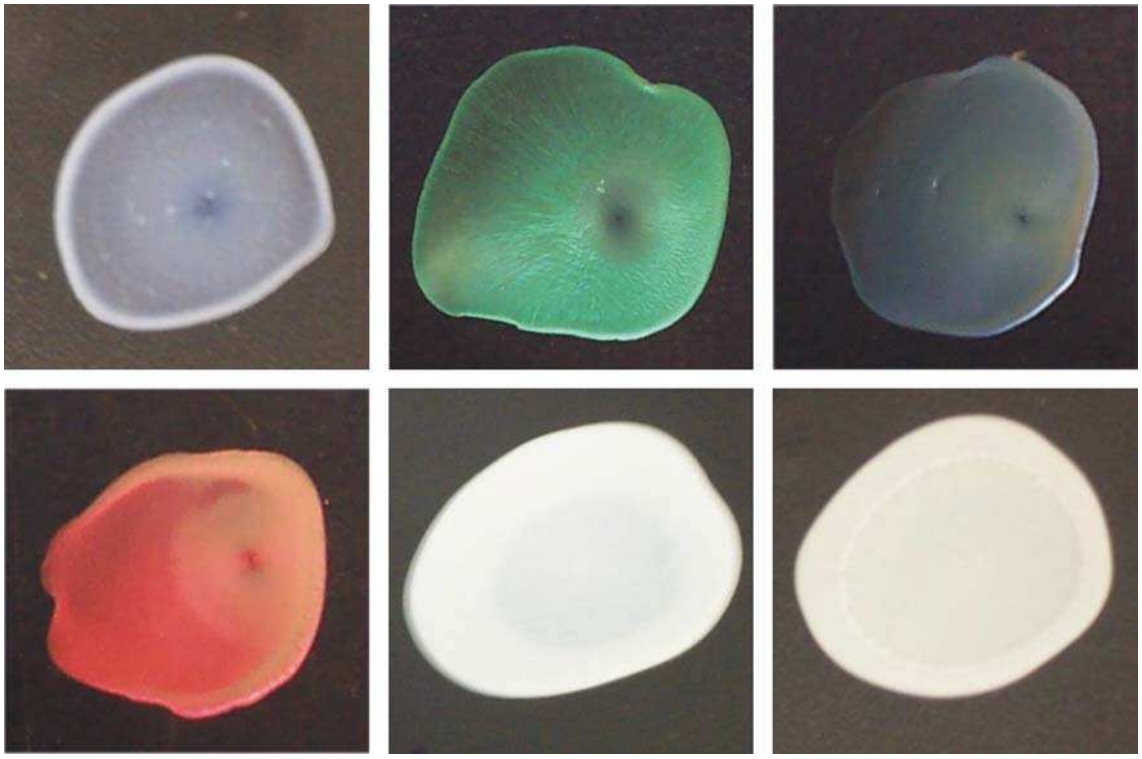

Figure 4.4 Digital camera images of dried samples of the pS-*co*-NIPAm particles: Top row, left to right: 150-1, 300-1, and 280-2 samples. Bottom row, left to right: 500-2, 600-1, and 600-2 samples.

Images were acquired using scanning electron microscopy to characterize the particle configurations for each of the dried pS-*co*-NIPAm samples, as shown in Figure 4.5. The top surfaces of the crystals composed of 150-1, 300-1, 280-2, or 500-2 particles display closely packed particles, which have adopted a hexagonal arrangement. This arrangement also persists throughout the tops of these samples, displaying long-range order two-dimensional order that is consistent with the uniformity of the diffraction colors seen by eye. This same hexagonal order is present on the surface of the 600-2 sample, but does not occur over the same length-scale as the previous samples. It should also be noted that this particular 600-2 sample was not prepared under ambient condition, but was instead prepared by drying under heated conditions, since these particles were

found to be thermoresponsive (*vide infra*). There does not appear to be any short nor long-range particle order at the surface of the 600-1 sample.

Images were also acquired at the cross-sections of some of these samples to characterize the three-dimensional particle arrangements throughout of these crystals. Cross-sectional images for the 280-2 and 500-2 dried samples are demonstrated in Figure 4.6. These images show that the particle order persists throughout the z-dimension of the samples. The pS-*co*-NIPAm particles appeared extremely stable along these crystal walls, which could be an effect of the apparent adhesive interactions that were observed in TEM images of discrete particles.

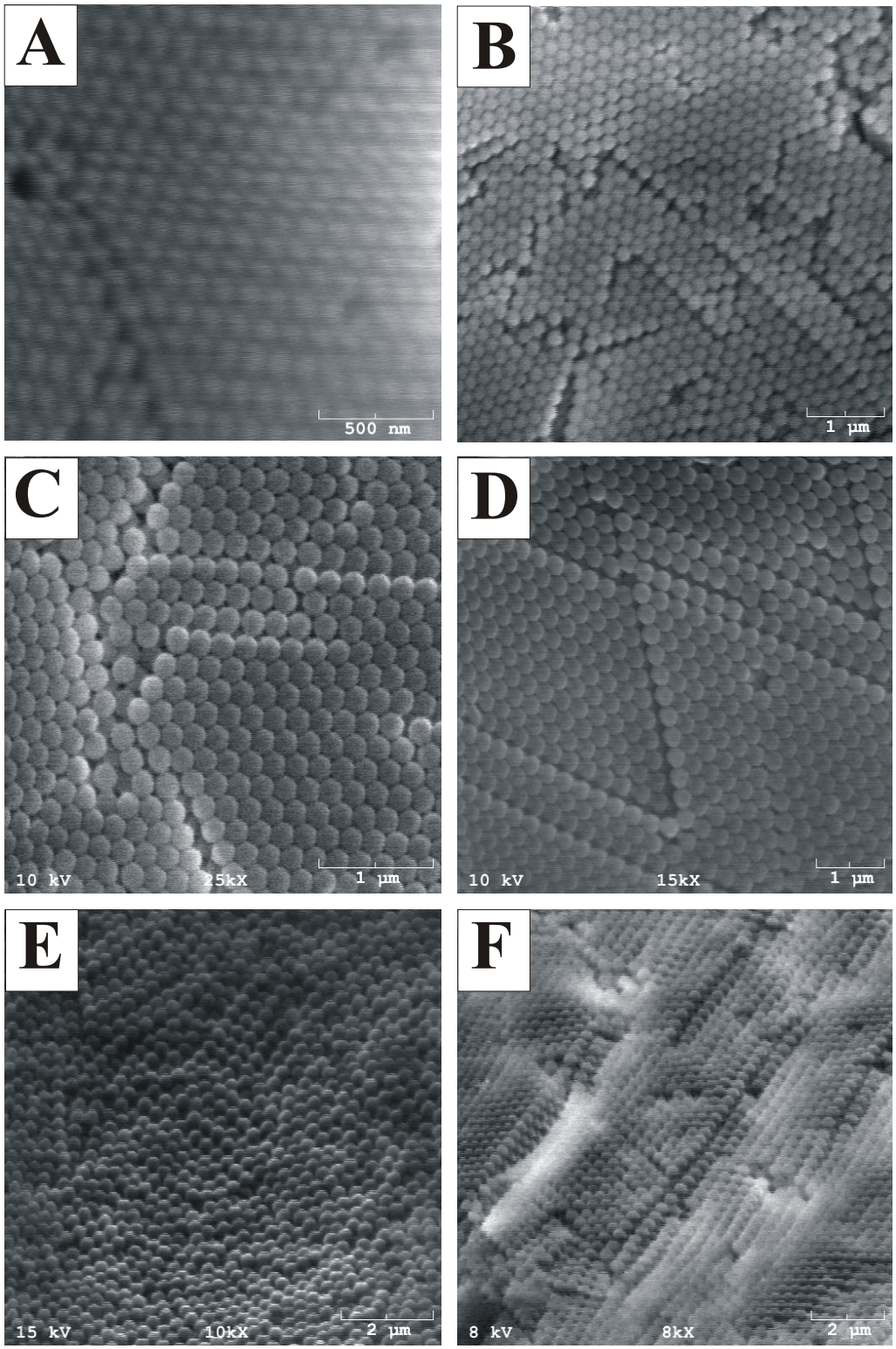

Figure 4.5 SEM images of the tops of dried crystals composed of the (A) 150-1, (B) 300-1, (C) 280-2, (D) 500-2, (E) 600-1, and (F) 600-2 pS-*co*-NIPAm particles. Panel F displays an image of a sample prepared by heating a suspension of 600-2 particles.

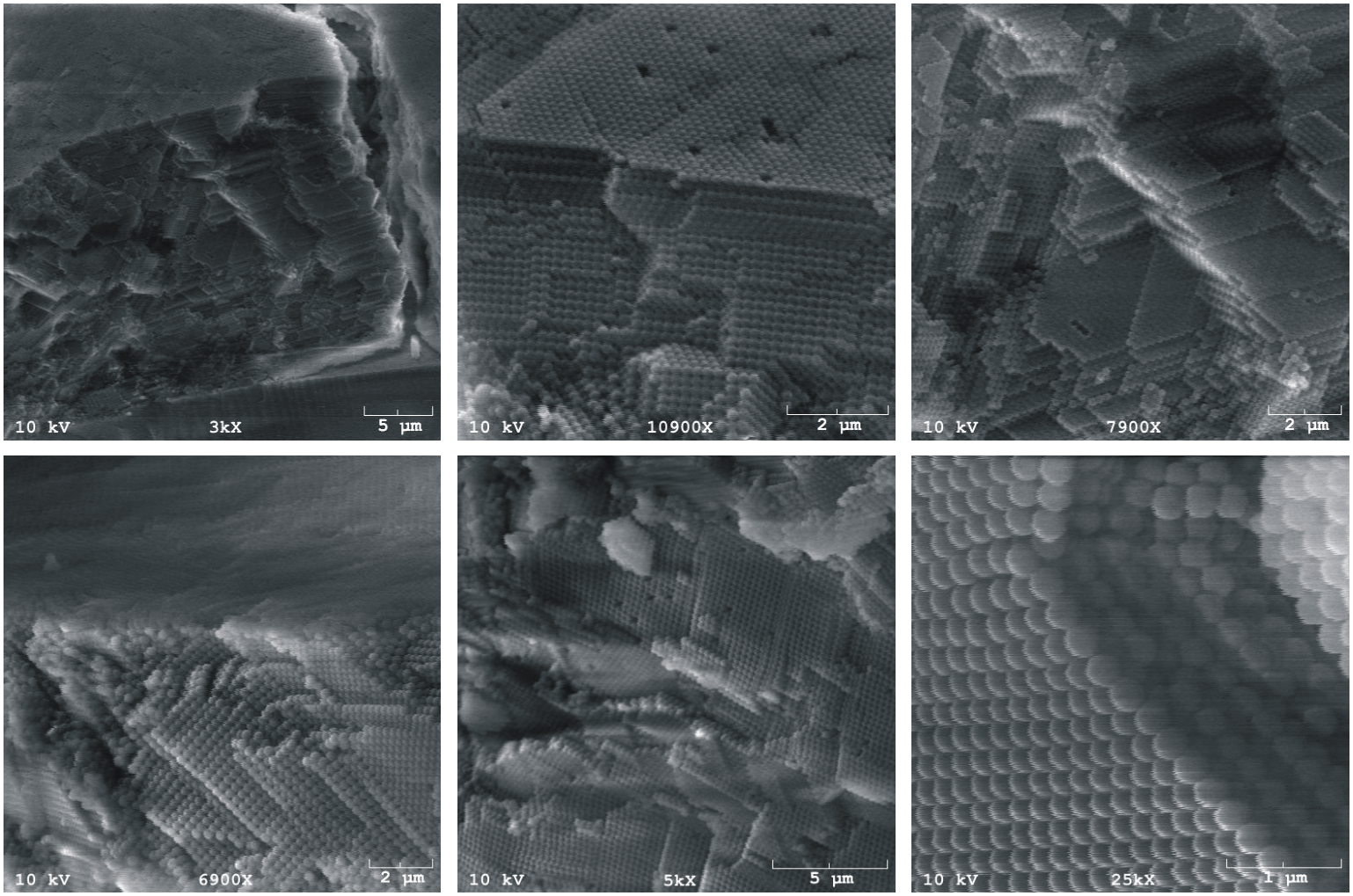

Figure 4.6 Images of crystal cross-sections, acquired by SEM. Top row: 280-2 pS-*co*-NIPAm particles. Bottom row: 500-2 pS-*co*-NIPAm particles.

Although SEM is a useful technique to visualize the particle order, it can only interrogate small regions of these crystals and it is difficult to use these images to confirm the crystalline order or the extent of these structured layers. Therefore, optical spectroscopy was employed to examine the quality of these crystals.[34] These samples were characterized by reflectance spectroscopy, as shown in Figure 4.7, to determine the wavelength of Bragg diffraction at near-normal incidence. The 150-1, 300-1, 280-2, and 500-2 samples demonstrated distinct diffraction peaks with strong intensities. Although the dried crystals composed of 600-1 or 600-2 particles did not show clear diffraction peaks, the spectra for these samples exhibited a slight shoulder at ~700 nm and ~760 nm, respectively. A further examination of these crystals was performed by acquiring the spectra of each crystal by interrogating the backside of the sample, through the cover slip, using the same reflectance setup. Interestingly, distinct diffraction peaks were observed from the backside compared to the spectra obtained when the tops of the samples were interrogated, as displayed in Figure 4.8. The first order diffraction peaks are very broad for each sample occurring at ~690 nm for the 600-1 sample and ~775 nm for the 600-2 sample, which occurred at wavelengths similar to the shoulders found in Figure 4.7. A second order diffraction peak is also observed to the blue side of these peaks, occurring at ~395 nm and ~440 nm, respectively.

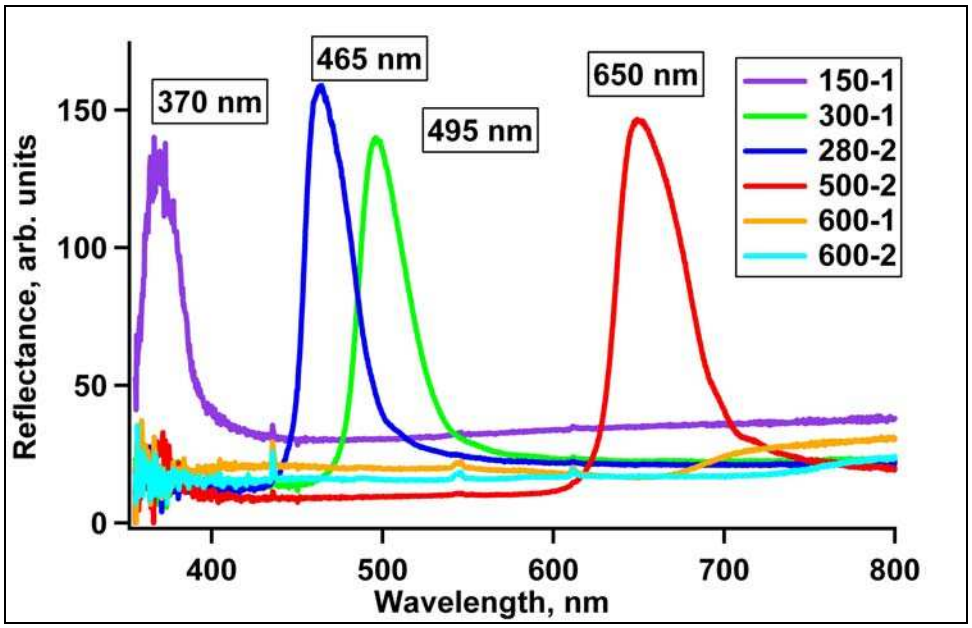

Figure 4.7 Diffraction peaks for the dried crystals composed of pS-*co*-NIPAm particles using reflectance spectroscopy. (Angle of incidence = 90˚)

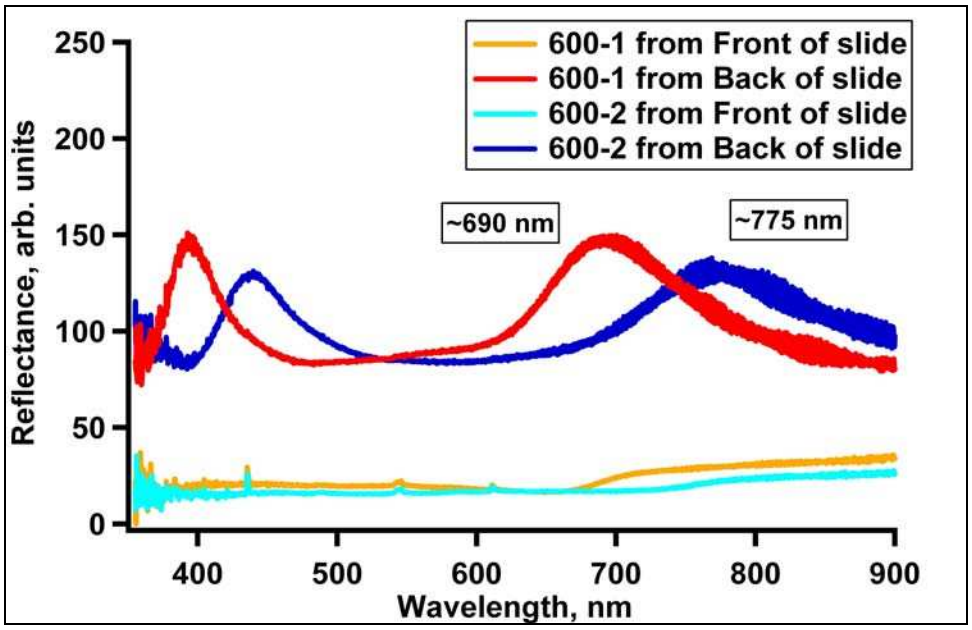

Figure 4.8 Diffraction peaks of samples composed of 600-1 or 600-2 particles, interrogated at the top of the sample from the backside of the crystal. (Angle of incidence = 90˚)

Since the size of the 600-1 and 600-2 pS-co-pNIPAm particles was determined to be dependent on temperature, an assessment was performed to examine the effect of temperature on the assembly process by characterizing the diffraction characteristics of dried crystals that were fabricated at different temperatures. Since the self-assembly process appears to be dependent on the interactions between neighboring particles (based on their soft, flexible peripheries), it is possible that the interactions between these thermoresponsive particles may be altered based on changes in temperature. Different samples were prepared by spreading the 600-1 or 600-2 pS-*co*-NIPAm particles on to glass cover slips and placing these samples onto a heating block that was set to different temperatures ranging from 22-51 ˚C. Reflectance spectra were collected by interrogating either the top of each sample or the backside of each sample, through the cover slip, for the dried 600-1 samples (Figure 4.9) and the 600-2 samples (Figure 4.10). The reflectance spectra of these samples that were formed while heated to different temperatures were compared to the spectra shown in Figure 4.8.

The positions and relative intensities for the diffraction peaks collected from the backside of the samples were found to be fairly independent of the drying temperature. However, the peak shapes changed and the signal intensities increased dramatically as the temperature was increased for the spectra that were acquired by interrogating the tops of the samples.

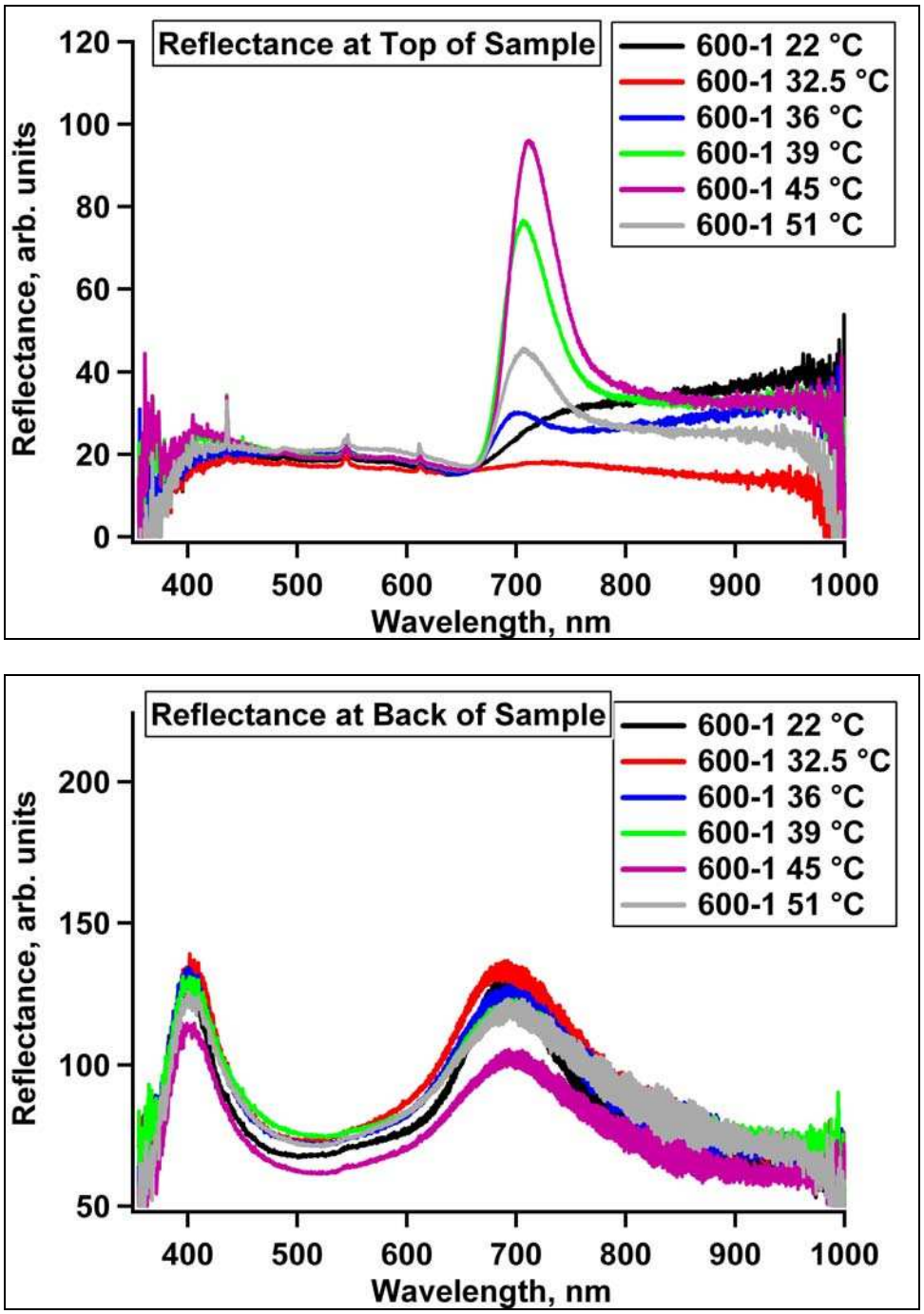

Figure 4.9 Reflectance spectra of dried samples of 600-1 pS-*co*-NIPAm particles prepared at different temperatures. Samples were interrogated from either the top of the sample (top) or from the backside of the cover slip (bottom). (Angle of incidence = 90˚)

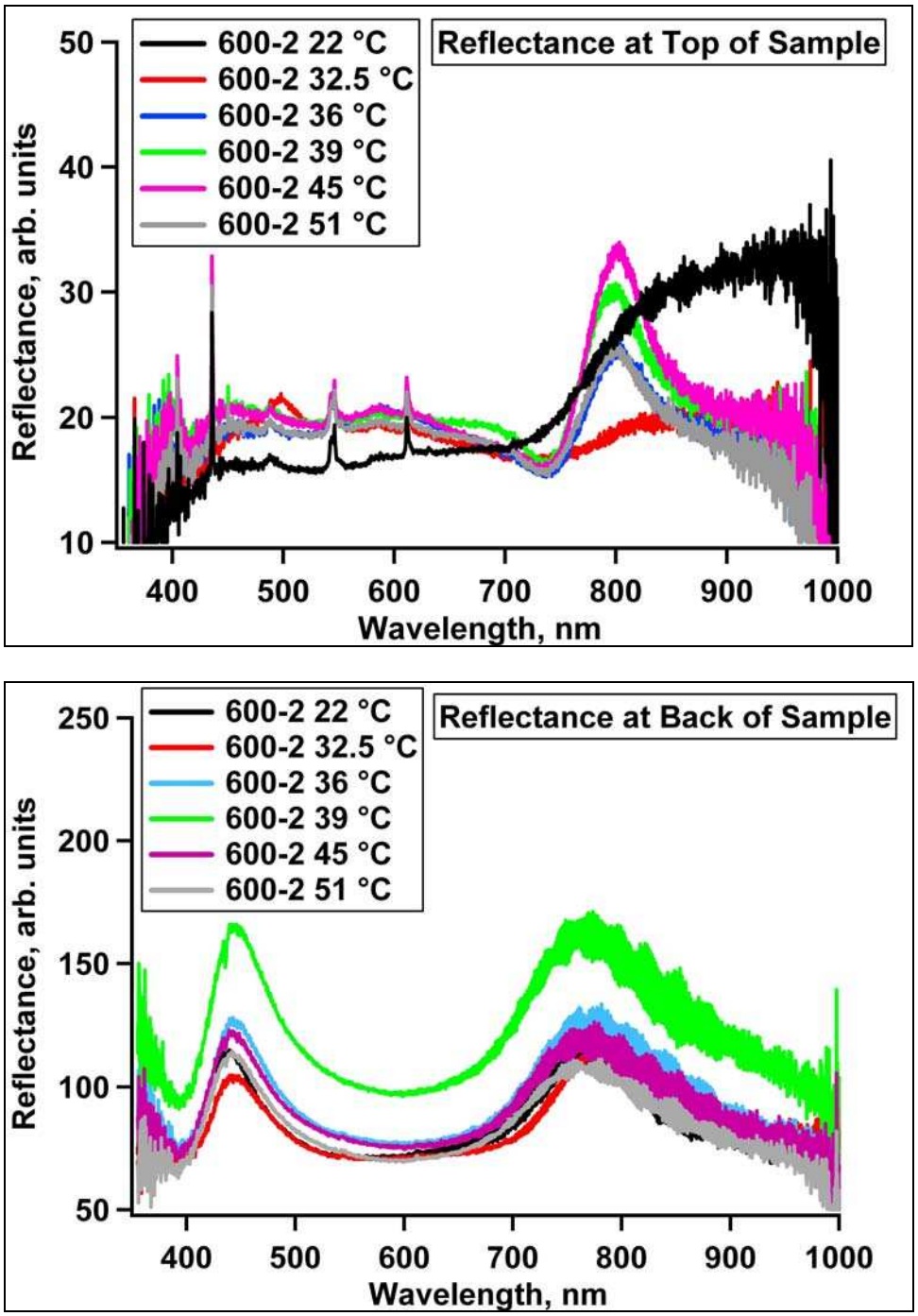

Figure 4.10 Reflectance spectra of dried samples of 600-2 pS-*co*-NIPAm particles prepared at different temperatures. Samples were interrogated from either the top of the sample (top) or from the backside of the cover slip (bottom). (Angle of incidence = 90˚)

In situ reflectance spectroscopy was performed to characterize the self-assembly process during drying. These experiments were performed by positioning the reflectance

probe about halfway between the center and the edge of the sessile drop of particles, so that the spectra could be collected as the sample changed from its wet state to its dry, stable state, which typically occurred on the order of minutes. Figure 4.11 shows the spectra that were obtained from drying suspensions of the 280-2 and 500-2 pS-co-pNIPAm particles represented by curves of different colors corresponding to different times during the drying process (such that $t_1<t_2<t_3<t_4<t_5$). For both samples, an initial diffraction peak is observed (497 nm and 728 nm for 280-2 and 500-2 pS-*co*-NIPAm samples, respectively) that is red-shifted compared to the diffraction peaks that were observed for the completely dried samples (Figure 4.7). The intensity of this initial peak increases and becomes blue-shifted over time (reaching a maximum intensity at ~493 nm for the 280-2 samples and ~706 nm for the 500-2 sample, without occurrence of a second peak). A second peak then appears, first as a shoulder to the blue side of the first peak, and then increases in intensity over time. As this occurs, the intensity of the first peak decreases over time and continues to blue shift over time. This transition for the initial peak occurs at different points for these two samples. For the 280-2 sample, the intensity of the first peak continues to increase during the onset of the second peak. For the 500-2 sample, the first peak begins to decrease in intensity as soon as the second peak begins to emerge. In both cases, the intensity of this second peak becomes stable once the sample has become fully dried. The wavelength of this final diffraction peak is consistent with the reflectance spectra of the completely dried samples. In both cases, this final diffraction is represented by the black curves.

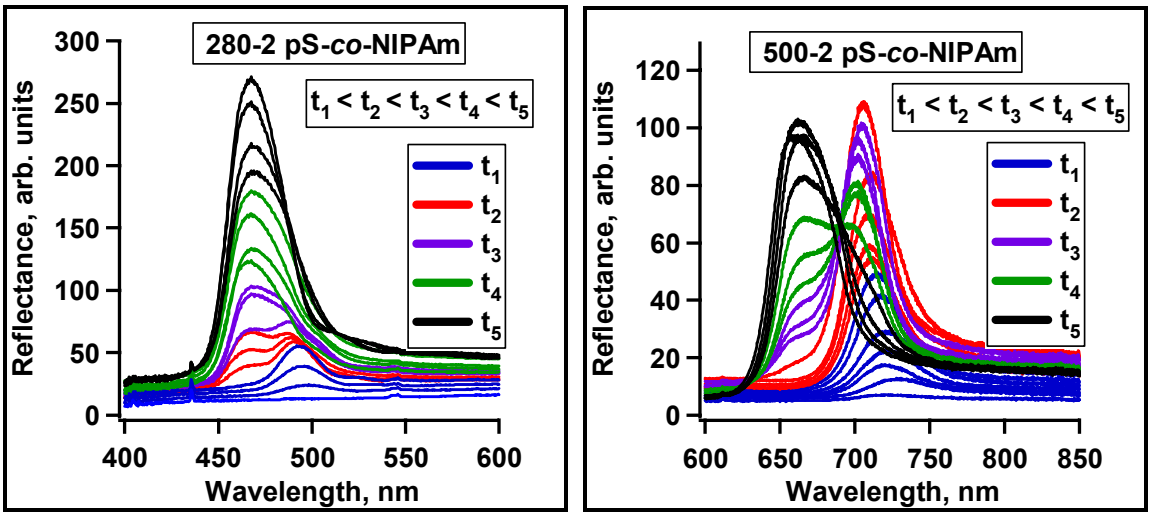

Figure 4.11 Reflectance spectra obtained while drying suspensions of 280-2 (left) and 500-2 (right) particles collected in situ over time (where $t_1<t_2<t_3<t_4<t_5$). The curves correspond to the onset of diffraction, the continuous the blue shift of this diffraction, and the emergence and final diffraction stabilization due to crystals composed of completely dried particles. (Angle of incidence = 90˚)

Since the structured layers that were interrogated using the in situ reflectance setup were located at or near the air/water interface of the drying drop, it cannot necessarily be assumed that the peaks are due to diffraction of the 111 plane composed of crystal(s) possessing homogenous lattice spacing. For instance, many different crystal lattices may exist due to particles with varying degrees of hydration due to evaporation because of contact with air. The lattice planes could also be tilted due to the contact angle of the drop as the suspension dries. To further characterize this assembly process, another experiment was performed whereby the drop was interrogated from the backside of the sample (through the glass cover slip) as the drop dried. Using this method, one can be fairly confident that the particle layers that are interrogated remain fairly hydrated since they exist at or near the glass/suspension interface. The in situ reflectance spectra that were collected from the backside of the samples during drying are shown in Figure 4.12 for the 280-2 and 500-2 particles, as wells as for the 300-1 particles (where $t_1<t_2<t_3<t_4<t_5$).

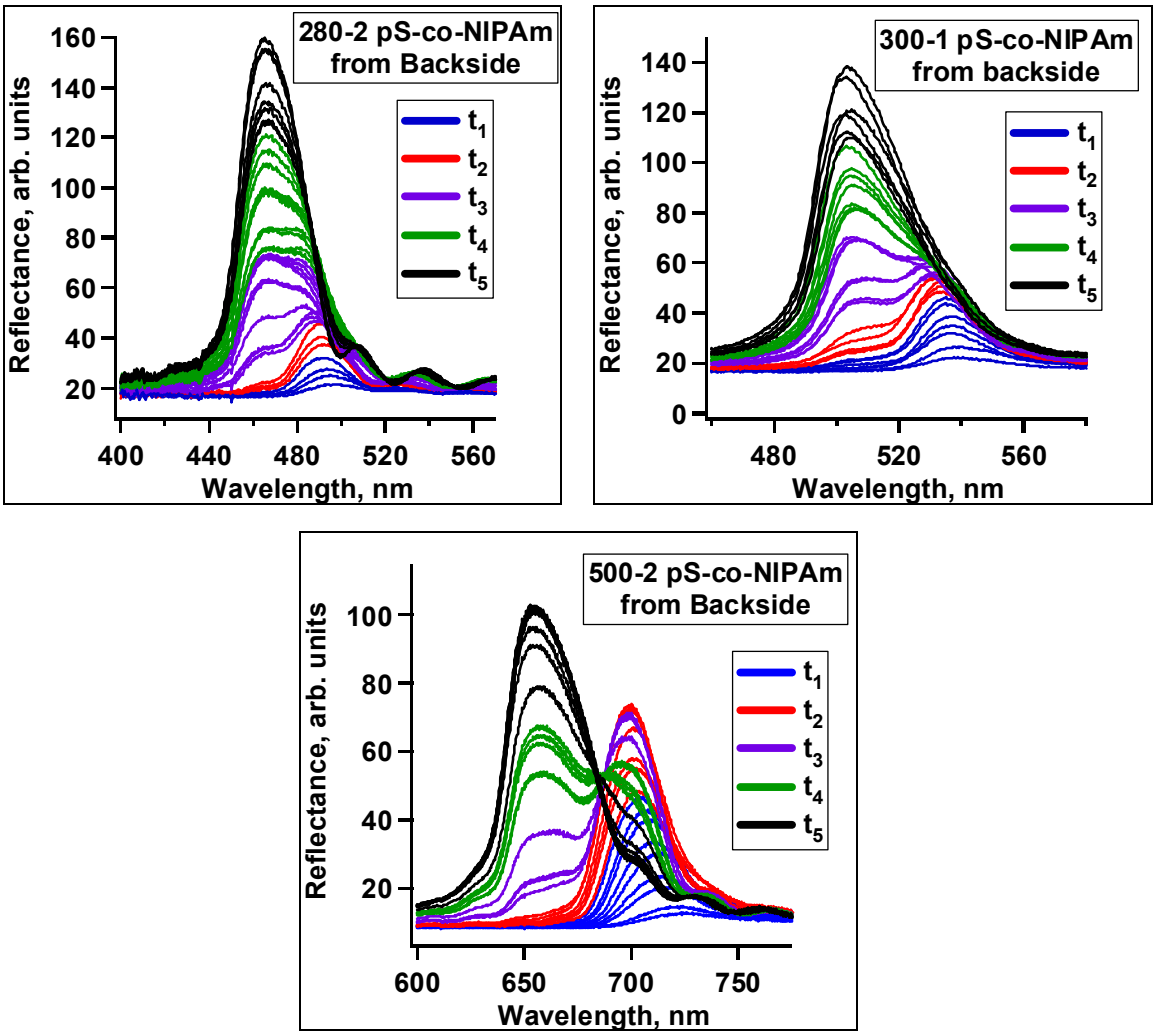

Figure 4.12. Reflectance spectra obtained while drying suspensions of 280-2 (top, left), 300-1 (top, right), and 500-2 (bottom) particles collected in situ over time (where $t_1<t_2<t_3<t_4<t_5$). These spectra were obtained by interrogating the backside of the suspensions as they dried. The curves correspond to the onset of diffraction, the continuous the blue shift of this diffraction, and the emergence and final diffraction stabilization due to crystals composed of completely dried particles. (Angle of incidence = 90˚)

4.4 Discussion

4.4.1 "150-1", "300-1", "280-2", and "500-2" pS-*co*-NIPAm Particles and Crystals

The dried crystals composed of 150-1, 300-1, 280-2, or 500-2 pS-*co*-NIPAm particles that were formed by simple drying demonstrated good particle order, as found using SEM, and exhibited high signal Bragg diffraction, which indicated high-quality crystalline structures. Since this crystalline self-assembly process appears to be due to the characteristics of its constituent building blocks, the characteristics particular to the individual pS-*co*-NIPAm microparticles were first investigated. The assessment of both the hard and soft sphere qualities of these particles were of particular importance, since these attributes appear to affect the self-assembly process and the final stability of the crystalline configuration.

Since exceptionally soft spheres, e.g., pNIPAm particles, cannot maintain crystalline order following drying, the rigidity of the pS copolymer spheres can afford particle stability throughout the drying process. The integrity of these pS-*co*-NIPAm particles can be observed in the TEM images of particles in their dried state. However, the extent of this volume decrease between the wet and dry states is rather large. This drastic reduction in size is atypical for hard sphere polymer particles in water, which are normally composed of purely hydrophobic polymer. This change in size is due to the loss of water from hydrogel, pNIPAm portions of the particle. The presence of such pNIPAm-rich regions suggests that soft interactions can occur between neighboring particles.

As shown in Table 4.2, these particles only show slight temperature dependent changes in the particle size in the wet state. Even though these particles swell in aqueous solution, this result indicates that the low NIPAm concentrations that were used in the particle synthesis yield particle that do not exhibit the same extreme softness found in pNIPAm-only particles. Fortuitously, due to their copolymer identity, all of these

particles maintain a spherical shape in both the wet and dried states and possess a narrow size distribution, which is necessary for crystalline order using spherical building blocks.

It should be noted that the a larger amount of NIPAm (relative to styrene) was used in the synthesis of the 280-2 particles compared to the other pS-*co*-NIPAm particles, which may explain why there are slight differences in the characteristics of these particles. These differences could contribute to differences in the self-assembly process. First, there is a slightly larger degree of particle thermoresponsivity for these particles (9% volume decrease as indicated by PCS) compared to the other initial pS-*co*-NIPAm particles. Secondly, the R_g/R_h ratio is different for the 280-2 and the 500-2 particles, which were prepared under the same reaction conditions. A sphere of uniform density exhibits an R_g/R_h value of 0.775[31] and the 280-2 and 500-2 pS-*co*-NIPAm particles demonstrated R_g/R_h values equal to 0.631 and 0.782, respectively. These results suggest that both sets of particles possess polymer compositions that are similar to that of a sphere of uniform polymer density. However, the slight discrepancy in the R_g/R_h values between the two sets of particles may be indicative of variations in the arrangement of the copolymer composition throughout the particle. Since the 280-2 particles possess a slightly larger percentage of NIPAm as well as a smaller R_g/R_h ratio, one might expect the smaller particles to be slightly more hydrated. Indeed, we find that the ratio of hydrated to dry volumes (61% to 40%, for the 280-2 and 500-2 particles, respectively) agrees at least semi-quantitatively with the measured R_g/R_h ratios for these two sets of particles.[31] These differences between the 280-2 and 500-2 particles are attributed to the variations in their monomer feed concentrations, yielding variations in the rates of polymerization and, thus, altering the polymer density profile of these particles. These results indicate that there may be a larger amount of flexible, lightly cross-linked polymer located near the particle exterior for the 280-2 particles, which may provide added polymer “softness”.

Unfortunately, it is difficult to ascertain the true composition of the copolymer combination in these particles, which seems significantly affect the particle properties, as described above. It is possible that some degree of phase separation of the two polymeric

components occurs due to the reactivity ratios and hydrophilicity and hydrophobicity of the NIPAm and styrene. This rationale has been used in the literature to explain why the exterior of certain types of pS-*co*-NIPAm particles is composed mostly of the more hydrophilic pNIPAm and the center of the particle consists of the more hydrophobic polystyrene.[21,24,35,36] Therefore, it is proposed that the wet-to-dry change in size is due primarily to the loss of water from a hydrated pNIPAm-rich periphery of the particle, while the spherical shape is effectively preserved as a result of the dense pS-rich hydrophobic core. The difference in the wet-to-dry particle sizes indicates the extent of surface flexibility, or softness, that can be realized with these copolymer particles, which appear to assist in particle self-assembly during the drying process. Despite these differences, these particular pS-*co*-NIPAm particles appear to possess ideal quantities of hard and soft polymer to afford easy self-assembly and impressive stability.

Despite differences in this apparent degree of softness of the particles, the TEM images of the samples that were prepared by drying dilute suspensions of particles suggest that there are specific interparticle interactions that occur during the drying process that may contribute to crystalline stability. Whereas the SEM images (Figure 4.5 and 4.6) indicate the existence of bulk crystalline stability of the dried pS-*co*-NIPAm particles using concentrated suspensions, the TEM images demonstrate the specific interactions that occur between neighboring particles. Figure 4.2 shows images found for each of the pS-*co*-NIPAm particles described thus far. As stated previously, all of the particles appear to be spherical in shape. However, their boundaries become unclear at the positions where neighboring particles are encountered and these particle peripheries appear to become joined together, suggesting an adhesive quality. This observation suggests that there may be interpenetration of the polymer network located near the periphery of the adjacent particles. This particle adhesiveness may be due to increasing hydrophobic interactions between the pNIPAm-rich regions of neighboring particles as the water content decreases. The shapes of these conjoined particles also become altered,

such that particle diameter is not uniform at all positions across each particle. These particles appear to stretch slightly in the direction of the particle connections.

This feature is evident for the 280-2 and 500-2 pS-*co*-NIPAm particles shown in Panels C and D, respectively. In comparison to the position of the noticeably dark regions located near the center of the particles, a lighter portion of the particles appears to be stretched towards the adjacent, neighboring particles. This variation in intensity is consistent with differences in the electron density of the material, such that the area of lighter density becomes redistributed. In the case of the image displaying the 280-2 particles (Panel C), the center particle, which is entirely surrounded by other particles, appears to be stretched equally in all directions. This stretching quality not only suggests that the soft polymer networks located at the particle exteriors interpenetrate to form connective adhesions, but that this quality may sustain particle uniformity in a bulk crystal. Interestingly, the interstitial spaces between these particles appear devoid of polymer material, which demonstrates that, even though the polymer is flexible in the wet state, the dried polymer only occurs in the vicinity of polymer-rich material.

The more concentrated particle array composed of the 500-2 pS-*co*-NIPAm particles also demonstrates a marked uniformity (Figure 4.3). In this case, the particles that are completely surrounded by neighboring particles adopt a non-spherical shape due to compression of the other particles in this array. This array conformation appears to occur spontaneously due to the flexibility of the particle periphery as these pS-*co*-NIPAm particles dry and progress into closer contact. The resulting structure is similar to features that have been observed when crystals composed of hard spheres that have been sintered by means of thermal annealing techniques.[27,37,38] Likewise, the adhesive quality of the soft interfaces of these pS-*co*-NIPAm particles seems to facilitate the stability of the final, compressed configuration. Even the particles at the edges remain secured to the hexagonal arrangement. Altogether, these TEM images demonstrate that the flexibility of the interparticle interactions assists in the assembly process and that these polymer

interactions at the particle exteriors facilitate adhesive interactions that maintain an ordered particle configuration.

These discrete particle adhesions appear to preserve the three-dimensional particle order that is observed in the SEM images of bulk crystals (Figure 4.6). This order also persists throughout the entire cross-sections, demonstrating stability on the order of tens of microns in thickness. Considering that the sample cross-sections were obtained by fracturing the sample, this particle order is tremendously stable. This three-dimensional order was also visible at cracks along the sample (Figure 4.6, bottom right). These cracks, which were found throughout the span of the dried crystal (Figure 4.13), are typically observed in colloidal crystals as result of the volume reduction associated with sphere shrinkage.[39] However, these cracks do not impinge on the long-range order of the crystal due to the remarkable stability provided by adhesive interactions of the particles.

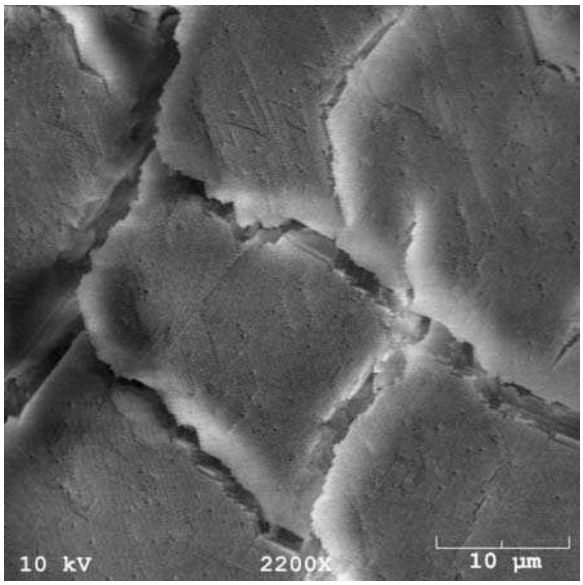

Figure 4.13 SEM image of cracks in a dried crystal composed of 500-2 pS-*co*-NIPAm particles.

For comparison, a representative hard-sphere crystal was prepared by drying polystyrene sulfate latex beads (diameter = 770 nm) on a glass surface and was characterized by SEM (Figure 4.14). Immediately, one notices the deficiencies in long-range particle order found at the top of the sample. In regions where there is long-range order, disorder occurs along the defect cracks, since these hard spheres are not securely fixed in place. This effect is very pronounced by viewing the sample along its cross-section, where particles are extremely disordered and even appear to fall off of the bulk sample, as demonstrated by loose particles to the bottom of the right panel. By contrast, the dried crystals composed of pS-*co*-NIPAm particles exhibit structures of enhanced stability. The reflectance spectrum of the standard polystyrene crystal also displays multiple peaks, demonstrating the significant polycrystallinity and inconsistency of the sample.

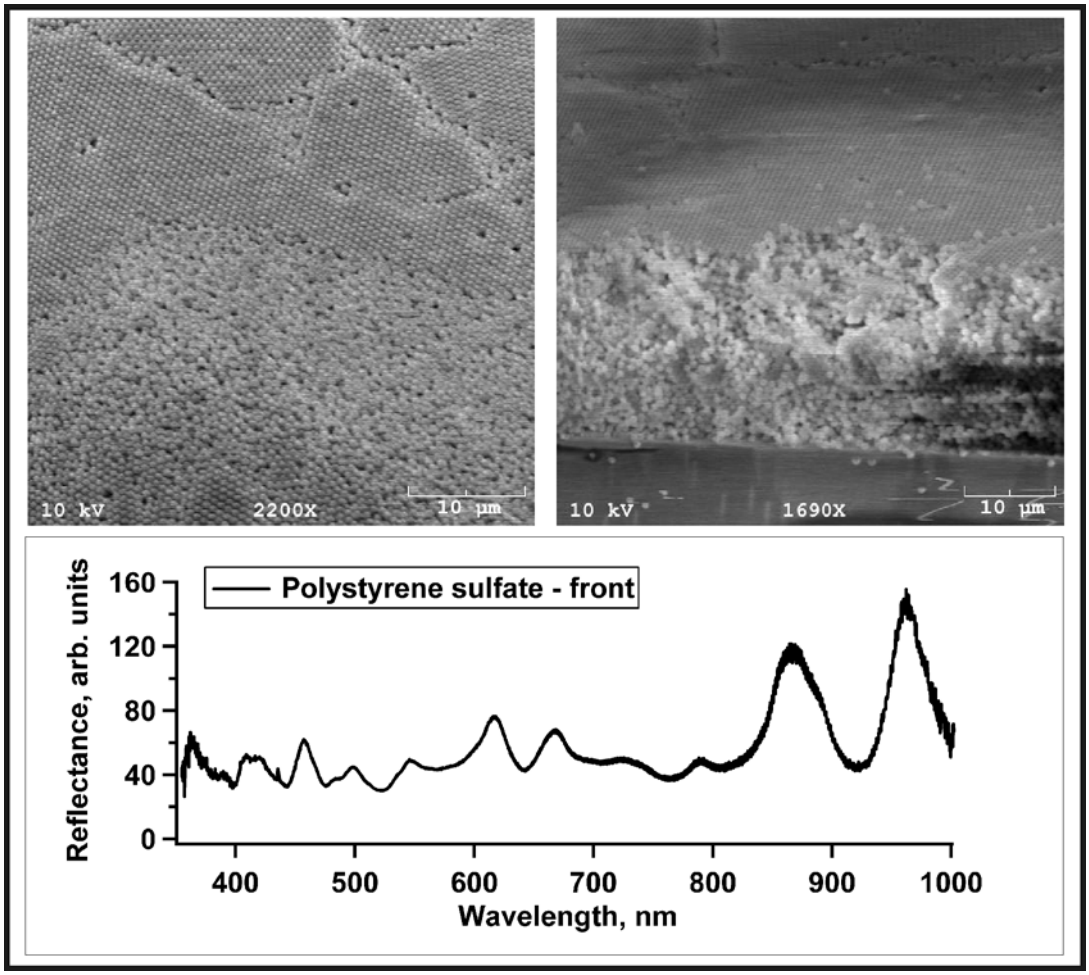

Figure 4.14 Images acquired by SEM demonstrating the particle order at the top and cross-section of a sample prepared with polystyrene sulfate particles

The SEM images that were obtained by observing the tops of the pS-*co*-NIPAm crystals exhibit particles that adopt a hexagonal packing arrangement. This type of order corresponds to a 111 crystalline plane, which is consistent with face-centered cubic (fcc), hexagonally-close packed (hcp), or randomly stacked crystal structures. However, it is difficult to use these SEM images to determine the exact crystalline structure and the extent of the structured layers.[34] Since these arrangements of spherical particles can exhibit Bragg diffraction,[11] optical spectroscopy is essential to demonstrate the uniformity of crystalline order.

The reflectance spectra shown in Figure 4.7 demonstrate the diffraction peaks that are exhibited by each dried crystal. These peaks correspond to the uniform diffraction colors that were observed across the length of the sample by visual inspection (Figure 4.4). These spectra also confirms crystallinity for the 150-1 sample, which was not apparent by visual inspection since the small size of these 150-1 particles produces diffraction in the UV region. The positions of these peaks follow Bragg's law, since the lattice spacing increases as the dried particle size increases (assuming that the samples possess similar effective refractive indices). The symmetry and breadth of each peak demonstrates the uniformity of crystalline order and the lack of additional peaks confirm the absence of gross polycrystallinity in these samples, which is typically observed with hard-sphere crystal systems unless complex assembly procedures are employed (Figure 4.14). It should be noted that these optical spectra represent diffraction characteristics for only a particular number of particle layers that are interrogated using reflectance spectroscopy (either at the top or bottom of the crystal). Standard transmission measurements demonstrated a high scattering background, which may be indicative of a higher defect density throughout the thickness of the crystal. This condition may be a result of the many cracks found throughout the sample due to the particle volume shrinkage during the drying process.

We can characterize these particular dried crystalline assemblies by comparing the effective refractive index of each final, dried sample. These values can be calculated using Bragg's Law. Since the diffraction wavelengths have been found experimentally, we can assume that the dried samples possess an fcc crystalline structure (which is the most common structure for crystals composed of spheres), and we can assume that the particle size for the dried crystal approximates the size found using TEM. As a result, the dried crystals for the 300-1, 280-2, and 500-2 crystals possess effective refractive indices of 1.38, 1.41, and 1.49, respectively. The refractive index for these three samples appears to be reasonably consistent for a crystal that contains these polymeric components. These

differences probably correspond to subtle differences in the pS-*co*-NIPAm compositions when dried. (The refractive index for the 150-1 crystal could not be calculated accurately due to uncertainties in the determination of the peak wavelength, since this peak is found near the limit of the wavelength range of the reflectance probe.) The effective refractive index is also a function of the volume fraction that is occupied by the individual components. Since the soft polymer exterior of the particles may occupy much of the interstitial void spaces,[10] as observed in the TEM images, the final polymer configurations could also affect the final volume fraction occupied by the spheres.

Since the soft properties of the pS-*co*-NIPAm particles appear to be integral to the self-assembly process, in situ reflectance measurements were used to elucidate the process of this crystalline assembly during drying (Figure 4.11). It is worth noting that repeating these in situ reflectance experiments by interrogating the samples through the backside of the drying sample demonstrated that this self-assembly process occurs in the same way at the glass/water interface as it does at the air/water interface (Figure 4.12). The only disparity is the presence of distortions in the spectra for the final, dried state. This feature is due to thin-film interference because of the existence of the glass cover slip between the sample and the light source.

Because a wide area of the sample is interrogated using this reflectance probe, the coexistence of multiple peaks is observed at certain points during the drying process. The continual changes in these diffraction curves, as depicted by curves of different colors over time in Figure 4.11 and 4.12, are presumably due to multiple lattice planes composed of particles of a broad range of intermediate sizes (partially dehydrated) that lie along this drying zone. Although the presence of the two predominant peaks indicates two different types of ordered states, it is impossible to ascertain the exact crystal lattice constants since there are continuous changes in the particle size (decreasing) and effective refractive index (increasing) during this evolution.

However, we can estimate the particle size for the initial diffraction peak found using in situ reflectance spectroscopy. This value can be calculated using the experimental wavelength of this first diffraction peak and by approximating the value of the refractive index. Since the onset of crystallization occurs at ~0.5 volume filling fraction, we can assume that this is the particle volume fraction at the emergence of the first peak (therefore, ~0.5 volume fraction is water). Since we know the volume-deswelling ratio between a fully hydrated particle at room temperature and the collapsed particle at high temperatures, we can assume that the refractive index of the swollen portion is similar to water (1.333) and the refractive index of the deswollen portion in similar to polystyrene (~1.5). Therefore, we can approximate the effective refractive index based on these estimated volume contributions using Equation 1.2. Using these refractive indices, shown in Table 4.4, and the wavelength of initial diffraction, we can apply Bragg's Law to calculate the estimated particle size at the onset of crystallization.

Table 4.4 Estimated effective refractive index (*n*), lattice spacing (*d*), and particle diameter (D) at the emergence of initial diffraction for each crystal.

Sample	Wavelength of Initial Diffraction, nm	*n*	*d*, nm	Estimated Diameter at Initial Diffraction, nm	Diameter, nm (PCS at 25 C)
300-1	538	1.39	193	237	246 (± 2)
280-2	497	1.37	182	223	278 (± 4)
500-2	728	1.38	265	324	318 (± 2)

The estimated particle size for the 280-2 sample and the 300-1 sample are somewhat smaller than the fully hydrated particles at room temperature. This result may

indicate that although these latter particles are mostly hydrated, they are also partially compressed at the state of initial ordering. Since a less dense, floppier exterior is suggested by the low R_g/R_h value for the 280-2 particles, this softer periphery may become compressed at this state. The estimated particle size for the 500-2 particles is almost identical to the fully swollen size found by PCS. This result could follow from the fact that the R_g/R_h for the 500-2 particles is approximately the same for a uniform sphere. This larger polymer density profile may preserve the fully hydrated size of these particles as the sample reaches ~0.5 particle volume fraction.

Upon further inspection, another observation can be made with respect to the differences in peak shifts and intensities. While the intensity of the initial peak nearly equals the intensity of the final peak for the crystal composed of 500-2 particles, the initial reflectance peak for the 280-2 and 300-1 particles is of a more moderate intensity. Also, the initial peak for the 500-2 particles reaches a maximum intensity prior to the emergence of the second peak, and then decreases in intensity as the second peak increases in intensity. For the 280-2 and the 300-1 particles, the initial peak continues to increase in intensity as the second peak appears, and blue shifts steadily until it merges with the second peak. These disparities during the early drying stages may be due to variations in the extent crystal formation, differences in the degree of particle deformation (due to the polymer density profile), or differences in the refractive index contrast of the particles.

Based on the in situ reflectance experiments, a proposed mechanism for crystallization for all pS-*co*-NIPAm particles is shown in Figure 4.15. Particles in the suspension initially exist in their fully hydrated state, moving freely in solution (blue circles). As the solvent evaporates, the pS-*co*-NIPAm particles come into close contact so as to form an ordered structure (light green circles). Based on the position of the initial diffraction wavelength, the particle size is estimated to be smaller than the fully hydrated size (with the exception of the 500-2 particles which appear to maintain a size similar to

the fully hydrated size). The observation of the first peak is designated as the point in time at which the particle concentration reaches the minimum extent necessary for entropically driven colloidal crystallization (~0.5 volume fraction).[11,40] As the suspension dries from the outer edge of the drop towards the center, diffraction peak blue shifts and increases in intensity, due to the decrease in particle size and increase in refractive index (dark, small green circles). The onset of the most blue-shifted peak is attributed to crystalline regions comprised of completely dried particles (black circles), since this final peak increases in intensity with ultimately no variation in wavelength and persists after the drying process is complete.

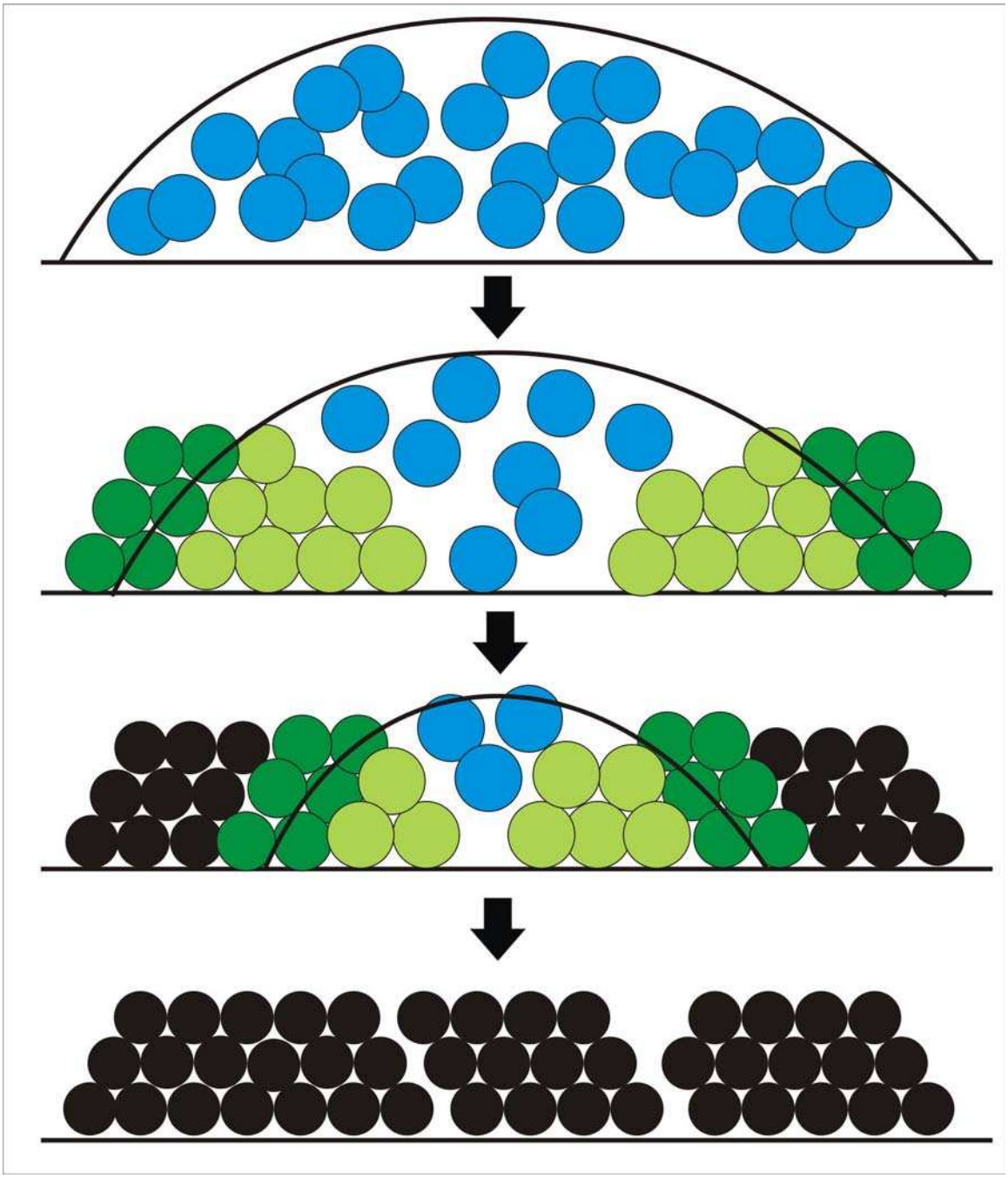

Figure 4.15 Proposed scheme for pS-*co*-NIPAm particle self-assembly: The blue circles represent fully hydrated particles in solution. The light green circles represent mostly-hydrated particles that possess particle order such that Bragg diffraction is observed. The dark green circles represent partially hydrated particles that are continually decreasing in size and increasing in polymer density as the sample dries. The black circles represent fully dried particles. This scheme correlates with the in situ reflectance spectra observed in Figure 4.11.

All of these pS-*co*-NIPAm samples produced crystals in an easily reproducible fashion. Since the self-assembly process and final, dried state is based upon the hard and soft polymeric qualities of the particle, the same optical properties can be achieved regardless of the precise particle concentration of the suspensions. Therefore, crystals of different thicknesses can be achieved by using different particle concentrations. Different shapes of bulk crystals can be also be formed by spreading the suspensions to match the desired pattern (Figure 4.16). Two-dimensional arrays of "colloidal strips" were also prepared by drying particles of two different sizes (Figure 4.17), using a design adapted from approaches used by the Marlow[41] and Xia[42] groups. This "barcode" format is useful for the development of optical tags with discrete optical configurations. The simplicity of this crystal formation and its ability to produce designed configurations demonstrates the application of these particles as processable photonic "inks" that can be used for the fabrication of optical materials.

Figure 4.16 "Crystal Graffiti": Paint-on application of pS-co-NIPAm suspensions as processable photonic inks (Left to right: 280-2, 500-2, 300-1 samples).

Figure 4.17 "Barcode" format of dried red and blue colloidal crystal strips, composed of 500-2 and 280-2 pS-*co*-NIPAm particles, respectively. Multiple strips were formed by subsequent drying of each suspension repeatedly.[41]

4.4.2 "600-1" and "600-2" pS-*co*-NIPAm Particles and Crystals

Whereas the aforementioned pS-*co*-NIPAm particles were able to form crystals with good order by simply drying a suspension of the particles straightaway, the 600-1 and 600-2 particles did not exhibit this same ease of assembly. Drying these suspensions resulted in fairly opaque samples (Figure 4.4) that demonstrated almost no detectable diffraction when the tops of the samples were interrogated and very broad diffraction when samples were interrogated through their backside (Figure 4.8). Since the former pS-*co*-NIPAm particles exhibited superior particle ordering throughout the sample (as demonstrated by comparable diffraction peaks at both sides of the sample throughout the drying process), the lack of distinctive optical qualities for the final dried structures of 600-1 and 600-2 particles was attributed to differences in the particle characteristics, causing deficiencies in good particle ordering when ordinary drying procedures were employed.

It appears that the 600-1 and 600-2 particles contain large amounts of pNIPAm-rich portions that lend towards a relatively large degree of particle softness, such that crystalline order does not remain stable. For pNIPAm particles and the former pS-*co*-NIPAm particles, this hydrogel identity allows for soft interactions, providing polymer

flexibility. This similar type of hydrogel quality is demonstrated by rather large decreases in the wet to dry volumes for both the 600-1 (66%) and 600-2 (83%) particles. pNIPAM particles also possess thermoresponsivity yielding changes in the particle size due to the hydrophobic interactions between flexible polymer chains. Whereas the pS-*co*-pNIPAm particles that were previously described demonstrated only small temperature-dependent changes in particle volume (ranging from 3-9%), the 600-1 and 600-2 particles demonstrated tremendous volume decreases of 55% and 61%, respectively, with increases in temperature. Figure 4.1 shows that this change in particle size even follows a trend similar to the phase-transition for pNIPAm-only particles. However, this transition is considerably broad, which may be due to the complex copolymer network formed with the polystyrene constituent.[43]

While the shapes of the 600-1 and 600-2 pS-*co*-NIPAm particles appear to be spherical in the dried state, the TEM images in Figure 4.2 also demonstrate that each sample possesses unique types of interparticle connections. In the case of the 600-1 particles, adjacent particles have broad interfacial connections as shown in Panel E. This feature is especially pronounced in the lower left corner of this image. This linkage is unlike the visible connections observed for pS-*co*-NIPAm particles, which demonstrate clear interstitial voids that appear free of polymer (Panel B and C). The distinctively broad adhesive feature for the 600-1 particles may be unique to such particles that display increased flexibility.

Conversely, all of the 600-2 particles adopt markedly separated positions (Panel F). A connection is sometimes observed between nearby particles, which appears as a long, thin, dark strand. This linkage is also observed for the 600-1 samples, between nearby particles as well as adjacent particles. This feature is probably due to the same polymer adhesiveness that was observed for the initial pS-*co*-NIPAm particles due to the copolymer identity at the periphery. However, since these 600-1 and 600-2 particles seem to have a larger prevalence of pNIPAm, this adhesive interaction may occur at a longer

range (compared to the dry particle size) due to the increased swellability of the particle. As the particles lose water and the particle size decreases, capillary forces do not draw the particles together in the same way as the other pS-*co*-NIPAm particles become attached. The lengths of these strands between the particles suggest the distance between particles as they dry and become stabilized individually.

Particle morphologies that are similar to these types of interparticle contacts have been observed by the Kawaguchi group, whereby grafted pNIPAm "hairs" form polymer bundles due to their adhesive interactions upon drying.[44-46] These bundles appeared stretched out from the particle core when dried at room temperature due to an extended conformation of the pNIPAm hairs, and were used to prepare particle arrays possessing definite spacing. When these particles were dried at elevated temperatures, they became aggregated and appeared stuck to each other due to the lack of extended volume.

A similar effect may occur during the drying of the 600-2 particles. For the initial pS-*co*-NIPAm particles, the particle adhesions may have been due to increasing hydrophobic interactions between the pNIPAm-rich regions of neighboring particles as the water content decreases. Since these hydrated exteriors are not as thick nor as flexible as the exteriors of the 600-2 particles, the initial pS-*co*-NIPAm particles are still in close proximity when these hydrophobic interactions begin to dominate. Conversely, the distinct particle spacing between the 600-2 particles (which possess the largest decrease in wet-to-dry volume) may be due to the extended conformation of the particle exterior, which may remain excessively hydrated during the inception of drying at room temperature (such that hydrophilic interactions dominate), preventing particle adhesion at this length scale.

The augmented degree of softness at the particle exterior for the 600-1 particles was confirmed by comparing the R_g/R_h value for this particle (0.56) to that for a uniform sphere (0.775). As demonstrated in Table 4.3, this value is also much smaller compared to the 280-2 and 500-2 particles, suggesting that a larger amount of the polymer exists

closer to the particle center for the 600-1 particles. Since self-assembly via drying yields much better order for the 280-2 and 500-2 particles, the increased amount of less dense polymer near the particle exterior of the 600-1 particles may contribute to particle instability during drying, yielding a lack of particle order as observed by SEM.

All of these characteristics that seem to be unique to the 600-1 and 600-2 particles appear to be due to an increased hydrogel (pNIPAm) character. The main difference between these particles and the ones discussed in Section 4.4.1 is that considerably larger absolute amounts of NIPAm were used in the 600-1 and 600-2 particle syntheses. Since acrylamides have been shown to be more reactive than styrene in similar syntheses using emulsion polymerization, the consumption of NIPAm monomer may be greater during the initial stages of polymerization.[24,36,47,48] Therefore, there may also be a larger degree of phase separation between the hydrophobic polystyrene and the hydrophilic pNIPAm, resulting in the increased flexibility of the particle exteriors,[21,35,36] producing the properties that were found for the 600-1 and 600-2 particles. This phase separation may be especially true for the 600-2 particles, since they were synthesized using a form of delayed monomer addition, resulting in the observed disparities in particle adhesion as observed by TEM.

These 600-1 pS-*co*-NIPAm particles did not show very good order upon drying, as shown in the SEM images (Figure 4.5, Panel E). The reflectance spectra of these particles, as well as for 600-2 particles dried at ambient conditions, exhibit no real diffraction peak. However, these samples demonstrate a diffraction peak when interrogated from the backside of the sample. This difference is probably due to a templating effect of the glass substrate and indicates that some order is possible. It appears that long-range particle order cannot remain stabilized during drying since these particles are extremely flexible.

Since these particles are thermoresponsive, increasing the temperature during drying could decrease the particle size during the course of the assembly process. One

could expect that this change in size would decrease the polymeric flexibility, since the hydrogel chains would have already become collapsed. Therefore, the particle softness could be adjusted to control the particle characteristics to obtain a particle exterior that provides an acceptable degree of softness to allow for self-assembly. The reflectance spectra of these heated samples show distinct diffraction peaks, demonstrating that particle order can be achieved and retained once fully dried (Figure 4.9 and 4.10). The SEM image for the 600-2 particles (Figure 4.5, Panel F), which were assembled under such heated conditions, demonstrates a hexagonal particle arrangement, similar to the initial crystalline samples. Since this decrease in particle softness prevents extensive particle deformation, these particles appear to possess an ideal polymeric density that is adequate for crystalline self-assembly via drying processes. The resulting conservation of particle order for these samples may be due to the adhesiveness of the hydrophobic interactions between neighboring particles since the pNIPAm chains already exist in collapsed conformation as a result of the increase in temperature. It should be noted that although the particle size is varied using this heated assembly process, diffraction of these samples occurs at approximately the same wavelengths for both the heated and non-heated samples. Since there may only be modest differences in the effective refractive index for these dried samples, the observation of these similar diffraction peaks demonstrates that the lattice spacing of the dried particles remains unaffected and, therefore, the final particle size is fairly constant for all of the dried samples, regardless of temperature. This result shows that the final optical properties are wholly dependent on the dried particle size.

4.5 pS-*co*-pNIPAm Microparticles as Photonic Inks for Ink Jet Printing

The ability to form discrete optically diffractive materials makes the application of pS-*co*-NIPAm microparticles an attractive approach for the formation of designed patterns. Although the “paint-on” approach described above provided a simple technique

for fabrication of stable, dried crystals, the patterns were rather unsophisticated and the drying process of such large volumes of the dispersions (even just a couple of drops) required a relatively long time for the samples to dry completely. These aspects would need to be improved upon in order to successfully develop the application of these pS-*co*-NIPAm particles for manufacturing purposes. To this end, the processability of the pS-*co*-NIPAm microparticles was evaluated by preparing dried samples using ink-jet printing. This process could be used to rapidly prepare distinct designs with high resolution using of these pS-*co*-NIPAm suspensions as "photonic inks".

Ink-jet printing deposition methods are not new to materials chemistry and have been used to deposit self-assembled monolayers,[49] protein arrays, and even cells.[50,51] These types of studies have shown that resolution can be attained at the sub-hundred nanometer scale[52] and that complex microarray patterns could be formed, which would be extremely valuable for sensing applications for a variety of systems.[53,54] The Moon group has also investigated the formation of colloidal crystals using nanoparticle "inks" using ink-jet printing techniques.[55-58] They were able to produce a variety of designed patterns using both silica and polystyrene nanoparticles, however, certain provisions were needed to ensure the assembly of particles with long-range order exhibited diffraction. For example, most of their samples were prepared with functionalized substrates or non-standard materials to yielded variations in the contact angle of the suspension, which contributed to the particle self-assembly.[55,57] Different solvent qualities and particle concentrations were also investigated.[58]

In this study, the 500-2 pS-*co*-NIPAm particles were investigated as an "ink" for ink-jet printing deposition, since these were the largest pS-co-NIPAm particles that were synthesized which also displayed good self-assembled order via simple drying. An Epson Stylus Photo R220 Series Ink-Jet Printer was utilized for this study, which was equipped with a tray for printing directly on to compact discs, which provided a useful method for printing directly on to the flat, non-porous substrates used in this study. Concentrations of

the aqueous 500-2 pS-*co*-NIPAm suspensions were similar to those used above and no additional solvent modification was performed. Additionally, standard glass cover slips were used as substrates. A Continuous Ink System (Print-on-a-Dime, Inc.) was employed to allow for easy introduction of the pS-*co*-NIPAm ink into the printer system. The suspension was added to one cartridge and the Epson software (Epson Print CD v.1.4A) settings were adjusted so that printing only occurred using that particular cartridge. One can imagine using multiple inks, with particles of difference sizes to form crystals with different diffraction properties, to produce specialized optical designs in the same printing step.

A simple, large rectangular block pattern was used as a prototypical shape for these initial investigations. Figure 4.18 shows an image (acquired using SEM) of a drop formed in the middle of this pattern using a single printing of this pattern. This structure adopts a ring shape, due to a concentration of particles at the periphery of the drop, which have been described as dissipative structures,[59-62] similar to those that have formed "coffee-stain" patterns.[63] The effects of the drying forces become more significant as the initial volume of the drop becomes smaller.[64,65] A closer look at the edge of this drop (Figure 4.18, right image) demonstrates particle order due to the self-assembly of the pS-*co*-NIPAm particles. Unfortunately, the concentration of particles that was used did not provide for a high surface coverage. This result was probably due to the small volumes of ink used by the printer. Also, the particle order does not appear to persist to the same length scale that was observed using the standard "paint-on" approach. This lack of order is probably due to the rapid drying of such small volumes.[65]

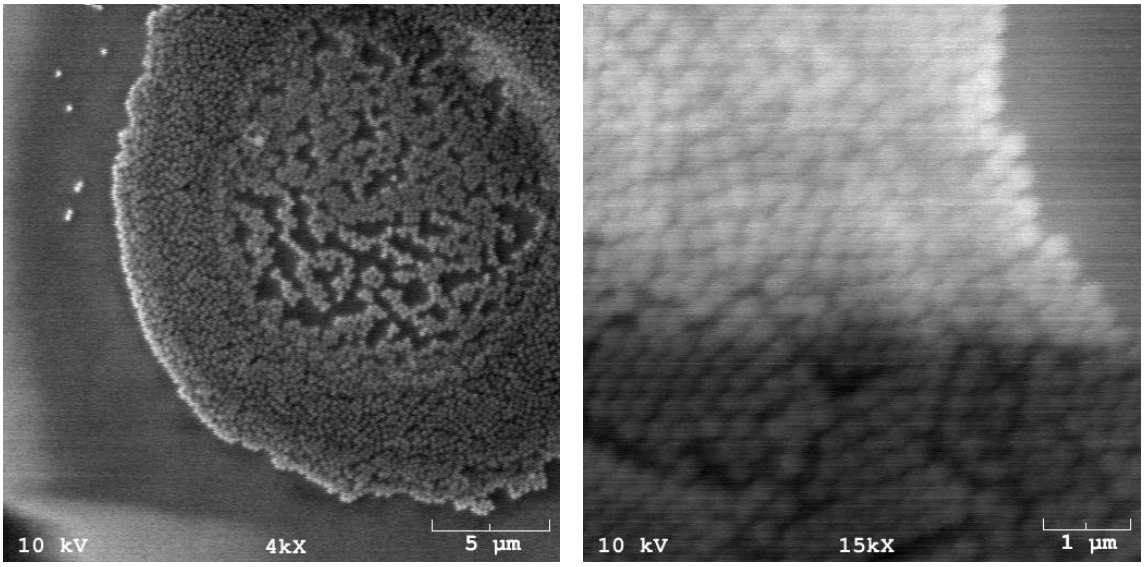

Figure 4.18 Images of drops of 500-2 pS-*co*-NIPAm particles desposited by ink-jet printing acquired by SEM. Right: particles at the edge of the drop.

Since printing this pattern one time did not yield a large enough population of pS-*co*-NIPAm particles to yield optimal coverage for long-range particle order, multiple depositions were performed on the same surface to introduce more particles. Figure 4.19 shows images of the layers acquired using optical microscopy (using a 10x objective). As the number of depositions increases, the drops become combined to cover larger areas and the boundaries of these regions become thicker due to higher concentrations of particles. A visual inspection of these samples shows a rewetting of the sample with each consecutive printing. This process potentially provides mode of re-self-assembling of particles that have already been deposited, while adding more particles to the system. As more printings were performed, dark regions that possess cracks begin to appear (for 7 and 10 printings), suggesting that thicker layers of particles have formed.

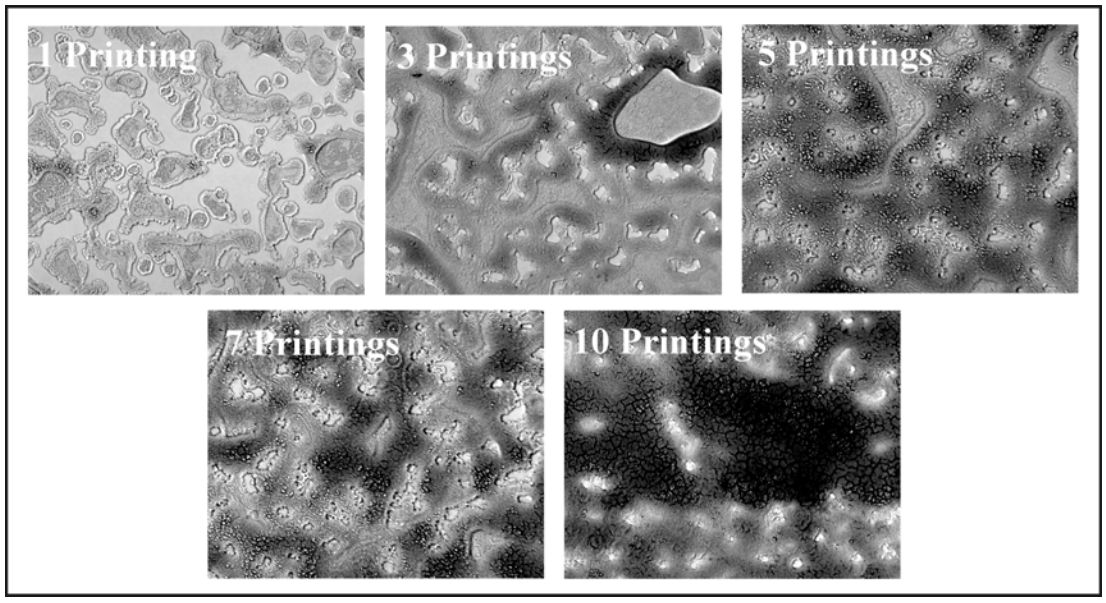

Figure 4.19 Optical microscopy images of multiple depositions of the 500-2 pS-*co*-NIPAm particles (10x objective).

The optical diffraction of these samples was measured using reflectance microscopy, as shown in Figure 4.20. There is hardly any sign of a diffraction peak with only one printing of the pS-*co*-NIPAm ink. However, multiple printings show the emergence of a peak at ~660 nm, which becomes narrower with successive printings. These results suggest that the particle order improves with each consecutive printing. This study shows how these pS-*co*-NIPAm particles can be used as photonic inks and further investigations of the particle concentration of the "ink" and the solvent interaction with the surface may provide for the formation of patterns of high resolution.

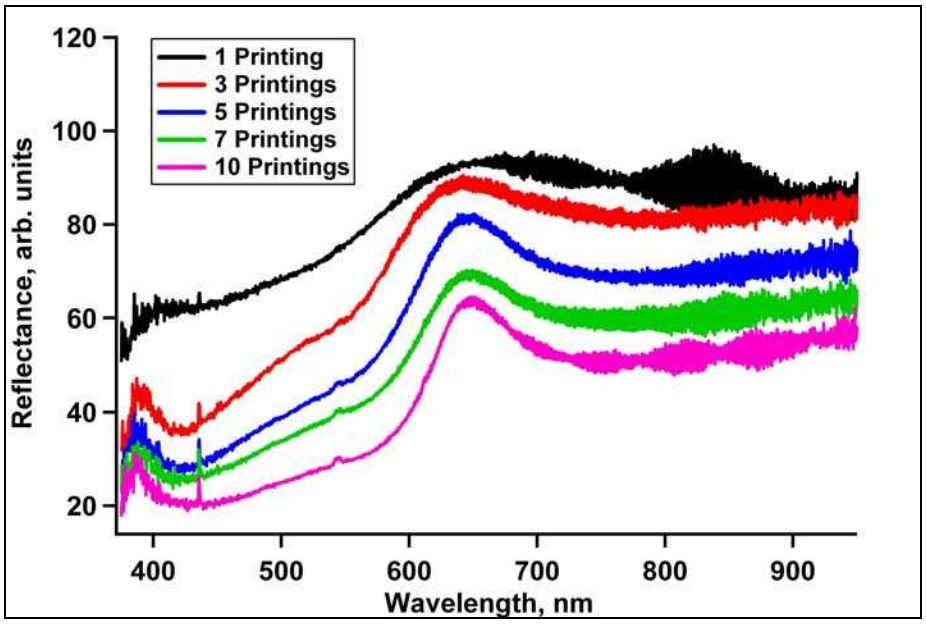

Figure 4.20 Reflectance spectra of multiple depositions of the 500-2 pS-*co*-NIPAm particles.

4.6 Conclusions

Microparticles composed of pS-*co*-NIPAm have been synthesized used to prepare stable crystalline materials that exhibit Bragg diffraction through self-assembly via a simple drying process. These particles exhibit properties that are characteristic of both hard and soft spheres, which fundamentally influence the assembly process and consequent stability of the bulk crystal. The flexible copolymer identity controls the self-assembly process through soft, interparticle contacts. This flexibility fortuitously occurs at the particle periphery due to the hydrophilicity of the minor pNIPAm constituent. The dense polymer characteristics, provided by the predominance of pS component, yield enhanced particle integrity that affords stability of the particle order in the dried state.

Increasing degrees of softness were found affect the flexibility of the particle, which can perturb the final particle order as a result of excessive particle deformation. In these cases, this property of increased softness correlated with increased levels of particle

thermoresponsivity, due to larger amounts of pNIPAm-rich regions. Consequently, the flexible polymer characteristics of these particles could be adjusted to enable the formation of crystals with stable particle order by taking advantage of the thermoresponisive qualities. Further polymer characterizations of the copolymer composition are necessary to develop a more thorough understanding of how the combination of NIPAm and styrene affects polymer composition and morphology of the particle.

In view of the fact that suspensions of these pS-*co*-NIPAm particles can form crystals using simple drying techniques, this assembly technique is amenable for the processing of optically relevant materials. Therefore, these particles can be used as photonic inks to prepare three-dimensional structures with predetermined configurations and patterns. Since these pS-*co*-NIPAm particles possess a unique capacity for ordered self-assembly that is inherent to their hard and soft copolymer character, this synthetic strategy provides a model approach for the design of ordered systems based upon the polymeric identity of the building block components.

References

[1] Yablonovitch, E. Inhibited spontaneous emission in solid-state physics and electronics. *Phys. Rev. Lett.* **1987**, *58*, 2059-62.

[2] John, S. Strong localization of photons in certain disordered dielectric superlattices. *Phys. Rev. Lett.* **1987**, *58*, 2486-9.

[3] Stoeber, W.; Fink, A.; Bohn, E. Controlled growth of monodisperse silica spheres in the micron size range. *J. Coll. Interface Sci.* **1968**, *26*, 62-9.

[4] Forcada, J.; Hidalgo-Alvarez, R. Functionalized polymer colloids: Synthesis and colloidal stability. *Current Organic Chem.* **2005**, *9*, 1067-1084.

[5] Vanderhoff, J. W. Well-characterized monodisperse polystyrene latexes as model colloids. *Pure and Appl. Chem.* **1980**, *52*, 1263-73.

[6] Fleischhaker, F.; Arsenault, A. C.; Kitaev, V.; Peiris, F. C.; von Freymann, G.; Manners, I.; Zentel, R.; Ozin, G. A. Photochemically and Thermally Tunable Planar Defects in Colloidal Photonic Crystals. *J. Am. Chem. Soc.* **2005**, *127*, 9318-9319.

[7] Ben-Moshe, M.; Alexeev, V. L.; Asher, S. A. Fast Responsive Crystalline Colloidal Array Photonic Crystal Glucose Sensors. *Anal. Chem.* **2006**, *78*, 5149-5157.

[8] Weissman, J. M.; Sunkara, H. B.; Tse, A. S.; Asher, S. A. Thermally switchable periodicities and diffraction from mesoscopically ordered materials. *Science* **1996**, *274*, 959-960.

[9] Holtz, J. H.; Asher, S. A. Polymerized colloidal crystal hydrogel films as intelligent chemical sensing materials. *Nature* **1997**, *389*, 829-832.

[10] Debord, S. B.; Lyon, L. A. Influence of Particle Volume Fraction on Packing in Responsive Hydrogel Colloidal Crystals. *J. Phys. Chem. B* **2003**, *107*, 2927-2932.

[11] Lyon, L. A.; Debord, J. D.; Debord, S. B.; Jones, C. D.; McGrath, J. G.; Serpe, M. J. Microgel Colloidal Crystals. *J. Phys. Chem. B* **2004**, *108*, 19099-19108.

[12] Debord, J. D.; Eustis, S.; Debord, S. B.; Lofye, M. T.; Lyon, L. A. Color-tunable colloidal crystals from soft hydrogel nanoparticles. *Adv. Mat.* **2002**, *14*, 658-662.

[13] Hellweg, T.; Dewhurst, C. D.; Bruckner, E.; Kratz, K.; Eimer, W. Colloidal crystals made of poly(N-isopropylacrylamide) microgel particles. *Colloid Polym. Sci.* **2000**, *278*, 972-978.

[14] Senff, H.; Richtering, W. Temperature sensitive microgel suspensions: Colloidal phase behavior and rheology of soft spheres. *J. Chem. Phys.* **1999**, *111*, 1705-1711.

[15] Hu, Z.; Lu, X.; Gao, J. Hydrogel opals. *Adv. Mat.* **2001**, *13*, 1708-1712.

[16] Reese, C. E.; Mikhonin, A. V.; Kamenjicki, M.; Tikhonov, A.; Asher, S. A. Nanogel Nanosecond Photonic Crystal Optical Switching. *J. Am. Chem. Soc.* **2004**, *126*, 1493-1496.

[17] Kamenjicki, M.; Lednev, I. K.; Mikhonin, A.; Kesavamoorthy, R.; Asher, S. A. Photochemically controlled photonic crystals. *Adv. Funct. Mater.* **2003**, *13*, 774-780.

[18] Asher, S. A.; Holtz, J.; Liu, L.; Wu, Z. Self-Assembly Motif for Creating Submicron Periodic Materials. Polymerized Crystalline Colloidal Arrays. *J. Am. Chem. Soc.* **1994**, *116*, 4997-8.

[19] Iwayama, Y.; Yamanaka, J.; Takiguchi, Y.; Takasaka, M.; Ito, K.; Shinohara, T.; Sawada, T.; Yonese, M. Optically Tunable Gelled Photonic Crystal Covering Almost the Entire Visible Light Wavelength Region. *Langmuir* **2003**, *19*, 977-980.

[20] Kamenetzky, E. A.; Magliocco, L. G.; Panzer, H. P. Structure of solidified colloidal array laser filters studied by cryogenic transmission electron microscopy. *Science* **1994**, *263*, 207-10.

[21] Hellweg, T.; Dewhurst, C. D.; Eimer, W.; Kratz, K. PNIPAM-co-polystyrene Core-Shell Microgels: Structure, Swelling Behavior, and Crystallization. *Langmuir* **2004**, *20*, 4330-4335.

[22] Yi, C.; Xu, Z. Synthesis and characterization of thermosensitive composite microsphere latex. *J. Appl. Polym. Sci.* **2005**, *96*, 824-828.

[23] Xiao, X.-C.; Chu, L.-Y.; Chen, W.-M.; Wang, S.; Xie, R. Preparation of Submicrometer-Sized Monodispersed Thermoresponsive Core-Shell Hydrogel Microspheres. *Langmuir* **2004**, *20*, 5247-5253.

[24] Duracher, D.; Sauzedde, F.; Elaissari, A.; Perrin, A.; Pichot, C. Cationic amino-containing N-isopropylacrylamide-styrene copolymer latex particles. Part 1. Particle size and morphology vs. polymerization process. *Colloid Polym. Sci.* **1998**, *276*, 219-231.

[25] Makino, K.; Yamamoto, S.; Fujimoto, K.; Kawaguchi, H.; Ohshima, H. Surface structure of latex particles covered with temperature-sensitive hydrogel layers. *J. Coll. Interface Sci.* **1994**, *166*, 251-8.

[26] Nakahama, K.; Fujimoto, K. Thermosensitive Two-Dimensional Arrays of Hydrogel Particles. *Langmuir* **2002**, *18*, 10095-10099.

[27] Cho, Y.-S.; Yi, G.-R.; Moon, J. H.; Kim, D.-C.; Lee, B.-J.; Yang, S.-M. Connected Open Structures from Close-Packed Colloidal Crystals by Hyperthermal Neutral Beam Etching. *Langmuir* **2005**, *21*, 10770-10775.

[28] Wyatt, P. J.; Villalpando, D. N. High-Precision Measurement of Submicrometer Particle Size Distributions. *Langmuir* **1997**, *13*, 3913-3914.

[29] Andersson, M.; Wittgren, B.; Wahlund, K. G. Ultrahigh molar mass component detected in ethylhydroxyethyl cellulose by asymmetrical flow field-flow fractionation coupled to multiangle light scattering. *Anal. Chem.* **2001**, *73*, 4852-61.

[30] Rasband, W. S., ImageJ, National Institutes of Health, Bethesda, Maryland, USA, http://rsb.info.nih.gov/ij/ **1997-2004.**

[31] Wyatt, P. J. Light scattering and the absolute characterization of macromolecules. *Anal. Chim. Acta* **1993**, *272*, 1-40.

[32] Arleth, L.; Xia, X.; Hjelm, R. P.; Wu, J.; Hu, Z. Volume transition and internal structures of small poly(N-isopropylacrylamide) microgels. *J. Polym. Sci. B* **2005**, *43*, 849-860.

[33] Wu, C. A comparison between the 'coil-to-globule' transition of linear chains and the \"volume phase transition\" of spherical microgels. *Polymer* **1998**, *39*, 4609-4619.

[34] Jiang, P.; Bertone, J. F.; Hwang, K. S.; Colvin, V. L. Single-Crystal Colloidal Multilayers of Controlled Thickness. *Chem. Mater.* **1999**, *11*, 2132-2140.

[35] Pelton, R. H. Polystyrene and polystyrene-butadiene latexes stabilized by poly(N-isopropylacrylamide). *J. Polym. Sci. A* **1988**, *26*, 9-18.

[36] Pelton, R. Temperature-sensitive aqueous microgels. *Adv. Colloid Interface Sci.* **2000**, *85*, 1-33.

[37] Gates, B.; Park, S. H.; Xia, Y. Tuning the photonic bandgap properties of crystalline arrays of polystyrene beads by annealing at elevated temperatures. *Adv. Mat.* **2000**, *12*, 653-656.

[38] Sun, Z. Q.; Chen, X.; Zhang, J. H.; Chen, Z. M.; Zhang, K.; Yan, X.; Wang, Y. F.; Yu, W. Z.; Yang, B. Nonspherical Colloidal Crystals Fabricated by the Thermal Pressing of Colloidal Crystal Chips. *Langmuir* **2005**, *21*, 8987-8991.

[39] Griesebock, B.; Egen, M.; Zentel, R. Large Photonic Films by Crystallization on Fluid Substrates. *Chem. Mater.* **2002**, *14*, 4023-4025.

[40] Debord, J. D.; Lyon, L. A. Thermoresponsive Photonic Crystals. *J. Phys. Chem. B* **2000**, *104*, 6327-6331.

[41] Li, H.-L.; Marlow, F. Controlled Arrangement of Colloidal Crystal Strips. *Chem. Mater.* **2005**, *17*, 3809-3811.

[42] Gates, B.; Xia, Y. Fabrication and characterization of chirped 3D photonic crystals. *Adv. Mat.* **2000**, *12*, 1329-1332.

[43] Andersson, M.; Hietala, S.; Tenhu, H.; Maunu, S. L. Polystyrene latex particles coated with crosslinked poly(N-isopropylacrylamide). *Colloid Polym. Sci.* **2006**, *284*, 1255-1263.

[44] Tsuji, S.; Kawaguchi, H. Temperature-Sensitive Hairy Particles Prepared by Living Radical Graft Polymerization. *Langmuir* **2004**, *20*, 2449-2455.

[45] Tsuji, S.; Kawaguchi, H. Self-Assembly of Poly(N-isopropylacrylamide)-Carrying Microspheres into Two-Dimensional Colloidal Arrays. *Langmuir* **2005**, *21*, 2434-2437.

[46] Tsuji, S.; Kawaguchi, H. Effect of Graft Chain Length and Structure Design on Temperature-Sensitive Hairy Particles. *Macromolecules* **2006**, *39*, 4338-4344.

[47] Ohtsuka, Y.; Kawaguchi, H.; Sugi, Y. Copolymerization of styrene with acrylamide in an emulsifier-free aqueous medium. *J. Appl. Polym. Sci.* **1981**, *26*, 1637-47.

[48] Kawaguchi, H.; Sugi, Y.; Ohtsuka, Y. Copolymerization of styrene with acrylamide derivatives in an emulsifier-free aqueous medium. *J. Appl. Polym. Sci.* **1981**, *26*, 1649-57.

[49] Pardo, L.; Wilson, W. C., Jr.; Boland, T. Characterization of Patterned Self-Assembled Monolayers and Protein Arrays Generated by the Ink-Jet Method. *Langmuir* **2003**, *19*, 1462-1466.

[50] Xu, T.; Jin, J.; Gregory, C.; Hickman, J. J.; Boland, T. Inkjet printing of viable mammalian cells. *Biomaterials* **2004**, *26*, 93-99.

[51] Boland, T.; Xu, T.; Damon, B.; Cui, X. Application of inkjet printing to tissue engineering. *Biotech. Journal* **2006**, *1*, 910-917.

[52] Sele, C. W.; von Werne, T.; Friend, R. H.; Sirringhaus, H. Lithography-free, self-aligned inkjet printing with sub-hundred-nanometer resolution. *Adv. Mat.* **2005**, *17*, 997-1001.

[53] Kido, H.; Maquieira, A.; Hammock, B. D. Disc-based immunoassay microarrays. *Anal. Chim. Acta* **2000**, *411*, 1-11.

[54] Carter, J. C.; Alvis, R. M.; Brown, S. B.; Langry, K. C.; Wilson, T. S.; McBride, M. T.; Myrick, M. L.; Cox, W. R.; Grove, M. E.; Colston, B. W. Fabricating optical fiber imaging sensors using inkjet printing technology: A pH sensor proof-of-concept. *Biosensors & Bioelectronics* **2006**, *21*, 1359-1364.

[55] Ko, H.-Y.; Park, J.; Shin, H.; Moon, J. Rapid Self-Assembly of Monodisperse Colloidal Spheres in an Ink-Jet Printed Droplet. *Chem. Mater.* **2004**, *16*, 4212-4215.

[56] Wang, D.; Park, M.; Park, J.; Moon, J. Optical properties of single droplet of photonic crystal assembled by ink-jet printing. *Appl. Phys. Lett.* **2005**, *86*, 241114/1-241114/3.

[57] Park, J.; Moon, J.; Shin, H.; Wang, D.; Park, M. Direct-write fabrication of colloidal photonic crystal microarrays by ink-jet printing. *J. Coll. Interface Sci.* **2006**, *298*, 713-719.

[58] Park, J.; Moon, J. Control of Colloidal Particle Deposit Patterns within Picoliter Droplets Ejected by Ink-Jet Printing. *Langmuir* **2006**, *22*, 3506-3513.

[59] Okubo, T.; Kimura, K.; Kimura, H. Dissipative structures formed in the course of drying the colloidal crystals of monodispersed polystyrene spheres on a cover glass. *Colloid Polym. Sci.* **2002**, *280*, 1001-1008.

[60] Okubo, T.; Yamada, T.; Kimura, K.; Tsuchida, A. Drying dissipative structures of the deionized aqueous suspensions of colloidal silica spheres ranging from 29 nm to 1 mm in diameter. *Colloid Polym. Sci.* **2005**, *283*, 1007-1015.

[61] Okubo, T. Sedimentation and drying dissipative structures of colloidal silica (1.2 mm in diameter) suspensions in a glass dish and a polystyrene dish. *Colloid Polym. Sci.* **2006**, *284*, 1395-1401.

[62] Okubo, T.; Itoh, E.; Tsuchida, A.; Kokufuta, E. Drying dissipative structures of the thermosensitive gels of poly(N-isopropyl acrylamide) on a cover glass. *Colloid Polym. Sci.* **2006**, *285*, 339-349.

[63] Mathur, A.; Brown, A.-D.; Erlebacher, J. Self-Ordering of Colloidal Particles in Shallow Nanoscale Surface Corrugations. *Langmuir* **2006**, *22*, 582-589.

[64] Schnall-Levin, M.; Lauga, E.; Brenner, M. P. Self-Assembly of Spherical Particles on an Evaporating Sessile Droplet. *Langmuir* **2006**, *22*, 4547-4551.

[65] Socol, Y.; Guzman, I. S. Fast Ring-Shape Self-Assembling in Water-Based Ink-Jetted Droplets. *J. Phys. Chem. B* **2006**, *110*, 18347-18350.

CHAPTER 5

CHARACTERIZATION OF POLY(STYRENE-*CO*-*N*-ISOPROPYLACRYLAMIDE) CORE/POLY(*N*-ISOPROPYLACRYLAMIDE) SHELL MICROPARTICLES AND THEIR COLLOIDAL CRYSTAL ASSEMBLIES

5.1 Introduction

Spherical, microparticle building blocks that possess both hard and soft polymeric properties have proven useful in the design and function of colloidal crystals, as exemplified by the pS-*co*-NIPAm microparticles discussed in the previous chapter. Fortunately, those particular particles exhibited an ideal combination of hard and soft characteristics derived from a distinct copolymer synthesis to yield particles that possessed a deformable exterior when wet and structural integrity when dry, which afforded crystalline self-assembly and stability.

Typically, our group's efforts to achieve microparticles that possess multiple properties are realized using a core/shell architecture.[1-5] Some groups have even applied this core/shell construct to provide specific properties that influence the self-assembly and properties of colloidal crystals.[6-9] In this chapter, an investigation of this core/shell design will be discussed, whereby different types of shells composed primarily of pNIPAm were added to some of the pS-*co*-NIPAm core particles discussed in Chapter 4 for the purposes of creating particles with additional functionalities that can be used for the self-assembly of colloidal crystals for a variety of applications.

Since colloidal crystals formed using thermoresponsive pNIPAm-only particles are not stable and lose their order upon drying, the objectives of this shell addition were twofold: to add a hydrogel shell to the hard pS-*co*-NIPAm core particles that 1) possesses

thermoresponsivity for the purposes of thermo-switchable crystalline self-assembly and 2) contains *functionality* that can yield inter-particle cross-links (located at the particle exterior) to afford crystalline stability during drying. The final structural stability would then be realized by the increased particle integrity achieved by the hard pS-*co*-NIPAm core, as illustrated by Figure 5.1. To achieve particle functionality, acrylic acid was included in two of these pNIPAm shell syntheses to provide a carboxylic acid group that would be available for the addition of cross-linking moieties. Although particular cross-linking strategies were not explored extensively in this project, the utilization of such functional groups could be examined in the future. Nevertheless, the ability to add functional groups using this stepwise core/shell synthesis demonstrates its potential as a design tool for the production of useful crystal building blocks. The following study primarily investigates the synthesis and characterization of these core/shell microparticles, as well as their application as thermoresponsive building blocks for colloidal crystal self-assembly. Large particle sizes were investigated so that colloidal crystals that exhibited infrared diffraction could be fabricated for the purposes of producing stealthy, optical tags.

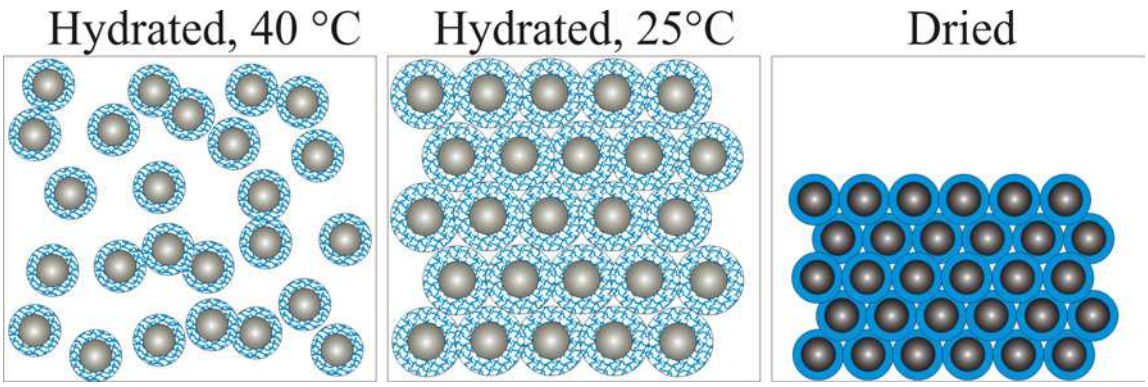

Figure 5.1 Formation of stable colloidal crystals via thermal annealing. Left: deswollen core/shell particles. Center: Colloidal crystal composed of swollen core/shell particles. Right: dried crystal depicting dehydrated shell and dense cores, which assist in maintaining crystal stability.

5.2 Experimental Section

5.2.1 Particle Synthesis

Materials

The materials used in this chapter are listed in the Experimental Sections of Chapters 2, 3, and 4.

Shell Synthesis

Thermoresponive pNIPAm shells were added to some of the pS-*co*-NIPAm cores (Chapter 4) using a similar "seed and feed" synthesis technique as described in Chapter 2. The initial methodology to construct stable crystals using core/shell microparticles included the addition of a functional group to the shell that would allow for covalent interparticle crosslinking after crystallization so that the particles would not disorder during drying. For this purpose, AAc was added as a comonomer in most of these shell syntheses, which provides a carboxylic acid functional group that can be used to covalently attach moieties that possess amine groups through EDC and DCC coupling.[10,11] One potential cross-linking route would be to use the AAc to couple 4-amino-benzophenone to the particle exterior to allow for photocrosslinking.[12-14]

For all of the pNIPAm shell syntheses (listed in Table 5.1), 50 mM total monomer concentration (TMC), containing 1 mol-% BIS, was used along with 0.015 mM Tween 80 and 1.0 mM APS for initiation (concentrations based on final reaction volume). For all syntheses, pS-*co*-NIPAm core particles (which were not cleaned and possessed the core synthesis stock concentration) were mixed with water and Tween 80 in a three-necked reaction flask (reaction set-up described previously), then heated to ~70 ˚C while purging with N_2 and stirring for at least 30 min. The NIPAm and BIS shell monomer were dissolved in water, and part (monomer-starved conditions for the 150-1 C/S AAc and 300-1 C/S AAc syntheses)[1] and or all (monomer flooded conditions for the 600-1

C/S synthesis)[15,16] of this solution was added to the core solution prior to initiation (amounts shown in Table 4.2). Acrylic acid (when used) was added just prior to initiation and constituted 10 mol-% of the total shell monomer. After initiation, the remaining amounts of the shell solution were added to the reaction at different times (at 10 min increments for 50 min for the 150-1 C/S AAc and 300-1 C/S samples). For the 600-1 C/S reaction, all of the shell monomer was added prior to initiation. The reaction times are listed in Table 5.1, and all of the core/shell samples were filtered and then cleaned by centrifugation after the synthesis was terminated (~45 min at 15,400 x *g* rcf at 25 ˚C).

Table 5.1 pNIPAm shell synthesis conditions using pS-*co*-NIPAm core particles.

Sample Name	Total Shell Monomer Concentration; mol-% (NIPAm:AAc:BIS)	Core Vol., mL	Water mL	NIPAm g	AAc g	Water for (Shell monomer) mL	Reaction Time
150-1 C/S AAc	50 mM (89:10:1)	20	67.5	0.5028	0.0357	Total: 10 (5 + 1*5)	4.5 hrs
300-1 C/S AAc	50 mM (89:10:1)	40	136	1.0108	0.0715	Total: 20 (10 + 2*5)	5 hrs
600-1 C/S	50 mM (99:0:1)	20	60	0.5643	N/A	Total: 20	5.5 hrs

5.2.2 Crystal Formation

Colloidal crystals were prepared using the thermoresponsive 150-1 C/S AAc, 300-1 C/S AAc, or 600-1 C/S core/shell particles via thermal annealing. Since lattice spacing between pNIPAm-type particles is dependent on the particle concentration, the polymer content was strictly monitored when preparing the suspensions for

crystallization, and, therefore, reported in terms of the percent polymer by weight (% wt), where

$$\% \, wt = \frac{grams \; of \;\; polymer}{\left(grams \; of \;\; polymer + grams \; of \;\; solvent\right)}. \qquad \text{(Eq 5.1)}$$

Accordingly, the polymer concentration of the stock solutions of particles was determined by freeze-drying a small, known volume of the stock solution for 24hrs (FreeZone 4.5, Labconco) and weighing the amount of resulting dried polymer. To prepare the samples, a known volume of the stock particles was centrifuged using pre-weighed centrifuge tubes, typically for ~15-30 min at 20,800 x *g* rcf at 25 ˚C. Upon forming a pellet, the supernatant was removed without disturbing the pellet, and the sample was re-weighed to determine the mass of the remaining polymer and solvent in the tube, so that the % wt of polymer could be determined (assuming that no polymer was extracted with the supernatant). Typically, these centrifuged samples possess a higher % wt than desired, in which case, water was added to the sample to dilute to the desired final % wt.

Sample cell compartments were prepared by sandwiching a chamber gasket (19 mm x 6 mm, 0.5 mm deep, Molecular Probes) between two glass cover slips (Fisher, 22 x 30 mm), as shown in Figure 5.2. The adhesive placed on the gasket during manufacturing was first removed by hand and the gaskets were soaked in ethanol to remove dirt and debris. One piece of Scotch tape was applied to each side of the gasket twice to transfer the tape adhesive to the gasket. Then, two cover slips were placed on either side of the sticky gasket and pressed together firmly using a cotton swab. This method was the best procedure to form a stable cell that exhibited no leaking, plus the gaskets could be easily reused by pulling the gasket out from the cover slips after soaking the cell in water.

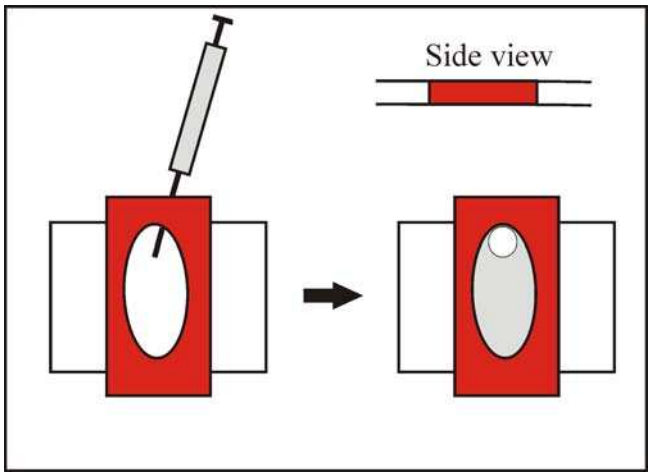

Figure 5.2 Sample cell used for thermal annealing of core/shell particles.

The suspensions of known % wt were heated to ~50 ˚C in a heating block (Temp-Blok, Lab-Line), making the suspension less viscous from the expulsion of water from the deswollen particles. The suspensions could then be made homogeneous by vortexing the sample. Hot samples were introduced to the sample cell by syringe injection through the rubber gasket. Typically, both the sample cell and the syringe were heated as well, to avoid any drastic drops in temperature that could make the sample more viscous. Because direct sample injection increases the pressure in the sample cell (which could cause leaks), a slight vacuum was made within the cell by extracting a small volume of air from within the chamber, prior to adding the sample. Once the sample was added, the pressure could be re-equilibrated by puncturing the gasket, once or twice, without pressing the plunger of the syringe. The sample cell was not completely filled with sample solution, allowing a small air bubble to exist in the cell. This was used to homogenize the sample by shaking it back and forth after heating to ensure low viscosity. The samples were placed on the heating block and covered with a plastic casing lined with glass wool to keep the samples insulated. After heating for about 15 min, the heating block was turned off, which provided a cooling rate slow enough to achieve crystalline self-assembly.

5.2.3 Characterization Techniques

Core/shell microparticles were characterized using photon correlation spectroscopy (PCS) and multi-angle laser light scattering (MALLS) to determine the particle hydrodynamic radius (R_h) and the radius of gyration (R_g), respectively. Detailed descriptions of these procedures can be found in Section 4.2.2. Additional methods were used for further characterization of the core/shell crystals:

Optical Microscopy

Differential interference contrast (DIC) images were acquired using an Olympus IX-70 inverted microscope using standard DIC optics.

Optical Spectroscopy

Reflectance spectroscopy was performed using a Cary 500 double beam scanning spectrophotometer (UV-VIS-NIR) operating in the spectral range: 175 nm – 3300 nm using an integrating sphere accessory and the accompanying WinUV software and Scan package, in collaboration with the Georgia Tech Research Institute (GTRI). A more accurate determination of reflectance intensity was obtained using this instrument compared to the Ocean Optics set-up in Section 4.2.2, by determining the specular reflectance (or "% Reflectance"),[17] which is found indirectly by subtracting the diffuse reflectance from the total reflectance (specular + diffuse) at near-normal incidence.

5.3 Results and Discussion

5.3.1 Core/Shell Microparticles

Hydrated particles sizes of the core/shell particles were determined using PCS (Table 5.2) at temperatures of 25 ˚C and 40 ˚C to assess particle thermoresponsivity, since these particles contain principally pNIPAm in the shell. For comparison, the

particles sizes of their constituent core particles are also shown. Since the presence of AAc (pK_a ~4.25)[18] in the shell polymer introduces pH responsivity, which impacts the hydrogel swelling, formate buffer (pH 3.5; 10 mM ionic strength) was used to prepare samples of these particles for PCS characterization. Non-buffered, aqueous solvent was used for all other samples.

Table 5.2 Hydrated particle sizes for core and core/shell particles acquired using PCS. (Standard deviations (±) for each measurement are shown in parentheses).

Sample	R_h @ 25 ºC, nm	R_h @ 40 ºC, nm	Volume Decrease, (PCS @ 25 ºC vs.PCS @ 40 ºC)
150-1 Core	91 (± 1)	89 (± 1)	7%
150 C/S AAc	417 (± 7)	242 (± 1)	81%
300-1 Core	123 (± 1)	122 (± 1)	4%
300-1 C/S AAc	297 (± 4)	151 (± 1)	87%
600-1 Core	229 (± 2)	176 (± 1)	55%
600-1 C/S	318 (± 6)	206 (± 2)	73%
600-2	273 (± 4)	200 (± 2)	61%

Since all of the core/shell samples demonstrated thermoresponsivity, these particles were used to make crystals via thermal annealing. As discussed in the previous section, the 150-1 and 300-1 pS-*co*-NIPAm core particles do not exhibit a significant temperature-dependent size variation. Understandably, the 150-1 C/S AAc and the 300-1 C/S AAc core/shell particles possessed a larger particle size compared to the particle size

of their corresponding cores at both high and low temperatures, indicating that this dense core structure is maintained. These types of core/shell particles may then serve as potential candidates to offer crystalline stability upon drying, since they still possess some degree of core structural integrity (Figure 5.1).

It is worth noting that even though similar amounts of shell monomer and core solution were used for the shell syntheses of the 150-1 C/S AAc and 300-1 C/S AAc particles (50 mM TMC), a considerable increase in shell volume (~3 times larger) was found for the hydrated 150-1 core/shell particles at 25 ˚C compared to the 300-1 C/S AAc particles at 25 ˚C. The reason for this discrepancy is due to the variability between the numbers of core precursor particles available in the given volumes of core solution. Larger shell monomer concentrations were examined using the same amount of "seed" particles. A 60 mM pNIPAm shell (10 mol-% AAc, 1 mol-% BIS) was added to 150-1 pS-*co*-NIPAm cores and a 70 mM (10 mol-% AAc, 1 mol-% BIS) shell was added to 300-1 pS-*co*-NIPAm core particles. However, this additional shell monomer in solution produced particles with slightly higher polydispersity than the corresponding core/shell samples described above, resulting in ineffective crystal assembly. Fortunately, the initial shell syntheses described above provided particles with shells of appropriate thickness to achieve crystals using thermal annealing procedures. Consequently, the synthesis conditions for the shell addition should be considered when fabricating core/shell particles for the purposes of crystalline assembly, by adjusting the amounts of core precursor particles or by using different amounts of shell monomer. Although the pNIPAm core/shell particles described in this chapter possessed shell thicknesses that were suitable for self-assembly, increases in the thickness of such a flexible, hydrogel shell may cause increased instability of the crystals composed of these core/shell particles due to shell deformation during the final drying step, as depicted in Figure 3. Hydrated core/shell particles that have a small shell thickness may deswell to an appropriate size upon drying to retain long-range order (top graphic). If the thickness is too large, order

may become disturbed during drying due to the increased magnitude of hydrogel shell shrinkage (bottom graphic), although some short-range order may exist as depicted by templating at the interface with the substrate. This type of mutual localized order and disorder was found for the 600-1 and 600-2 particles for the dried samples described in Chapter 4.

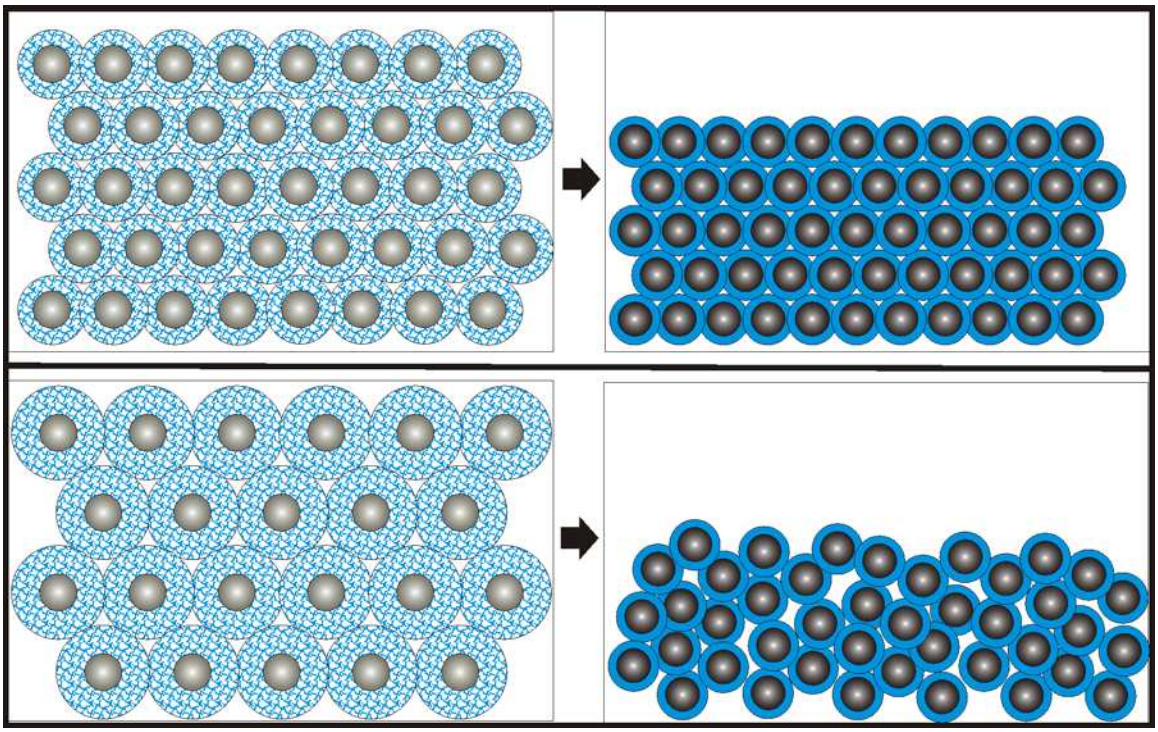

Figure 5.3 Implications of shell thickness upon crystal drying. Top graphic: illustration of core/shell particles possessing a moderate shell thickness that can maintain long-range order upon drying. Bottom graphic: illustration of particles with a large shell thickness that predominantly result in particle disorder upon drying due to considerable shifts in particle position.

As discussed in Section 4.4, unlike the other pS-*co*-NIPAm core particles, the 600-1 and 600-2 core particles displayed thermoresponsivity. This quality may be due to the comparatively large absolute amounts of NIPAm used in these particular core syntheses, since acrylamides have been shown to be more reactive than styrene in similar

syntheses using emulsion polymerization[19] and there may be some degree of phase separation between the hydrophobic polystyrene and the hydrophilic pNIPAm.[20-22] Although these cores did not form well-ordered crystals while drying these particles under ambient conditions, these cores were investigated as components for colloidal crystals because of their thermoresponsive properties. Interestingly, the deswollen 600-1 C/S particles at 40 ˚C achieve a size smaller than the swollen 600-1 cores at 25 ˚C (unlike the 150 C/S AAc and 300-1 C/S AAc core/shell particles, which consist of rather dense, non-thermoresponsive cores). This mechanical feature is consistent with core/shell particles that possess thermoresponsive core and shell regions.

Figure 5.4 illustrates the temperature dependent volume phase transition for the 150-1 C/S AAc and 300-1 C/S AAc particles, using a buffered solution (pH = 3.5). The range of this volume phase transition appears very broad compared to the sharp transition usually observed for cross-linked, pNIPAm homopolymer particles (Chapter 1).

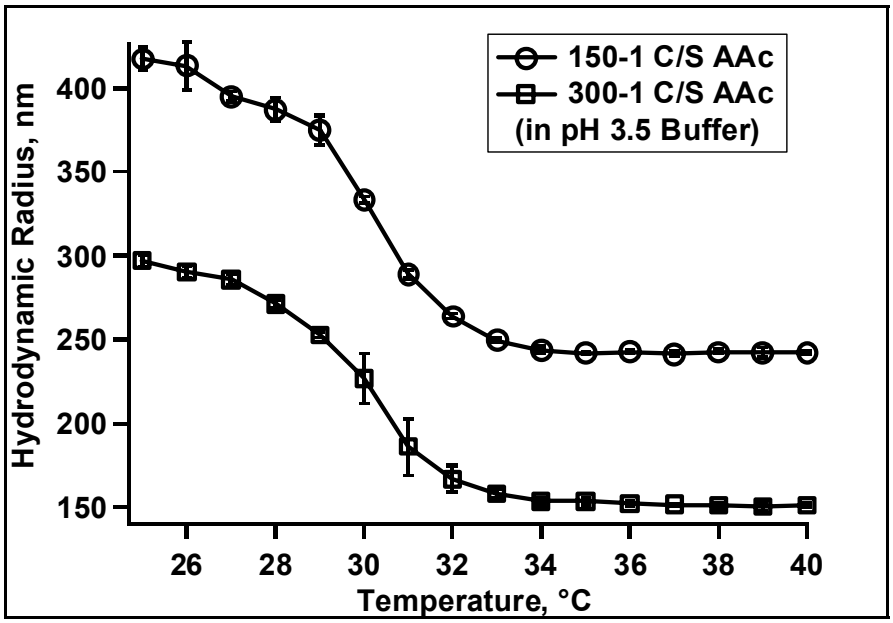

Figure 5.4 Temperature dependent changes in particle size: 150-1 C/S AAc and 300-1 C/S AAc.

Figure 5.5 demonstrates the phase transition for the 600-1 C/S particles, as well as the transitions for the 600-1 and 600-2 core particles. Again, all of these volume phase transitions are broad compared to typical pNIPAm particles.

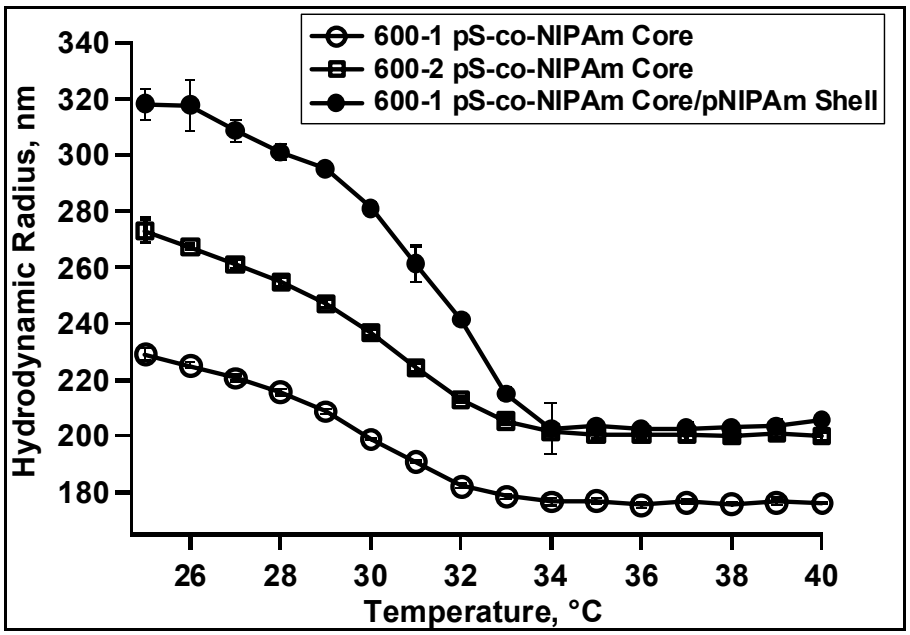

Figure 5.5 Temperature dependent changes in particle size: 600-1 and 600-2 Cores and 600-1 C/S.

Let us first consider the volume phase transitions for the 600-1 and 600-2 core particles. Since the 600-1 and 600-2 core particles were formed using a copolymer synthesis (adding styrene and NIPAm together), the particularly broad transitions may be due to these polymer blends forming complex, interpenetrating polymer networks, with varying degrees of phase separation. Conversely, the volume phase transitions for the core/shell particles appear somewhat sharper than the transitions for the 600-1 and 600-2 cores. This overall sharp transition is probably due to the rather thick, distinct pNIPAm shell,[23,24] although some interpenetration could be occurring at the interface of the soft

shell and the denser core polymer,[25] since curve breadth is maintained for the curve of the core/shell particles, compared to pNIPAm-only particles.

The pNIPAm shell addition to the 600-1 Core particles was also characterized using MALLS to determine the radius of gyration (R_g). Table 5.3 shows the values of these measurements along with the radius of hydration (R_h) and the ratio of R_g to R_h, including comparisons to values found for 2% BIS cross-linked pNIPAm particles.

Table 5.3 Comparisons of radius of gyration to radius of hydration for pNIPAm-type particles.

Sample	DLS: R_h @ 25 ˚C	MALLS: R_g @ 25 ˚C	R_g/R_h
2% BIS, pNIPAm	111 (± 1)	81.3 (0.2%)	0.74
600-1	229 (± 2)	127.3 (0.2%)	0.56
600-1 C/S	318 (± 6)	133.9 (0.3%)	0.42

As discussed previously, a sphere of uniform density yields an R_g/R_h ratio of 0.775.[26] The R_g/R_h value for the pNIPAm homopolymer particles corresponds with this uniform sphere structure, which has also been demonstrated by other groups.[27,28] Core/shell particles consisting of pNIPAm as the main monomer component for both the core and the shell also possess similar qualities of a sphere (Chapter 2). Some of the non-thermoresponsive pS-*co*-NIPAm particles that were presented in Section 4.3.1 also demonstrate these characteristics of a uniform sphere. However, the R_g/R_h for the 600-1 cores is considerably less and the R_g/R_h for the 600-1 C/S particles is even lower. Since R_g is a function of radial mass distribution (or polymer chain segment density), the lower R_g/R_h value for the 600-1 core particles indicates that a larger polymer mass exists closer

to the particle center. Consequently, this measurement may indicate some degree of phase separation for the 600-1 core particles, whereby the less-dense pNIPAm hydrogel network extends farther into the aqueous media, yielding a relatively larger apparent R_h. For the 600-1 C/S particles, this considerably lower R_g/R_h again follows from this radial mass distribution, since only a lightly cross-linked shell has been added (yielding two distinct polymeric regions), with most of the polymer mass still contained within the core. From these results, it is evident that the examination of R_g/R_h can be utilized to semi-quantitatively characterize the polymeric structural properties of these particles.

Even though it has been suggested that the hard and soft properties of pS-*co*-NIPAm particles may be due to phase separation (as discussed in Chapter 4), it is still difficult to obtain a clear understanding of the exact polymer composition of the particle that explains the apparent localization of polymer flexibility at the exterior. Nevertheless, these particular studies of the comparisons R_g/R_h may provide more insight as to the distribution of polymer mass.

5.3.2 Core/Shell Crystals

Crystals composed of different % wt of polymer were prepared using the thermoresponsive particles listed in Table 5.1, using thermal annealing procedures. Since these crystals are composed of swollen particles, the resulting crystals will be referred to as "wet crystals" as opposed to the dry crystals considered in Chapter 4. Observations using optical microscopy can yield an initial indication of particle order. Figure 5.6 demonstrates the long-range order found for a crystal fabricated using 300-1 C/S AAc particles via thermal annealing (left image). The bright spots that correspond to individual core/shell particles can be easily observed (right image), since they have a rather large particle size and because the polystyrene copolymer in the core contributes to a larger refractive index contrast with the surrounding aqueous media. These particles are also distinguishable from each other, owing to a markedly darker region between

neighboring bright spots. This observation may be due to a combination of both the low weight percent of polymer used for this sample (as observed with crystals composed of pNIPAm particles[29]) as well as the refractive index contrast between the core and the shell (*vide infra*).

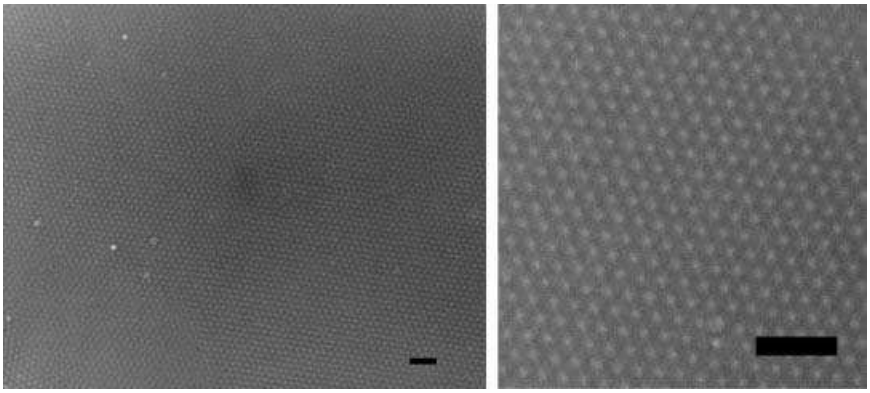

Figure 5.6 Optical microscopy images of crystal formed with 300-1 C/S AAc particles, 1.0 % wt. (right image: zoom-in image from image at left). Scale bar = 1 μm.

Reflectance spectroscopy was used to determine the Bragg diffraction wavelength and reflectance intensities of the wet crystals formed using the core/shell particles (Figure 5.7). The peak wavelengths ranged from the visible/near-IR region to well into the IR region, which was encouraging for the objectives of producing stealthy, optical tags.

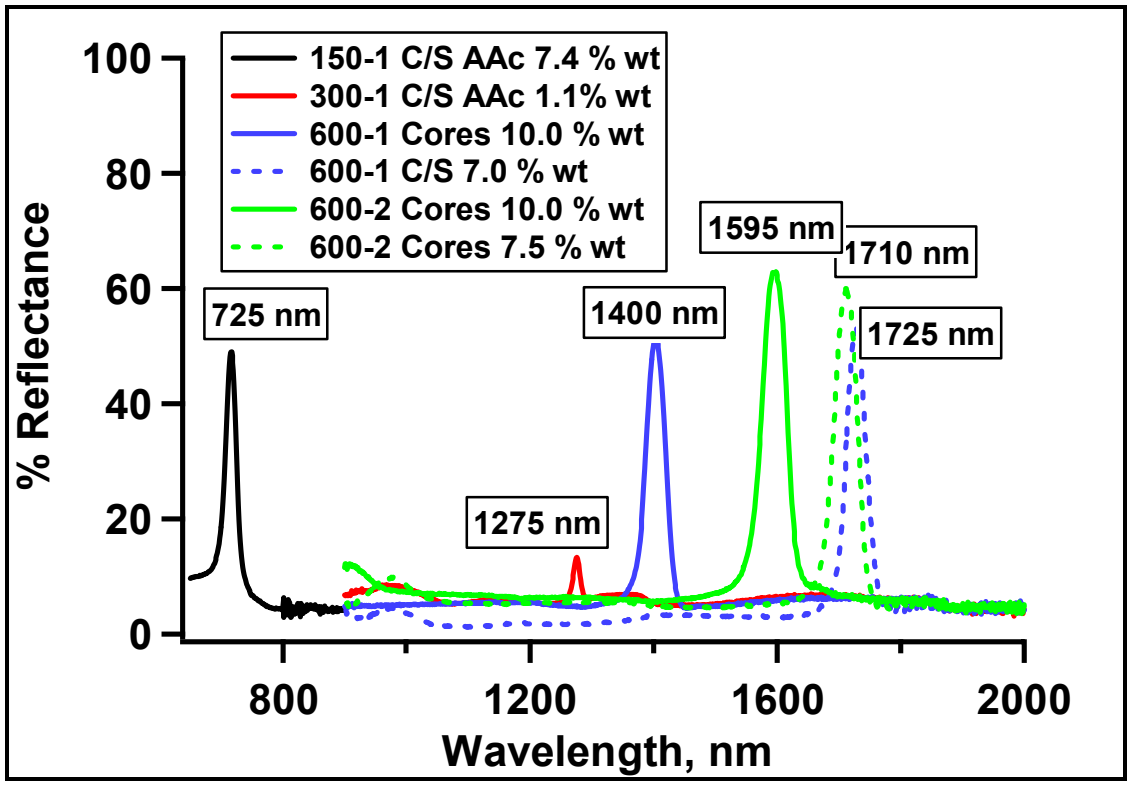

Figure 5.7 Reflectance measurements of crystals prepared using thermoresponsive core and core/shell particles.

Since these observed peaks are a function of the center-to-center distance between particles (from Bragg's Law), the spectra demonstrate the variability in the diffraction wavelength that can be achieved by changing the particle size, either by using thermoresponsive core/shell particles of different sizes or by varying the concentration (% wt) of the polymer, as demonstrated in other works.[29-32] The wavelengths were easily tuned by varying the polymer % wt, as shown for the 600-2 Core samples. Additionally, when acrylic acid is used in the shell, the particle spacing can be varied by adjusting the pH to change the shell thickness.

In most cases, the Bragg diffraction exhibited intensity peaks that were high above the baseline (40-65%). This high signal intensity arises from the increased refractive index contrast provided by the polystyrene (since hompolymer polystyrene latexes typically possess a refractive index of ~1.5-1.6).[33] Similar crystals formed using

large pNIPAm hydrogels showed reflectance of no more than 30% above the baseline (data not shown). This limit is probably due to the fact that as hydrogels, the pNIPAm particles are nearly refractive index matched with water.

As mentioned in Chapter 1, photonic materials that offer large contrasts in their refractive indices can provide more efficient components for optical devices by reducing losses in light intensity. For colloidal crystals, the diffraction wavelength is also a function of this refractive index of the crystal, as determined by Bragg's law, as discussed in Chapter 1. The effective refractive index for a crystal is given by weighted sum of the individual components[33,34] given by,

$$n_{eff} = \sum_{a=1}^{\infty} n_a \cdot \phi_a \,, \qquad \text{(Eq 5.2)}$$

where n_{eff} is the effective refractive index of the sample, based on the refractive index of each component times the volume fraction (ϕ) of each component. For a colloidal crystal composed of pNIPAm particles,

$$n_{eff} = n_m(1-\phi) + n_p \cdot \phi \,, \qquad \text{(Eq 5.3)}$$

where n_p is the refractive index of the particle and n_m is the refractive index of the medium (in this case, n_m = 1.333 for water), and ϕ is the particle volume fraction. Since pNIPAm particles are water-swollen gels, they are nearly refractive index matched with the bulk water medium, and hence, there is very little refractive index contrast in pNIPAm colloidal crystals.[32,34,35] Therefore, pS-*co*-NIPAm core/pNIPAm shell particles

can provide an enhanced contrast as a direct result of their polymer composition, which can provide a means for controlling the optical properties of the resulting crystals.

Since the core/shell particles under investigation included acrylic acid in the shell, the refractive index contrast could be greatly augmented by adding TiO_2 nanoparticles, which can become bound to pendant acrylic acid groups.[36,37] The anatase form of TiO_2 possesses a refractive index of ~2.5, which would allow for a tremendous increase in RI contrast. However, previous studies by our group have suggested that the addition of TiO_2 must occur after crystallization, since this binding event tends to induce aggregation, preventing crystallization. This potential extension of this project could still be implemented by employing different versions of freestanding crystal films, wherein crystals have been stabilized prior to TiO_2 addition. This initiative is discussed further in Chapter 7.

5.3.3 Colloidal Crystal "Bar-code" Optical Tag

An infrared optical tag that possessed a bar-code format was considered using a wet crystal that exhibited Bragg diffraction at ~1550 nm. This particular wavelength is important to the optical communications industry and its magnitude is useful for the fabrication of stealthy, optical tags. A large crystal composed of 600-2 Core particles (~10% wt) was prepared via thermal annealing, using a crystal sample cell that employed a gasket larger than those previously used. The desired format was to obtain an "on/off/on/off" configuration, whereby the thermally annealed portion would serve as the "on" state. The proposed method for producing the "off" state was to heat a localized area of the crystal to cause particle deswelling, followed by immediate cooling to cause a loss of order by forming a kinetically trapped glassy state.[32] This localized heating was performed by applying a hot glass stirring rod to different regions of the crystal. This procedure produced an immediate change in the crystal diffraction colors along the length of this area. An infrared camera was employed to determine the reflectance changes in

the different regions. Figure 5.8 illustrates the differences in infrared intensity along the crystal using false-color imaging to show intensity changes of the IR reflection signal. The arrows indicate the position of the rod across the crystal sample.

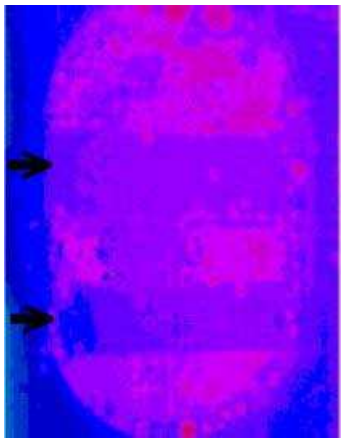

Figure 5.8 False-color image of a "bar-code" optical tag using pS-*co*-NIPAm core/pNIPAm shell particles. (Pink/purple region: low-intensity reflectance; Blue region: high-intensity reflectance).

Surprisingly, the blue region of the crystal (where the hot stirring rod was applied) indicates higher reflectance intensity than the pink/purple region. This observation conflicts with the projected outcome since the region of heating/cooling was expected to be disordered and, thus, display no or at least a lower reflectance intensity than the non-heat-treated region. A further investigation of the crystal using reflectance spectroscopy showed that the heated/cooled portion exhibited a narrow diffraction peak at 1566 nm with a reflectance intensity of 81% compared to the diffraction of the non-heated region, which exhibited a broader peak at 1554 nm with an intensity of only 58%.

The origin of this difference may be due a temperature gradient effect that could have occurred during the heating process.[32,38] Since the glass rod was only applied to one side of the crystal sample cell, the particles at this surface would become the most

deswollen, whereas deeper-lying particles may have only partially deswollen or may not have deswelled at all. These latter particles may have caused a templating effect as the deswollen particles reswelled, and may have, in effect, "ironed out" any crystalline defects. This scheme would explain the narrowing of the diffraction peak in this heated region. The slight red shift in the diffraction wavelength may be due to increases in spatially varied lattice constants that have formed due to this gradient, such that particles in the heated/cooled region that were nearer to the glass surface cooled more quickly and were able to swell to larger degrees due to the localized increase in free volume.

5.4 Conclusions

Core/shell microparticles were prepared by the addition of a soft pNIPAm shell using hard, pS-*co*-NIPAm cores as precursor particles (or "seeds"). Such core/shell particles were found to be thermoresponsive, due to their lightly cross-linked, pNIPAm shell, which facilitates their use as building blocks for the fabrication of colloidal crystals. The optical properties of such crystals can be tuned by varying the shell thickness, polymer concentration, pH, or even temperature (as in the case of the "bar-code" optical tag). This particular core/shell construct also provides a large contrast in refractive index that can be beneficial for the manipulation of light, which is important property for producing high-quality optical materials. By adding particular functionalities to the shell, cross-linking techniques have been envisioned so that crystalline order can be maintained during the drying of these core/shell crystals, and the hard pS-*co*-NIPAm can provide structural support for the final stability. This design provides a useful strategy for the self-assembly of robust, optical materials.

References

[1] Jones, C. D.; Lyon, L. A. Synthesis and Characterization of Multiresponsive Core-Shell Microgels. *Macromolecules* **2000**, *33*, 8301-8306.

[2] Gan, D.; Lyon, L. A. Tunable Swelling Kinetics in Core-Shell Hydrogel Nanoparticles. *J. Am. Chem. Soc.* **2001**, *123*, 7511-7517.

[3] Gan, D.; Lyon, L. A. Synthesis and Protein Adsorption Resistance of PEG-Modified Poly(N-isopropylacrylamide) Core/Shell Microgels. *Macromolecules* **2002**, *35*, 9634-9639.

[4] Nayak, S.; Lee, H.; Chmielewski, J.; Lyon, L. A. Folate-mediated cell targeting and cytotoxicity using thermoresponsive microgels. *J. Am. Chem. Soc.* **2004**, *126*, 10258-10259.

[5] Nayak, S.; Lyon, L. A. Ligand-functionalized core/shell microgels with permselective shells. *Angew. Chem. Int. Ed.* **2004**, *43*, 6706-6709.

[6] Kalinina, O.; Kumacheva, E. A \"Core-Shell\" Approach to Producing 3D Polymer Nanocomposites. *Macromolecules* **1999**, *32*, 4122-4129.

[7] Kumaraswamy, G.; Dibaj, A. M.; Caruso, F. Photonic Materials from Self-Assembly of \"Tolerant\" Core-Shell Coated Colloids. *Langmuir* **2002**, *18*, 4150-4154.

[8] Wang, D.; Rogach, A. L.; Caruso, F. Composite Photonic Crystals from Semiconductor Nanocrystal/Polyelectrolyte-Coated Colloidal Spheres. *Chem. Mater.* **2003**, *15*, 2724-2729.

[9] Rugge, A.; Ford, W. T.; Tolbert, S. H. From a Colloidal Crystal to an Interconnected Colloidal Array: A Mechanism for a Spontaneous Rearrangement. *Langmuir* **2003**, *19*, 7852-7861.

[10] Hermanson, G. T. *Bioconjugate Techniques; 1st ed.*; Academic Press: San Diego, 1996; Vol. 1.

[11] Kim, J.; Singh, N.; Lyon, L. A. Label-free biosensing with hydrogel microlenses. *Angew. Chem. Int. Ed.* **2006**, *45*, 1446-1449.

[12] Dorman, G.; Prestwich, G. D. Benzophenone Photophores in Biochemistry. *Biochemistry* **1994**, *33*, 5661-73.

[13] Griep-Raming, N.; Karger, M.; Menzel, H. Using Benzophenone-Functionalized Phosphonic Acid To Attach Thin Polymer Films to Titanium Surfaces. *Langmuir* **2004**, *20*, 11811-11814.

[14] Matsukuma, D.; Yamamoto, K.; Aoyagi, T. Stimuli-Responsive Properties of N-Isopropylacrylamide-Based Ultrathin Hydrogel Films Prepared by Photo-Cross-Linking. *Langmuir* **2006**, *22*, 5911-5915.

[15] Jones, C. D.; Lyon, L. A. Dependence of Shell Thickness on Core Compression in Acrylic Acid Modified Poly(N-isopropylacrylamide) Core/Shell Microgels. *Langmuir* **2003**, *19*, 4544-4547.

[16] Jones, C. D.; Lyon, L. A. Shell-Restricted Swelling and Core Compression in Poly(N-isopropylacrylamide) Core-Shell Microgels. *Macromolecules* **2003**, *36*, 1988-1993.

[17] Koh, Y. K.; Wong, C. C. In Situ Monitoring of Structural Changes during Colloidal Self-Assembly. *Langmuir* **2006**, *22*, 897-900.

[18] Lide, D. R. *Handbook of Chemistry and Physics, 74th ed.*; CRC Press: Boca Raton, FL, 1994.

[19] Duracher, D.; Sauzedde, F.; Elaissari, A.; Perrin, A.; Pichot, C. Cationic amino-containing N-isopropylacrylamide-styrene copolymer latex particles. Part 1. Particle size and morphology vs. polymerization process. *Colloid Polym. Sci.* **1998**, *276*, 219-231.

[20] Pelton, R. Temperature-sensitive aqueous microgels. *Adv. Colloid Interface Sci.* **2000**, *85*, 1-33.

[21] Pelton, R. H. Polystyrene and polystyrene-butadiene latexes stabilized by poly(N-isopropylacrylamide). *J. Polym. Sci. A* **1988**, *26*, 9-18.

[22] Hellweg, T.; Dewhurst, C. D.; Eimer, W.; Kratz, K. PNIPAM-co-polystyrene Core-Shell Microgels: Structure, Swelling Behavior, and Crystallization. *Langmuir* **2004**, *20*, 4330-4335.

[23] Makino, K.; Yamamoto, S.; Fujimoto, K.; Kawaguchi, H.; Ohshima, H. Surface structure of latex particles covered with temperature-sensitive hydrogel layers. *J. Coll. Interface Sci.* **1994**, *166*, 251-8.

[24] Nakahama, K.; Fujimoto, K. Thermosensitive Two-Dimensional Arrays of Hydrogel Particles. *Langmuir* **2002**, *18*, 10095-10099.

[25] Andersson, M.; Hietala, S.; Tenhu, H.; Maunu, S. L. Polystyrene latex particles coated with crosslinked poly(N-isopropylacrylamide). *Colloid Polym. Sci.* **2006**, *284*, 1255-1263.

[26] Wyatt, P. J. Light scattering and the absolute characterization of macromolecules. *Anal. Chim. Acta* **1993**, *272*, 1-40.

[27] Arleth, L.; Xia, X.; Hjelm, R. P.; Wu, J.; Hu, Z. Volume transition and internal structures of small poly(N-isopropylacrylamide) microgels. *J. Polym. Sci. B* **2005**, *43*, 849-860.

[28] Wu, C. A comparison between the 'coil-to-globule' transition of linear chains and the \"volume phase transition\" of spherical microgels. *Polymer* **1998**, *39*, 4609-4619.

[29] Debord, S. B.; Lyon, L. A. Influence of Particle Volume Fraction on Packing in Responsive Hydrogel Colloidal Crystals. *J. Phys. Chem. B* **2003**, *107*, 2927-2932.

[30] Debord, J. D.; Lyon, L. A. Thermoresponsive Photonic Crystals. *J. Phys. Chem. B* **2000**, *104*, 6327-6331.

[31] Debord, J. D.; Eustis, S.; Debord, S. B.; Lofye, M. T.; Lyon, L. A. Color-tunable colloidal crystals from soft hydrogel nanoparticles. *Adv. Mat.* **2002**, *14*, 658-662.

[32] Lyon, L. A.; Debord, J. D.; Debord, S. B.; Jones, C. D.; McGrath, J. G.; Serpe, M. J. Microgel Colloidal Crystals. *J. Phys. Chem. B* **2004**, *108*, 19099-19108.

[33] Pan, G.; Sood, A. K.; Asher, S. A. Polarization dependence of crystalline colloidal array diffraction. *J. Appl. Phys.* **1998**, *84*, 83-86.

[34] Weissman, J. M.; Sunkara, H. B.; Tse, A. S.; Asher, S. A. Thermally switchable periodicities and diffraction from mesoscopically ordered materials. *Science* **1996**, *274*, 959-960.

[35] Hu, Z.; Lu, X.; Gao, J. Hydrogel opals. *Adv. Mat.* **2001**, *13*, 1708-1712.

[36] Liufu, S.; Xiao, H.; Li, Y. Adsorption of poly(acrylic acid) onto the surface of titanium dioxide and the colloidal stability of aqueous suspension. *J. Coll. Interface Sci.* **2005**, *281*, 155-163.

[37] Chibowski, S. Effect of functional groups of polyacrylamide and polyacrylic acid on their adsorption onto titania surface. *J. Coll. Interface Sci.* **1990**, *140*, 444-9.

[38] Jones, C. D.; Serpe, M. J.; Schroeder, L.; Lyon, L. A. Microlens Formation in Microgel/Gold Colloid Composite Materials via Photothermal Patterning. *J. Am. Chem. Soc.* **2003**, *125*, 5292-5293.

CHAPTER 6

SYNTHESIS OF LARGE POLY(STYRENE-*CO*-*N*-ISOPROPYLACRYLAMIDE) MICROPARTICLES BY DELAYED MONOMER ADDITION

6.1 Introduction

Many potential configurations can be employed to form arrays that possess refractive index periodicities for the purposes of manipulating light for optical applications.[1] The organization of spherical micro- and nanoparticles presents an especially attractive design for these types of materials as a result of their ability to adopt a variety of three dimensional, closely-packed arrangements that emulate the structures of atomic crystals.[2,3] Such crystals can be fabricated without difficulty using self-assembly procedures[4,5] and a variety of synthesis techniques are available to prepare particles that possess a range of sizes, which can be used to prepare crystals that exhibit specific optical properties.[6-10] Most efforts to achieve high-quality crystals using such particles typically explore different assembly methods. However, the specific functionalities that are particular to the particle's identity can additionally benefit the assembly process. Such particle characteristics can be introduced by including a specific comonomer directly into a polymer particle synthesis[11,12] or by utilizing the comonomer as a functional group to allow for post-polymerization modification of the particle. These types of approaches are not only advantageous for the purposes of producing crystal building blocks, but are also important for the production of functional colloidal particles for many other applications. Unfortunately, the production of many potentially useful types of polymer colloids is limited because the essential comonomers may disrupt the particle synthesis or can only be added in small amounts or else risk broad distributions in particle size.

Winnik and coworkers have found that specific comonomers, which have ordinarily caused problems when introduced to the polymer particle synthesis or can only be added in small amounts, could be incorporated into such colloids without disturbing the particle formation by using a two-stage synthesis technique.[13] In this approach, the additional comonomer is added to the synthesis during the particle growth stage, after the more sensitive nucleation stage is complete, which typically occurs at ~1% monomer conversion for styrene syntheses using dispersion polymerizations[14]. This method was successful for adding dyes,[15] crosslinkers,[13,16] and chain transfer agents[17,18] to polystytrene particles. In particular, they were also able to add greater amounts of polar monomers, such as carboxylic acid,[19] which have traditionally been more difficult to add directly to polystyrene syntheses in large concentrations.[8,20-23]

As discussed in Chapter 4, NIPAm monomer could be added directly to the emulsion polymerization of styrene to form poly(styrene-co-N-isopropylacrylamide) (pS-*co*-NIPAm) spherical microparticles with very narrow size distributions. These copolymer particles possessed both hard and soft polymeric properties and readily formed crystalline assemblies upon drying. Large amounts of monomer were utilized for the purposes of producing large pS-*co*-NIPAm particles that could be used to form dried crystals that yielded Bragg diffraction in the infrared region, so as to allow for the fabrication of stealthy, optical tags. In these cases, however, coagulum tended to form and the particles were found to be thermoresponsive. This thermoresponsive characteristic indicated the presence of excess pNIPAm, which yielded a more hydrogel-like composition that proved to be too flexible to allow for simple particle assembly by drying. Since the NIPAm comonomer has a significant impact on the particle characteristics, it is also possible that the addition of this more polar, hydrophilic comonomer affects the nucleation stage of particle formation due to its higher reactivity in aqueous media as a result of its hydrophilicity.[23-26]

In this chapter, the two-stage synthesis method for NIPAm addition is investigated by introducing the NIPAm monomer at different delay times during the emulsion polymerization of styrene. Samples of the growing particles were obtained throughout the course of the syntheses. Accordingly, the particle growth could be evaluated by determining the size of these particles, using photon correlation spectroscopy. The particles' ability to form robust, dried crystals via simple drying procedures was also evaluated by reflectance spectroscopy in an effort to determine which types of particle afforded the largest increases in diffraction wavelengths.

6.2 Experimental Section

6.2.1 Synthesis Strategies

Materials

The materials used in this chapter are listed in the Experimental Sections of Chapters 2 and 4.

Particles Synthesis

Large microparticles composed of poly(styrene-*co*-*N*-isopropylacrylamide) (pS-*co*-NIPAm) were prepared by emulsion polymerization, using either a batch or a delayed monomer addition method. Large total monomer concentrations (TMC) were employed (either 500 mM or 1000 mM, based on the total reaction volume) in an effort to produce large particles. All syntheses were prepared using 90 mol-% styrene and 10 mol-% NIPAm. These syntheses utilized a lower mole-% of NIPAm compared to the syntheses for the pS-*co*-NIPAm particles described in Chapter 4, so that the pNIPAm constituent would not impart excessive flexibility to the particles, which can result in a lack of particle order upon drying. Nevertheless, this 90:10 monomer ratio can be used to

achieve particles that possess similar hard and soft polymeric properties as found for pS-*co*-NIPAm particles.[23,27-29]

Although a cross-linking agent was used for the syntheses of the pS-*co*-NIPAm particles described in Chapter 4, no cross-linker was used in the synthesis of these particles, since the objective of the current investigation was to examine the effects of NIPAm on polystyrene particle synthesis. The decision to omit the cross-linker was predicated by the work of other groups who have also explored syntheses of styrene with NIPAm without the use of a crosslinker[23,27,29] and have even shown that NIPAm assists in stabilizing the growing polystyrene latex.[24,30] The Frisken group has also found that NIPAm possesses the ability to self-cross-link, even in syntheses that include hydrophobic monomers, such as stryene.[31]

The batch polymerization method was employed by adding all of monomer components together prior to initiation, and the delayed monomer addition method was performed by adding the NIPAm monomer at 30 min, 60 min, or 120 min after initiation. The amounts of the reactants used for the pS-*co*-NIPAm syntheses are shown in Table 6.1. The sample names correspond to the TMC for each synthesis and designate the delay time that was used for the NIPAm monomer addition or whether the NIPAm was added prior to initiation.

Table 6.1 Synthesis conditions for pS-*co*-NIPAm particles using batch or delayed monomer addition polymerization methods.

Sample Name	Styrene, mL	NIPAm, g	APS, g	Reaction Time
500-Batch	5.16	0.5671	0.0052	22 hrs
500-30	5.16	0.5660	0.0055	23.5 hrs
500-60	5.16	0.5683	0.0057	22 hrs
500-120	5.16	0.5665	0.0054	22 hrs
1000-Batch	10.31	1.1321	0.0053	21 hrs
1000-30	10.31	1.1334	0.0058	23.5 hrs
1000-60	10.31	1.1319	0.0054	21 hrs
1000-120	10.31	1.1320	0.0055	22 hrs

In all cases, a total volume of 100 mL of water was used. Styrene was added to ~90 mL of water in a three-necked, round-bottom flask equipped with a condenser, thermometer, and inlet for gas purging the water and the styrene emulsion was prepared by thorough stirring prior to heating. In all cases, NIPAm was dissolved in ~10 mL of water and filtered using a 0.2 ∝m filter to remove any dust particulates that could affect the particle nucleation stage.

In the case of batch polymerization, the NIPAm solution was also added to the styrene emulsion prior to heating. While stirring, this monomer solution was heated to ~70 ˚C while purging with N_2 for at least 30 min. Next, APS, dissolved in ~0.5 mL water, was added to initiate the polymerization. A small amount of APS was consistently used for all reactions (~0.25 mM APS, based on the total reaction volume), to produce relatively large particle sizes and so that all particles could be compared on the merits of the TMC of the reaction using the different methods of NIPAm addition. This same

procedure was used for the delayed monomer addition; however, the NIPAm monomer solution was added at the designated delay times after initiation. When the batch method was used, the solution generally became turbid within about 10 min after initiation. When the NIPAm monomer addition was delayed, the styrene polymerization typically became turbid at least 15 min after initiation.

To characterize the growing particles, ~2 mL aliquots of the reaction solution were obtained at different points in time during the synthesis. All aliquots of particles were cleaned three times by centrifugation to remove unreacted monomer or oligomeric species, using distilled, deionized water for resuspension of the pellet. Different centrifugation speeds and times were used due to differences in the particle sizes. In some cases, when aliquots were obtained early in the reaction, phase separation was observed after centrifugation due to a large amount of unreacted, hydrophobic styrene monomer. The particles visibly partitioned to this styrene phase producing an opaque film at the tops of the centrifugation tubes (given that styrene is less dense than water) and a large volume of clear solution underneath. In these situations, a small amount of ethanol was added to the centrifugation tube to promote styrene dispersion. Subsequent centrifugation resulted in the formation of an adequate pellet at the bottom of the tube, which could then be redispersed and recentrifuged using water alone, since a majority of the styrene monomer had been removed. After cleaning for a total of three times by centrifugation, these solutions were filtered using a 5 ∝m filter, since large aggregates sometimes formed during the reaction. The final product that was collected at the end of the reaction was filtered using a Whatman filter paper (No. 2) to remove any coagulum and cleaned three times by centrifugation.

Crystal Sample Preparation

Concentrated, aqueous suspensions of these pS-*co*-NIPAm particles, typically ranging between 5-65 mg/mL, were used for crystal fabrication via sample drying. Dried

crystals were prepared by spreading a drop of each suspension on a glass cover slip (VWR, 22 x 30 mm), to encompass an area of approximately 2 cm in diameter. The sessile drop was allowed to dry open to the atmosphere, which occurred after 60-90 minutes at ambient temperature. This sample preparation was used to prepare samples for reflectance spectroscopy characterizations.

6.2.2 Characterization Techniques

Photon correlation spectroscopy (PCS) and reflectance spectroscopy were respectively employed to characterize the particle size of the pS-*co*-NIPAm microparticles and the optical properties of their resulting colloidal crystals. The details of these procedures can be found in the experimental section of Chapter 4.

6.3 Results

6.3.1 Particle characterization

The hydrated pS-*co*-NIPAm particle size was determined for samples that were obtained at different points during the polymerization, as well as for the final product for the purposes of characterizing the particle growth over the course of the synthesis (Figure 6.1). Since this data was acquired at 25 ˚C, which is well below the volume phase transition temperature for pNIPAm, the particles exist in their swollen conformation. Particle size data is shown for syntheses that used 500 mM or 1000 mM TMCs using both batch and delayed monomer addition methods. Aliquots were removed at 3, 4, 6, 6.5, or 8 hrs after initiation and the reactions were ended between 21-24 hrs. Although samples were not taken at exactly the same times the trends in particle growth are easily observed in this plot. The scale bars represent ± one standard deviation about the average of three measurements. Indistinguishable scale bars are due to small standard deviation values that are hidden by the data point markers. It should be noted that the 500-30 and 500-120 reactions resulted in excessive aggregation prior to the end of the reaction, such

that the sizes for individual particles could not be determined. This result was probably due to an accumulation of coagulum on the stir bar, causing stirring to cease and causing the reaction to become unstable.

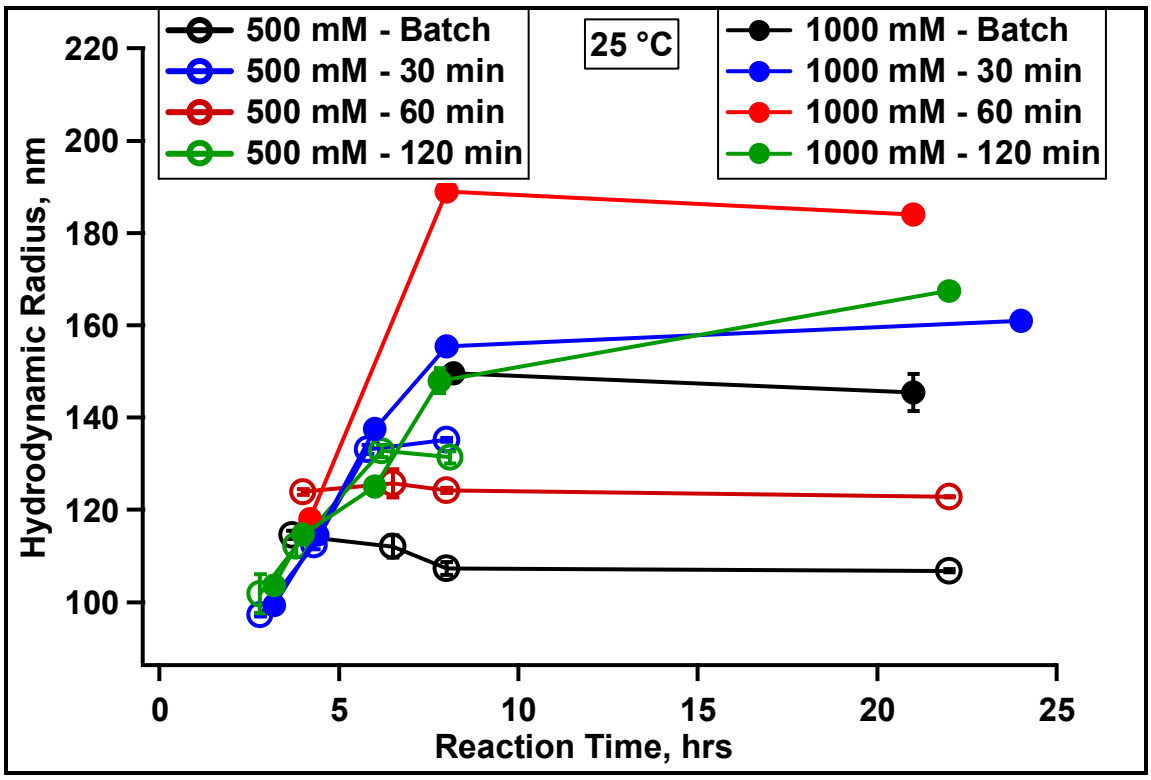

Figure 6.1 pS-*co*-NIPAm particle sizes obtained at different times during the reaction for the different 500 mM and 1000 mM TMC syntheses using batch and delayed monomer addition strategies. (Due to similarities in the particle sizes for samples that were collected at 3, 4, 6, 6.5, 8 hrs, the x-axis positions of the data points are offset slightly for clarity).

Particles that contain NIPAm as a constituent may be thermoresponsive due to the lower critical solution temperature of pNIPAm (~30.8 ˚C). This effect was evaluated for these pS-*co*-NIPAm particles using PCS at 40 ˚C. However, no significant change in particle size was found for all samples (data not shown).

6.3.2 Crystal Characterization

The capability of these particles to self-assemble to form crystal structures using simple drying procedures can be recognized by the presence of Bragg diffraction using reflectance spectroscopy. The optical properties can also indicate the dry particle size using Bragg's Law. Reflectance spectra were collected for crystals that were formed using the particles shown in Figure 6.1 to evaluate these qualities. Spectra for each of the dry samples that employed particles that were formed using syntheses with a 500 mM TMC are shown in Figure 6.2. The spectra in Figure 6.3 were obtained using the particles from syntheses where a 1000 mM TMC was employed. Each panel shows the spectra from dried samples using particles formed using the different synthesis strategies, which were collected at different times (as represented by different colors) for each of the different methods of monomer addition. Most of the spectra were collected by interrogating the tops of the dry samples. However, when dry samples were fabricated using particles that were formed early during the polymerization, the crystal showed more distinct spectra when the back of the sample was interrogated, which may indicate differences in the structural identity of the particles. Spectra obtained using these circumstances are labeled appropriately.

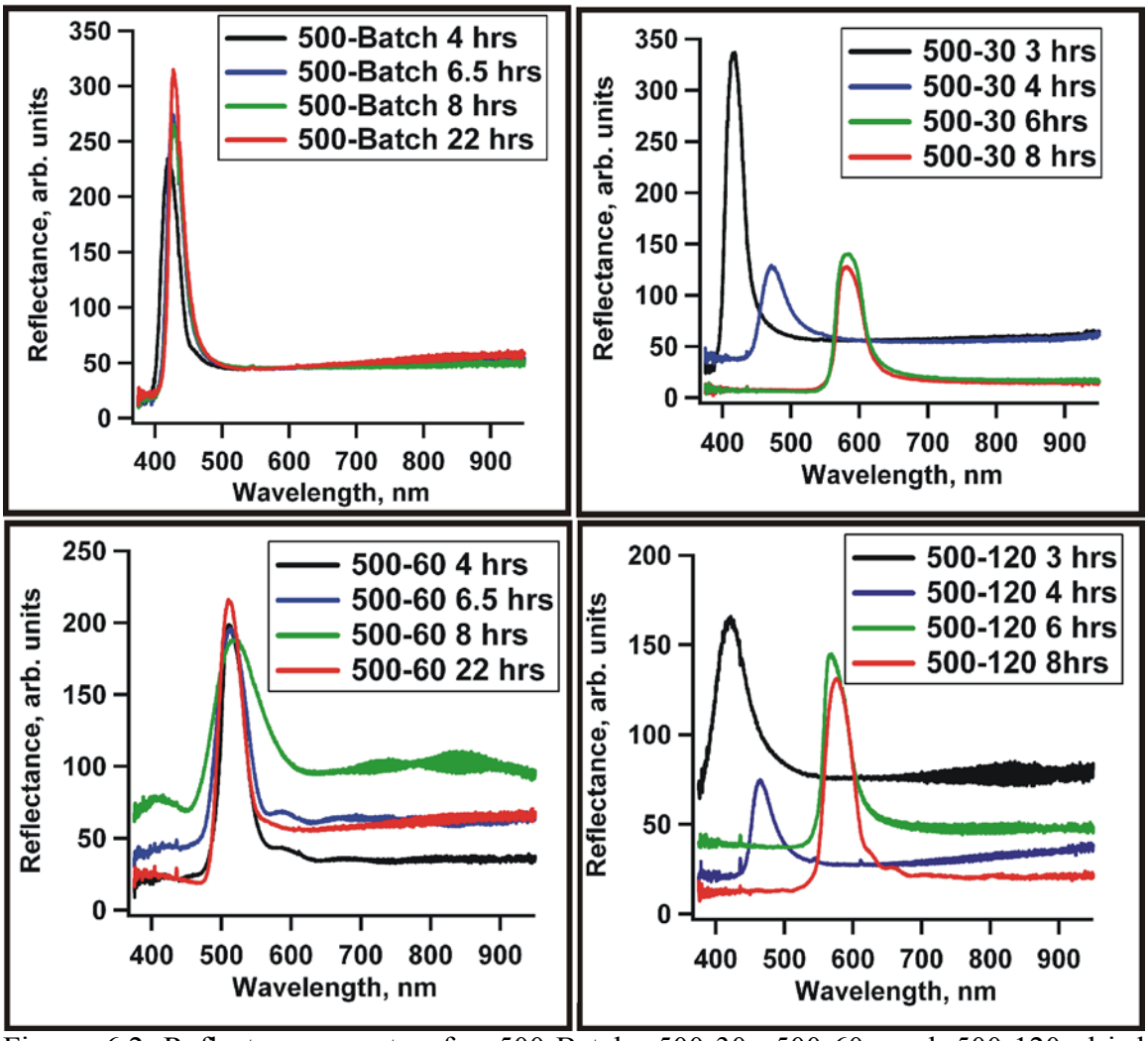

Figure 6.2 Reflectance spectra for 500-Batch, 500-30, 500-60, and 500-120 dried crystals. Particles that were obtained at different times during the reaction are depicted by curves of different colors.

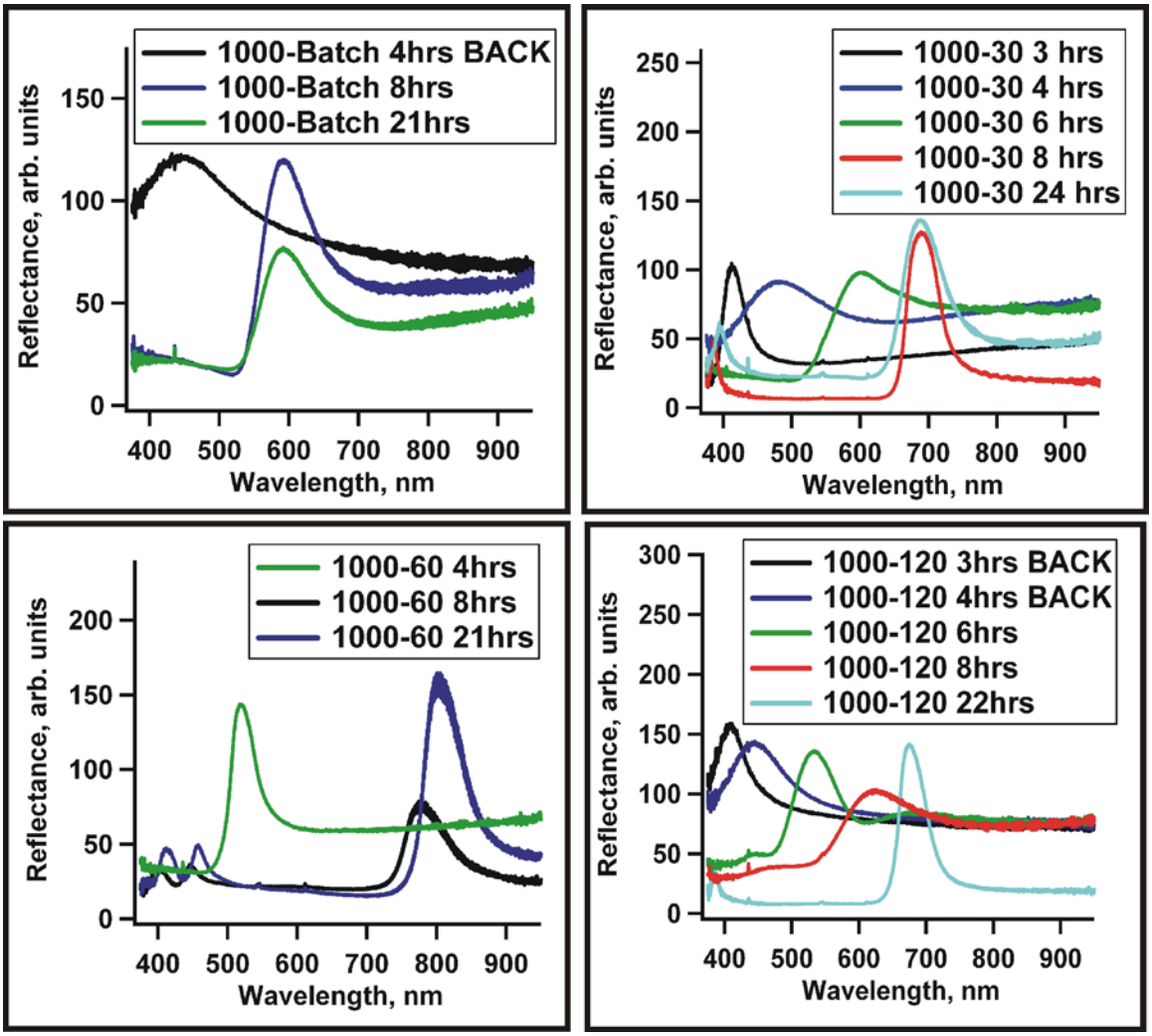

Figure 6.3 Reflectance spectra for 1000-Batch, 1000-30, 1000-60, and 1000-120 dried crystals. Particles that were obtained at different times during the reaction are depicted by curves of different colors.

6.4 Discussion

The data acquired using PCS at 25 °C demonstrate the increases in the pS-*co*-NIPAm particle sizes during the course of both batch and delayed monomer addition polymerization methods (Figure 6.1). Since the particles show no substantial change in size at 40 °C, the implementation of the 90:10 styrene to NIPAm ratio worked well to

avoid the production of particles with thermosensitivity. It is worth noting that thermoresponsivity was also not present when the NIPAm monomer was added at long delay times (120 min), which would have been the most likely candidate to show this property due to the possibility of concentrated pNIPAm homopolymer regions. Consequently, this result suggests that copolymer chains are still forming even at 2 hrs after initiation.

Figure 6.1 displays noticeable trends in particle growth, demonstrating an increase in the particle size over time until the particle size stabilizes, indicating reaction completion. For the 500 mM TMC reactions, the 500-Batch particles possess sizes similar to the 500-30, 500-60, and 500-120 reactions at early times during the synthesis, but remain comparatively small at later times in the synthesis as the particles formed by delayed monomer addition become larger over time. A similar result is found for the particles formed using the 1000 mM TMC. The final particle size for the 1000-Batch reaction is significantly smaller than the particles formed from the 1000-30, 1000-60, and 1000-120 reactions. These data indicate that particle growth may become hindered as a result of the presence of NIPAm during the nucleation stage or due to a prevalence of pNIPAm, since NIPAm has a higher reactivity than styrene. Continuous particle growth may be disrupted during batch polymerizations due to the poorer accessibility of styrene to swell a particle that is composed mainly of hydrophilic pNIPAm.[23,24,30,32] Surprisingly in quite a few cases (500-Batch, 500-60, 500-120, 1000-Batch, 1000-60), there is actually a slight decrease in the particle size at longer times. This effect may be due to some degree of phase separation occurring late in the copolymerization process.

Based on the swollen particle size, the largest particles for the 500 mM syntheses were formed using a 30 min delay time. The particle sizes for the 500-30, 500-60, and 500-120 reactions are fairly similar at 8 hrs after initiation. These delays suggest that the growing particles are relatively stable at the point of NIPAm addition, such that the NIPAm does not severely inhibit the particle growth and may even assist in stabilizing

the growing particle at that point in time. Although the 500-30 and 500-120 particles aggregated during the prolonged reaction time, the last comparison between the 500 mM reactions can be made at 8 hrs after initiation. The 500-30 particles achieved the largest size, with the 500-120 sample possessing a slightly smaller size. The 500-60 sample demonstrated the smallest particle size at 8 hrs among the particles formed using delayed monomer addition, and did not become any larger even at longer reaction times. These comparisons indicate that the particular delay time has a particular impact on the final particle size and, conceivably, on the final copolymer identity.

Similarly, the delay time also influenced the final particle size for the 1000 mM reactions, with the largest particles formed using a 60 min delay time. Compared to the 30 min delay that yielded the largest particle size for the 500 mM syntheses, this longer delay time required to form the largest particles using 1000 mM syntheses may be because longer times are needed for the formation of stable polystyrene precursor particles using such large initial monomer concentrations. As with the batch methods, introducing NIPAm too early in the particle formation may cause a non-ideal phase separation due to the higher degrees of NIPAm reactivity. Differences in the particle sizes using the different delay times may also be due to variations in the amounts of styrene monomer that remain at the point of NIPAm monomer addition.

The extent of potential phase separation may also vary due to the hydrophobic/hydrophilic character of the particles at different times. Pichot and coworkers have shown that phase separation may be restricted due to viscosity differences within the growing particle.[23] These conditions could affect the final hard and soft characteristics of the particles if there are larger degrees of localized homopolymer. Interestingly, the 1000-60 particles are much larger than the particles from both 1000-30 and 1000-120 syntheses at 8 hrs after initiation and actually become slightly smaller after >20hrs, whereas the 1000-30 and 1000-120 particles become slightly larger over time. These results demonstrate yet again that the timing of the presence of NIPAm has a

significant effect on particle growth and that the hydrophilic/hydrophobic interactions may have a significant impact on the particle characteristics over the course of the reaction.

It is important to note that although the particle sizes are different for the different types of reactions as well as for the different sampling times, these data represent the hydrated particle size. The optical properties of crystals formed by drying suspensions of these pS-*co*-NIPAm particles are dependent on the fully *dry* particles size, as discussed in Chapter 4. Bragg's Law tells us that the diffraction wavelength is dependent on both the refractive index and the particle lattice spacing. Because differences in the effective refractive index (which may only be slight since the same components are used in each synthesis) contribute to a lesser degree to the diffraction wavelength compared to the particle size, we can make correlations between the diffraction wavelength and the dry particle size. Any such estimates require the assumption that the particles adopt an fcc crystal structure (as were found for the dried pS-*co*-NIPAm crystals that were previously described in Chapter 4) and that the spectra are obtained at near-normal incidence.

The reflectance spectra for the samples indicate that crystals can be formed using simple drying procedures for all of the particles obtained from the 500 mM and 1000 mM reactions. The fabrication of crystals using this assembly process suggests that these particles possess similar hard and soft characteristics to the pS-*co*-NIPAm particles described in Chapter 4, which were derived from the same type of copolymer synthesis. In most cases, the Bragg diffraction peaks shifted to higher wavelengths as the hydrated particle size increased. This result also suggests that the dry particle size increases, since this shift in wavelength indicates that lattice spacing increases as the particles were obtained at later times during the synthesis. In some cases, the peak positions were found to stabilize, such that these crystals that demonstrated a constant diffraction wavelength. This result indicates that there is probably no significant change in dry particle size, in those cases.

In the cases where the hydrated particle size actually became smaller over time, the diffraction peaks did not exhibit a concomitant blue shift that would have been expected given a reduction in particle size, but instead these peaks also remained stable. For instance, PCS data demonstrates that the 500-Batch, 500-60, 1000-Batch, and 1000-60 particles became slightly smaller during the full extent of the reaction (ranging from a 3-7 nm decrease in hydrodynamic radius), but the diffraction wavelengths for their corresponding crystals do not change. These results indicate that although there may be differences in the polymeric architecture of these particles in their hydrated state, demonstrated by incongruities in particle size, the final dry particle size does not vary. In other cases where the hydrated particle size continued to become larger (1000-30 and 1000-120), the diffraction wavelength also remained stable. This result also suggests that these variations in the polymeric identity that occur later in the reaction for these syntheses probably contribute little to the final, dry particle size. Instead, the dry particle size is characterized mainly by events that occur earlier in the synthesis. Fortunately, these changes also do not affect the ability of these particles to self-assemble via drying.

In the cases for both 500 mM and 1000 mM total monomer syntheses, the lowest final diffraction wavelengths were found for crystals formed using the batch synthesis method. This result is consistent with the small hydrated particle sizes found for these same particles. Diffraction occurred at longer wavelengths using the delayed monomer addition methods and could be continuously red shifted using particles that were obtained at later times during the synthesis. These data suggest that the particles that possess a large size in the hydrated state particle also show a larger dry particle size, based on these continuous red shifts in diffraction wavelength. Therefore, these delayed monomer addition strategies can be used to enhance particle growth and the large particles sizes that are attained can influence the optical properties of the resulting crystals.

The longest diffraction wavelengths occurred for using a 30 min delay of NIPAm addition for the 500 mM syntheses (~580 nm) and a 60 min delay for the 1000 mM

syntheses (~800 nm). These results correspond to the observation that these particles also show the largest hydrated particle size. Since the longest diffraction wavelengths that could be attained for the 500-Batch and 1000-Batch syntheses occurred at ~430 nm and ~590 nm, respectively, the large shifts in Bragg diffraction found for the 500-30 and 1000-60 crystals demonstrate that these particular delayed monomer addition methods are useful for producing large, stable pS-*co*-NIPAm particles that can be used to form crystals with an improved range of optical properties. Although the greatest degrees of Bragg diffraction were obtained in the near-IR region, the knowledge gained from these synthesis methods is beneficial for further synthesis investigations to achieve even larger pS-*co*-NIPAm particles that could be used to fabricate dried crystals that exhibit IR diffraction.

6.5 Conclusions

Delayed monomer addition strategies were found to be useful for the preparation of large pS-*co*-NIPAm particles by adding the NIPAm monomer at different times after the initiation of the emulsion polymerization of styrene. By adding NIPAm later in the reaction, the polystyrene nucleation and initial particle growth stages remained stable and the subsequent copolymerization with NIPAm occurred more efficiently than the batch polymerization method to form large microparticles.

All of the particles could be used to form dried crystals via simple drying processes, suggesting that all of the particles possessed hard and soft polymeric characteristics that afforded particle self-assembly and stability. The optical properties of these dried samples varied based on the method of delayed monomer addition and the reaction times, which corresponded to changes in hydrated particle size. However, small changes in particle size that occurred towards the end of the synthesis did not affect the diffraction properties of the resulting crystals, which suggested that the dry particle size is characterized mainly by events that occur early in the synthesis. The diffraction

wavelengths of the resulting dried crystals were also found to be much higher than crystals formed from particles synthesized using batch polymerization methods. These results demonstrated that these innovative synthesis strategies are beneficial for the fabrication of the crystalline materials that possess desirable optical properties.

References

[1] Joannopoulos, J. D.; Villeneuve, P. R.; Fan, S. Photonic crystals: putting a new twist on light. *Nature* **1997**, *387*, 830.

[2] Clark, N. A.; Hurd, A. J.; Ackerson, B. J. Single colloidal crystals. *Nature* **1979**, *281*, 57-60.

[3] Gast, A. P.; Russel, W. B. Simple ordering in complex fluids: colloidal particles suspended in solution provide intriguing models for studying phase transitions. *Phys. Today* **1998**, *51*, 24-30.

[4] Xia, Y.; Gates, B.; Li, Z.-Y. Self-assembly approaches to three-dimensional photonic crystals. *Adv. Mat.* **2001**, *13*, 409-413.

[5] Norris, D. J.; Arlinghaus, E. G.; Meng, L.; Heiny, R.; Scriven, L. E. Opaline photonic crystals: How does self-assembly work? *Adv. Mat.* **2004**, *16*, 1393-1399.

[6] Stoeber, W.; Fink, A.; Bohn, E. Controlled growth of monodisperse silica spheres in the micron size range. *J. Coll. Interface Sci.* **1968**, *26*, 62-9.

[7] Pieranski, P. Colloidal crystals. *Contemporary Physics* **1983**, *24*, 25-73.

[8] Tseng, C. M.; Lu, Y. Y.; El-Aasser, M. S.; Vanderhoff, J. W. Uniform polymer particles by dispersion polymerization in alcohol. *J. Polym. Sci. A* **1986**, *24*, 2995-3007.

[9] Ober, C. K.; Lok, K. P.; Hair, M. L. Monodispersed, micron-sized polystyrene particles by dispersion polymerization. *J. Polym. Sci., Polym. Lett. Ed.* **1985**, *23*, 103-8.

[10] Ober, C. K.; Lok, K. P. Formation of large monodisperse copolymer particles by dispersion polymerization. *Macromolecules* **1987**, *20*, 268-73.

[11] Ganachaud, F.; Sauzedde, F.; Elaissari, A.; Pichot, C. Emulsifier-free emulsion copolymerization of styrene with two different amino-containing cationic monomers. I. Kinetic studies. *J. Appl. Polym. Sci.* **1997**, *65*, 2315-2330.

[12] Sauzedde, F.; Ganachaud, F.; Elaissari, A.; Pichot, C. Emulsifier-free emulsion copolymerization of styrene with two different amino-containing monomers: II. Surface and colloidal characterization. *J. Appl. Polym. Sci.* **1997**, *65*, 2331-2342.

[13] Song, J.-S.; Tronc, F.; Winnik Mitchell, A. Two-stage dispersion polymerization toward monodisperse, controlled micrometer-sized copolymer particles. *J. Am. Chem. Soc.* **2004**, *126*, 6562-3.

[14] Yasuda, M.; Seki, H.; Yokoyama, H.; Ogino, H.; Ishimi, K.; Ishikawa, H. Simulation of a Particle Formation Stage in the Dispersion Polymerization of Styrene. *Macromolecules* **2001**, *34*, 3261-3270.

[15] Song, J.-S.; Tronc, F.; Winnik, M. A. Monodisperse, controlled micron-size dye-labeled polystyrene particles by two-stage dispersion polymerization. *Polymer* **2006**, *47*, 817-825.

[16] Song, J.-S.; Winnik, M. A. Cross-Linked, Monodisperse, Micron-Sized Polystyrene Particles by Two-Stage Dispersion Polymerization. *Macromolecules* **2005**, *38*, 8300-8307.

[17] Song, J.-S.; Winnik, M. A. Monodisperse, micrometer-sized low molar mass polystyrene particles by two-stage dispersion polymerization. *Polymer* **2006**, *47*, 4557-4563.

[18] Song, J.-S.; Winnik, M. A. Monodisperse, Micron-Sized Reactive Low Molar Mass Polymer Microspheres by Two-Stage Living Radical Dispersion Polymerization of Styrene. *Macromolecules* **2006**, *39*, 8318-8325.

[19] Song, J.-S.; Chagal, L.; Winnik, M. A. Monodisperse Micrometer-Size Carboxyl-Functionalized Polystyrene Particles Obtained by Two-Stage Dispersion Polymerization. *Macromolecules* **2006**, *39*, 5729-5737.

[20] Yang, W.; Tao, Z.; Hu, J.; Wang, C.; Fu, S. Morphological investigations of polymer microspheres prepared by dispersion copolymerization. *Macromolecular Symp.* **2000**, *150*, 211-217.

[21] Yang, W.; Yang, D.; Hu, J.; Wang, C.; Fu, S. Dispersion copolymerization of styrene and other vinyl monomers in polar solvents. *J. Polym. Sci. A* **2001**, *39*, 555-561.

[22] Zhang, H.-T.; Huang, H.; Sun, R.; Huang, J.-X. Preparation of micron-size monodispersed PS/P(St/MAA) microspheres by seeded dispersion polymerization. *J. Appl. Polym. Sci.* **2006**, *99*, 3586-3591.

[23] Duracher, D.; Sauzedde, F.; Elaissari, A.; Perrin, A.; Pichot, C. Cationic amino-containing N-isopropylacrylamide-styrene copolymer latex particles. Part 1. Particle size and morphology vs. polymerization process. *Colloid Polym. Sci.* **1998**, *276*, 219-231.

[24] Pelton, R. Temperature-sensitive aqueous microgels. *Adv. Colloid Interface Sci.* **2000**, *85*, 1-33.

[25] Kawaguchi, H.; Hoshino, H.; Ohtsuka, Y. Preparation of amphoteric latex by modification of styrene-acrylamide copolymer latex. *J. Appl. Polym. Sci.* **1981**, *26*, 2015-22.

[26] Kawaguchi, H.; Sugi, Y.; Ohtsuka, Y. Copolymerization of styrene with acrylamide derivatives in an emulsifier-free aqueous medium. *J. Appl. Polym. Sci.* **1981**, *26*, 1649-57.

[27] Xiao, X.-C.; Chu, L.-Y.; Chen, W.-M.; Wang, S.; Xie, R. Preparation of Submicrometer-Sized Monodispersed Thermoresponsive Core-Shell Hydrogel Microspheres. *Langmuir* **2004**, *20*, 5247-5253.

[28] Yi, C.; Xu, Z. Synthesis and characterization of thermosensitive composite microsphere latex. *J. Appl. Polym. Sci.* **2005**, *96*, 824-828.

[29] Deng, Z. W.; Hu, X. X.; Li, L.; Xu, Z. S.; Yi, C. F. Self-assembled poly(styrene-co-N-isopropylacrylamide) film induced by capillary force. *J. Appl. Polym. Sci.* **2006**, *99*, 3514-3519.

[30] Pelton, R. H. Polystyrene and polystyrene-butadiene latexes stabilized by poly(N-isopropylacrylamide). *J. Polym. Sci. A* **1988**, *26*, 9-18.

[31] Gao, J.; Frisken, B. J. Influence of Secondary Components on the Synthesis of Self-Cross-Linked N-Isopropylacrylamide Microgels. *Langmuir* **2005**, *21*, 545-551.

[32] Hellweg, T.; Dewhurst, C. D.; Eimer, W.; Kratz, K. PNIPAM-co-polystyrene Core-Shell Microgels: Structure, Swelling Behavior, and Crystallization. *Langmuir* **2004**, *20*, 4330-4335.

CHAPTER 7

FORMATION OF ROBUST, TUNABLE CRYSTAL FILMS BY CROSS-LINKING OF POLY(STYRENE-*CO*-*N*-ISOPROPYLACRYLAMIDE) MICROPARTICLES

7.1 Introduction

In Chapter 4, the investigation of the synthesis and characterization of pS-*co*-NIPAm spherical microparticles demonstrated their significance as building blocks towards the fabrication of robust colloidal crystals. Simple drying of suspensions of these particles allowed for the fabrication of high-quality optical materials that could form defined patterns. The enhanced processability of these particles provides advantages for many applications. This attribute of the pS-*co*-NIPAm particles has been exploited to form advanced crystalline configurations, e.g. optical tags using a 2D barcode format, and to develop "photonic inks" by employing ink-jet printing deposition techniques. The fabrication and subsequent stability of such assemblies was attributed to the coexisting hard and soft qualities of the particle inherent to its copolymer identity.

However, the stability of such constructs depends upon the interparticle adhesions that are maintained in the dry state. Since this structure is a result of soft, polymeric linkages that consist of hydrogel components, the crystalline order can be easily disrupted by the introduction of aqueous solvent, which will redisperse the particles, resulting in a loss of optical properties and film dissolution. Although this imperfection may not be particularly detrimental when these crystals are used in a controlled environment, this factor limits their use in many potential applications. This shortcoming is unfortunate since stable colloidal crystals composed of hydrogels can offer unique advantages due to their fundamental permeability of their polymer networks, which is useful for sensor applications in liquid settings.

Many designs have been investigated to fabricate robust, three-dimensional colloidal crystals for optical applications that require stable materials. The goals of such approaches are to not only stabilize the particle order, but also to allow for tunability of the optical properties for the purposes of creating functional materials. Most fabrication methods that have been explored employ the introduction of some type of matrix between neighboring particles that, in effect, "glues" the particles together, affording stability of the preformed colloidal crystal. Polymerized colloidal crystal arrays (PCCA's) have been investigated extensively by the Asher group whereby a hydrogel polymer is used to "lock-in" the preexisting particle order, which preserves the optical properties of the colloidal crystal.[1-3] They have employed a variety of polymeric components and crystalline building blocks to increase the functionality of such optical materials.[4-7] The Xia group and others have also stabilized polystyrene or silica particles by infiltrating the crystal with an elastomer polymer matrix.[8-11] By swelling these assemblies using an organic solvent, the optical properties can be tuned. Such assemblies were recommended as constituents for the fabrication of photonic papers or inks. However, the crystal fabrication methods and the post-crystallization stabilizing procedures can be quite complex, since many ingredients and production steps are required.

Physical cross-linking between neighboring particles has also been a popular stabilization technique. One particular advantage to this approach is that no additional materials are necessary to establish robustness to the particle order, using only the functional characteristics of the particle to accomplish this interparticle cross-linking. One distinct design that has been explored to achieve this stability takes advantage of the glass transition temperature (T_g) of the particle's composition. By heating the crystal to temperatures near the T_g of its material components, the particles can effectively be melted together.[12-20] The subsequent changes in particle morphology provided by this interparticle sintering process can also offer a means to produce materials that possess different optical properties. Core/shell particle morphologies were also particularly useful

for producing stable crystals based on the T_g's of the discrete components.[19,20] Kumacheva and coworkers have applied this method to form stable structures composed of core/shell building blocks where the polymer shell possesses a lower T_g than that of the core.[19] In this way, crystals could be stabilized by annealing the samples at temperatures between T_g's of the core and shell to form a continuous, stable matrix around the sturdy core particles. This simple procedure can be employed to produce functional crystalline constructs based on the functional identities of the particle building blocks.[21,22] Although this methods is particularly useful for quick stabilization of the crystal based primarily on the particle identity, such structures tend to form a rigid framework that does not allow for the permeability required by many sensing platforms and other valuable optical materials where tuning of the optical properties is key.

This method of thermal modification was applied to the dried pS-*co*-NIPAm colloidal crystals described in Chapter 4. Cross-linked colloidal crystals were produced via simple heating of the structures to temperatures near the glass transition temperature of polystyrene. These crystal films not only remained stable when exposed to aqueous solvents, such that the diffractive properties were retained, but the optical properties became altered due to swelling of the hydrogel network. This simple sintering approach avoids the numerous, complicated post-crystallization steps that have been employed by other groups, since the fabrication is based solely on the identity of the particle building blocks. The hydrogel character of the pS-*co*-NIPAm particles provides a useful construct for many potential applications, such as in situ sensing in liquid environments. Functional cross-linked colloidal crystals were also explored by using core/shell particles that possessed localized functional groups in the polymer shell. The stability of these cross-linked crystals combined with inherent processability of these particles is beneficial for the purposes of designing many useful optical formats (such as crystalline multilayers[23]) that can be used in many diverse optical applications.

7.2 Experimental Section

7.2.1 pS-*co*-NIPAm Particle Synthesis and Crystal Cross-linking

Materials

Most of the materials used in this chapter are listed in the Experimental Sections of Chapters 2, 3, and 4. Additionally, buffered solvents, which were adjusted to pH 3.0, 3.5, 4.5, or 6.0 (formate or MES; 10 mM ionic strength), were used to characterize the pH responsive properties of the samples.

pS-*co*-NIPAm Microparticle Synthesis

Four of the polystyrene-*co*-N-isopropylacrylamide (pS-*co*-NIPAm) core particle sets used in this study were prepared as described in Chapter 4, which included the 150-1, 300-1, 280-2, and 500-2 particles. Purified suspensions of these particles were used without modification. Two additional types of particles were prepared with a core/shell morphology using a "seed-and-feed" synthesis, whereby the pS-*co*-NIPAm core were prepared using methods similar to those described in Chapter 4, and a poly(pNIPAm-*co*-acrylic acid (pNIPAm-*co*-AAc) shell was added using the same synthesis methods that were described in Chapter 5. The AAc was initially included for the purposes of interparticle cross-linking using covalent attachments to stabilize the colloidal crystals (as discussed in Chapter 5); however, the AAc also imparted pH responsivity to the particles. The presence of this functional group as a constituent of particles was also investigated as a way to achieve functionality of the cross-linked crystal films.

The pS-*co*-NIPAm core/shell particles were prepared by first synthesizing core particles using the same pS-*co*-NIPAm synthesis procedures described in Chapter 4. Two types of core particles were prepared using 75 mol-% styrene, 24 mol-% NIPAm, 1 mol-% BIS, using total monomer concentrations (TMC) of 200 mM ("200-1") and 500 mM ("500-1), using 200 mL total volume of water. The amounts of the synthesis components

are shown in Table 7.1. It should be noted that a smaller amount of APS was used for the 200-1 synthesis for the purposes of trying to achieve larger particles.

Table 7.1 Synthesis ingredients used for the core and core/shell particle polymerizations.

Sample	Styrene, g	NIPAm, g	BIS, g	AAc, μL	Tween 80, mM	APS, g
200-1	3.127	1.0854	0.0629	------	------	0.0013
200-1 C/S AAc	------	1.4240	0.0227	96	0.015	0.0456
500-1	7.187	2.7225	0.1543	------	------	0.0114
500-1 C/S AAc	------	1.4166	0.0226	96	0.015	0.0459

The shell polymer, which consisted of 89 mol-% NIPAm, 10 mol-% AAc, 1 mol-% BIS (70 mM TMC based on 200 mL total reaction volume) was added to both of the 200-1 and 500-1 pS-*co*-NIPAm core particles, to yield the 200-1 C/S AAc and 500-1 C/S AAc core/shell samples. The synthesis procedures for the shell addition can be found in Chapter 5, and the specific synthesis components used for both of these shell polymerizations are listed in Table 7.1. For the shell synthesis on to 200-1 pS-*co*-NIPAm core particles, 40 mL of non-purified 200-1 core stock solution, 7.5 mL of NIPAm and BIS monomer (dissolved in 20 mL water), and Tween 80 (0.015 mM based on the total reaction volume) was added to 135 mL of water. This reaction solution was heated to 70 °C and purged with N_2 while stirring for ~30 min. AAc was added to the reaction mixture prior to initiation with APS (1.0 mM based on total volume), which was dissolved in ~1 mL water. The remaining shell monomer solution was added to the reaction using monomer starved conditions,[24] by adding 2.5 mL to the reaction at 10 min intervals, for a total of 5 times. This shell synthesis was allowed to react for 17.5 hrs.

This same procedure was used to add the pNIPA-*co*-AAc shell on to 500-1 pS-*co*-NIPAm core particles, although only 5 mL of the shell monomer solution was added prior to initiation. The remaining shell monomer was added using the same monomer starved conditions[24] by adding 2.5 mL increments every 15 min after initiation. This reaction continued for ~6.5 hrs. All core and core/shell particles described above were cleaned by centrifugation for ~45 min at 15,400 x *g* rcf at 25 ˚C, three times using water for the resuspension of the pellet.

Formation of Crystal Cross-links

Dried colloidal crystals of pS-*co*-NIPAm particles (150-1, 300-1, 280-2, and 500-2) and pS-*co*-NIPAm core/pNIPAm shell particles (200 C/S AAc, 500-1 C/S AAc) were formed using the exact same methods as described in Chapter 4. Briefly, a few drops of a suspension of the particles was placed on a glass cover slip and spread out to cover an area of ~1-2 cm^2, and these samples were allowed to dry at ambient conditions. Cross-linking was achieved by placing these dried crystals in an oven on a flat glass petri dish. These samples were baked using two different temperatures (~110 ºC or 140 ºC) over extended lengths of time, between 1-7 days.

7.2.2 Characterization Techniques

Photon correlation spectroscopy and transmission electron microscopy were employed to determine the hydrated and dried particle sizes for the pS-*co*-NIPAm core and pS-*co*-NIPAm core/pNIPAm-*co*-AAc shell particles. Reflectance spectroscopy was employed to characterize the Bragg diffraction for the wet and dry crystals. The specific procedures for these characterization techniques can be found in the Experimental Section of Chapter 4.

Differential Scanning Calorimetry

The glass transition temperatures for the some copolymer pS-*co*-NIPAm particles were determined using differential scanning calorimetry (Mettler-Toledo DSC820 system). Dry samples were prepared using freeze-drying methods (Chapter 5) and 1-5 mg was placed in an aluminum sample pan and heated/cooled between 25 °C to 165 °C three times using a scanning rate of 10 °C/min.

7.3 Results and Discussion

Particle Characteristics

The sizes for the pS-*co*-NIPAm core and pS-*co*-NIPAm core/pNIPAm-*co*-AAc shell particles are shown in Table 7.2. The sizes have been determined for particles that are in their fully hydrated state (PCS at 25 °C), their collapsed hydrated state (PCS at 40 °C), and in their completely dried state (TEM). Particle sizes were also obtained for the core/shell particles using pH 3.5 and 6.0 buffers, demonstrating an increase in the particle size of these core/shell particles. These data confirmed the presence of pH responsivity of these particles. Figure 7.1 also demonstrates the temperature dependent particles sizes for the 200-1 C/S AAc and 500-1 C/S AAc samples (pH = 3.5). As discussed in Chapter 4, pS-*co*-NIPAm particles that possess too much polymer flexibility can result in dried samples that lack long-range particle order. As shown in Table 7.2, the 200-1 C/S AAc particles possess a relatively thick shell and, in contrast, there is only a thin shell on the 500-1 C/S AAc particle. As discussed in Chapter 5, even though the shell TMC may be identical, the extent of the shell thickness can depend on the number of core particles available for seeding, as well as the initial core size. Regardless of these particle characteristics, the resulting dried crystalline films still displayed diffractive properties, which indicated that the particle order had been retained.

Table 7.2 Particle sizes for pS-*co*-NIPAm core particles and pS-*co*-NIPAm core /pNIPAm shell particles in their swollen and deswollen hydrated states and their dried states.

Sample	Diameter, nm (PCS at 25 °C)	Diameter, nm (PCS at 40 °C)	Volume Decrease (PCS @ 25 °C v. PCS @ 40 °C)	Diameter, nm (TEM)	Volume Decrease (PCS @ 25 °C vs. TEM)
150-1	182 (± 1)	178 (± 2)	7%	126 (± 3)	66%
300-1	246 (± 2)	243 (± 1)	4%	219 (± 8)	29%
280-2	278 (± 4)	270 (± 3)	9%	203 (± 5)	61%
500-2	318 (± 2)	312 (± 2)	5%	268 (± 7)	40%
200-1	136 (± 3)	134 (± 1)	5%	---	---
200 C/S AAc (pH=3.5)	177 (± 4)	139 (± 2)	51%	---	---
200 C/S AAc (pH=6.0)	230 (± 4)	---	---	---	---
500 C/S AAc (pH=3.5)	194 (± 1)	187 (± 2)	11%	---	---
500 C/S AAc (pH=6.0)	217 (± 1)	---	---	---	---

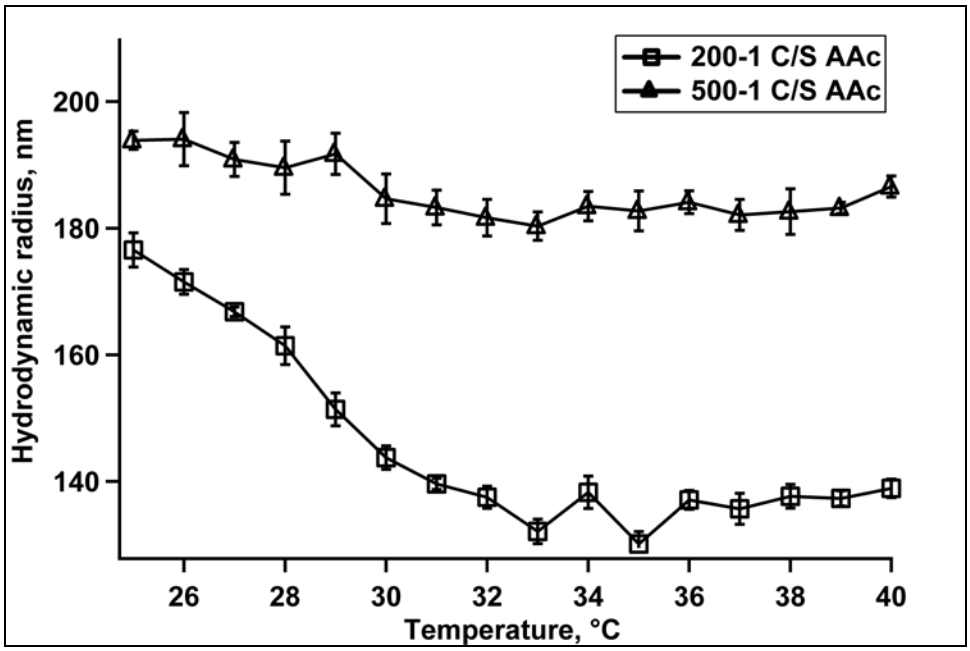

Figure 7.1 Temperature dependent hydrated particle sizes for the 200-1 C/S AAc and 500-1 C/S AAc particles (pH = 3.5).

The glass transition temperatures for the 500-2 pS-*co*-NIPAm core particles were determined by DSC, as shown in Figure 7.2, by performing three thermal heating/cooling scans between 25-165 °C. By zooming in at the appropriate range, two distinct transition temperatures become apparent, but only for the first run (Figure 7.2, top right). By taking the derivative of this first scan, the transition temperatures were determined to occur at 111.5 °C and 134.5 °C. The second and third runs did not show further glass transitions.

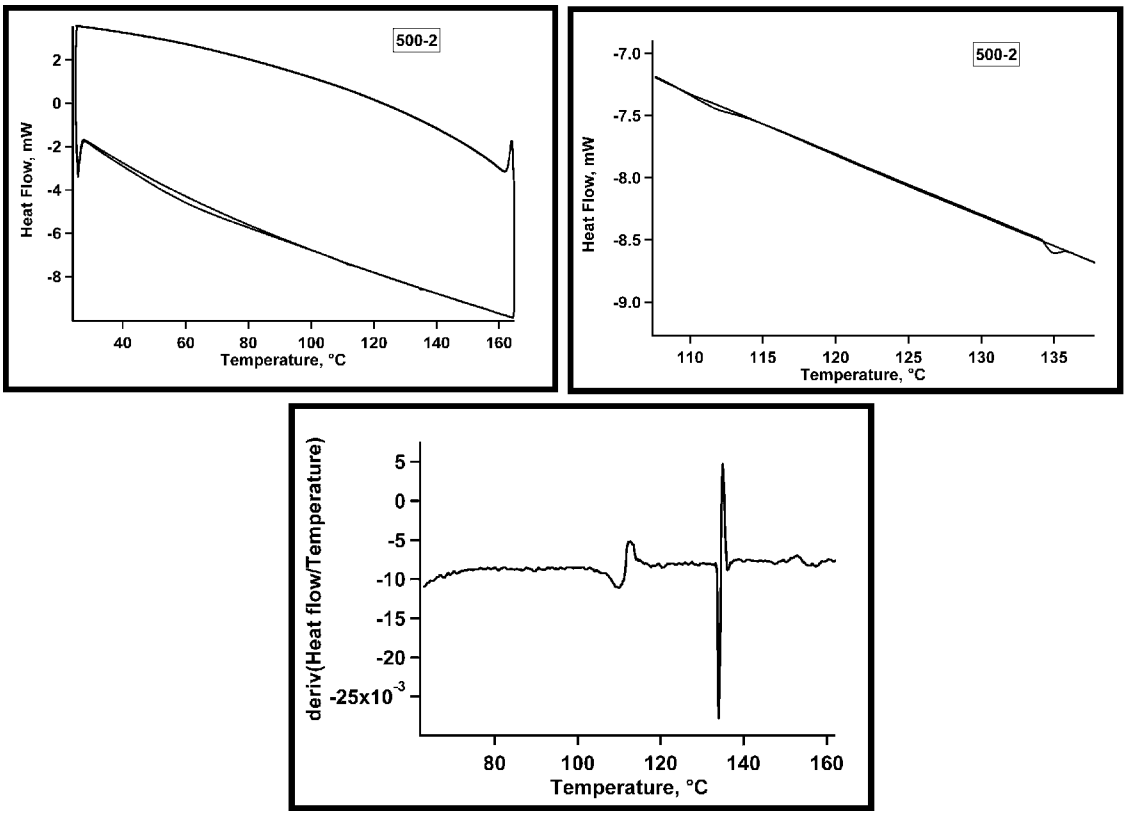

Figure 7.2 DSC curves for the 500-2 pS-*co*-NIPAm core particles. The top left image displays the three thermal scans were performed between 25-165 °C. The top right image is a zoomed-in portion of these scans. The derivative of the first thermal scan is shown in the bottom image.

The glass transition temperatures for polystyrene and pNIPAm homopolymer occur at about 105 °C and 134 °C, respectively.[25] Copolymer blends composed of polystryrene and pNIPAm have demonstrated slight differences in these values, and these measurements have been used to determine the extent of homo- and hetero-polymer regions in materials that contain these components.[25-27] The two distinct glass transitions found for the 500-2 pS-*co*-NIPAm particles suggest that the particle is comprised of two distinct polymeric regions. Since the second T_g is almost that same as the T_g of pNIPAm homopolymer, there are probably large regions of pNIPAm homopolymer. Because the first T_g for the 500-2 particles is higher than the T_g for pure polystyrene, this result suggests that pS-*co*-NIPAm heterocopolymer or blend also exists. Since there is no

evidence of a T_g during successive heating scans, the individual polymeric particles are probably irreparably destroyed due to the high maximum temperature of 165 °C.

Cross-linked pS-*co*-NIPAm crystals

Based on the glass transition temperatures for a typical pS-*co*-NIPAm particle, the dried crystals composed of 150-1, 300-1, 280-2, and 500-2 particles were baked in an oven at ~110 °C to determine if such an annealing process would assist in physical cross-linking of the particles. Examples of oven-baked and non-oven baked samples prepared from dried 280-2 crystals are shown in Figure 7.3. The sample on the left was baked in an oven at ~110 °C for ~5 days and the sample on the right was not baked. As the photographs indicate, wetting the samples with aqueous solvent produces remarkably different outcomes. In the case of the non-baked sample, the diffraction color is immediately lost as the particle order is disturbed due to redispersion of the particles. The baked sample, however, not only remains diffractive, but the color is also shifted from blue to green. This latter sample appears very stable and does not break up and disperse like the non-baked sample. As the solvent dried from the wet, oven-baked sample, the blue diffraction color of the original dried sample is restored.

This reversibility in diffraction color is demonstrated in Figure 7.4 where a dried crystal formed using 300-1 pS-*co*-NIPAm particles (baked at ~110 °C for 48hrs) was wetted with water and allowed to dry at ambient conditions. Initially, the crystal displays a green diffraction color in its dried state. The crystal turns orange after applying water, then returns back to its original state when re-dried, exhibiting a green diffraction color once again. This feature of reversible optical tuning was found for all of the oven-baked pS-*co*-NIPAm crystals.

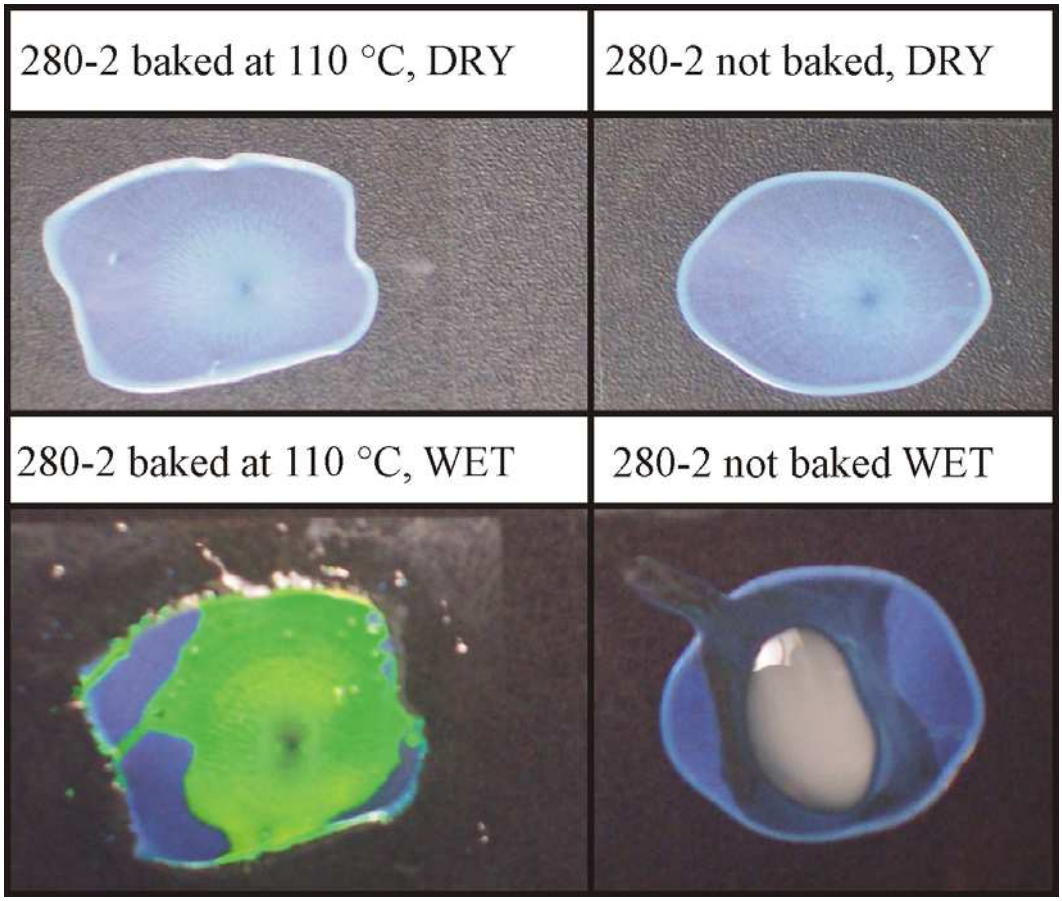

Figure 7.3 Photographs of oven-baked and non-baked crystals composed of 280-2 pS-*co*-NIPAm particles. The top images display the dry crystals and the bottom samples were wetted with water.

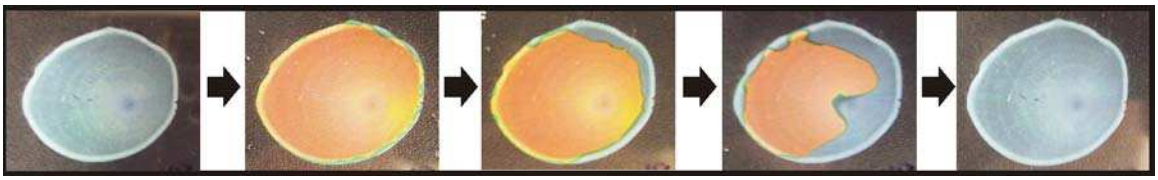
Figure 7.4 Reversibility of wet to dry diffraction colors using a dried crystal composed of 300-1 pS-*co*-NIPAm particles (baked at ~110 °C for 48 hrs).

The conservation of the optical diffraction suggests that the particle order is preserved even when the sample is wet. These crystal films also remained attached to the glass substrate, which not only demonstrates the robust stability of the cross-linked film,

but also shows that the particles at the bottom of the film adhere to the glass interface. The obvious shift in diffraction color suggests that the dry hydrogel component becomes rehydrated and swells when exposed to liquid, yielding an increase in the crystal lattice spacing, while the overall particle order is retained due to interparticle polymeric interactions that result from the baking process.

Reflectance Spectroscopy

Reflectance spectra were collected for each of the oven-baked samples to determine the precise extent of the changes in diffraction color, as shown in Figure 7.5. All of the samples exhibit a red shift in Bragg diffraction under the wet conditions. This data confirms the increase in particle spacing, based on Bragg's Law. In most cases, the spectra for the oven-baked dried crystals appear to be slightly blue-shifted in comparison to the spectra for ordinary, non-oven-baked dried crystals. This effect may be due to interparticle sintering as a result of the high baking temperatures, such that the particle lattice spacing decreases slightly.[13,28]

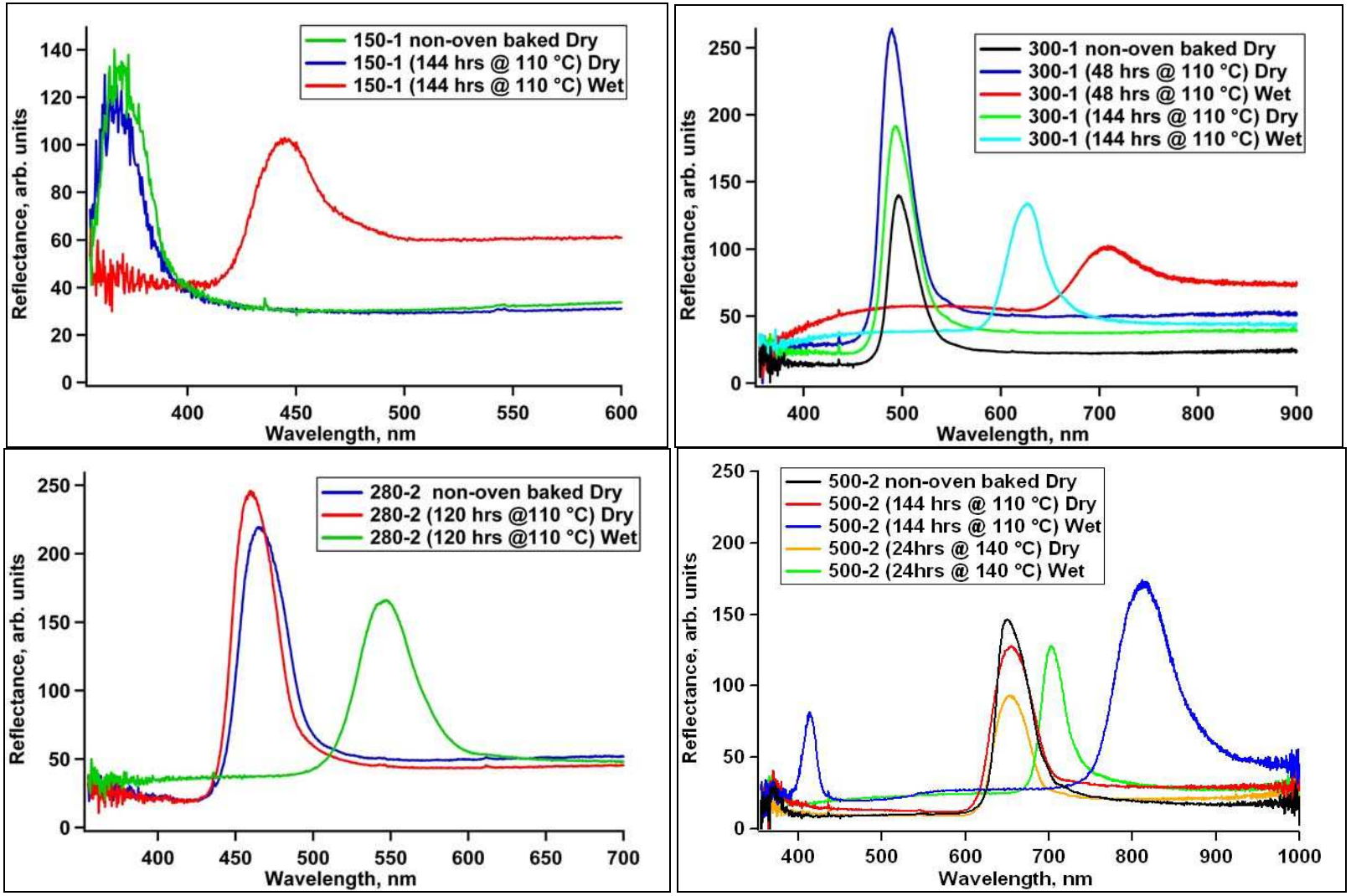

Figure 7.5 Spectra of dried, non-oven baked crystals and oven-baked crystals (wet and dry) using the 150-1, 300-1, 280-2, and 500-2 pS-*co*-NIPAm particles.

The 150-1 and 280-1 samples show diffractions shifts of 80 nm and 85 nm, respectively, when swollen with water. Additionally, the shift in diffraction wavelength for the wet crystals was found to be dependent on the length of the baking time. For example, the 300-1 crystal that had been baked for 48 hrs demonstrated a peak shift of 220 nm with the addition of aqueous solvent, and the crystal that had been baked for 144 hrs only displayed a shift of 130 nm under wet conditions. This shorter shift that was realized using longer baking times indicates that the swelling capacity of the particles is hindered, due to smaller lattice spacing, which may be due to an increased degree of interparticle cross-linking. The wet-to-dry wavelength shift was also found to be dependent on the temperature level. For instance, a 500-2 crystal that was heated for 144 hrs at 110 °C demonstrated a peak shift of 160 nm when wet, whereas the same type of crystal that was heated at 140 °C for only 24 hrs displayed a shift of only 50 nm. When this elevated temperature was used to bake 150-1, 300-1, and 280-2 dried crystals, the resulting films appeared transparent and neither the dry nor wet states exhibited diffractive properties. This outcome suggests that the particle film actually melted together due to the high temperature, such that discrete particles were no longer present. It is clear from this data that the polymeric interactions at temperatures near the glass transition temperature affect the physical cross-linking of the particle film. These interactions depend significantly on the heating process that is employed as well as the individual copolymeric identity of the particles.

In Situ Reflectance Spectroscopy

The wet-to-dry transition for these cross-linked crystal films was characterized more thoroughly by collecting in situ reflectance spectra as the aqueous solvent evaporated from the oven-baked samples. Figure 7.6 displays the in situ spectra collected for some of the same crystals shown in Figure 7.5, including the 150-1 crystal oven-baked for 144 hrs at 110 °C, the 300-1 crystal oven-baked for 48 hrs at 110 °C, the 300-1

crystal oven-baked for 144 hrs at 110 °C, the 500-1 crystal oven-baked for 144 hrs at 110 °C, and the 500-1 crystal oven-baked for 24 hrs at 140 °C. The drying of these cross-linked crystals occurred on the order of minutes, where $t_1 < t_2 < t_3 < t_4$.

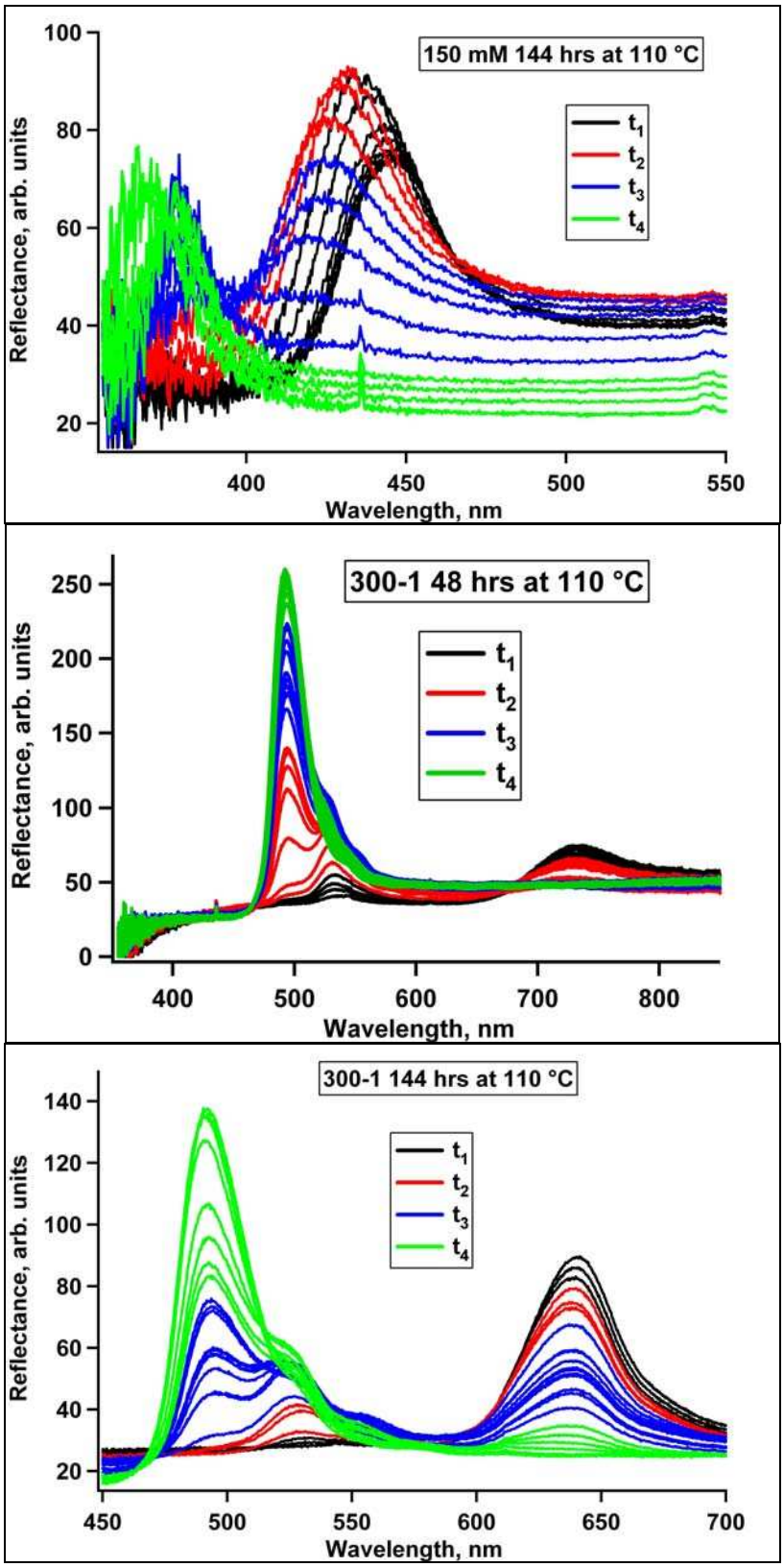

Figure 7.6 In situ reflectance spectra collected during the wet-to-dry transition for 150-1, 300-1, and 500-2 crystals that were oven-baked using specific times and temperatures.

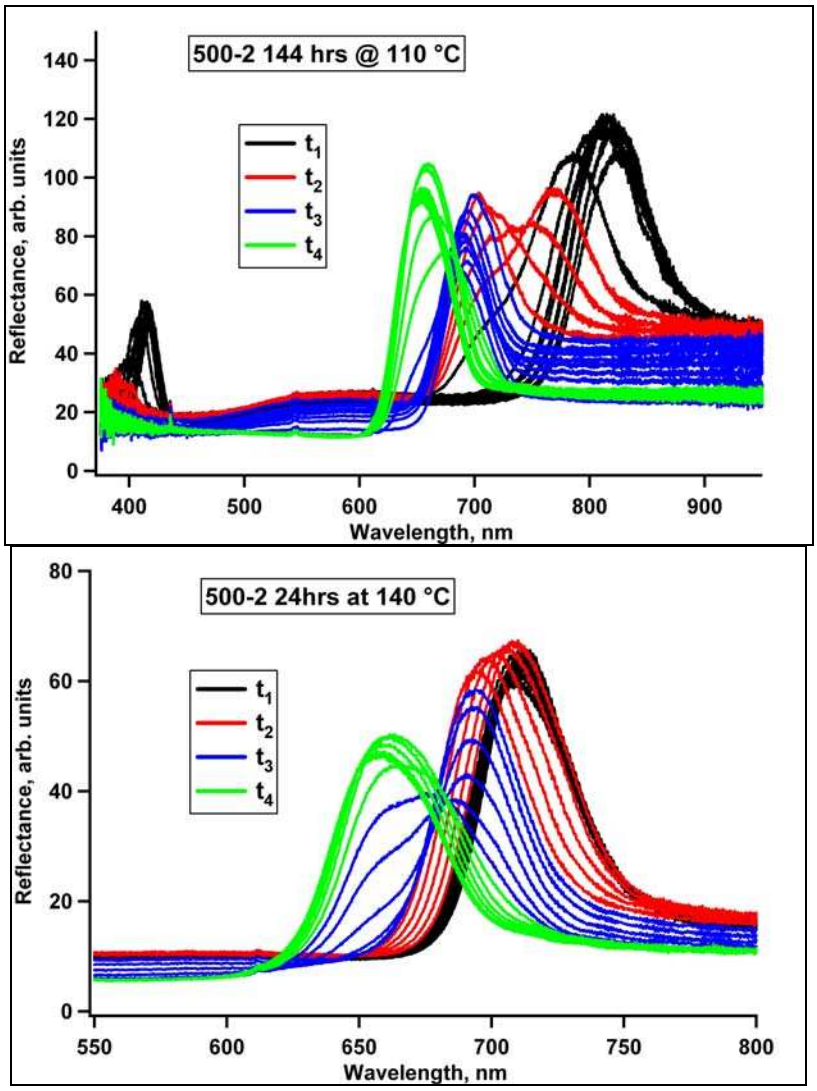

Figure 7.6 (continued)

When the sample is entirely wet, only one diffraction peak is apparent at first, which is shifted to longer wavelengths compared to the original diffraction found for the dry oven-baked sample. Generally, as the sample dries, the intensity of this peak decreases and blue shifts, and eventually the diffraction peak of the dried sample dominates once the solvent has completely evaporated. However, these details of these transitions vary for each of the oven-baked samples.

For the 150-1 crystal, the initial peak found for the wet sample simply blue shifts and decreases in intensity, while the final, dry diffraction peak emerges and is maintained after the solvent completely evaporates. The transition for the 500-2 crystal baked at 140 °C shows a similar trend. Interestingly, the 500-2 crystal baked at 110 °C shows three distinct regions. The initial peak intensity at 810 nm decreases and blue shifts, then increases in intensity near 700 nm, and then decreases in intensity and blue shifts yet again while the final diffraction peak emerges at ~660 nm.

In the cases of the 300-1 cross-linked crystals, the intensity of the initial peak for the wet sample diminishes completely as a second peak emerges that located just to the red side of the final, dry diffraction peak. Shortly after the emergence of this second peak, a third peak appears at the same wavelength of the final, dry crystal. At the same time, the intensity of the second peak diminishes and blue shifts until it becomes a shoulder to the red side of the third distinct peak. Finally, the shoulder disappears completely and the final diffraction peak for the dried sample dominates. These trends are identical for both of the 300-1 oven-baked samples, which had been baked for 48 hrs or 144 hrs, with the exception of the location of the initial diffraction peak, as discussed earlier. Consequently, it is surprising that the emergence of the intermediate peak at ~530 nm is identical for both cases. This occurrence is also identical to the initial peak found using in situ reflectance spectroscopy to track the drying process of particle suspensions (Chapter 4, Figure 4.12). A similar type of correlation was found for the 500-2 crystal that was baked at 110 °C (Figure 7.6), where the peak at ~700 nm became dominant for a short time during drying. A peak was also found at this wavelength using in situ reflectance spectroscopy when suspensions of individual 500-2 particles were dried (Chapter 4, Figures 4.11 and 4.12). The analogous locations of these peaks suggest that two distinct drying phases are occurring during the drying of these oven-baked crystal films based on the configuration of the interparticle associations within the film. The final transition appears due to the gradual reduction in the size of the individual particles as they dry,

while maintaining an ordered configuration, as discussed in Chapter 4. Alternatively, the initial peaks for the wet, oven-baked samples are indicative of particles that have become completely swollen, while remaining cross-linked, or are even barely connected at their peripheries (based on the extent of the wavelength shift). The drastic decrease in the intensity of these initial diffraction peaks may be due to the rapid decrease in particle spacing due to the sparse interparticle connections formed during heating.

Although the particular interparticle linkages of the cross-linked pS-*co*-pNIPAm particles were not investigated in detail, the specific impact of the particle's identity on the precise lattice spacing of the particles provides a unique method of tuning the optical properties based on the copolymeric characteristics of the particle. It is important to recall that the samples are heated to temperatures near the first T_g that was observed for the 500-2 pS-*co*-NIPAm particles (Figure 7.2). This T_g is associated with the denser, hydrophobic, styrene-rich regions that are probably located close to the particle center (as discussed in Chapter 4). This polymer blend may have the opportunity to flow from its initial position and fill in the spaces between the particles, [19] creating durable interparticle connections upon cooling that are comparable to the durability of the copolymer core. Further characterizations are necessary to determine how these particles are truly connected.

Functional Cross-linked Crystals

Cross-linked crystal fabrication by the implementation of simple baking procedures avoids the need for complex post-crystallization modification steps to achieve particle stability. However, many such modification methods have proven useful for the introduction of particular functional groups that can be used to tune the optical properties of the crystal, which is particularly advantageous for many optical applications. This functionality can be afforded to the cross-linked crystals, described here in, by

introducing functional groups directly into the synthesis of the particle building blocks. This method simplifies the fabrication of tunable colloidal crystals.

Dried, oven baked samples were prepared using the 200-1 C/S AAc and the 500-1 C/S AAc particles. Acrylic acid has been routinely used to impart pH responsivity to hydrogel materials.[24,29,30] Protonation and deprotonation of the AAc groups can be used to cause swelling or deswelling of the hydrogel, due to the changes in the Coulombic repulsion of nearby AAc groups. Since the acrylic acid groups are located in the shells of these particles, these moieties will be situated presumably within the continuous matrix of the swollen, cross-linked film. Therefore, this matrix may become swollen and deswollen based upon changes in the pH of the solvent used to hydrate the dry, cross-linked core/shell particles. This responsive property was investigated as a means for tuning the optical properties of the crystal films. Since the pK_a for AAc is ~4.25,[31] buffered solvents that had been adjusted to different pH's (3.0, 4.5, and 6.0) were used to swell these crystalline films. Figures 7.7 and 7.8 demonstrate the reflectance spectra for the 200-1 C/S AAc and the 500-1 C/S AAc crystals, respectively, which had been baked in the oven for 7 days at ~110 °C. Spectra that were acquired when the different buffers were employed are depicted by different colors. Reflectance spectra for the non-baked dried core/shell crystals is also shown, for comparison.

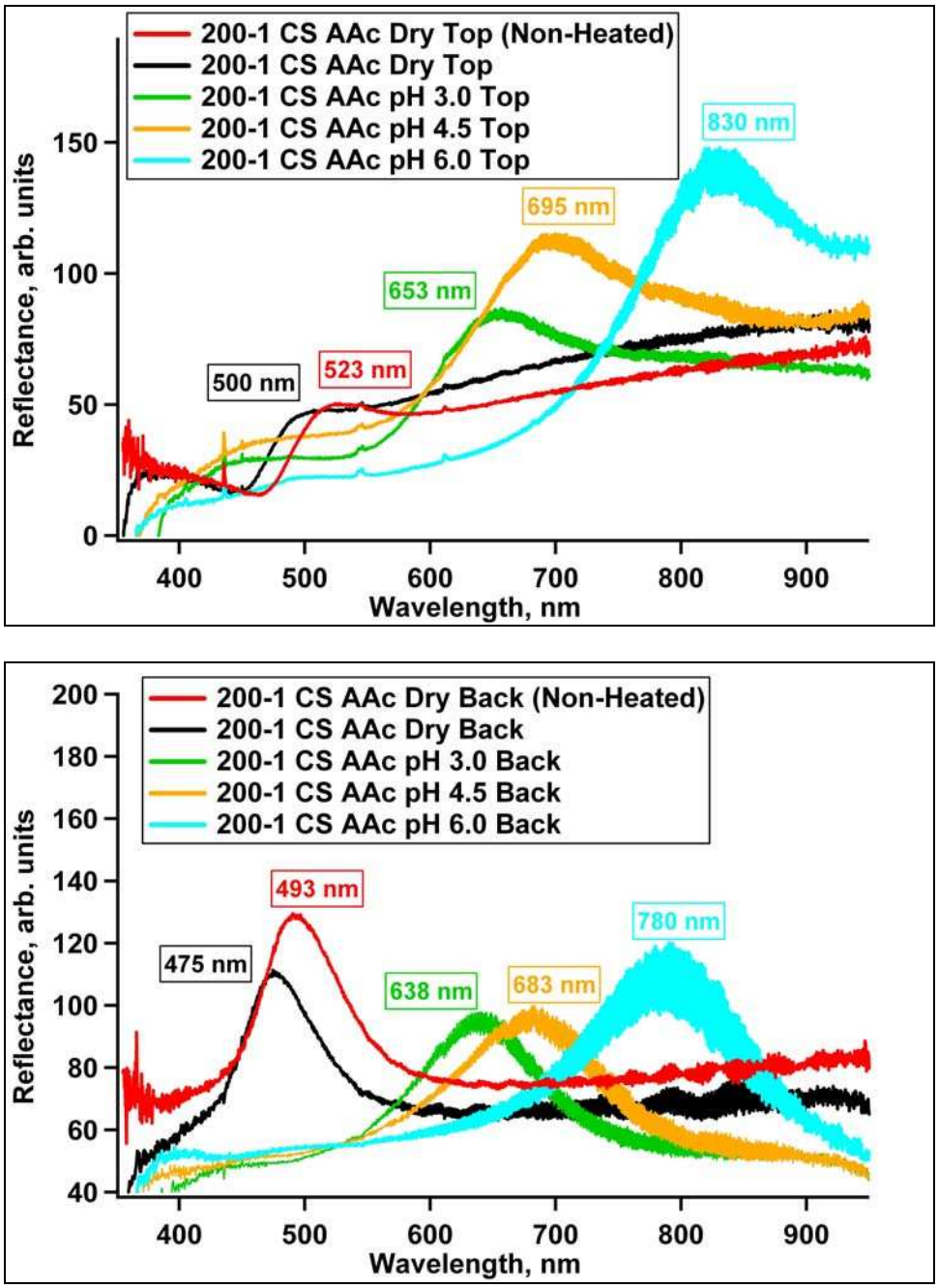

Figure 7.7 Reflectance spectra of oven-baked crystals composed of 200-1 C/S AAc particles in the dry state and swollen using buffers of different pH's. (Samples were interrogated at the top of the crystal or through the back of the crystal, through the glass cover slip).

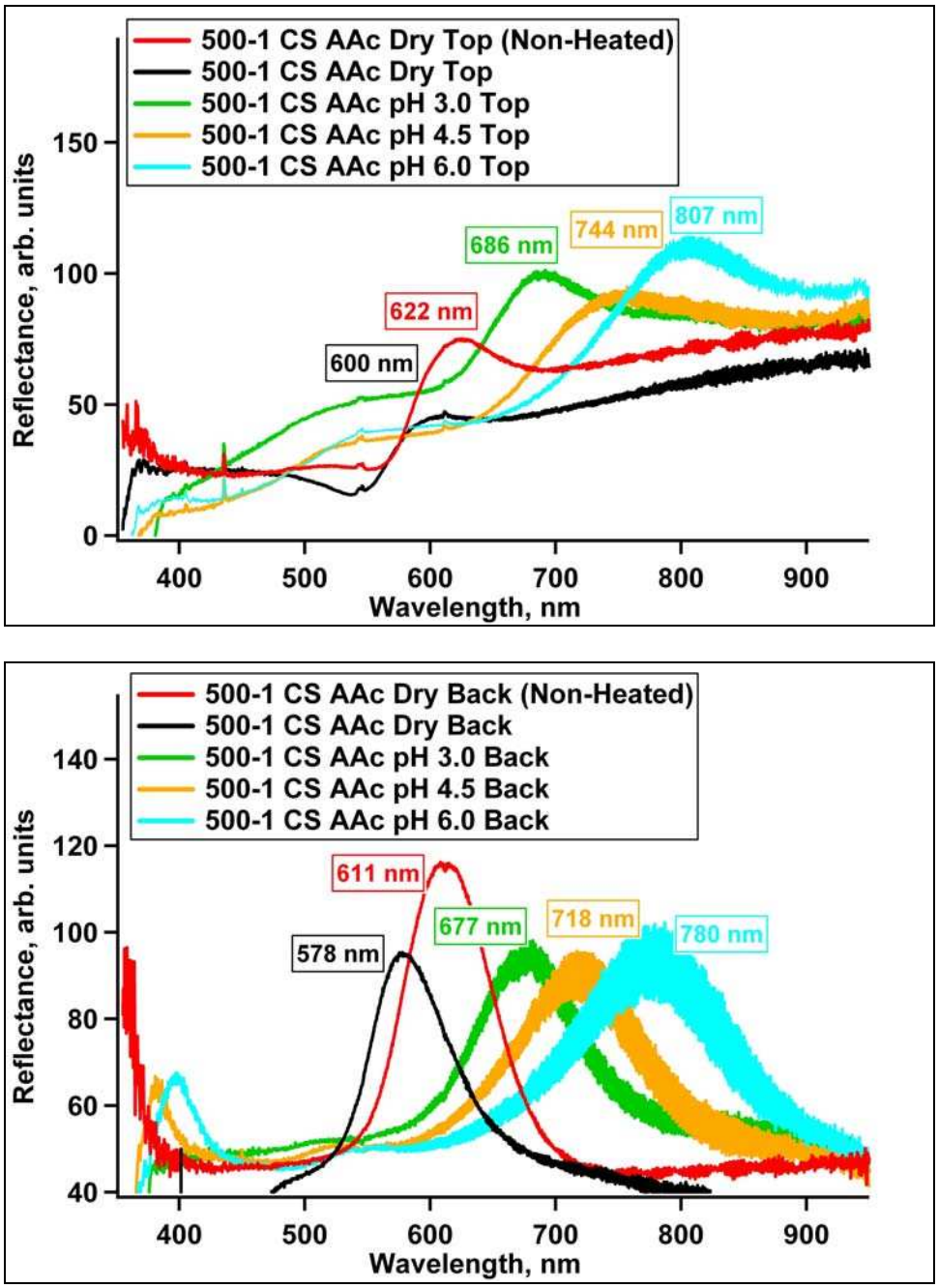

Figure 7.8 Reflectance spectra of oven-baked crystals composed of 500-1 C/S AAc particles in the dry state and swollen using buffers of different pH's. (Samples were interrogated at the top of the crystal or through the back of the crystal, through the glass cover slip).

Both 200-1 C/S AAc and 500-1 C/S AAc oven-baked crystals demonstrated pH tunability, whereby the diffraction peaks shifted to longer wavelengths as the pH became

more basic. These transitions in diffraction wavelength suggest that the particles and/or the continuous matrix swell to an increasingly larger degree, thereby increasing the center-to-center distance between particles, as more acrylic acid groups become deprotonated. The dried, oven-baked samples also demonstrated a slight blue-shift compared to the non-oven-baked dried crystals. This effect was similar to the shift found with the baked and non-baked pS-*co*-NIPAm cores crystals, which suggests that the particle lattice spacing also decreases slightly upon baking. Interestingly, different spectral characteristics were found when these samples were interrogated from the back compared to the top of the samples. Whereas the dried pS-*co*-NIPAm crystals that were interrogated from the back side in Chapter 4 demonstrated only slight blue shifts in the diffraction wavelength, the peaks for the 200-1 C/S AAc and 500-1 C/S AAc particles exhibit larger discrepancies. This disparity is particularly noticeable for the 200-1 C/S AAc particles when the pH 6.0 buffer is employed, demonstrating a difference of ~50 nm. Since both sets of these particles have very flexible polymer shell exteriors, this effect may be due to irregular cross-linking density throughout the crystal, such that the swelling capacity of particles located towards the bottom of the film is hindered, while the particles nearest to the top of the crystal can swell unabatedly. Consequently, this effect demonstrates that these cross-links must be thoroughly characterized in order to fully understand the optical properties of these crystal films.

Crystal Multilayers

The ability to use oven-baked pS-*co*-NIPAm dried crystals as a substrate for subsequent crystal formation was also investigated, so as to form crystal multilayers. Crystals were prepared by deposition of pS-*co*-NIPAm particle suspensions (150-1, 300-1 or 500-2) on top of an oven-baked, cross-linked crystal composed of 280-2 pS-*co*-NIPAm particles. Reflectance spectra for the resulting multi-layered crystals are shown in Figure 7.9. The spectra for each multi-layer region demonstrate distinct diffraction peaks

at the wavelengths typical for 280-2 dried crystals, as well as for the additional crystals. This example demonstrates the versatility of these cross-linked crystal films as advantageous materials for designing constructs for optical applications.

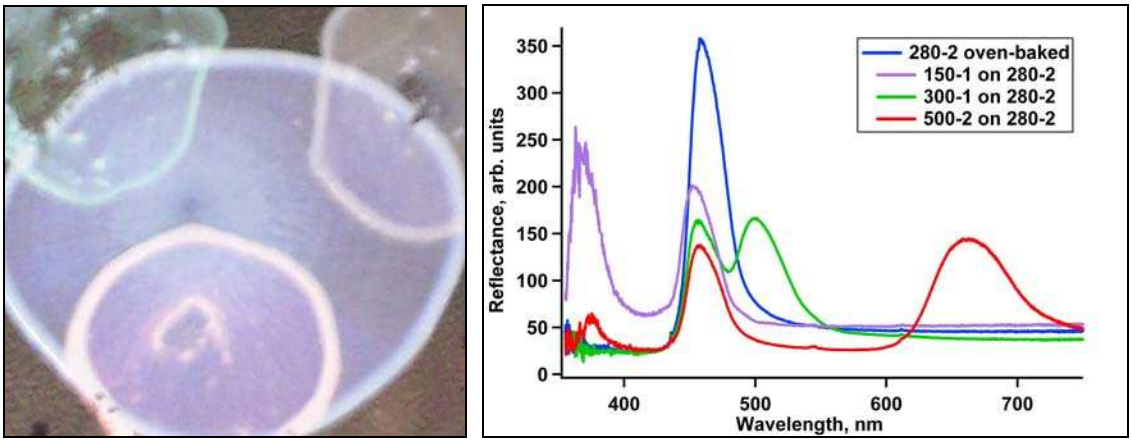

Figure 7.9 Crystal multi-layers formed by drying 150-1, 300-1, or 500-2 pS-*co*-NIPAm particles on top of a dried, oven-baked crystal composed of 280-2 pS-*co*-NIPAm particles. Left: Photograph of the 300-1 (green), 150-1 (violet), and 500-2 (red) crystals on top of the 280-2 (blue) crystal. Right: Reflectance spectra of each multi-layer crystal region shown in the photograph.

7.4 Conclusions

Cross-linked, colloidal crystals composed of pS-*co*-NIPAm particles were produced using simple baking procedures. Whereas non-baked pS-*co*-NIPAm crystal films fell apart when exposed to aqueous solvents, these cross-linked, crystal films remained stable and continued to exhibit Bragg diffraction, indicating that the particle order had been preserved. The wavelength of this diffraction was red-shifted compared to the optical properties of the dried crystal, which suggested an increase in the crystal lattice spacing that could be attributed to swelling of the hydrogel network of the particles. This optical shift between the wet and dry states was found to be reversible, which exemplifies the robustness of these cross-linked films as stable, tunable crystals.

The copolymer characteristics, baking time, and baking temperature all contribute to the precise lattice spacing of the cross-linked crystal, which provides a means for varying the optical properties of these crystals. Since the fabrication of these cross-linked crystals is based solely on the identity of the particle building blocks, numerous complicated post-crystallization steps to achieve crystal stability can be avoided. The swelling capacity of the pS-*co*-NIPAm hydrogel network also provides a advantageous construct for many diverse potential applications, such as in liquid sensing. The permeability of this hydrogel matrix afforded the opportunity to fabricate functional, cross-linked colloidal crystals using core/shell particles that possessed pH responsivity. The ability to add such functional groups directly to the particle synthesis also helps to avoid complex modification steps. Crystal multi-layers could also be prepared by using dried, cross-linked crystals as substrates for subsequent crystal formation. The ease of assembly, inherent processability, and enhanced stability afforded by these structures provides an attractive approach for designing a variety of useful optical materials.

References

[1] Asher, S. A.; Holtz, J.; Liu, L.; Wu, Z. Self-Assembly Motif for Creating Submicron Periodic Materials. Polymerized Crystalline Colloidal Arrays. *J. Am. Chem. Soc.* **1994**, *116*, 4997-8.

[2] Weissman, J. M.; Sunkara, H. B.; Tse, A. S.; Asher, S. A. Thermally switchable periodicities and diffraction from mesoscopically ordered materials. *Science* **1996**, *274*, 959-960.

[3] Holtz, J. H.; Asher, S. A. Polymerized colloidal crystal hydrogel films as intelligent chemical sensing materials. *Nature* **1997**, *389*, 829-832.

[4] Holtz, J. H.; Holtz, J. S. W.; Munro, C. H.; Asher, S. A. Intelligent Polymerized Crystalline Colloidal Arrays: Novel Chemical Sensor Materials. *Anal. Chem.* **1998**, *70*, 780-791.

[5] Reese, C. E.; Baltusavich, M. E.; Keim, J. P.; Asher, S. A. Development of an Intelligent Polymerized Crystalline Colloidal Array Colorimetric Reagent. *Anal. Chem.* **2001**, *73*, 5038-5042.

[6] Asher, S. A.; Alexeev, V. L.; Goponenko, A. V.; Sharma, A. C.; Lednev, I. K.; Wilcox, C. S.; Finegold, D. N. Photonic crystal carbohydrate sensors: Low ionic strength sugar sensing. *J. Am. Chem. Soc.* **2003**, *125*, 3322-3329.

[7] Ben-Moshe, M.; Alexeev, V. L.; Asher, S. A. Fast Responsive Crystalline Colloidal Array Photonic Crystal Glucose Sensors. *Anal. Chem.* **2006**, *78*, 5149-5157.

[8] Fudouzi, H.; Xia, Y. Photonic papers and inks: Color writing with colorless materials. *Adv. Mat.* **2003**, *15*, 892-896.

[9] Fudouzi, H.; Xia, Y. Colloidal Crystals with Tunable Colors and Their Use as Photonic Papers. *Langmuir* **2003**, *19*, 9653-9660.

[10] Toyotama, A.; Kanai, T.; Sawada, T.; Yamanaka, J.; Ito, K.; Kitamura, K. Gelation of Colloidal Crystals without Degradation in Their Transmission Quality and Chemical Tuning. *Langmuir* **2005**, *21*, 10268-10270.

[11] Arsenault, A. C.; Miguez, H.; Kitaev, V.; Ozin, G. A.; Manners, I. A polychromic, fast response metallopolymer gel photonic crystal with solvent and redox tunability: A step towards photonic ink (P-ink). *Adv. Mat.* **2003**, *15*, 503-507.

[12] Miguez, H.; Meseguer, F.; Lopez, C.; Blanco, A.; Moya, J. S.; Requena, J.; Mifsud, A.; Fornes, V. Control of the photonic crystal properties of fcc-packed submicrometer SiO2 spheres by sintering. *Adv. Mat.* **1998**, *10*, 480-483.

[13] Gates, B.; Park, S. H.; Xia, Y. Tuning the photonic bandgap properties of crystalline arrays of polystyrene beads by annealing at elevated temperatures. *Adv. Mat.* **2000**, *12*, 653-656.

[14] Matsushita, S.; Shimomura, M. Light-propagation patterns in freestanding two-dimensional colloidal crystals. *Colloid Surf., A: Physicochem. Eng. Asp.* **2006**, *284+285*, 315-319.

[15] Egen, M.; Zentel, R. Tuning the Properties of Photonic Films from Polymer Beads by Chemistry. *Chem. Mater.* **2002**, *14*, 2176-2183.

[16] Scott, R. W. J.; Yang, S. M.; Coombs, N.; Ozin, G. A.; Williams, D. E. Engineered sensitivity of structured tin dioxide chemical sensors: Opaline architectures with controlled necking. *Adv. Funct. Mater.* **2003**, *13*, 225-231.

[17] Blanco, A.; Chomski, E.; Grabtchak, S.; Ibisate, M.; John, S.; Leonardo, S. W.; Lopez, C.; Meseguer, F.; Miguez, H.; Mondia, J. P.; Ozin, G. A.; Toader, O.; Van Driel, H. M. Large-scale synthesis of a silicon photonic crystal with a complete 3-dimensional bandgap near 1.5 micrometres. *Nature* **2000**, *405*, 437-440.

[18] Busch, K.; John, S. Photonic band gap formation in certain self-organizing systems. *Phys. Rev. E* **1998**, *58*, 3896-3908.

[19] Kalinina, O.; Kumacheva, E. A \"Core-Shell\" Approach to Producing 3D Polymer Nanocomposites. *Macromolecules* **1999**, *32*, 4122-4129.

[20] Rugge, A.; Ford, W. T.; Tolbert, S. H. From a Colloidal Crystal to an Interconnected Colloidal Array: A Mechanism for a Spontaneous Rearrangement. *Langmuir* **2003**, *19*, 7852-7861.

[21] Gao, J.; Lee, D.; Yang, Y.; Holdcroft, S.; Frisken, B. J. Self-Assembly of Surface-Charged Latex Nanoparticles: A New Route to the Creation of Continuous Channels for Ion Conduction. *Macromolecules* **2005**, *38*, 5854-5856.

[22] Gao, J.; Yang, Y.; Lee, D.; Holdcroft, S.; Frisken, B. J. Self-Assembly of Latex Particles into Proton-Conductive Membranes. *Macromolecules* **2006**, *39*, 8060-8066.

[23] Masse, P.; Ravaine, S. Engineered Multilayer Colloidal Crystals with Tunable Optical Properties. *Chem. Mater.* **2005**, *17*, 4244-4249.

[24] Jones, C. D.; Lyon, L. A. Synthesis and Characterization of Multiresponsive Core-Shell Microgels. *Macromolecules* **2000**, *33*, 8301-8306.

[25] Ding, X.; Sun, Z.; Zhang, W.; Peng, Y.; Chan, A. S. C.; Li, P. Characterization of Fe3O4/poly(styrene-co-N-isopropylacrylamide) magnetic particles with temperature sensitivity. *Colloid Polym. Sci.* **2000**, *278*, 459-463.

[26] Zheng, C.; He, W.-D.; Liu, W.-J.; Li, J.; Li, J.-F. Novel one-step route for preparing amphiphilic block copolymers of styrene and N-isopropylacrylamide in a microemulsion. *Macromolecular Rapid Comm.* **2006**, *27*, 1229-1232.

[27] Mano, V.; Ribeiro E Silva, M. E. S.; Barbani, N.; Giusti, P. Blends composed of poly(N-isopropylacrylamide) and an ethylene/vinyl alcohol copolymer: thermal and morphological studies. *J. Appl. Polym. Sci.* **2004**, *91*, 501-505.

[28] Cho, Y.-S.; Yi, G.-R.; Moon, J. H.; Kim, D.-C.; Lee, B.-J.; Yang, S.-M. Connected Open Structures from Close-Packed Colloidal Crystals by Hyperthermal Neutral Beam Etching. *Langmuir* **2005**, *21*, 10770-10775.

[29] Jones, C. D.; Lyon, L. A. Dependence of Shell Thickness on Core Compression in Acrylic Acid Modified Poly(N-isopropylacrylamide) Core/Shell Microgels. *Langmuir* **2003**, *19*, 4544-4547.

[30] Jones, C. D.; Lyon, L. A. Shell-Restricted Swelling and Core Compression in Poly(N-isopropylacrylamide) Core-Shell Microgels. *Macromolecules* **2003**, *36*, 1988-1993.

[31] Lide, D. R. *Handbook of Chemistry and Physics, 74th ed.*; CRC Press: Boca Raton, FL, 1994.

CHAPTER 8

PROBING COLLOIDAL CRYSTALS COMPOSED OF POLY(*N*-ISOPROPYLACRYLAMIDE-*CO*-ACRYLIC ACID) MICROGELS USING SILVER NANOPARTICLES AS TRACERS

8.1 Introduction

Colloidal tracer particles have been successfully used to probe the microenvironments of many experimental systems.[1-3] The thermal diffusion that originates from the intrinsic Brownian motion of these colloidal particles can be investigated using particle tracking experiments based on passive microrheology methods that employ video microscopy.[4-12] Many different types of tracer particles are commercially available for these types of applications. Polystyrene particles are widely used due to their spherical shape, low polydispersity, and their ability to possess multiple chemical functionalities that can be incorporated during the particle synthesis. It follows that knowledge of the specific chemical properties of the particle is crucial to avoid unfavorable interactions with the system that is being probed.[10] Certain provisions may also be necessary to ensure adequate stability of these particles in the experimental environment. Also, tracer particles must be large enough to observe using standard bright-field optical microscopy techniques or must possess certain properties, such as fluorescence to allow for visualization.

Unfortunately these requirements severely limit the range and the diversity of the microrheology experiments that can be accomplished, since particles typically need to be >500 nm in size for standard optical microscopy experiments and smaller particles that possess fluorescent groups have a tendency to photobleach over time or when high intensity light sources are employed. The passive microrheology methods that are employed in these types of particle tracking experiments are also dependent on the fixed

amount of thermal energy associated with Brownian motion. Therefore, measurements of the diffusion of large particles is limited by the detection resolution of the microscopy setup.[10] Consequently, smaller tracer particles will move faster with the same amount of thermal energy, and if such tracer agents can be easily observed and are inert to the sampling environment, they would prove to be particularly beneficial to enhance the scope of experiments that employ particle-tracking microrheology.

Silver (Ag) nanoparticles can provide a unique alternative to standard tracer agents due to their high efficiency for scattering light.[13-17] As discussed in Chapter 3, interaction with an electromagnetic field can cause Ag nanoparticles to exhibit surface plasmon resonances. These surface plasmons (surface-charge oscillations) are due to both non-radiative absorption and a near-field interaction that evolves into far-field scattering.[14,17] As the Ag particle size approaches the wavelength of light, the contribution of scattering increases due to the multipolar character of the surface plasmons.[13,17-19] The Ag particle size that is necessary to achieve these high scattering efficiencies is significantly small (20-80 nm)[15] compared to the sizes of the tracer agents that are regularly employed for microrheology experiments. Ag nanoparticles can provide additional advantages relative to other tracer agents, since they have the ability to withstand high intensity radiation without photobleaching and are relatively chemically and physically robust.[20]

Such particle tracking techniques described above have proven useful for the investigation of the particle dynamics of colloidal crystals, without the use of tracer agents.[21-23] These experiments were been performed by directly tracking the individual particles that comprised the crystal lattice. In the present study, the microenvironment of colloidal crystals was investigated by tracking the movements of small (~70 nm in diameter) Ag nanoparticles incorporated into crystals that were assembled with large (~800 nm diameter) microparticles composed of poly(*N*-isopropylacrylamide-*co*-acrylic acid) (pNIPAm-*co*-AAc). The Ag nanoparticles could be easily dispersed in concentrated

samples of pNIPAm-*co*-AAc particles to form a binary mixture. Upon crystallization via thermal annealing procedures,[24-27] the small Ag particles were located in the interstitial spaces between the soft hydrogel particles and the positions of the Ag particles were found to shift substantially, while the pNIPAm-*co*-AAc particles maintained in their ordered configuration. The particle trajectories of the Ag nanoparticles and the pNIPAm-*co*-AAc microparticles for colloidal crystals that were fabricated using different polymer weight percentages of the soft spheres were examined to investigate the microenvironments of such tunable systems. This study also serves as a proof-of-concept for using Ag nanoparticles as tracer agents.

8.2 Experimental Section

8.2.1 Sample Preparation

Materials

The materials used in this chapter are described in the Experimental Sections of Chapters 2 and 3.

Colloidal Crystal Fabrication

Large, thermoresponsive particles that were used for the fabrication of colloidal crystals were prepared by surfactant-free, precipitation polymerization using a large total monomer concentration (TMC) of 150 mM. The comonomer, AAc, was also included in the synthesis of these particles so that Coulombic repulsion of the charged groups increases the degree of particle swelling to yield particles large enough to be easily observed using bright-field microscopy. It should also be noted that the AAc functional groups introduce pH responsivity, which can be used to tune particle size, can additionally result in attractive forces between nearby particles.[25,28] The pH of the stock solutions of pNIPAm-*co*-AAc was ~3.6, which is below the pK_a for AAc (~4.25).[29]

Therefore, the AAc groups are mostly protonated and can allow for crystal fabrication via thermal annealing procedures to cause particle deswelling.[25,30]

The monomers for the particle synthesis consisted of 88 mol-% NIPAm (2.9846 g), 10 mol-% AAc (0.206 mL), and 2 mol-% BIS (0.0925 g). The NIPAm and BIS were dissolved in 200 mL of water and transferred to a three-necked, round bottom flask equipped with a condenser, gas inlet, and thermometer. The solution was heated to 70 °C and purged with N_2 gas for 45 min. Since AAc tends to autopolymerize, this comonomer was added just prior to initiation. The microgel synthesis was initiated using 0.0103 g of APS dissolved in ~1 mL (0.25 mM, based on total volume). The reaction was allowed to proceed for ~4 hrs and the particles were cleaned by centrifugation three times for ~30-40 min at 25 °C using a centrifugation speed of 15,400 x *g* rcf.

The procedures that were used to fabricate the pNIPAm-*co*-AAc colloidal crystals can be found in the Experimental Section of Chapter 5. Three different samples were prepared in which the particle concentrations were varied by adjusting the percent of polymer by weight (% wt) to 2.0%, 3.0%, and 6.0% (using Eq 5.1) by centrifugation of the particle solution and removal of the supernatant, followed by quantitative addition of water to attain the desired concentration. These variations in % wt give rise to differences in the effective volume fraction of the particles.[25] These concentrated dispersions of pNIPAm-*co*-AAc particles were made homogenous by vortexing. Next, 30 ∝L of Ag particle stock solution (which was first sonicated for ~15 min to break up possible aggregates) was added to each sample and each sample was vortexed once again. These binary mixtures of particles were thermally annealed, by heating to ~50 °C for about 10 min, followed by slow cooling, to produce the crystalline assemblies.

8.2.2 Characterization Techniques

Microscopy and Particle Tracking

Most of the procedures used for the sample observations via video microscopy and the subsequent particle tracking analysis can be found in the Experimental Section of Chapter 3. Tracie Owens and Jae Kyu Cho, members of Breedveld Group at Georgia Tech, assisted in performing all of the particle tracking experiments for this study. All movies were collected using the Hamamatsu C9100 CCD camera (1000 x 400 pixels) with a frame rate of 30 frames/second. Additionally, the movies for the particle tracking of the pNIPAm-*co*-AAc particles were obtained using bright-field optical microscopy, whereas the movies for the tracking of Ag particles were collected using reflectance microscopy.

8.3 Results and Discussion

Figure 8.1 demonstrates the microscopy images that were acquired for the pNIPAm-*co*-AAc microgels (bright-field microscopy) and the Ag nanoparticles (reflectance microscopy), using the 3.0% wt sample. The pNIPAm-*co*-AAc particles adopt a hexagonally ordered arrangement, while the Ag particles appear to be randomly dispersed. Movies were collected using both microscopy techniques to track both types of particles.

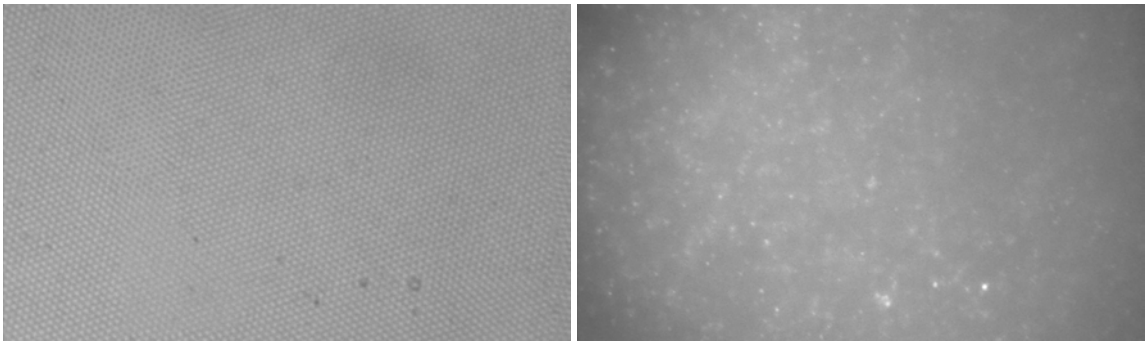

Figure 8.1 Images of the 3.0 % wt crystal collected using bright-field (left) and reflectance (right) microscopy.

The particle trajectories for both the Ag nanoparticles and the pNIPAm-*co*-AAc microgels in the 2.0% wt, 3.0% wt, and 6.0% wt crystals are shown in Figure 8.2, 8.3, and 8.4, respectively. The images are superimposed so that the positions of the particle movements can be correlated. There are obvious differences in the movements between the two types of particles. The pNIPAm-*co*-AAc particles for all of the samples remain relatively stationary, maintaining their hexagonal arrangement. However, the shapes and sizes of the trajectories for these particles are different in each case. For the 2.0% wt sample, the pNIPAm-*co*-AAc particles appear to move, while retaining their respective ordered positions in the assembly, as demonstrated by the large shape of the particle trajectories. This effect is due to more free volume available due to the low particle concentration.[25] As the % wt increases, the size of these trajectories decreases and the spacing becomes smaller, due to compression of the soft, hydrogel particle.

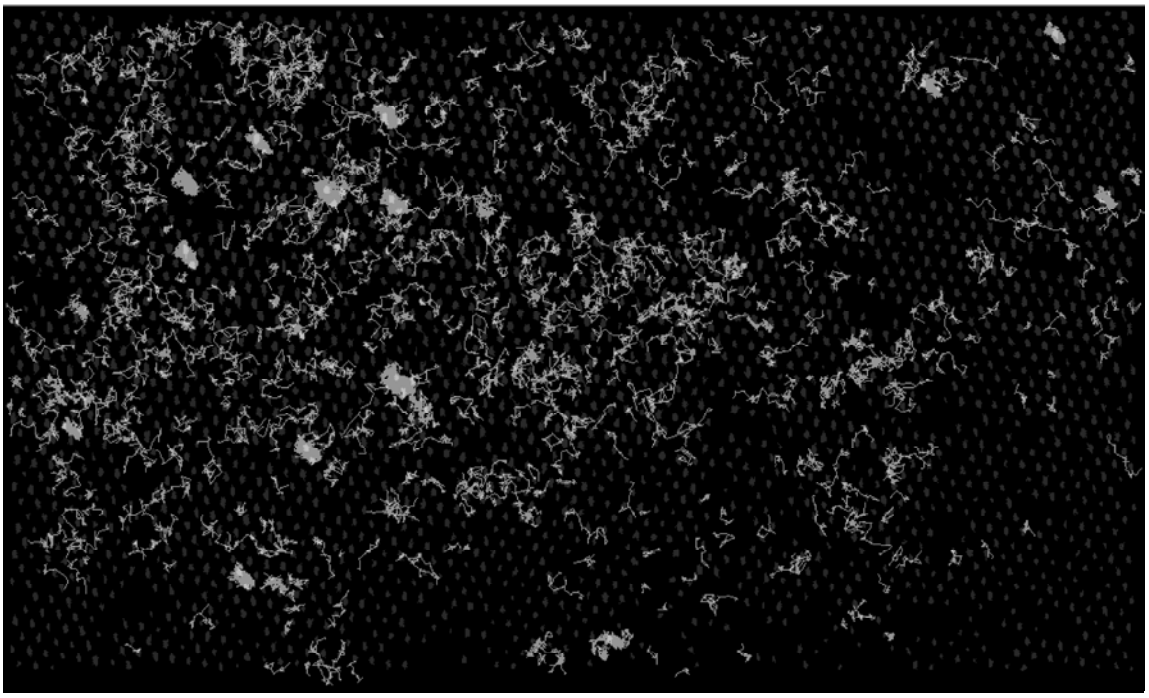

Figure 8.2 Particle trajectories for the Ag nanoparticles and pNIPAm-*co*-AAc microgels for the 2.0 % wt crystal.

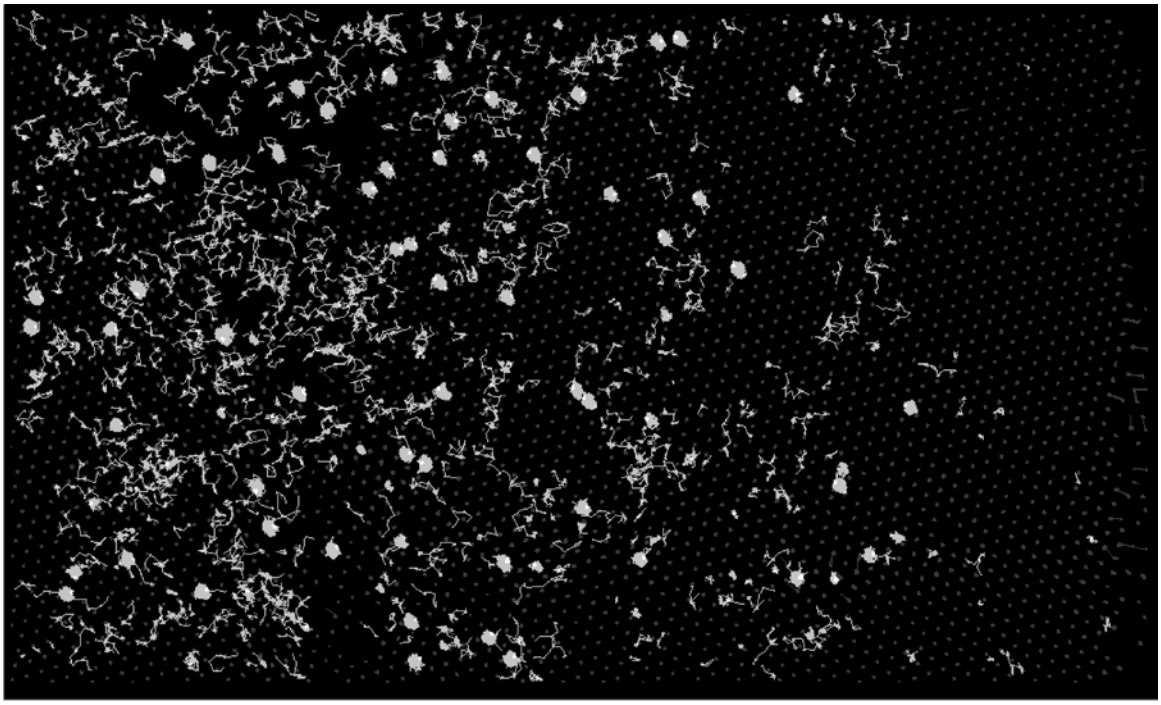

Figure 8.3 Particle trajectories for the Ag nanoparticles and pNIPAm-*co*-AAc microgels for the 3.0 % wt crystal.

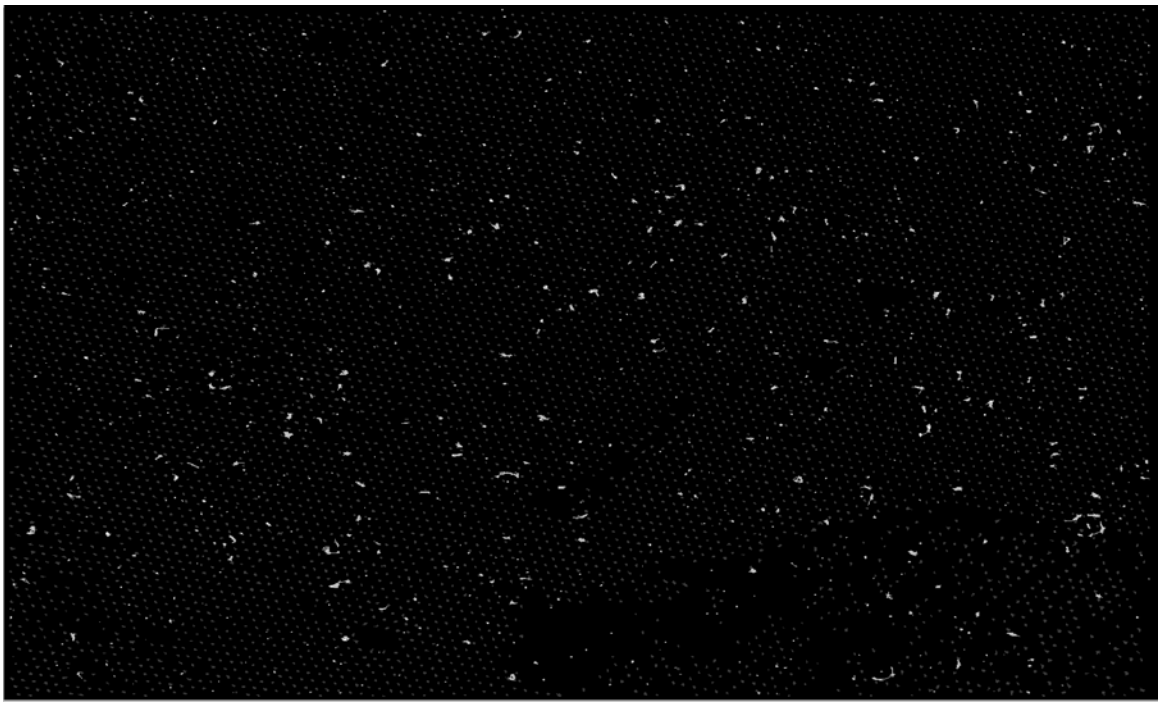

Figure 8.4 Particle trajectories for the Ag nanoparticles and pNIPAm-*co*-AAc microgels for the 6.0 % wt crystal.

On the other hand, the Ag nanoparticles have a larger range of motion. This movement is clear for both the 2.0% wt and 3.0% wt samples, where the Ag particles appear to move around the large pNIPAm-*co*-AAc particles in defined patterns. These confined movements demonstrate that the Ag particles are located in the voids between the large microgel particles. Remarkably, this movement does not disrupt the order of the pNIPAm-*co*-AAc particles. This effect may be due to attractive forces between the microgels due to their AAc side groups. This aspect has been demonstrated previously in crystal samples of pNIPAm-*co*-AAc microgels where the effective volume fraction is much lower than the that typically found for crystalline phases using hard spheres.[25] There is a slightly noticeable difference in the Ag trajectories for these samples in that the movement of the Ag particles appears to be slightly more constrained in the 3.0% wt sample than for the 2.0% wt sample, as demonstrated by more defined movements. This

effect could be due to the reduced amount of free volume available to the Ag particles in the 3.0% wt sample.

Pockets of localized Ag movement also exist in both samples, as demonstrated by areas of concentrated trajectory movements, which appear round in shape. These observations suggest that the Ag particles occupy the space available at point defects in the crystal structure. These trajectories have a more defined shape for the 3.0% wt crystal, suggesting that one or more Ag particles is kinetically "trapped" in the crystal due to the large amount of free volume available at the point defects compared to the other interstitial channels. There are fewer of these areas in the 2.0% wt crystal, which may suggest that the interstitial volume throughout the crystal is large enough to allow for release of these Ag particles.

The trajectories for the Ag particles are extremely different for the 6% wt crystal (Figure 8.4). Almost all of the Ag particles are stationary, with only a few particle displaying slight lateral movements. Additionally, the pNIPAm-*co*-AAc particles also remain stationary, and even though the concentration of pNIPAm-*co*-AAc particles is very high for this sample, the particles still demonstrate long-range order due to the compressibility of the soft hydrogel. The extent of this particle packing (high pNIPAm-*co*-AAc effective volume fraction) reduces the interstitial volume by such a large degree that Ag movement is effectively hindered.

Figure 8.5 shows graphs of the mean-squared displacement of these particles vs. the lag time. All of the data for the three pNIPAm-*co*-AAc movies demonstrates that these particles are effectively trapped in place. There is a small slope to the curve for the 2.0% wt sample, which indicates that there is some particle movement, but since this data plateaus quickly, all of the particles are essentially stationary. Although the exact effective particle size was not established for the pNIPAm-*co*-AAc particles in these crystals, the MSD levels at the positions of the plateau regions correspond to the extent of pNIPAm-*co*-AAc particle spacing (i.e. size). As the % wt of the pNIPAm-*co*-AAc

crystals was increased, these MSD values decrease, demonstrating that there is a decrease in the spacing of the pNIPAm-*co*-AAc particles at higher particle concentrations.

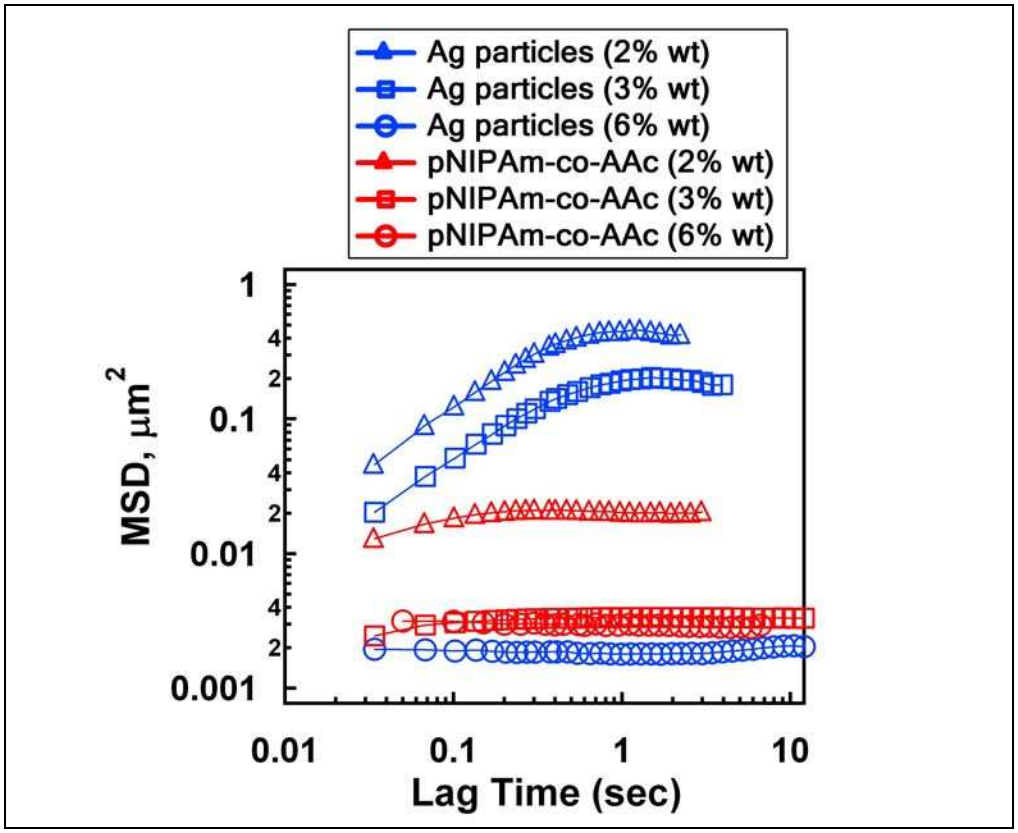

Figure 8.5 Mean-squared displacement of the Ag and the pNIPAm-*co*-AAc particles over time.

The MSD curves for the Ag particles demonstrate the high degree of motion for the particles in the 2.0% wt and 3.0% wt samples, which is due to both fast moving (more free) and caged particles. The motion of Ag particles is fluid-like due to the ability of the particles to move freely through the interstitial voids between the rather stable pNIPAm particles. However, the MSD eventually plateaus and movement of the Ag particles is restricted to certain directions as demarcated by the order of the pNIPAm particles, which is attributed to a caging effect of the particles.[21,23] Furthermore, the MSD data for the

6.0% wt crystal indicate that Ag particle motion is almost completely obstructed by the high effective volume fraction of the pNIPAm-*co*-AAc particles.

It should be noted that the free volume that is available to the Ag particles is not necessarily empty volume. Such lightly cross-linked pNIPAm particles (2 mol-% BIS in this case) have been shown to possess a radial distribution of cross-links, such that there are more loosely cross-linked polymer chains near the periphery of the particles (as discussed in Chapter 2). Although the chains of the pNIPAm-*co*-AAc particles probably extend into the interstitial voids of the crystals, the lower degree of polymer density near these interstitial spaces may allow for movement of the Ag particles until the effective volume fraction is sufficiently increased. The particle tracking of these Ag tracer particles provides a unique method for characterizing the tunability of these pNIPAm-*co*-AAc colloidal crystals, especially for the purposes of producing binary systems or structures.

Fortunately, the Ag nanoparticles that were employed in this study possessed a particle size (~ 70 nm diamter) that was appropriate for movement within the interstitial spaces of these rather large pNIPAm-*co*-AAc crystals. The softness of these ordered particles also allowed for enhanced freedom of movement of the Ag particles. Since the method that was used synthesize the Ag nanoparticles can be used to control the particle size,[17,31] one can imagine fabricating even smaller Ag tracer particles to probe colloidal crystals where the lattice building blocks are too small to be observed using standard microscopy techniques. Further, investigations are still be necessary to determine the limit of the Ag nanoparticle size for these applications due to decreases in the far-field scattering for smaller Ag particles.

8.4 Conclusions

Small (~70 nm) Ag nanoparticles were investigated as a new type of tracer agent for particle tracking experiments by using these particles to characterize the interstitial spaces of colloidal crystals composed of large pNIPAm-*co*-AAc microgels. The Ag

particles were easily detected using reflectance microscopy due to the high scattering efficiency of the Ag, and the movements of both types of particles were recorded by video microscopy. These observations demonstrated that variations in the pNIPAm-*co*-AAc particle concentrations led to changes in the available free volume within the crystal structure as well as the detection of point defects. This study demonstrates the enhanced capabilities of Ag nanoparticles as highly resolvable, robust tracer agents as a result of their scattering character and composition.

References

[1] Garbow, N.; Mueller, J.; Schaetzel, K.; Palberg, T. High-resolution particle sizing by optical tracking of single colloidal particles. *Physica A: Stat. Theoret. Phys.* **1997**, *235*, 291-305.

[2] Mason, T. G.; Weitz, D. A. Optical measurements of frequency-dependent linear viscoelastic moduli of complex fluids. *Phys. Rev. Lett.* **1995**, *74*, 1250-3.

[3] Solomon, M. J.; Lu, Q. Rheology and Dynamics of Particles in Viscoelastic Media. *Current Opinion Coll. Inter. Sci.* **2001**, *6*, 430-437.

[4] Crocker, J. C.; Grier, D. G. Methods of digital video microscopy for colloidal studies. *J. Coll. Interface Sci.* **1996**, *179*, 298-310.

[5] Wit, P. J.; Noordmans, J.; Busscher, H. J. Tracking of colloidal particles using microscopic image sequence analysis. Application to particulate microelectrophoresis and particle deposition. *Colloid Surf., A: Physicochem. Eng. Asp.* **1997**, *125*, 85-92.

[6] MacKintosh, F. C.; Schmidt, C. F. Microrheology. *Current Opinion Coll. Inter. Sci.* **1999**, *4*, 300-307.

[7] Mukhopadhyay, A.; Granick, S. Micro- and nanorheology. *Current Opinion Coll. Inter. Sci.* **2001**, *6*, 423-429.

[8] Valentine, M. T.; Kaplan, P. D.; Thota, D.; Crocker, J. C.; Gisler, T.; Prud'homme, R. K.; Beck, M.; Weitz, D. A. Investigating the microenvironments of inhomogeneous soft materials with multiple particle tracking. *Phys. Rev. E: Stat., Nonlin., Soft Matt. Phys.* **2001**, *64*, 061506/1-061506/9.

[9] Briggs, M. E.; Sengers, J. V.; Francis, M. K.; Gaspard, P.; Gammon, R. W.; Dorfman, J. R.; Calabrese, R. V. Tracking a colloidal particle for the measurement of dynamic entropies. *Physica A: Stat. Mech. Appl.* **2001**, *296*, 42-59.

[10] Breedveld, V.; Pine, D. J. Microrheology as a tool for high-throughput screening. *J. Materials Sci.* **2003**, *38*, 4461-4470.

[11] Slopek, R. P.; McKinley, H. K.; Henderson, C. L.; Breedveld, V. In situ monitoring of mechanical properties during photopolymerization with particle tracking microrheology. *Polymer* **2006**, *47*, 2263-2268.

[12] Chou, C. Y.; Eng, B. C.; Robert, M. One-dimensional diffusion of colloids in polymer solutions. *J. Chem. Phys.* **2006**, *124*, 044902/1-044902/6.

[13] Messinger, B. J.; Von Raben, K. U.; Chang, R. K.; Barber, P. W. Local fields at the surface of noble-metal microspheres. *Phys. Rev. B: Cond. Matt. Mater. Phys.* **1981**, *24*, 649-57.

[14] Bohren, C. F.; Huffman, D. R. *Absorption and Scattering of Light by Small Particles*; John Wiley and Sons, Inc.: New York, 1998.

[15] Sönnichsen, C.; Franzl, T.; Wilk, T.; von Plessen, G.; Feldmann, J. Plasmon Resonances in Large Nobel-Metal Clusters. *New J. Phys.* **2002**, *4*, 93.1-93.8.

[16] Bohren, C. F. How can a particle absorb more than the light incident on it? *Am. J. Phys.* **1983**, *51*, 323-7.

[17] Evanoff, D. D., Jr.; Chumanov, G. Size-Controlled Synthesis of Nanoparticles. 2. Measurement of Extinction, Scattering, and Absorption Cross Sections. *J. Phys. Chem. B* **2004**, *108*, 13957-13962.

[18] Chumanov, G.; Sokolov, K.; Cotton, T. M. Unusual Extinction Spectra of Nanometer-Sized Silver Particles Arranged in Two-Dimensional Arrays. *J. Phys. Chem.* **1996**, *100*, 5166-8.

[19] Kumbhar, A. S.; Kinnan, M. K.; Chumanov, G. Multipole Plasmon Resonances of Submicron Silver Particles. *J. Am. Chem. Soc.* **2005**, *127*, 12444-12445.

[20] Malynych, S.; Chumanov, G. Coupled planar silver nanoparticle arrays as refractive index sensors. *J. Optics A: Pure and Appl. Opt.* **2006**, *8*, S144-S147.

[21] Weeks, E. R.; Crocker, J. C.; Levitt, A. C.; Schofield, A.; Weitz, D. A. Three-dimensional direct imaging of structural relaxation near the colloidal glass transition. *Science* **2000**, *287*, 627-631.

[22] Gasser, U.; Weeks, E. R.; Schofield, A.; Pusey, P. N.; Weitz, D. A. Real-space imaging of nucleation and growth in colloidal crystallization. *Science* **2001**, *292*, 258-262.

[23] Alsayed, A. M.; Islam, M. F.; Zhang, J.; Collings, P. J.; Yodh, A. G. Premelting at Defects Within Bulk Colloidal Crystals. *Science* **2005**, *309*, 1207-1210.

[24] Debord, J. D.; Lyon, L. A. Thermoresponsive Photonic Crystals. *J. Phys. Chem. B* **2000**, *104*, 6327-6331.

[25] Debord, S. B.; Lyon, L. A. Influence of Particle Volume Fraction on Packing in Responsive Hydrogel Colloidal Crystals. *J. Phys. Chem. B* **2003**, *107*, 2927-2932.

[26] Lyon, L. A.; Debord, J. D.; Debord, S. B.; Jones, C. D.; McGrath, J. G.; Serpe, M. J. Microgel Colloidal Crystals. *J. Phys. Chem. B* **2004**, *108*, 19099-19108.

[27] Debord, J. D.; Eustis, S.; Debord, S. B.; Lofye, M. T.; Lyon, L. A. Color-tunable colloidal crystals from soft hydrogel nanoparticles. *Adv. Mat.* **2002**, *14*, 658-662.

[28] Israelachvili, J. *Intermolecular and Surface Forces, 2nd ed.*; Academic Press: San Diego, 1992.

[29] Lide, D. R. *Handbook of Chemistry and Physics, 74th ed.*; CRC Press: Boca Raton, FL, 1994.

[30] Jones, C. D.; Lyon, L. A. Synthesis and Characterization of Multiresponsive Core-Shell Microgels. *Macromolecules* **2000**, *33*, 8301-8306.

[31] Evanoff, D. D., Jr.; Chumanov, G. Size-controlled synthesis of nanoparticles. 1. Silver-only aqueous suspensions via hydrogen reduction. *J. Phys. Chem. B* **2004**, *108*, 13948-13956.

CHAPTER 9

FUTURE DIRECTIONS

This body of work demonstrates that many advanced colloidal crystal materials can be developed through the implementation of creative design techniques, especially by employing the core/shell topology. Many suggestions for further development are presented throughout the work. However, some specific, fundamental studies would be valuable to obtain a greater understanding of these materials and to develop their application in a number of different fields.

Chapters 4-7 discuss how pS-*co*-NIPAm microparticles can be used for producing stable, robust colloidal crystals that are easily processable. More fundamental studies of the synthesis of these particles would provide more control over the assembly of these materials. Specifically the hydrophobicity/hydrophilicity of the polystyrene and pNIPAm-rich regions should be explored to determine what effects these copolymer syntheses have on the final particle identity. Different types of polymerization techniques could also be explored, such as dispersion polymerization using different solvents (such as ethanol), which may lead to the development of more stable and larger particles.

The processability of these particles allows for more complex three-dimensional designs and creative microstructures (such as inks for fingerprinting applications). The ability to form cross-linked, robust structures using these particles while retaining their hydrogel features provides an excellent construct that can be applied for sensor strategies in liquid environments or in constructing colloidal crystal membranes. However, more experiments need to be performed to ascertain the origin and form of these cross-links, as well as extent of the cross-links throughout the z-dimension of the films. These features can be ascertained by a more in depth characterization of the pS-*co*-NIPAm particles as well as methods development of the baking process. The core/shell construct can also be used to introduce different types of functional moieties or other components into the

colloidal crystal. The investigation of their interactions while situated in this structure can be useful for producing interesting optical materials. Introduction of such components can also be used with the cross-linked crystals to form innovative sensing materials.

A few advancements have been made in the generation of binary colloidal crystals where two types of particles that possess different sizes have been used to produce structures that resemble atomic structures other than typical than structures found using traditional colloidal crystals. The simple self-assembly technique and processability afforded by pS-*co*-NIPAm particles may allow for the fabrication of such structures using pS-*co*-NIPAm particles of different sizes. Similarly, the ability to incorporate silver nanoparticles into the interstitial spaces of colloidal crystals (Chapter 8) demonstrates how such binary structures may be accomplished using soft spheres. This configuration would allow for the modification of the size of the interstitial voids by tuning the size of the crystal building blocks by a variety of means. This capability may prove useful for providing a controlled location for reactions to occur to, in effect, produce ordered arrays of microreactors. This design may also be useful for the fabrication of multifunctional particles with distinctly positioned regions of functionality on the particle surface. The ability for the silver particles to move within the interstitial spaces demonstrates the potential for using colloidal crystals as a separation system, where the pNIPAm particles could possess functionalities that interact with an analyte while the separation channels could be controlled by adjusting the pNIPAm volume fraction.

Additional syntheses could be performed to scale up the amount of silver core/pNIPAm shell particles that were discussed in Chapter 3. In this way, the ability to form colloidal crystals via thermal annealing procedures using the pNIPAm shell could be evaluated. This would allow for an investigation of the cooperative plasmon modes of the ordered silver particles based on their interparticle distances, to ascertain their properties and use them to prepare interesting optical materials.